

Physics of associative polymers; bridging time and length scales

Promotoren Prof. dr. M.A. Cohen Stuart,
 hoogleraar fysische chemie en kolloïdkunde,
 Wageningen Universiteit

 Prof. dr. ir. F.A.M. Leermakers,
 persoonlijk hoogleraar bij de leerstoelgroep
 Fysische Chemie en Kolloïdkunde,
 Wageningen Universiteit

Copromotor Dr. ir. J. van der Gucht,
 universitair docent bij de leerstoelgroep
 Fysische Chemie en Kolloïdkunde,
 Wageningen Universiteit

Samenstelling promotiecommissie:

Prof. dr. B.M. Mulder	Wageningen Universiteit
Prof. dr. D.A. Weitz	Harvard University, Cambridge, USA
Prof. dr. J.-F. Berret	Université Paris 7 - Denis Diderot, France
Prof. dr. J.K.G. Dhont	Forschungszentrum Jülich, Germany

Dit onderzoek is uitgevoerd binnen de onderzoeksschool VLAG

Physics of associative polymers; bridging time and length scales

Joris Sprakel

Proefschrift
ter verkrijging van de graad van doctor
op gezag van de Rector Magnificus
van Wageningen Universiteit,
Prof. dr. M.J. Kropff,
in het openbaar te verdedigen
op vrijdag 12 juni 2009
des namiddags te vier uur in de Aula

ISBN: 978-90-8585-365-7

“WHENEVER A THEORY APPEARS TO YOU AS THE ONLY POSSIBLE ONE,
TAKE THIS AS A SIGN THAT YOU HAVE NEITHER UNDERSTOOD THE THEORY
NOR THE PROBLEM WHICH IT WAS INTENDED TO SOLVE”

Karl Popper

This research forms part of the research program of the Dutch Polymer Institute (DPI), Technology Area Coating Technology, DPI project #564.

Contents

1	Introduction	1
	Associative Polymer Self-Assembly	13
2	Comprehensive theory for star-like polymer micelles	15
3	Micellization of telechelic associative polymers	37
4	Phase behavior of flowerlike micelles	53
	Associative Polymers at Surfaces	77
5	Equilibrium capillary forces with Colloid Probe AFM	79
6	Capillary adhesion in the limit of saturation	89
7	Dynamics of polymer bridge formation and disruption	117
8	Hierarchical adsorption of associative polymers	127
	Rheology of Associative Polymers Networks	141
9	Brownian particles in transient polymer networks	143
10	Shear banding in associative polymer networks	163
11	Intermittent dynamics in shear-banded networks	185
12	MR velocimetry of telechelic polymer networks	195
	Summary & General Discussion	207
	Samenvatting	225
	List of Publications	231
	Dankwoord	233
	Levensloop	237

Chapter 1

Introduction

In this dissertation the work of my PhD project is presented. This project, part of the research program of the Dutch Polymer Institute and carried out within the Laboratory of Physical Chemistry and Colloid Science at Wageningen University, was officially titled "SF²: Colloidal interactions modified by associative thickeners in waterborne paint formulations. Surface forces and Scheutjens-Fleer modeling". As you can see, the thesis in front of you bears a title, "Physics of Associative Polymers", much broader in definition (and a bit more concise). During the course of this project we came across a variety of interesting phenomena and decided to pursue several routes, some closer to the original working plan than others.

1.1 Paints

Coatings are ubiquitous in everyday life. These layers are applied to almost any imaginable surface for various reasons, ranging from protecting the underlying surface from corrosion, weathering or microbial attack, to giving the surface specific properties such as electric conductance, light reflectance (shine) or water repellency, and not to forget purely aesthetical reasons such as providing surfaces (e.g. walls) with a desired color. Because of their widespread use, the coating industry is also economically of significance in the world economy; in 2008 thirty billion liters of coating products (paints, powders, etc.) have been sold worldwide, at a total turn-over of around 100 billion euro.

One of the ways to apply a coating is by means of a paint, that according to the Merriam-Webster Dictionary is "*a mixture of a pigment and a suitable liquid to form a closely adherent coating when spread on a surface in a thin coat*". A paint is thus a vehicle with which a coating can be applied. Nevertheless, these terms are often used interchangeably.

Most paints consist of 3 basic components; i) a solvent, that thins the paint to facilitate application in the form a thin coat, ii) a binder, that forms the final coating after evaporation of the solvent, and which holds iii) the pigment, that gives the coating its opacity and color. This basic lay-out is already found in some of the oldest known paint formulations; for example the so-called tempera paints, used in the earliest European civilizations, consisted of egg yolk (binder), pigments and water as a thinner. In the middle ages, slow-drying and curing (i.e. plastic-forming) vegetable oils, such as linseed oil, replaced egg yolk as a binder. Synthetic (man-made) plastics (polymers) became largely available as modern binder materials in the twentieth century, starting with the introduction of nitrocellulose as a binder by DuPont in 1920.

Modern decorative paints, e.g. for painting in- and exteriors of buildings and other structures, can be split up into two main categories, either solvent-based or water-based, depending on the type of liquid that carries the pigments and the binder.

In solvent-based paints, that have dominated the decorative coatings market for decades, the binder is dissolved in a volatile apolar, organic solvent, together with various additives. While these traditional systems have a high performance in terms of leveling, resistivity to water, durability and aesthetics (e.g., gloss), they pose a serious threat to both the environment and to consumers that handle the paints, as significant quantities of harmful substances are released into the air during drying of the paint. In recent years it has been established that prolonged exposure

Table 1.1: Maximum allowed VOC content in grams per liter of paint, for either water based (WB) and solvent based (SB) paints, as indicated in Directive 2004/42/CE of the European Union/European Council. Phase 1 has commenced in January 2007, Phase 2 will start in 2010.

Product category	Product type	Phase 1	Phase 2
Interior matt wall paints	WB	75	30
	SB	400	30
Interior gloss wall paints	WB	150	100
	SB	400	100
Exterior stone/brick wall paints	WB	75	40
	SB	450	430
Exterior/Interior wood paints	WB	150	130
	SB	400	300

to a solvent-enriched atmosphere can cause a variety of severe health problems. The best-documented of these is the so-called painter's disease, or chronic solvent-induced encephalopathy, leading to memory problems, dysfunctional mental and motorial speed and impaired concentration. Moreover, emission of volatile organic compounds (VOCs) leads to ozone formation in the troposphere, and is thought to contribute to global warming and climate change. Paints, lacquers and glues are identified as the second largest contributors to the emission of VOCs, the first place being held by VOCs released during the combustion of fossil fuels.

For the reasons stated above, the European Union has adopted strict guidelines (EU directive 2001/81/EC) for the further production and use of VOC-rich products, and has the intention to eventually phase-out these products completely. The current agreements to reduce the VOC content of paints consist of two phases, the first one is currently in action (started in 2007). In the second phase, starting in 2010, even more drastic reductions in VOC contents must be accomplished (see Table 1.1 for an example of allowed VOC contents of paints). Note that in 2010 almost all VOCs must be removed from paints used in closed areas, for the health reasons mentioned above. Similar recommendations are also part of international agreements such as the Kyoto-protocol (UN directive FCCC/CP/1997/L.7/Add.1).

Several technologies are currently available to reduce the VOC emission from coatings:

- Waterborne paints: water is used as the main solvent
- High solids paints: reduction of the VOC content by increasing the concen-

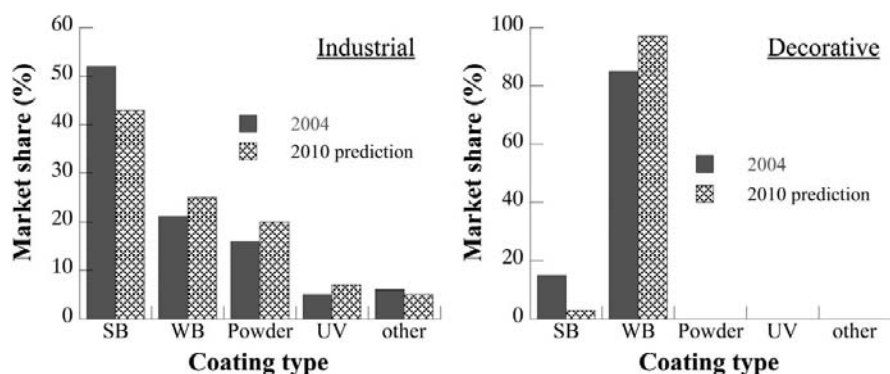


Figure 1.1: Market share of various coating types (SB: solvent-based, WB: water-based, UV: UV-curable coatings) for either industrial use or decorative purposes (consumer market) in 2004 and prediction for 2010. Data courtesy of Akzo Nobel.

tration of solid materials (pigments, binders) in the paint

- Powder coatings: the solvent is completely removed and the coating is applied as a dry powder, which is cured with a heat treatment
- Reactive solvent technology: the solvent is not released but becomes part of the coating by reacting during a curing process.

An overview of the market share of these various paint systems, compared to solvent-based paints, is given in Fig.1.1. It is clear that already in 2004, waterborne paints are the most important alternative to traditional VOC-rich paints. From their introduction in the 1980s, waterborne systems have achieved a significant market share in the industrial market and have almost completely replaced solvent-based paints in the consumer market.

Whereas the binder material is dissolved in an organic solvent in traditional paints, binder materials are typically not soluble in water. To create a suitable waterborne paint, the binder must be dispersed in small (typically between 10-1000 nanometers) droplets or particles. Such a dispersion of small polymer colloids in water is called a latex, giving its name to the well known latex paints. A typical latex paint consists of 25 wt% binder particles, 25% titanium dioxide (a white pigment that gives the final coating its opacity), 5 wt% surfactants (i.e. surface-active compounds used mainly for stabilization of the binder and pigment particles), 1 wt% thickeners and 44 wt% of water.

To establish the intended shift in the coatings market, it is essential that modern water-based paints can offer the same performance as their traditional, solvent-

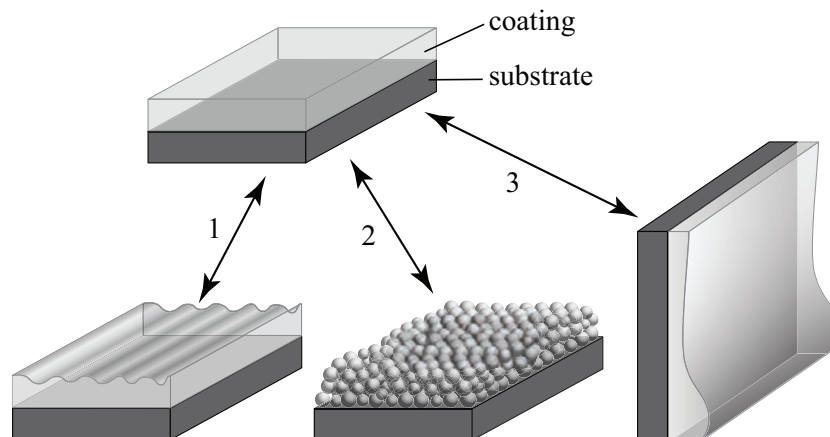


Figure 1.2: Illustration of some problems that can lead to poor coating quality. An ideal coating (top picture) is a flat homogeneous layer of uniform thickness. Complications in aqueous paint systems include (bottom row from left to right): i) poor leveling; brush or spray marks remain visible in the final coating. ii) inhomogeneous film; lack of coalescence of the latex particles gives an irregular and porous film. iii) sagging; the paint flows due to gravity if the viscosity of the paint does not increase fast enough during drying.

based, counterparts. However, there are many issues with the formulation and application of aqueous paints that must be solved in order to reach this objective. Such issues include homogeneity of the film formed from the binder material, resistivity to water after drying and leveling of the paint after brushing or spraying. See Fig.1.2 for an illustration of several of the complications when working with aqueous paints.

In solvent-based paints, the binder material is dissolved, i.e. the polymer chains of the binder are swollen, and ensure a high viscosity of the paint so that it does not sag or drip once it is applied. In water-based paints, the polymer (latex) particles, have only a very small effect on the viscosity of the paint, and without the addition of thickeners the paint would be approximately as viscous as milk. Thickeners are therefore essential for the performance of the paint during application. Unfortunately, it seems that the thickeners of choice, so-called associative thickeners, which can provide a paint with all the desired flow properties, have an adverse effect on the colloidal stability of the binder and pigment suspension. This destabilization is thought to lead to a phenomenon known as syneresis or clear-liquid separation, in which the paint expels a clear liquid phase.

In this dissertation we have studied the mechanisms that underly both the

desired and undesired behavior of these associative thickeners in aqueous systems. Improving the performance of thickeners in waterborne paints is one of the steps towards the further phasing-out of solvent-based paints.

1.2 Associative Thickeners

Associative thickeners for aqueous applications are macromolecules (polymers), with a part that is soluble in water, the so-called backbone or spacer, to which two or more moieties that do not dissolve in water, the stickers, are attached. The hydrophilic backbone of associative thickeners can be any water-soluble macromolecule, either linear, branched or star-shaped and can be neutral or bear charges. The hydrophobic stickers can be any type of water-fearing molecule, such as small hydrocarbon or fluorocarbon chains or apolar polymer chains. The simplest class of associative polymers, which we have used in this thesis as a model system for associative thickeners in general, are telechelic associative polymers, in which two end-anchored hydrophobic stickers are connected by a watersoluble, flexible polymer chain (Fig.12.6a). More specifically, we have used the HEUR (hydrophobically-modified ethoxylated urethanes) class of thickeners; composed of a poly(ethylene oxide) backbone with hydrocarbon tails at both chain ends.

In general, molecules with distinguishable hydrophilic (water-loving) and hydrophobic (water-fearing) parts are known as amphiphiles. Amphiphilic molecules are very common in nature, such as phospholipids that form the membranes around cells and almost all proteins. Another well known class of amphiphiles are soaps, or surfactants, which are widely used as detergents, emulsifiers, foaming agents, and so on.

Amphiphiles in solution can spontaneously form supramolecular structures, i.e. objects formed from multiple molecules, in a process commonly known as self-assembly. The parts of these molecules that do not like the surrounding solvent tend to cluster in order to reduce the unfavorable contacts with solvent molecules. On the other hand, the solvophilic parts of amphiphiles do not want to be clustered, so that they can maximize their contact with the solvent. A delicate balance between these two opposing forces, a growth and a stopping force, is responsible for the formation of well-defined structures, such as micelles (see Chapter 2), vesicles, membranes, and networks. The type of structure that is formed depends on the structure of the amphiphile, its concentration in solution, the solvent in which it is dissolved and many more physicochemical factors.

When telechelic associative polymers are dissolved in water at sufficient con-

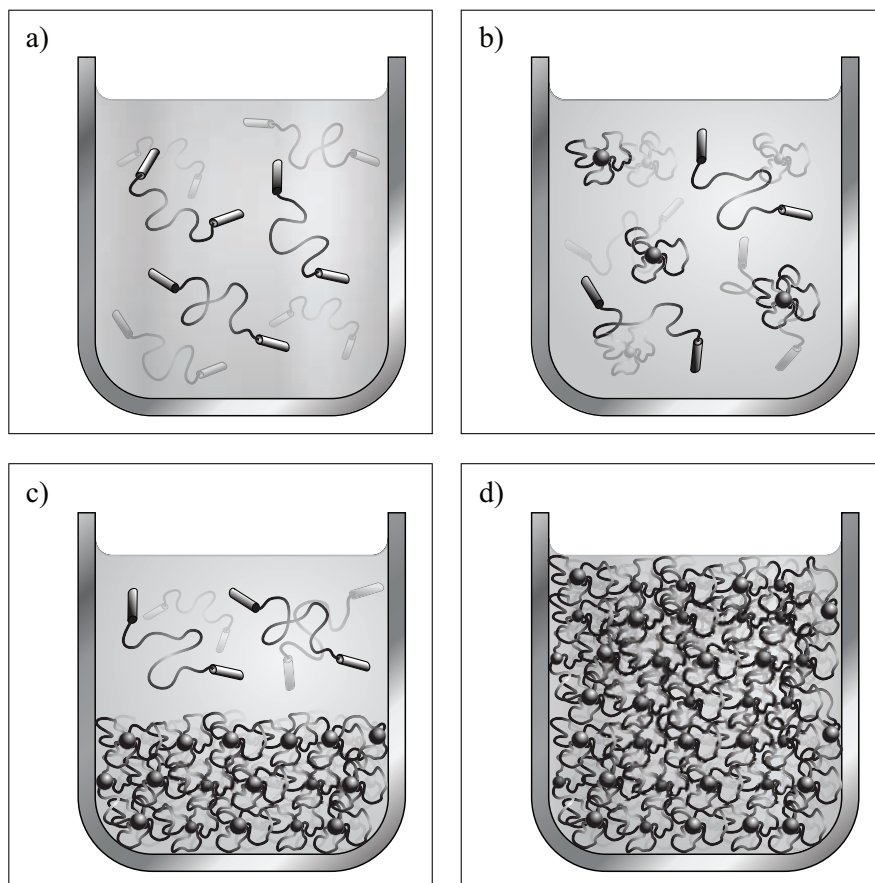


Figure 1.3: Illustration of the 4 different states of telechelic associative polymer solutions with increasing concentration from a to d; a) at concentrations below the critical micelle concentration (cmc) the chains exist as isolated unimers, b) above the cmc the telechelic polymers associate into flowerlike micelles, c) at intermediate concentrations (typically between 0.1 and 1 wt%) some systems (depending on the molecular architecture) show a demixing into a percolated polymer-rich phase and a polymer-poor phase that contains some isolated micelles and unimers, d) above the percolation concentration a sample-spanning transient network is formed in which micellar cores form the network nodes, interconnected by flexible polymer chains. At even higher concentrations, depending on the molecular weight of the spacers, additional crosslinks due to chain entanglements are formed.

centration (i.e. above the critical micelle concentration), hydrophobic interactions between the end-blocks and the preference for the spacer to remain in contact with the solvent cause the thickeners to self-assemble into micelles. In dilute solutions, when the average distance between the micelles is much larger than the size of the micelles, both stickers will reside in the same micellar core, forcing the flexible spacer into a loop configuration (Fig.12.6b). As these looped chains resemble the petals of a flower, these micelles are referred to as flowerlike micelles. The formation of flowerlike micelles, and of polymeric micelles in general, is discussed in Chapters 2 & 3.

As the polymer concentration is increased, the number of micelles increases. At some point, the average distance between the micelles is on the order of the size of a micelle, allowing a chain to have one of its associating ends in one micelle while the other end forms part of a neighboring micelle. In this way bridges are formed between micelles. This gives rise to a purely entropic attraction between the flowerlike micelles, which can cause demixing of the solution into a phase rich in polymer and a phase containing mainly excess solvent and some micelles and unimers (Fig.12.6c). This behavior is not observed for all systems of telechelic polymers and depends strongly on the molecular architecture, as is discussed in Chapter 4.

At high enough concentrations, all micelles will be interconnected by polymer bridges, leading to a sample-spanning network (Fig.12.6d). Due to the dynamic character of the micelles, the nodes or crosslinks in these networks are not permanent, but have a finite lifetime. That is why these networks are called transient or reversible, in contrast to, e.g., rubbers in which the polymer chains are connected through covalent, chemical bonds that are permanent.

Networks formed by associative thickeners show two main features that makes them interesting rheology modifiers for coatings. First of all, these systems have a high viscosity compared to solutions of unmodified polymers, due to the efficient structure of the networks they spontaneously form. A high viscosity in rest prevents sagging of the paint after application and before drying is complete. Secondly, all of these associative polymer networks display non-Newtonian behavior. In general this signifies that the viscosity depends on the rate of deformation, whereas a Newtonian fluid (such as water) has a viscosity that does not depend on the rate with which the liquid is deformed. More specifically, these transient networks show pronounced shear thinning, that is a viscosity that decreases with increasing flow rate. This facilitates the application of the paint and improves the leveling, which is the spreading of the paint directly after application so that no brush marks are visible in the final coating. The microscopic interpretation and consequences of

this shear thinning are discussed are Chapters 9 to 11.

In order to understand the function of associative thickeners in paints, we must realize that paints are highly complex systems. As discussed above (paragraph 1.1), a typical latex paint contains only 44 % of water, while the remainder consists of various particulate materials (binder, pigments) and a large variety of additives (surfactants, co-solvents). Many of these components interact with each other. The thickener can adsorb onto the particle surfaces, but must compete with the surfactant to do so. Moreover, the surfactants that remain in the bulk will assemble together with the thickener, which can either enhance or reduce the thickening action, depending on the relative amounts of both species.

In my PhD work I adopted a bottom-up approach. I started by studying the self-assembly and phase behavior of bulk solutions of telechelic associative polymers in thermal and mechanical equilibrium (Part 1). Subsequently, I investigated the behavior of these polymers at and near solid surfaces (Part 2). Finally, I studied the mechanical properties of networks formed by associative polymers, and how these properties are influenced by shear flow (Part 3).

1.3 Bridging time and length scales

Aside from the practical relevance described above, associative polymers are interesting from a purely academic point of view. They are ideally suited to study a number of topical themes in soft matter physics, such as hierarchical self-assembly, non-newtonian fluid mechanics, phase equilibria and colloidal interactions. In a way, these systems are a playground for soft matter scientists, which I have explored in this thesis.

One of the fascinating aspects of these associative polymers, due to their tendency to assemble into structures at various levels, is that interesting physics can be found across many time and length scales. Hence the sub-title of my dissertation.

In Fig.1.4 some of the phenomena under study are categorized according to the typical time scale on which they occur. Starting from the dynamics of colloidal particles embedded in associative polymer networks, as discussed in Chapter 9, that show a Rouse-like motion on microsecond timescales, to the elastic caging of the same particles on timescales on the order of the relaxation time of the networks, which depends on sticker chemistry and length, temperature and concentration. For the systems explored here this microscopic relaxation time is typically between 0.1 and 100 milliseconds. At longer timescales, we find more cooperative processes, such as the capillary condensation described in Chapters 5 and 6. Due to the

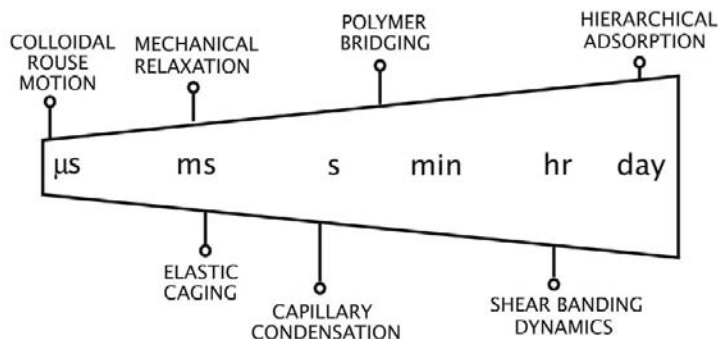


Figure 1.4: Illustration of the various time scales and associated phenomena in associative polymer systems reported in this thesis.

ultralow interfacial tension between the two coexisting phases and the small length scales, this condensation process was still fast enough (order 25 milliseconds) to allow us to measure capillary forces in full thermodynamic equilibrium for the first time. Although the formation of polymeric bridges between two surfaces, as discussed in Chapter 7, is not a cooperative process (i.e. it does not require several chains to perform the same action simultaneously), it is significantly slower than the capillary condensation. This is due to the fact that bridging requires the polymer chains to desorb, which is inherently slow. In our study of mechanical instabilities in associative polymer networks under shear flow, as described in Chapters 10 to 12 we found processes on even longer timescales. These are associated with the formation of shear bands, which are coexisting zones of varying shear rate and different internal structure, and the subsequent erratic fluctuations in the banded structure. Again, these long time scales are the result of cooperative processes that are further hindered by the velocity gradients between neighboring fluid elements due to the flow. At time scales of a day to several days we find the hierarchical adsorption of telechelic polymers from dilute solutions onto an air-water interface, discussed in Chapter 8. The 'normal' adsorption modes, i.e. diffusion towards the bare interface and reorganizations at the interface, which are also found for other types of amphiphiles, are relatively fast. However, the formation of a secondary sub-surface layer of pendant micelles, a specific feature of the network-forming polymers studied in this dissertation, may take up to 10^6 seconds to complete.

In the same way we can categorize some of the phenomena that we have studied according to the typical length scale on which they occur. The smallest relevant

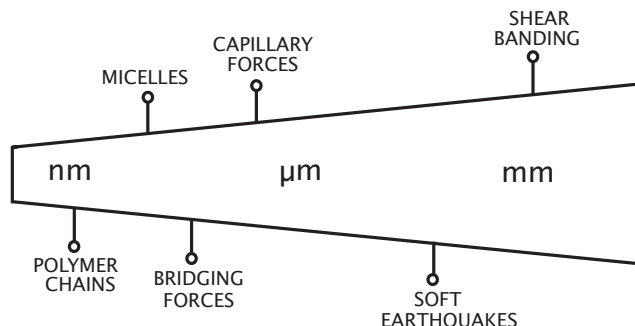


Figure 1.5: Illustration of the various length scales and associated phenomena in associative polymer systems reported in this thesis.

length scale is obviously the size of a single telechelic polymer molecule. Here we have worked with telechelic polymers with a radius of gyration between 2 - 5 nm. Above the critical micelle concentration (see Chapters 2 - 4), several of these molecules associate to form the flowerlike micelles discussed above. There are typically around 10-20 polymers in a single micelle, yielding micelles with a radius of 10 - 20 nanometers. When two hydrophilic surfaces covered with these flowerlike micelles are brought in close contact, bridges between the two surfaces can be formed, as we show in Chapter 7. When we subsequently increase the distance between these surfaces again, a polymer bridge is stretched like a spring, until the restoring force becomes too large, and the bridge detaches from one of both surfaces. Here we found that the polymer chains are typically stretched to ~ 5 times (i.e. 15-40 nm) their preferred size, before the bridges are broken. Between very hydrophobic surfaces however, where there is a strong tendency for the hydrophobic stickers to adsorb, we find attractive forces that range up to 300 nm. In Chapters 5 and 6 we attribute this attraction to a phenomenon called capillary condensation, i.e. a condensation (phase separation) of a polymer-rich liquid between the two surfaces. Finally, we have studied a phenomenon that occurs on macroscopic length scales (millimeters): shear banding (Chapter 10). Under steady deformation, networks of these polymers may become unstable. Rather than a thermodynamic phase transition, shear banding can be regarded as a mechanical phase separation. The fluid splits up into two macroscopic bands that differ in viscosity and internal structure. Around the boundary between these layers we have found anomalous fluctuations in fluid velocity, resulting in large stress fluctuations (Chapter 11). These non-linear dynamics, that we have colloquially called 'soft

earthquakes' also occur on macroscopic length scales (0.1 - 1 millimeter).

The Chapters in this dissertation are written as independent scientific papers, and each one deals with one (or several) of the phenomena listed above. However, in the final chapter of this thesis, the *General Discussion*, I have tried to bring together and connect some of the observations from the various chapters. This discussion also serves to speculate in which direction one has to look for possible solutions to the remaining questions.

Part I

Associative Polymer Self-Assembly



Chapter 2

Comprehensive theory for star-like polymer micelles

In this Chapter a comprehensive theory is proposed that combines classical nucleation and polymer brush theory to describe star-like polymer micelles. With a minimum of adjustable parameters, the model predicts properties such as critical micelle concentrations and micellar size distributions. The validity of the present theory is evidenced in direct comparison to experiments. Furthermore, we show that the predicted saddle points in the free energy correspond to those solutions that are accessible with self-consistent field methods for self-assembly.

This chapter was published as:

J. Sprakel, F.A.M. Leermakers, M.A. Cohen Stuart and N.A.M. Besseling: *Comprehensive theory for star-like polymer micelles; combining classical nucleation and polymer brush theory*, Phys. Chem. Chem. Phys. **10** (2008), 5308.

2.1 Introduction

Micellization can be regarded as arrested, mesoscopic demixing. Solvophobic tails segregate from a solvent, but the growth of droplets is restricted by the build-up of a lateral pressure at the interface between the segregated droplet and the surrounding solvent phase. This lateral pressure in the so-called micellar corona, essentially comes from the solvation of the head groups and can be described either by electrostatic interactions between charged head groups (ionic surfactants), or by steric effects between neutral solvophilic head groups. Without this stop mechanism, the growth of nuclei would ultimately lead to the formation of a macroscopic phase, separated from the solvent by a flat interface. Because of the two counteracting forces at play, a thermodynamic equilibrium is reached between unimers and well-defined objects of a finite size, i.e. micelles. This conceptual picture basically decomposes any micellization problem into two main issues: the micellar core and the micellar corona. This division is also found in many of the theoretical investigations of surfactant and polymer self-assembly.

Nagarajan and Ruckenstein [1] describe three main contributions to the free energy of micellization for small surfactants, that are associated with the micellar core; i) the transfer of a solvophobic block from the solvent to the micellar core, ii) the deformation energy of solvophobic tails in the core and iii) the work of forming the interface between the core and the surrounding solvent. Zhulina et al. [2] consider the same three core-contributions in their model for spherical polymeric micelles. They argue however, that contribution i) can be ignored, since the solvophobic block will be in a collapsed state even for unassociated molecules, i.e. unimers. Of course this argument is only valid when the solvophobic block consists of many statistical segments. When the associating block is a short alkyl-tail, with only 2 or 3 statistical segments, collapse of this block in the unimer state is not very likely. Moreover, when contribution i) is omitted the theory can no longer predict a critical micelle concentration. In other, more approximate, models, contributions i) and ii) are neglected, and only the interfacial energy is accounted for [3, 4]. In the model that we propose in this Chapter we will account for contributions i) and iii) using classical nucleation theory [5], and use Semenov's approach [6] to account for the deformation of the tails in the core. A nucleation approach to the formation of micelles was employed by Besseling and Cohen Stuart [7], in the context of a self-consistent field theory, leading to the conclusion that nucleation in solutions of amphiphiles is significantly different from nucleation in systems of immiscible simple fluids. In this work they have also shown that the free energy barrier for the dissociation of micelles is zero below the cmc and that

it increases with concentration above the cmc. Similar conclusions follow from our analytical model. For small surfactants, a comprehensive micellization theory, based on classical thermodynamics of nucleation, has been extensively reported by Rusanov and co-workers [8, 9].

For the self-assembly of small, neutral surfactant molecules, the steric interactions in the corona can be described reasonably well with a 2D van der Waals equation of state, since the head groups consist of only one or a few statistical segments [1]. This has also been attempted for polymeric amphiphiles [10], which is however not accurate, as it neglects the conformational entropy change of stretched chains in the micellar corona with respect to unassociated, relaxed chains. The elastic deformation of chains in the corona of micelles can be accounted for using so-called blob models, as shown by Zhulina *et al.* [2]. For spherical micelles consisting of neutral polymers, which is the topic of this Chapter, we use the approach of Halperin [11] that is based on the Daoud-Cotton blob model for the conformation of star-shaped polymers [12]. Many of the previous theoretical efforts in polymer micellization are in a scaling approach. An interesting comparison between experiments on strongly segregated polymer micelles and existing scaling predictions is given by Forster *et al.* [13].

Many of the analytical approaches discussed above, contain approximations, such as the strong stretching approximation wherein only the most likely trajectories of the polymer chains are evaluated. If one prefers to avoid these approximate, yet explicit, methods, there are numerical methods for exactly solving Edward's diffusion equations, which have been shown to be ideally suited to study self-assembling systems [14]. The downside to these techniques, which depend on the self-consistent field method, are limited to finding saddle points in the free energy landscape. Interpretation of the results of these numerical techniques can therefore be troublesome in the sense that the underlying physical concepts are not transparent. In this Chapter we argue that the advantages of both approaches can be joined if one combines classical nucleation theory with polymer brush theory. Moreover, we will show how the classical theory for self-assembly (using analytical polymer brush theory, scaling concepts, etc.) is related to the corresponding analysis making use of the self-consistent field theory.

2.2 Nucleation-based model

In this Chapter we will elaborate the ideas brought forward in the Introduction, by constructing a minimal model describing the micellization of amphiphilic, neutral

polymers. We assume ideal, dilute solutions of unimers and micelles and only consider the formation of spherical micelles.

We consider an amphiphilic AB diblock copolymer that consists of a solvophobic A -block (tail) and a solvophilic B -block (head). It is dissolved in a solvent S . The chains are divided into statistical Kuhn segments, with a corresponding Kuhn length l_i for $i = A, B$, resulting in amphiphiles consisting of N_A solvophobic segments and N_B solvophilic segments. This allows accounting for differences in excluded volume and flexibility between the A and B blocks.

As a starting point, we use classical nucleation theory [5]. For the time being, we consider the solvophobic A -blocks as separate molecules, that are dissolved in the solvent S . The reversible work of formation W of a nucleus with volume V and surface area A is given by:

$$W = \gamma A - \Delta P V \quad (2.1)$$

where γ is the interfacial tension between the newly formed A -rich phase and the surrounding solution. The Laplace pressure ΔP is coupled to the (super)saturation of the A -tails in the bulk phase by Kelvin's law. For a two-component system of a droplet rich in A coexisting with a solvent S , the Kelvin equation reads

$$\Delta P = \frac{\varphi_A^c}{v_A} (\mu_A - \mu_A^s) \quad (2.2)$$

where φ_A^c is the volume fraction of A in the droplet, i.e. the micellar core, v_A is the volume per molecule A (for isometric segments $v_A = N_A l_A^3$). μ_A is the chemical potential of A in the bulk and the reference state μ_A^s is the chemical potential of species A at saturation (i.e. binodal value). We can find the chemical potential difference $\Delta\mu_A = (\mu_A - \mu_A^s)$, for ideal dilute solutions of unimers, from $\Delta\mu_A = k_B T \ln(\rho_A(1)/\rho_A^s)$, where $\rho_A(1)$ is the actual number concentration of unimers A in solution and ρ_A^s their saturation concentration. The number concentration $\rho_A(1)$ of A blocks is equal to the number concentration of AB unimers $\rho(1)$ in the bulk.

The saturation concentration ρ_A^s for solvophobic A -blocks can be described by:

$$\rho_A^s = c_1 \exp \left[\frac{-\Delta G_A}{k_B T} \right] = c_1 \exp [-c_2 N_A] \quad (2.3)$$

where c_1 and c_2 are constants [15]. ΔG_A is the free energy change (i.e. increase) associated with the transfer of an A -block from a pure A phase to the solvent S . When A is a linear chain, ΔG_A is proportional to the number of A segments in the molecule. The proportionality constant c_2 represents an interaction parameter between A segments and the solvent. The expression to the right, in terms of N_A , is

only accurate for A -blocks of only several statistical segments. These short blocks cannot collapse onto themselves, hence each segment is in contact with the solvent. The more general form in terms of ΔG_A is of course valid in all cases.

In the following we will express all thermodynamic properties in terms of the molecular parameters (such as N_A and N_B) and micellar properties, such as the aggregation number f , which is the number of AB chains in a micelle.

The volume of the core of a micelle with aggregation number f , composed of A -segments and (some) solvent, is given by

$$V_c = \frac{fv_A}{\varphi_A^c} \quad (2.4)$$

For a spherical core, the surface area A_c is thus given by

$$A_c = 4\pi \left(\frac{3fv_A}{4\pi\varphi_A^c} \right)^{\frac{2}{3}} \quad (2.5)$$

and its radius by

$$R_c = \left(\frac{3fv_A}{4\pi\varphi_A^c} \right)^{\frac{1}{3}} \quad (2.6)$$

We can now write the reversible work of formation of a single micellar core as

$$\frac{W_{nuc}}{k_B T} = \tilde{\gamma} 4\pi \left(\frac{3fv_A}{4\pi\varphi_A^c} \right)^{\frac{2}{3}} - \ln \left(\frac{\rho(1)}{\rho_A^s} \right) f \quad (2.7)$$

where $\tilde{\gamma} = \gamma/k_B T$ is the scaled interfacial tension between the core and the bulk.

This nucleation approach (Eqn 2.7) assumes that the composition of the core is similar to a macroscopic A phase and that the interface between the core and corona is sharp, i.e. the thickness of this interface $\ll R_c$. Of course this is an approximation when dealing with micelles, and it can be expected to break down when the quantity fN_A is small [5].

So far we neglected that the A blocks in the micellar core do not have the same freedom as in a random phase of A chains. As the coronal B -blocks are permanently coupled to one end of the A blocks, this end of the A block is restricted to reside at or near the core-corona interface. This leads to a decrease in the entropy of the tails in the core. We can correct for this, using Semenov's approach [6], by counting the local deformation energy of the tails. Following Nagarajan and Ruckenstein [1], we can express this correction as a change in chemical potential, per polymer chain in the micelle, due to this deformation

$$\frac{\Delta\mu_{def}}{k_B T} = \frac{9\pi P R_c^2}{80 N_A l_A^2} \quad (2.8)$$

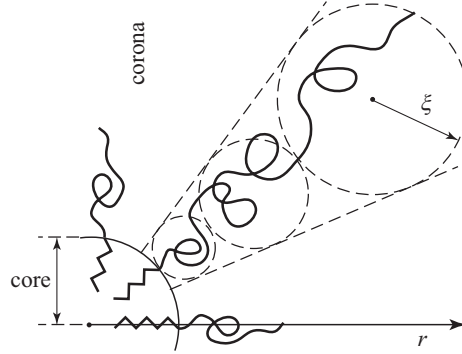


Figure 2.1: a) Schematic illustration of the 'blob' model to describe the conformation of polymer chains in the corona of a star-like micelle. The 'blob' size ξ is a function of the distance from the center of the micelle r , and can be described using a variation on the Daoud-Cotton model [12], that takes the finite size of the micellar core into account [4].

where P is the so-called packing factor, which equals $\frac{1}{3}$ for spherical micelles and R_c is the radius of the micellar core (Eqn 2.6). The total correction due to tail deformation $W_{def} = f\Delta\mu_{def}$, can now be written as

$$\frac{W_{def}}{k_B T} = \frac{a_{def} f^{\frac{5}{3}}}{N_A^{\frac{1}{3}} \varphi_A^c{}^{\frac{2}{3}}} \quad (2.9)$$

where the numerical constant $a_{def} = 3^{5/3} \pi^{1/3} / (4^{2/3} 80) \approx 0.05$. W_{def} is always positive, and as such acts as the first stopping force, that balances the tendency of the micellar core to grow to macroscopic dimensions as predicted by nucleation theory. We can see that this term becomes of more importance for shorter A blocks, as these are forced to stretch more in order to reach the center of the micellar core, for a given aggregate size.

The main stopping mechanism for growth of neutral polymeric micelles is due to the elastic deformation of the B -blocks in the corona. The Daoud-Cotton model [12] describes the stretching of polymer chains making up a star-branched polymer for which the geometry is spherical as well. For spherical micelles, that by definition have a non-zero core size, some corrections are needed for an accurate description of the stretching energy (see also Chapter 3).

We start by defining 'blobs' at a distances r from the center of the micelle, see also Fig.2.1. Each 'blob' represents $1 k_B T$ of stretching energy. The blob size $\xi(r)$ follows from geometric arguments and is given by:

$$\xi(r) = \frac{a_{dc}r}{f^{1/2}} \quad (2.10)$$

where a_{dc} is an unknown proportionality constant. Following Halperin [11], the local osmotic pressure in the corona is taken as $k_B T / \xi(z)^3$. Hence, the increase in energy of the system due to elastic deformation in the corona is found by integrating the osmotic pressure over the volume of the corona. This gives

$$\frac{W_{dc}}{k_B T} = \int \frac{\Pi}{k_B T} dV_{corona} = 4\pi \int_{R_c}^{R_m} \frac{r^2}{\xi^3} dr = a_{dc} f^{\frac{3}{2}} \ln \left[\frac{R_m}{R_c} \right] \quad (2.11)$$

This result is similar to what we derive in Chapter 3. In this expression, R_m is the radius of the micelle and R_c that of the corona (Eqn 2.6). In this same Daoud-Cotton model we can derive that, under θ -conditions for the B -blocks, the radius of the entire micelle R_m is given by

$$R_m = l_B f^{\frac{1}{4}} (N_B + f^{\frac{1}{144}} N_A^{\frac{1}{9}})^{\frac{1}{2}} \approx l_B f^{\frac{1}{4}} N_B^{\frac{1}{2}} \quad (2.12)$$

where l_B is the Kuhn length of the B -blocks that form the micellar corona [4]. The second expression is an approximation of the exact result, which is valid when $N_B \gg f^{1/144} N_A^{1/9}$. In this latter form, which is an approximation for micellar objects, it is exactly the correction for the finite core size which is omitted, hence it corresponds to the original Daoud-Cotton result for star-shaped polymers [12]. For the numerical calculations in the following parts of the Chapter, we however use the exact result for accuracy.

When the B -blocks are in a good solvent, the expression for the radius of the micelle is slightly different, and given by

$$R_m = l_B f^{\frac{1}{5}} \nu^{\frac{1}{5}} (N_B + (f^{\frac{2}{15}} N_A^{\frac{1}{3}})^{\frac{5}{3}})^{\frac{3}{5}} \approx l_B f^{\frac{1}{5}} \nu^{\frac{1}{5}} N_B^{\frac{3}{5}} \quad (2.13)$$

Again, the right-hand side of Eqn 2.13, is the original Daoud-Cotton result, where the finite size of the micellar core has been neglected. This equation now includes the Edwards excluded volume parameter $\nu = 1 - 2\chi_{BS}$, where χ_{BS} is the Flory-Huggins interaction parameter between the B -segments and the solvent S [16]. The exponent $\frac{3}{5}$ that relates the micelle radius to the chain length, can be recognized as the Flory exponent for the dependence of the coil size of a polymer on its length [17].

Using Eqns 2.7, 2.9 and 2.11, we can now write the total reversible work of formation W_t of a micelle with aggregation number f as

$$W_t(f) = W_{nuc}(f) + W_{def}(f) + W_{dc}(f) \quad \forall \quad f \geq 2 \quad (2.14)$$

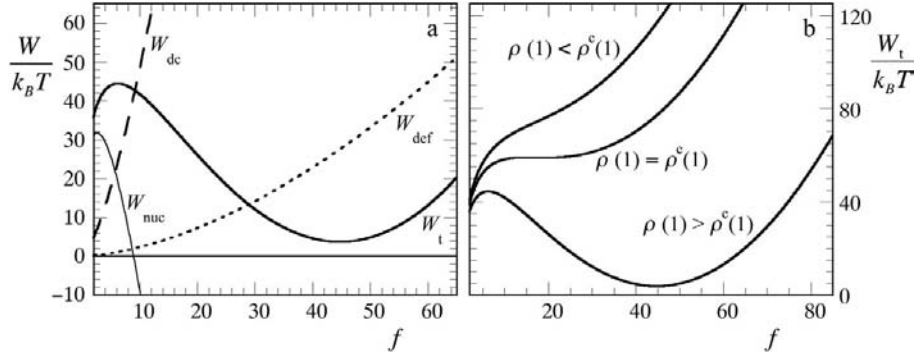


Figure 2.2: a) Total reversible work of formation of a micelle W_t (Eqn 2.14) versus aggregation number and its separate contributions; nucleation term W_{nuc} (Eqn 2.7), core entropy correction W_{def} (Eqn 2.9) and stretching energy W_{dc} (Eqn 2.11). For $N_A = 25$, $N_B = 250$ and θ -conditions for the B -blocks, $\tilde{\gamma} = 1.2$ (in units $k_B T / l_i^2$), $l_i = 1 \forall i$, $a_{dc} = 1$, $\varphi_A^c = 1$ and $\ln(\rho(1)/\rho_A^s) = 0.96$. b) Effect of unimer bulk concentration $\rho(1)$ on W_t , for the same parameters as in a), shown are three limits; i) bulk concentration smaller than a critical value $\rho^c(1)$ ($\ln[\rho(1)/\rho_A^s] = 0.85$), ii) concentration equal to critical value ($\ln[\rho(1)/\rho_A^s] = 0.89$) and iii) concentration above critical value ($\ln[\rho(1)/\rho_A^s] = 0.96$).

For sake of simplicity, we will consider all objects with $f \geq 2$ to be a micelle. Of course Eqn 2.14 is not valid for $f = 1$, as the work of formation of a unimer, from a unimer, should be zero.

In adsorption problems, the Gibbs equation relates the adsorbed amount (an excess quantity) to the derivative of the free energy with respect to the chemical potential. Within our model, we can do the same for a micellar system (Eqn 2.14):

$$\frac{\partial W_t}{\partial \Delta \mu_A} = -f \quad (2.15)$$

Where the aggregation number f is now the excess quantity, as it represents the excess number of molecules in a system with respect to the reservoir (bulk) phase. This illustrates that our theory complies with classical thermodynamics.

2.3 Small systems

With the expression for the total work of formation for a single micelle (Eqn 2.14), we can explore the energy landscape of micellization in detail. In this section we will still consider the formation of a single micelle from a solution of unimers, hence this section is denoted *Small systems*. In a following section we will expand our

view to macroscopic systems composed of many micelles.

In Fig.2.2a an example of the total work of formation as a function of aggregation number is shown together with the three contributions that it is composed of. The nucleation term W_{nuc} shows the characteristic profile of classical nucleation theory. The first term in Eqn 2.7, which increases with $f^{2/3}$ dominates for small f , leading to the increase in W_{nuc} . At some point, for larger f , the second term that decreases with f , becomes dominant. This leads to the maximum in W_{nuc} .

The other two terms in W_t , both represent stopping mechanisms as they increase with increasing f . The strength of both stopping forces depends largely on the system and conditions. The stretching term W_{dc} (Eqn 2.11) becomes more important for longer chains and when the solvency of the chains is increased. The entropic correction of the tails in the core W_{def} (Eqn 2.7) becomes larger when the tails become shorter, as they must stretch more to reach the center of the micellar core. For most conditions W_{dc} dominates W_{def} .

When all three terms are combined in W_t , the shape of the function that results depends strongly on the concentration of unimers in the bulk, i.e. on the ratio $\rho(1)/\rho_A^s$ in Eqn 2.7. In Fig.2.2b we see how $W_t(f)$ changes with concentration. This Figure shows strong resemblance to results derived by Rusanov *et al.* for the micellization of small surfactants [8]. When the unimer concentration in the bulk is relatively small, W_t is a continuously increasing function, without any stationary points. When we go to relatively high concentrations, two stationary points, i.e. $\partial W_t/\partial f = 0$, appear in the function. We see a maximum at small f and a minimum at higher f . The aggregation number for which W_t has its maximum can, in analogy with classical nucleation, be regarded as critical nucleus size.

Since the features are significantly different for low and high concentrations, there must be some transition point. This is also shown in Fig.2.2b. At some concentration, the first stationary point, appears in the form of an inflection point, i.e. $\partial W_t/\partial f = \partial^2 W_t/\partial f^2 = 0$. All concentrations above this critical bulk concentration $\rho^c(1)$ will show a maximum and minimum in $W_t(f)$. At concentrations below this critical threshold, $W_t(f)$ is an increasing function, and as a result any association would lead to an increase in the free energy of the system. Hence at concentrations below this threshold no micelles are formed.

From these considerations we can identify this critical bulk unimer concentration $\rho^c(1)$ as the concentration where the first stable micelle will appear. In other words this concentration can be regarded as a critical micelle concentration (cmc). We now have a simple criterion for the critical micelle concentration, i.e. the concentration for which $W_t(f)$ has an inflection point, i.e. a point where both the first and second derivative of this function with respect to f are zero. As we will also

deal with another, more macroscopic, definition of the cmc, we will refer to the criterion above as the "microscopic cmc".

2.4 Connection with SCF models

Numerical self-consistent field (SCF) methods, such as that developed by Scheutjens and Fleer [16] (SF-SCF), are often employed to study self-assembling systems. In Chapters 3 and 4, we use an SCF method to study the micellization and phase behavior of telechelic associative polymers. In the past, similar methods have been used to study self-assembly of, e.g., non-ionic surfactants [14], ionic surfactants [18] and also block copolymers [19]. An overview of the possibilities for using self-consistent field theory in micellization problems can be found in [20].

In SCF methods, thermodynamic equations are solved numerically by finding extrema in the free energy. It is important to note that as a result, all self-consistent solutions that are found correspond to stationary points in the free energy landscape, similar as the minima, maxima and horizontal inflection point in Fig.2.2. Interpretation of the primary outcome of these calculations is often based on the thermodynamics of small systems, as founded by Hill [21] and applied to micellar solutions by Hall and Pethica [22].

The basis of small system thermodynamics is the classical expression for the change in internal energy U of a macroscopic and homogeneous system, with changes in entropy S , volume V and number of molecules n_i , which is complemented with a term to account for energy stored in the micelles:

$$dU = TdS - PdV + \sum_i \mu_i dn_i + \mathcal{E}d\mathcal{N} \quad (2.16)$$

where T is the temperature, P the pressure and μ_i the chemical potential of species i . The micellar term, consists of the number of micelles \mathcal{N} and the subdivision potential \mathcal{E} . In a macroscopic system consisting of micelles, unimers and solvent, the number of micelles is not a controlled variable. This means that a system, with a fixed volume V , temperature T and composition $\{n_i\}$, will change \mathcal{N} , by changing the mean aggregation number \bar{f} , until the free energy $F = U - TS$ is minimal. As a result, the work of formation per micelle \mathcal{E} must vanish:

$$\left(\frac{\partial F}{\partial \mathcal{N}} \right)_{V,T,\{n_i\}} = \mathcal{E} = 0 \quad (2.17)$$

In self-consistent field calculations however, the number of micelles *is* a controlled variable, since a single micellar object is considered ($\mathcal{N} = 1$). In our model above,

we also regard the work of formation of a single micelle. This is the first indication for the connection between SCF theory and our minimal model.

In SCF methods the micellar object is normally translationally restricted by pinning it to the center of the coordinate system. In the work of formation of a micelle W_t (Eqn 2.14), as formulated above, translational entropy is also not included. The total work of formation of a micelle W_t in our model, has a similar physical meaning as the grand potential Ω in self-consistent field theory, which is defined as $\Omega \equiv F - \sum_i \mu_i n_i$. The main difference is that in our model the entire landscape of the work of formation can be produced, whereas only stationary points are found in SCF calculations. To complete the connection between the results of our model and self-consistent field calculations, we introduce W_t^* , which represents all values of W_t , for which $\partial W_t / \partial f = 0$. This quantity is exactly the same as the grand potential in the SCF models.

Since \mathcal{E} must be zero and the translational entropy S_{tr} is not included yet, we can derive that for the mesoscopic models (here given in terms of the grand potential Ω)

$$\mathcal{E} = -TS_{tr} + \Omega = 0 \quad (2.18)$$

The finite values found for the work of formation (either Ω or W_t^*), must be compensated by the translation entropy. Eqn 2.18 together with Eqn 2.16 forms the connection between the mesoscopic models and macroscopic thermodynamics.

In Fig.2.3a we have plotted the work of formation W_t obtained from our minimal model (Eqn 2.14) as a function of the chemical potential and aggregation number f . In this same plot the stationary points, i.e. for which $\partial W_t / \partial f = 0$, are connected with the thick line. These stationary points represent the solutions that are also found in SCF calculations. When these stationary points, denoted W_t^* , are projected onto the appropriate planes, as shown in Fig.2.3b, we obtain results which show strong resemblance to typical results from SCF calculations (see Chapter 4, Fig.4.3).

The microscopic cmc, to be found where $\partial W_t / \partial f = \partial^2 W_t / \partial f^2 = 0$, is found at the maximum $W_t^*(f)$ (Fig.2.3b), as this point corresponds to the inflection point in W_t (Fig.2.3a).

In the analysis of self-consistent field calculations, often the same definition of the cmc is used, i.e. the cmc is found where $\Omega(f)$ has a maximum. Interestingly, this definition can also be derived from small system thermodynamics. The Gibbs-Duhem equation for micellization in the SCF method (analogous to Eqn 2.15), is $-\partial \Omega / \partial \mu = f$, μ is the chemical potential of the unimers. Note that this equation

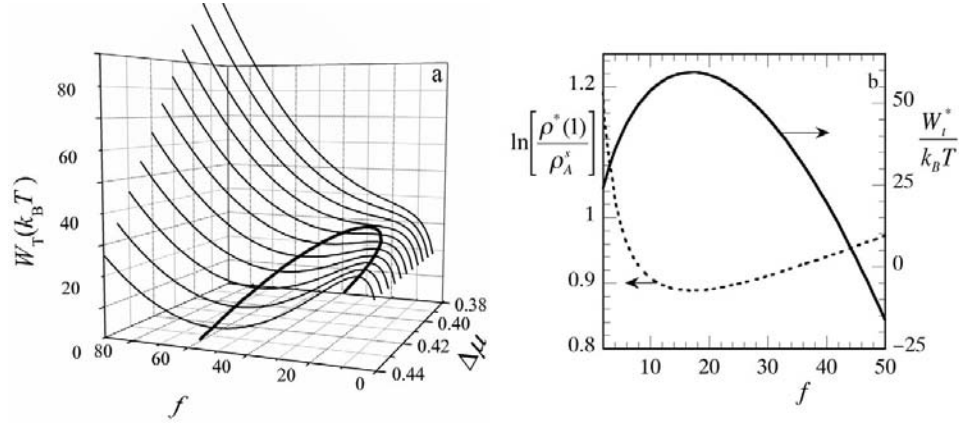


Figure 2.3: a) Work of micellization versus scaled chemical potential of unimers $\Delta\mu = \ln[\rho(1)/\rho_A^s]$ and aggregation number f , for the same parameters as in Fig.2.2a; drawn lines represent $W_t(f)$ for given chemical potentials, thick drawn line connects all stationary points, i.e. points for which $\partial W_t/\partial f = 0$. b) Projection of the stationary points in a) onto the (f, W_t) - and $(f, \ln[\rho(1)/\rho_A^s])$ -planes. Stationary solutions of $W(t)$ are indicated here with an asterix (W_t^* and $\rho^*(1)$).

is analogous to Eqn 2.15. Fluctuations in f are proportional to $\partial f/\partial \mu$, a quantity that is > 0 by definition. As a result, micelles that are macroscopically stable must obey the so-called stability constraint $\partial \Omega/\partial f < 0$. In other words, all micelles for which $\partial \Omega/\partial f > 0$ are not stable, and hence the first stable micelle appears at $\partial \Omega/\partial f = 0$. We have now returned to the same result as found in our nucleation-based approach.

2.5 Case study: CMCs of PEO-laurates

The validity of our micellization model is demonstrated here in comparison to experimental results for the cmc of poly(ethylene oxide) (PEO) chains modified with a single $C_{12}H_{25}$ alkyl (laurate) tail. To do so we need to enter realistic values for the model parameters. The interfacial tension between a homogeneous laurate phase and pure water is approximately 50 mN/m [23] and hardly any water dissolves in the laurate phase, so $\varphi_A^c \approx 1$ [24]. The saturation concentration of pure dodecane ($C_{12}H_{26}$) in water is $5 \cdot 10^{-8}$ mol/l [25].

To divide the PEO chains and the alkyl tails into statistical segments, we use the Kuhn length of PEO chains, which is approximately 7\AA , corresponding to 2

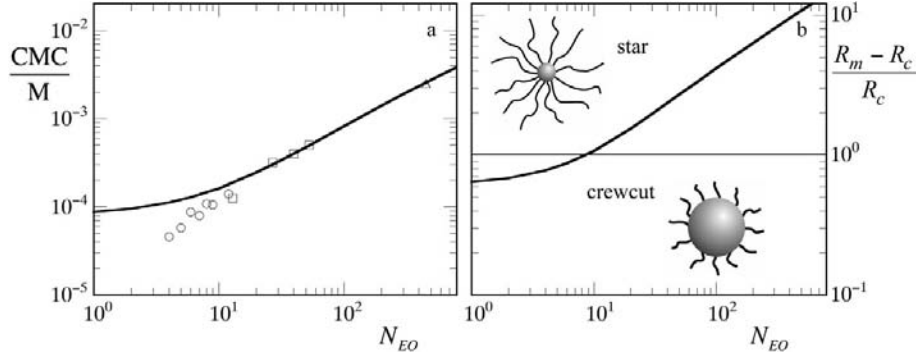


Figure 2.4: a) Experimental critical micelle concentrations for PEO-laurates as a function of number of EO units per head group, from van Os *et al.* (\circ , [28]), Reddy *et al.* (\square , [29]) and Gourier *et al.* (\triangle , [30]). Drawn line is the prediction of our nucleation-based theory. b) Predicted ratio of the corona radius $R_m - R_c$ (Eqns 2.12 and 2.6) over the core radius R_c (Eqn 2.6); when this ratio is > 1 the micelles are star-like, for values < 1 we have crew-cut micelles.

EO units [26]. This same discretization length is expected to be quite accurate for alkyl tails, hence we count 6 CH_2 groups for every Kuhn segment. This means that N_B is equal to half the number of EO units in the PEO chains, and for laurate ($N_{CH_2} = 12$) $N_A = 2$. In this way we realistically account for the flexibility of the two blocks. PEO in water at room temperature is close to theta conditions [27], so we use Eqn.2.12 to describe the radius of the micellar objects. With these parameters fixed, there is just one remaining unknown, i.e. the proportionality constant a_{dc} in the stretching term (Eqn 2.11). This constant will be determined by comparing the model to experimental data.

Experimentally determined critical micelle concentrations for PEO-laurates were found in various sources [28, 29, 30] and are shown as symbols in Fig.2.4a as a function of the number of EO monomers N_{EO} in the head group. Because the Daoud-Cotton model [12] is only accurate for polymer chains with many statistical segments, we take the experimental cmc of a laurate surfactant with a large head group ($N_{EO} = 450$) to calibrate our model. Experimentally a cmc of 2.5 mmol/l is found [30]. In our model the (microscopic) cmc is determined by finding the concentration for which $W_t(f)$ shows an inflection point. For $a_{dc} = 0.2$, the model gives a cmc of 2.55 mmol/l. With this value of a_{dc} , we can use the model to predict the cmc for different N_{EO} . These predictions are shown in Fig.2.4a as the drawn line.

We see that our model works well for relatively large N_{EO} , however when $N_{EO} \approx 10$ or smaller the model prediction starts to deviate from the experimental data. The Daoud-Cotton model, used here to account for the chain stretching in the corona, only applies when the micelles have a star-like structure. This means that the corona must be larger than the core. The corona size can be found by subtracting the core radius R_c (Eqn 2.6) from the radius of the entire micelle R_m (Eqn 2.12). The ratio of the corona radius over the core radius $((R_m - R_c)/R_c)$ is the determining parameter. When this ratio is > 1 the micelles are star-like. For $((R_m - R_c)/R_c < 1)$ we are dealing with crew-cut micelles [31]. In Fig.2.4b this ratio is shown, and we see where the Daoud-Cotton model is no longer valid. The transition from the star regime to the crew-cut regime (i.e $(R_m - R_c)/R_c = 1$), occurs almost at the same point where our theoretical model starts to fail in describing the experimental data, i.e. for $N_{EO} = 10$. This illustrates the limitation of our model when predicting the micellization of oligomeric surfactants, resulting from the choice for the Daoud-Cotton model to describe the lateral pressure in the corona.

For small values of N_{EO} , W_{dc} (Eqn 2.11) underestimates the true osmotic pressure in the corona, which leads the model to predict very large aggregation numbers for these parameters. As a result, the correction term for the tails in the core W_{def} (Eqn 2.9) increases drastically, which in turn leads to the overestimation of the cmc, as seen in Fig.2.4a.

Another important aspect of the transition from stars to crew-cut micelles, is that crew-cut micelles are inherently unstable. They will be prone to strong shape fluctuations, and at concentrations above the cmc might undergo a morphological transition from spherical micelles to wormlike objects. In the current Chapter we only consider spherical micelles, but the model can in principle be adjusted relatively easily toward other geometries such as cylinders or even bilayers.

2.6 Micellar size distributions

An interesting feature of our model is that it allows predicting the entire size distribution of micelles ($f \geq 2$) in a macroscopic system, i.e. a system composed of many micelles. We can find the number concentration of unimers that are associated in an aggregate of size f , from a simple Boltzmann argument:

$$\rho(f) = f \exp \left[-\frac{W_t(f)}{k_B T} \right] \quad \forall \quad f \geq 2 \quad (2.19)$$

The expression for the total reversible work of micellization W_t (Eqn 2.14), is only

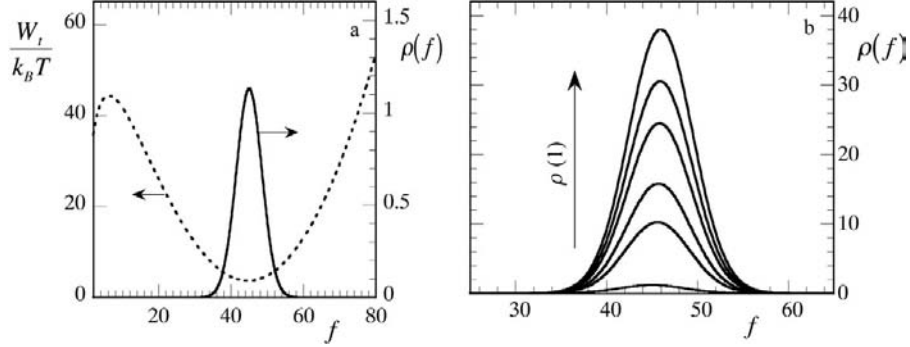


Figure 2.5: a) Work of micellization $W_t(f)$ (dotted line) and probability distribution $p(f)$ of finding a unimer in an aggregate of size f for the same parameters as in Fig.2.2a. b) Effect of bulk unimer concentration $\rho(1)$ on the number distribution $\rho(f)$ (in units ρ_A^s) of unimers in micelles ($f > 1$) for the same system parameters as in a).

applicable for $f \geq 2$. We can now calculate the micellar size distribution for a given chemical potential, i.e. given value of $\rho(1)$.

In Fig.2.5a, an example is shown of a distribution of micellar sizes with the corresponding work of micellization. Of course, the peak position in the distribution corresponds to the minimum in W_t , as this is the most favorable configuration. The width of the peak in $\rho(f)$ is directly related to the curvature around the minimum in W_t .

In Fig.2.5b, we can see the evolution of the size distribution of micelles $\rho(f)$ with increasing concentration. Of course all concentrations shown are above the microscopic cmc, as there will be no micelles present below the cmc. When the bulk concentration of unimers is increased, the total number of unimers in the system that is present in micelles, in other words that is in a state with $f > 1$, increases. We also see that the position of the peak in $\rho(f)$ does not shift significantly, which indicates that the mean aggregation number \bar{f} is fairly constant. We must realize that in these micellar systems, the chemical potential of the unimers is buffered above the cmc, i.e. large changes in overall composition of the system lead only to slight changes in chemical potential, i.e. small changes in $\rho(1)$. This in turn implies that over a wide overall concentration range only a small part of the curve in Fig.2.3b is probed, hence the mean aggregation number is only a very weak function of the overall concentration.

The results in Fig.2.5b are typical for a closed-association process, with the difference that there is a degree of polydispersity in the micelles that are formed,

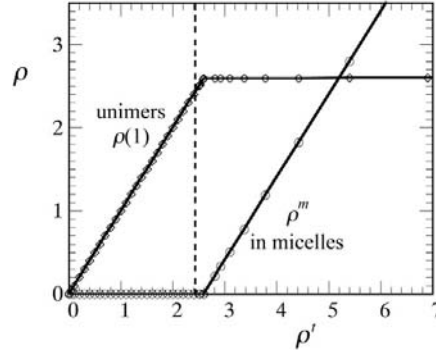


Figure 2.6: Number concentration of unimers $\rho(1)$ (\square) and of polymer chains associated in micelles ρ_m (\circ) versus the total number of AB molecules per unit volume ρ_t , all expressed in units of the reference state ρ_A^s . The dotted line is the microscopic critical micelle concentration, as discussed in a previous section. Model parameters as in Fig.2.2.

as we will discuss below. In the simplest closed-association model, unimers coexist with a monodisperse population of micelles. In open-association processes, the size of the object continues to grow with increasing concentration, which is not the case here (see Fig.2.5b). Open-association processes are expected for linear objects such as wormlike micelles or living polymers [32].

Now that we have a way to calculate the size distribution of micelles for a given concentration of unimers $\rho(1)$, we can easily obtain the total number of molecules in micelles ρ_m , i.e. the number of AB polymers that are associated with $f > 1$, with

$$\rho_m = \int_2^\infty \rho(f) df = \int_2^\infty f \exp \left[-\frac{W_t(f)}{k_B T} \right] df \quad (2.20)$$

From which we can obtain the total polymer concentration in the system, i.e. the total number of AB molecules per unit volume $\rho_t = \rho(1) + \rho_m$.

This analysis gives rise to a classical picture, as shown in Fig.2.6. In this plot we can see how the number of unimers and the number of molecules in micelles changes with the overall concentration. We see that for concentrations below the microscopic cmc, which was the point where the first and second derivative of $W_t(f)$ (Eqn 2.14) with respect to f are both zero, the number of unimers increases linearly with concentration, as expected. For these concentrations, no micelles are formed, so $\rho_m = 0$. Just above the microscopic cmc, we see a rather sudden change after which the number of unimers seems to remain practically constant and it is the number of associated molecules that increases linearly with concentration.

The microscopic cmc (dotted line in Fig.2.6), as discussed above, represents the concentration where the first stable micelle appears. At this concentration the number of micelles is therefore very low, and impossible to observe in experiments. A definition of the cmc that is more in line with experimental methods is to choose the cmc as the concentration where one macroscopically observes the formation of micelles. Here we choose to define such a "macroscopic cmc" as the concentration where the sharp transition in Fig.2.6 is found.

Many experimental techniques are sensitive to the number of micelles that are present, such as spectroscopic techniques employing solubilization of dye molecules, or scattering techniques. By extrapolating the output of these experiments to the point where the signal due to the micelles reaches zero, the "macroscopic cmc" can be obtained. It is interesting that the microscopic and macroscopic definition of the cmc, as proposed above, are found relatively close together. It also implies that the microscopic definition of the cmc, associated with the thermodynamics of small systems, is not that different from an experimentally observable parameter.

2.7 Polydispersity

If we take another look at Fig.2.5, we see that the predicted distributions appear to be close to Gaussian. The Gaussian shape of these curves indicates that the work of micellization has a parabolic shape around the minimum, as can be seen in Fig.2.5. Gaussian distributions are defined by two parameters, i.e. the average and the variance. The average corresponds to the position of the peak in the distribution and the variance, which is the square of the standard deviation, corresponds to the width of the distribution. The width of the distribution is coupled to the curvature around the minimum of the work of micellization, as fluctuations become less likely if their energy increase with respect to the minimum of the free energy is much larger than $k_B T$.

In Fig.2.3 we can see that the minimum in W_t is infinitely shallow at the critical micelle concentration, as the curvature, given by the second derivative at that point, is zero. When we increase the concentration of unimers the minimum becomes sharper. This directly implies that the width of the distribution of micellar aggregation numbers should decrease with increasing concentration. Qualitatively this can be seen in Fig.2.5b.

For a quantitative analysis, we first notice that $\rho(f)$ as defined in Eqn.2.19, gives the concentration of *molecules* in micelles of size f . The concentration of micelles of size f is given by $\rho(f)/f$. The standard deviation in aggregation number σ_f in

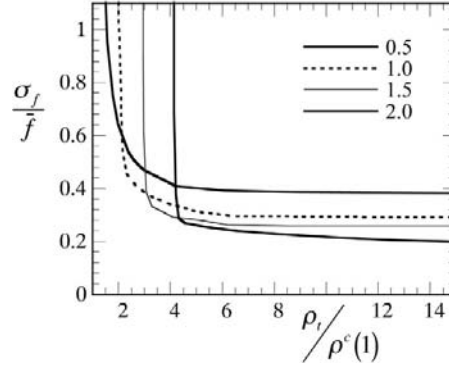


Figure 2.7: Relative standard deviation σ_f/\bar{f} in aggregation number versus normalized concentration $\rho_t/\rho^c(1)$, as a function of the strength of the segregation of the core, set by means of the scaled interfacial tension $\tilde{\gamma}$ (in units $k_B T/l^2$), other parameters as in Fig.2.2.

a distribution of micelles is given by:

$$\sigma_f = \sqrt{\frac{\int_2^\infty (f - \bar{f})^2 \rho(f)/f df}{\int_2^\infty \rho(f)/f df}} \quad (2.21)$$

where \bar{f} is the average aggregation number, given by

$$\bar{f} = \frac{\int_2^\infty \rho(f) df}{\int_2^\infty \rho(f)/f df} \quad (2.22)$$

It is convenient to define a relative standard deviation, as σ_f/\bar{f} , which reflects the relative width of the distribution.

Fig.2.7 shows how σ_f/\bar{f} develops as a function of the total polymer concentration scaled with respect to the microscopic cmc; the microscopic cmc is found at $\rho_t/\rho^c(1) = 1$. Upon approaching the critical micelle concentration, the polydispersity strongly increases. Interestingly, we find that the strength with which the micellar core segregates from the solvent, set with $\tilde{\gamma}$, influences how the polydispersity develops.

The stronger the segregation, the steeper the divergence of σ_f/\bar{f} close to the cmc. Even small differences, here shown a maximum difference in interfacial tension of a factor of 4, can change the divergence of the standard deviation in the limit of the cmc, from a smooth incline ($\tilde{\gamma} = 0.5$), to a sharp transition ($\tilde{\gamma} = 2$). The relative concentration $\rho_t/\rho^c(1)$ where the polydispersity starts to diverge is also a function of the segregation strength, and occurs at higher relative concentrations

for stronger segregating systems. The absolute value of the cmc is of course a decreasing function of the segregation strength.

Recent experiments also show that the polydispersity increases significantly upon approaching the cmc [33]. The micellar size distributions that were derived in these experiments show resemblance with what is shown in Fig.2.5b and also the values for the relative standard deviation are of the same order of magnitude as predicted here.

At concentrations well above the cmc, the polydispersity levels off but continuously decreases with increasing concentration. Experiments are often carried out at concentrations of at least several times the cmc, and we can expect the polydispersity to be somewhere in this quasi-plateau. This means that for strongly segregating systems, such as polymers modified with alkyl tails, the polydispersity in the experimental domain will be smaller, than for comparable systems with low interfacial tensions between the core and corona, such as micelles formed by complexation of oppositely charged components [34].

2.8 Conclusions

In this Chapter we have proposed a comprehensive model for the micellization of polymeric amphiphiles and shown that it can be used to describe the behavior of real polymeric surfactants. A direct comparison with experiments revealed that our approach remains valid even for solvophilic corona blocks of only several statistical segments, as long as the corona of the micelle is larger than the core. The complementary character of this model with respect to self-consistent field calculations was discussed using some concepts from the thermodynamics of small systems.

The model developed in this Chapter describes the micellization of polymers with a single, neutral solvophilic and a single solvophobic block, from ideal solutions, into spherical micelles. Hence, interactions between micelles are ignored in our model. For uncharged micellar systems, interactions only become important when the typical distances between the objects becomes of the order of twice their radius. The approach chosen here is therefore expected to be valid up to relatively high concentrations. Several expansions of our minimal model toward more complicated systems would be of interest. One might think of introducing a term accounting for loop formation of the solvophilic blocks, such as that proposed by ten Brinke en Hadziioannou [35], to predict the micellization of polymers with solvophobic blocks at both chain ends, also known as telechelic associative polymers. Adding a term to account for the formation of bridges between micelles, might also

lead to a model describing the higher-order assembly of these telechelic polymers into percolated networks. For polymeric systems with strongly segregating core blocks (e.g. alkyl-tails in water), the corona is much larger than the compact core, and the spherical conformation is favored. Systems with only weakly segregating cores, such as, e.g., micelles in which the core is formed by complex coacervation, can be expected to have a much larger core as a result of the higher content of solvent and the lower interfacial tension. In these system we can therefore expect that morphology changes, e.g. from spherical to cylindrical or lamellar structures, occur more often, although experimental results indicating such changes are scarce [36]. Implicating different geometries in the model would require alternate descriptions for the stretching of the corona blocks.

References

- [1] Nagarajan, A.; Ruckenstein, E. *Langmuir* **1991**, *7*, 2934.
- [2] Zhulina, E. B.; Adam, M.; LaRue, I.; Sheiko, S. S.; Rubinstein, M. *Macromolecules* **2005**, *38*, 5330.
- [3] Meng, X. X.; Russel, W. B. *Macromolecules* **2005**, *38*, 593.
- [4] Sprakel, J.; Besseling, N. A. M.; Leermakers, F. A. M.; Cohen Stuart, M. A. *J. Phys. Chem. B* **2007**, *111*, 2903.
- [5] Laaksonen, A.; Talanquer, V.; Oxtoby, D. W. *Annu. Rev. Phys. Chem.* **1995**, *46*, 489.
- [6] Semenov, A. N. *Zh. Eksp. Teor. Fiz.* **1985**, *61*, 733.
- [7] Besseling, N. A. M.; Cohen Stuart, M. A. *J. Phys. Chem.* **1999**, *110*, 5432.
- [8] Rusanov, A. I.; Kuni, F. M.; Grinin, A. P.; Shchekin, A. K. *Colloid J.* **2002**, *64*, 605.
- [9] Kuni, F. M.; Shchekin, A. K.; Grinin, A. P.; Rusanov, A. I. *Colloid J.* **2003**, *65*, 459.
- [10] Nagarajan, R.; Ganesh, K. *J. Phys. Chem.* **1989**, *90*, 5843.
- [11] Halperin, A. *Macromolecules* **1987**, *30*, 2943.
- [12] Daoud, M.; Cotton, J. *J. Physique* **1982**, *43*, 531.
- [13] Forster, S.; Zisenis, M.; Wenz, E.; Antonietti, M. *J. Chem. Phys.* **1996**, *104*, 9956.
- [14] Leermakers, F. A. M.; Lyklema, J. *Colloids Surf.* **1992**, *67*, 239.
- [15] Tanford, C. *The hydrophobic effect: formation of micelles and biological membranes*; Wiley (New York), 1980.
- [16] Fleer, G. J.; Cohen Stuart, M. A.; Scheutjens, J. M. H. M.; Cosgrove, T.;

- Vincent, B. *Polymers at Interfaces*; Chapman and Hall (London), 1993.
- [17] Flory, P. J. *Principles of polymer chemistry*; Cornell University Press (Ithaca), 1953.
- [18] Lauw, Y.; Leermakers, F. A. M.; Cohen Stuart, M. A. *J. Phys. Chem. B* **2007**, *111*, 8158.
- [19] Cogan, K. A.; Leermakers, F. A. M.; Gast, A. P. *Langmuir* **1992**, *8*, 429.
- [20] Leermakers, F. A. M.; Eriksson, J. C.; Lyklema, J. In *Fundamentals of Interface and Colloid Science. Volume V: Soft Colloids*; Academic Press Ltd., London, 2005; chapter 4.
- [21] Hill, T. L. *Thermodynamics of Small Systems, Parts 1 and 2*; Dover Pub. Inc. (New York), 1994.
- [22] Hall, D. G.; Pethica, B. A. In *Nonionic Surfactants*; Marcel Dekker Inc.: New York, 1967; chapter 16.
- [23] Zeppieri, S.; Rodriguez, J.; de Ramos, A. L. L. *J. Chem. Eng. Data* **2001**, *46*, 1086.
- [24] Maczynski, A.; Goral, M.; Wisniewska-Gocłowska, B.; Skrzecz, A.; Shaw, D. *Monatsh. Chem.* **2003**, *134*, 633.
- [25] Sutton, C.; Calder, J. A. *Environ. Sci. Technol.* **1974**, *8*, 654.
- [26] Pattanayek, S. K.; Juvekar, V. A. *Macromolecules* **2002**, *35*, 9574.
- [27] Zaslavsky, B. Y.; Bagirov, T. O.; Borovskaya, A. A.; Gulaeva, N. D.; Miheeva, L. H.; Mahmudov, A. U.; Rodnikova, M. N. *Polymer* **1989**, *30*, 2104.
- [28] van Os, N.; Haak, J.; Rupert, L. *Physico-chemical properties of selected anionic, cationic and nonionic surfactants*; Elsevier, Amsterdam, 1993.
- [29] Reddy, N. K.; Foster, A.; Styring, M. G.; Booth, C. *J. Colloid Interface Sci.* **1990**, *136*, 588.
- [30] Gourier, C.; Beaudoin, E.; Duval, M.; Sarazin, D.; Maitre, S.; Francois, J. *J. Colloid Interface Sci.* **2000**, *230*, 41.
- [31] Lauw, Y.; Leermakers, F. A. M.; Cohen Stuart, M. A.; Borisov, O. V.; Zhulina, E. B. *Macromolecules* **2006**, *39*, 3628.
- [32] Nyrkova, I. A.; Semenov, A. N. *Eur. Phys. J. E* **2005**, *17*, 327.
- [33] English, R. J.; Ratcliffe, I.; Blanchard, R. L.; Parsons, B. J. *Macromolecules* **2007**, *40*, 6699.
- [34] Cohen Stuart, M. A.; Besseling, N. A. M.; Fokkink, R. G. *Langmuir* **1998**, *14*, 6846.
- [35] ten Brinke, G.; Hadziioannou, G. *Macromolecules* **1987**, *20*, 486.
- [36] Koide, A.; Kishimura, A.; Osada, K.; Jang, W. D.; Yamasaki, Y.; Kataoka, K. *J. Am. Chem. Soc.* **2006**, *128*, 5988.

Chapter 3

Micellization of telechelic associative polymers

We present numerical results, from self-consistent field calculations, on the micellization of telechelic associative polymers and their monofunctional analogues. These results are confronted with relatively simple scaling concepts. We find a good agreement between the numerical dependence of the aggregation number upon both backbone and terminal hydrophobe length and an analytical expression that was derived from the well-known Daoud-Cotton model by introducing a correction for the finite size of the micellar core.

This chapter was published as:

J. Sprakel, N.A.M. Besseling, F.A.M. Leermakers and M.A. Cohen Stuart: *Micellization of telechelic associative polymers: Self-consistent field modeling and comparison with scaling concepts*, J. Phys. Chem. B **111** (2007), 2903.

3.1 Introduction

Aqueous telechelic associative polymers are watersoluble polymer chains end-capped with hydrophobic moieties. A well-known class of associative polymers are so-called HEURs or hydrophobically modified ethoxylated urethanes, which are polyethylene oxides with paraffinic tails grafted at both ends of the chain. They are analogues of simple nonionic surfactants.

In a polar solvent, at concentrations above the critical micelle concentration (CMC), these telechelics self-assemble into spherical, flowerlike micelles. At higher concentrations, above a percolation threshold, they form transient, micellar networks [1]. Some of the polymers in this class have been reported to show an entropically driven demixing, into a dilute (micellar) phase and a condensed phase with a higher polymer concentration (typically 1 wt%) [2].

For a better understanding of the phase behavior of these associative polymers, which is of practical importance in the formulation of e.g. paints and inks, we first study their micellization in detail.

Some crude analytical models for the properties of telechelic micelles have been reported [3, 4]. Francois et al. [4] apply the scaling concepts of Halperin and Alexander [5, 6] to explain experimental neutron scattering data. However, they neglect the loop entropy contribution to the free energy of these micelles, leading to underestimation of the CMC. The large influence of this entropic penalty associated with loop formation on the micellization of telechelics was first stressed by Ten Brinke and Hadzioannou [7] and further elaborated by, e.g., Balsara et al. [8].

In order to predict aggregation numbers for telechelic micelles Meng and Russel [9] balanced the interfacial and configurational free energy of the micellar core chains against the elastic stretching of the coronal chains. To account for the latter they use a model by Li and Witten [10], which was published earlier by Wijnmans and Zhulina [11]. In these models for the conformation of spherical brushes 2 zones are predicted; in the inner zone, closest to the core, the density decay of the chains is predicted to show power-law behavior, after which (outer zone) the density follows a parabolic profile. This parabolic density profile, for curved polymer brushes, was first observed by Dan and Tirrel in numerical self-consistent field calculations [12]. The power-law behavior close to the core was predicted by Daoud and Cotton, in their model for the conformations of star-shaped polymers [13].

We use the discrete self-consistent field theory of Scheutjens and Fleer [14] to study the properties of isolated micelles assembled from telechelic chains, adopting a model that has been shown to be effective in predicting the micellization of nonionic surfactants [15]. These numerical results are confronted with approximate,

yet insightful, scaling arguments, where our main focus is on the dependencies of the CMC and the aggregation number on the molecular architecture.

3.2 Thermodynamics and SCF modeling

For a proper analysis of micellization we start from the thermodynamics of small systems, as described in the classical work of Hill [16] and Hall & Pethica [17]. For micellar systems, the classical expression for the change of the internal energy U of a macroscopic system, with a change in entropy S , volume of the system V and/or the numbers of molecules n_i of each component i , is extended with an additional term, to account for the energy stored in the micelles:

$$dU = TdS - PdV + \sum_i \mu_i dn_i + \mathcal{E}d\mathcal{N} \quad (3.1)$$

with \mathcal{E} the subdivision potential, easily identified as the grand potential (Ω) per micelle, \mathcal{N} the number of micelles, P the pressure, μ the chemical potential and T the temperature. From the Helmholtz energy $F = U - TS$ we can formulate two constraints;

$$\left. \frac{\partial F}{\partial \mathcal{N}} \right|_{n_i, V, T} = \mathcal{E} = 0 \quad (3.2)$$

to ensure that the macroscopic thermodynamics are conserved, and

$$\left. \frac{\partial^2 F}{\partial \mathcal{N}^2} \right|_{n, V, T} = \left. \frac{\partial \mathcal{E}}{\partial \mathcal{N}} \right|_{n_i, V, T} > 0 \quad (3.3)$$

that assures the stability of the micelles.

In the calculations we are restricted to considering a single micellar object. To apply the constraints above, formulated for a macroscopic system of many micelles, to a single-micelle system we use the following argument; we can consider the system with a single micelle to be a sub-system of a larger closed ensemble (constant n_i , V , T) of many micelles. In this system an increase in the aggregation number n_{agg} , results in an equivalent decrease of the number of micelles. Now, using the grand potential per micelle $\Omega = \frac{F}{\mathcal{N}} - \sum_i \mu_i \frac{n_i}{\mathcal{N}} + p \frac{V}{\mathcal{N}}$, we can write the stability constraint as

$$\left. \frac{\partial \Omega}{\partial n_{agg}} \right|_{n_i, V, T} < 0 \quad (3.4)$$

that will give us ground for defining the critical micelle concentration in a subsequent section of this Chapter.

The self-consistent field method is ideally suited to obtain information on the grand potential for micellar systems in a molecular model. In this Chapter we apply a self-consistent field method, using the discretization scheme of Scheutjens and Fleer [14, 18, 19, 20]. In this method the same length scale (l) is used to subdivide space into lattice sites and molecules into segments. For the sake of brevity we will only discuss the major premisses.

The first step is to make a choice for a lattice geometry, with the direct consequence that the shape of the self-assembled object is fixed. We shall consider a micelle pinned in the centre of a spherical coordinate system, where sites of equal volume (l^3) are arranged in concentric layers. The number of sites in layer z is proportional to z^2 . The mean-field approximation is applied to all sites in a layer, implying that inhomogeneities are allowed in the radial direction only. The radial distance from the centre of the lattice is z . Segments, with rank number $s = 1 \cdots N$, are placed on the lattice as step-weighted walks, giving freely-jointed chains in a self-consistent potential field. In effect, in a self-consistent field model there exists a pair of conjugated functions per segment type j ; the volume fraction profiles $\varphi_j(z)$ and the corresponding segment potential profiles $u_j(z)$. In the potentials there are contributions of packing and nearest-neighbor interactions, accounted for by Flory-Huggins interaction parameters.

The probability of finding a molecule i in a conformation c is proportional to the Boltzmann weight $p = \exp(-u_i^c/k_B T)$ of the corresponding segment potential $u_i^c = \sum_s u(z_{s,i}^c)$, where $z_{s,i}^c$ is the coordinate of segment s of molecule i in conformation c . The volume fraction profiles $\varphi_i(z)$ of all species i are found after normalization of the sum of the Boltzmann weights of all possible conformations. The self-consistent field equations are satisfied when the segment potentials and volume fractions are consistent, meaning that the potentials both determine and follow from the volume fractions. This solution is obtained by a numerical iteration procedure. The correct solution obeys the incompressibility constraint: $\sum_i \varphi_i(z) = 1 \forall z$.

When a consistent solution for the volume fractions and potentials is found, the grand potential for a single micelle $\Omega(\{\varphi_i(z)\}, \{u_i(z)\})$, that is a functional of the profiles $\varphi_i(z)$ and $u_i(z)$, can be calculated. It can be interpreted as the translationally restricted subdivision potential, because we neglect the translational entropy of the micelle that is pinned in the centre of the lattice. In this Chapter we will focus on the most probable micelle, but in this same method it is possible to obtain information on the size distribution of micelles through analysis of the fluctuations in the aggregation number [21].

We model the telechelic associative polymers of the HEUR type using 2 types of segments, labeled C , which stands for CH_2 or CH_3 , and O . Their general

structure is $C_{N_T}(CCO)_{N_{EO}}C_{N_T}$, where CCO represents an ethylene oxide (EO) monomer, and C_{N_T} is an aliphatic tail. Their mono-functional analogues are given by $C_{N_T}(CCO)_{\frac{1}{2}N_{EO}}$. Because the polymers are modeled as freely-jointed chains the Kuhn length equals 1 segment. Hence the number of Kuhn segments in a polymer backbone N_B is $3N_{EO}$. A solvent molecule takes 5 lattice sites ($N_S = 5$); it consists of a central segment connected to 4 neighbors, all of type W . This approach has proven to be successful in the modeling of simple non-ionic surfactants [15].

The various interactions can be tuned with the Flory-Huggins interaction parameters (χ) between the different segments [22]. The hydrophobic interaction between the tails, that drives the micellization, is set by χ_{CW} , in these calculations χ_{CW} is constant at a value of 1.1. χ_{CO} is set at 2, which suppresses the solubility of the polymeric backbone in the hydrophobic core of the micelle. The solvency of the EO -backbone can be tuned with χ_{OW} . The effective interaction parameter for an averaged backbone segment with the solvent can be calculated with

$$\chi_{BW} = \chi_{CW}\mathcal{F}_C + \chi_{OW}\mathcal{F}_O - \chi_{CO}\mathcal{F}_C\mathcal{F}_O \quad (3.5)$$

where $\mathcal{F}_C = \frac{2}{3}$ and $\mathcal{F}_O = \frac{1}{3}$ are the fractions of C and O segments in the backbone, respectively. For chains in a non-monomeric solvent we can define the Edwards excluded volume parameter τ for the polymer backbone as

$$\tau \equiv 1 - 2\chi_{BW}N_S \quad (3.6)$$

From Equations 3.5 and 3.6 and the choices mentioned for χ_{CW} and χ_{CO} , we find that χ_{OW} needs to be set at -0.57 to reach theta conditions for the polymer backbone ($\tau = 0$). A more negative value for χ_{OW} will increase the solvent quality ($\tau > 0$).

3.3 Results and Discussion

3.3.1 CMC

There are various ways to define the critical micelle concentration in these SF-SCF calculations. The most straightforward definition of the CMC is the polymer concentration where a first stable micelle appears. In Fig.3.1 a typical result from the SF-SCF calculations is shown. We calculate these quantities for a single micelle, that we consider as one sub-system of a larger ensemble of equal cels (n_i, V, T constant). An increase in aggregation number inherently results in a decrease in the number of micelles in the ensemble. This justifies using the stability constraint

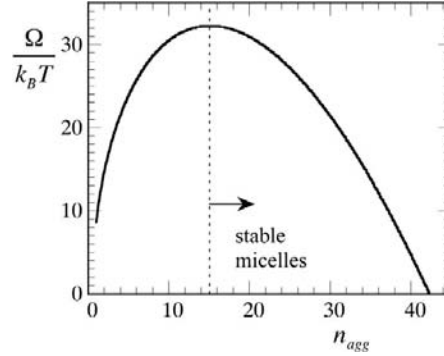


Figure 3.1: Grand potential Ω and polymer bulk volume fraction φ_{bulk} versus aggregation number n_{agg} for a $C_{20}EO_{200}C_{20}$ micellar system in a theta solvent ($\tau = 0$).

in Eqn.3.3 for defining the CMC. An alternative explanation of this CMC criterion is derived in Chapter 2.

At low aggregation numbers we first enter an unstable regime, where the system does not yet obey the stability constraint 3.4. At a given aggregation number the quantity $\frac{\partial \Omega}{\partial n_{agg}}$ will be zero, which can be regarded as the condition where the first stable micelle is formed. The unimer bulk concentration where this occurs will be our definition for the CMC [23]. Experimental CMCs will obviously be higher than this thermodynamic criterion for the CMC, as experimental methods are not sensitive enough to measure a single micelle. The experimental CMC is found when the number of micelles is significantly large, depending on the method. In fact, the scaling behavior of the CMC or the aggregation number is independent of the criterion chosen for the CMC, as long as it is unambiguously defined.

In Fig.3.2 we see how the CMC, under theta conditions for the polymer backbone ($\tau = 0$), changes with hydrophobic tail length N_T and hydrophilic backbone length N_{EO} , for mono-functional chains (Fig.3.2a) and telechelics (Fig.3.2b). The CMC is given as a number concentration; the number of molecules per lattice unit volume (l^3).

The exponential decay of the CMC with hydrophobe size, known as Traube's rule [24], for the mono-functional chains $CMC \propto \exp(-0.8N_T)$, is in good agreement with what is experimentally found for simple nonionic surfactants [25].

It is known that the critical micelle concentration is proportional to $e^{-F^m/k_B T}$, where F^m is the free energy change associated with transfer of a unimer from

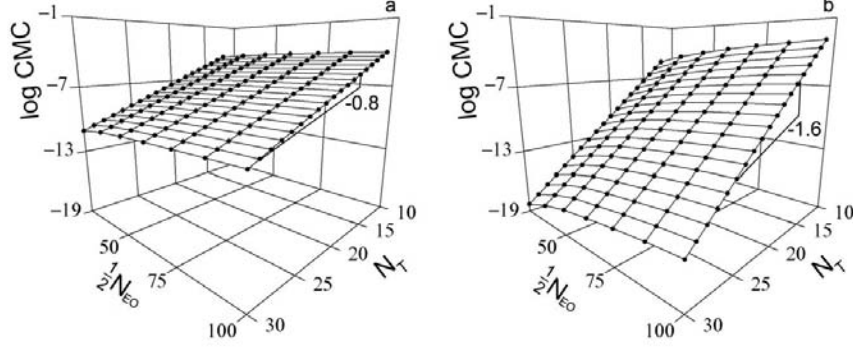


Figure 3.2: Dimensionless critical micelle number concentrations for a) a mono-functional polymeric surfactant of type $C_{N_T}EO_{\frac{1}{2}N_{EO}}$ where $CMC = \varphi^{CMC}/(1\frac{1}{2}N_{EO} + N_T)$ and b) telechelic associative polymer of type $C_{N_T}EO_{N_{EO}}C_{N_T}$ where $CMC = \varphi^{CMC}/(3N_{EO} + 2N_T)$, under theta conditions for the backbone ($\tau = 0$).

solution into a micelle. Note that $F^m < 0$ for a stable micelle. A telechelic unimer that transfers from solution into a micelle gains twice as much interaction energy compared to the mono-functional unimer, while it loses the same amount of translational entropy. This leads to an exponential decay of the CMC with N_T that is twice as strong as compared to the mono-functional associating polymers (Fig.3.2b). Hence for the telechelic polymers we find that $CMC \propto \exp(-1.6N_T)$.

Fig.3.3a takes a closer look at the scaling of the CMC with N_B . Ten Brinke and Hadziioannou [7] were the first to argue that the entropic penalty due to loop formation, as predicted by Jacobson and Stockmayer for single Gaussian chains [26], has a strong effect on the micellization of loop-forming polymers.

The free energy increase, corresponding to a loss of conformational entropy, due to loop formation, F^{loop} , for a micelle composed of n_{agg} chains, with backbones of N_B Kuhn segments long, is given by

$$F^{loop} = \frac{3}{2}\beta n_{agg}k_B T \ln N_B \quad (3.7)$$

where the factor $\frac{3}{2}k_B T \ln N_B$ originates from the decrease in possible conformations of a single Gaussian chain when it is required to loop back to its origin [26]. β is a parameter accounting for non-ideality of the chains. Under theta conditions β should be unity, and Eqn.3.7 returns to the Gaussian limit. For the CMC of telechelic chains we can derive that

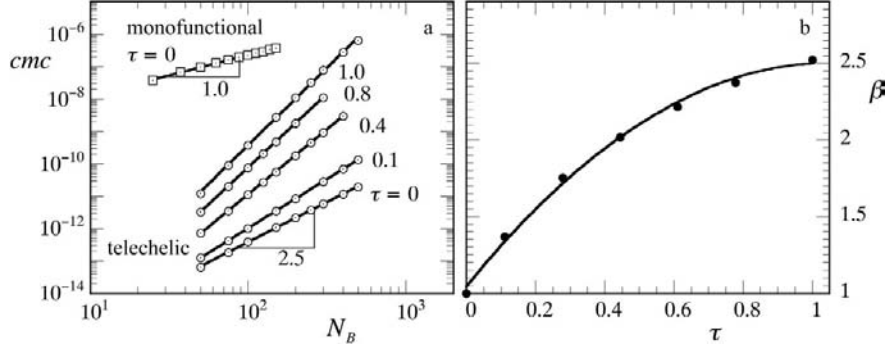


Figure 3.3: a) The dependence of the CMC upon the number of Kuhn segments in the backbone $N_B = 3N_{EO}$, as a function of the solvent quality, for a system of $C_{20}EO_{N_{EO}}C_{20}$ chains and a mono-functional analogue $C_{20}EO_{\frac{1}{2}N_{EO}}$. b) Ten Brinke's β -parameter versus the Edwards excluded volume parameter for the polymer backbone τ as found from the numerical results for $C_{20}EO_{N_{EO}}C_{20}$ chains. Solid line is a parabolic fit; $\beta = 1 + 2.5\tau - \tau^2$.

$$CMC \propto \exp\left(\frac{F^m + F^{loop}}{k_B T}\right) \quad (3.8)$$

where $CMC = \varphi^{CMC}/(3N_{EO} + 2N_T)$ is the dimensionless critical micelle number concentration for telechelic chains and here F^m is the free energy change associated with transfer of a telechelic unimer into a micelle without the contribution of the formation of loops.

From the calculations we find that for mono-functional chains $CMC \propto N_B^k$, where k is an exponent that ranges from 0.9 to 1.8 depending on N_T yet independent of the solvent quality, in the range considered here ($0 < \tau < 1$). The N_T dependence of the exponent k is possibly linked to the complicated dependence of the aggregation number on N_T and N_B , as will be shown in a following section of this Chapter. Fig.3.3a shows the result for theta conditions ($\tau = 0$) and an alkyl length of 20. For these chains we find that $k = 1.0$.

We can now derive the following expression for telechelic chains, using Eqn.3.7 and 3.8

$$CMC \propto N_B^{\frac{3}{2}\beta + k} \quad (3.9)$$

For telechelics with C_{20} alkyl tails, under theta conditions for the polymer backbone, the numerical exponent is found to be $\frac{5}{2}$. From Eqn.3.9, knowing that for the equivalent mono-functional chains $k = 1$, we find that $\beta = 1$ for $\tau = 0$, as was

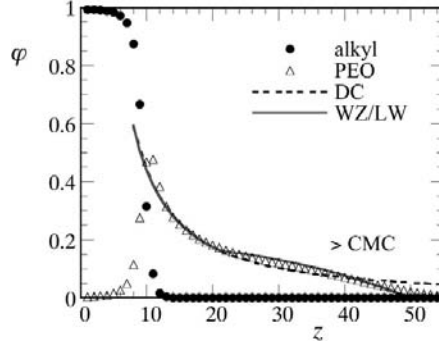


Figure 3.4: Volume fraction profile for a micelle of $C_{20}(EO)_{200}C_{20}$ chains in a good solvent for the polymer backbone ($\tau = 1$). z is the radial distance to the centre in lattice units. The drawn lines are the profiles for the alkyl tails and backbones. Dashed line is the decay predicted by the Daoud-Cotton model (DC), dotted line is the 2-zone model predicted by Wijmans-Zhulina and Li-Witten (WZ/LW).

predicted [26]. In the same way we can extract the values for β from the numerical results for chains in a good solvent, for which the value of β was so far unknown. In Fig.3.3b we have plotted β as a function of the excluded volume parameter τ , for molecules with C_{20} tails. We find the following empirical relationship, for $0 < \tau < 1$; $\beta = 1 + 2.5\tau - \tau^2$. Similar result are found for all tail lengths examined here (from C_{12} to C_{30}). The fact that the penalty associated with loop formation is larger for non-ideal chains was already predicted by des Cloizeaux for a single self-avoiding chain [27].

3.3.2 Micellar Structure

Information on the structure of the micelles follows most directly from the density profiles of the various segments. In Fig.3.4 the volume fraction profiles are shown for the core (alkyl) and corona (EO) segments of a $C_{20}(EO)_{200}C_{20}$ micelle in a good solvent for the polymer backbone ($\tau = 1$) at the CMC.

The volume fraction of alkyl tails in the core is almost 1, as expected for micellar cores in the strong segregation limit. The strong decay of the tails in the z direction indicates a sharp interface between the core and the surroundings. We see a peak in φ_{EO} at the surface of the hydrophobic core, indicating adsorption of the coronal segments onto the core/solvent interface to shield the core from the solvent. Note that this effect is not taken into account in the models that will be discussed below.

In their model for the conformations of a star-shaped polymer, Daoud and

Cotton (DC) [13] predict a density decay in the radial direction, starting from the centre of the star, that goes with either z^{-1} for theta conditions and $z^{-4/3}$ for chains with excluded volume interactions. For a flowerlike micelle consisting of telechelic polymers, in a good solvent for the polymer backbones, we compare the DC model to our numerical results (dashed line in Fig.3.4). We see that the DC-regime is only found in the first few lattice layers outward from the core, after which the volume fraction of the coronal chains follows a parabola-like profile.

Wijmans and Zhulina [11] and Li and Witten [10] have described the structure of spherical brushes using a two-zone profile. These models consist of an exclusion zone close to the core where the chain ends cannot penetrate (the so-called *dead-zone* [28]), where DC behavior prevails, which is complemented by an outer zone that the chain ends can freely access. Hence they derive the following description for the density decay in a spherical brush of swollen chains [10], adjusted for a micelle with finite core size r_{core} :

$$\varphi_{EO}(z) = \begin{cases} \left(\frac{z+r_{core}}{r_{excl}} \right)^{-4/3} \varphi_{EO}(r_{excl}) & \forall \quad (z+r_{core}) < r_{excl} \\ \frac{11B}{2\nu} (h^{*2} - (z+r_{core})^2) & \forall \quad r_{excl} < (z+r_{core}) < r \end{cases} \quad (3.10)$$

where φ_{EO} is the volume fraction of EO chains, $r_{excl} = 0.86(n_{agg}N_B^3a^2\nu)^{1/5}$ is the radius of the exclusion zone, h^* is a height given by the size of the exclusion zone $r_{excl}/h^* = 0.94$ and r is the radius of micelle. B is given by $9/(25N_B^2a^2)$, where a is the Kuhn length, in this lattice model $a = 1$, and ν is the swelling exponent ($\nu = \frac{3}{5}$ for chains in a good solvent).

In Fig.3.4 we compare this model with a typical SCF result for the density decay in the corona of the flowerlike micelles and see that this addition to the Daoud-Cotton model significantly improves the agreement with our numerical result. This implicates that the models for the structure of spherical brushes can also be used to predict the structure of micelles assembled from telechelic chains, and that the formation of loops does not significantly affect the micellar structure.

3.3.3 Aggregation number

In the following, the aggregation number (n_{agg}) is defined as the number of hydrophobic tails in the micellar core. The aggregation numbers are calculated at $\Omega = 0$, meaning that we neglect translational entropy of the micelles. In other words we are calculating the aggregation number at concentrations $\gg CMC$.

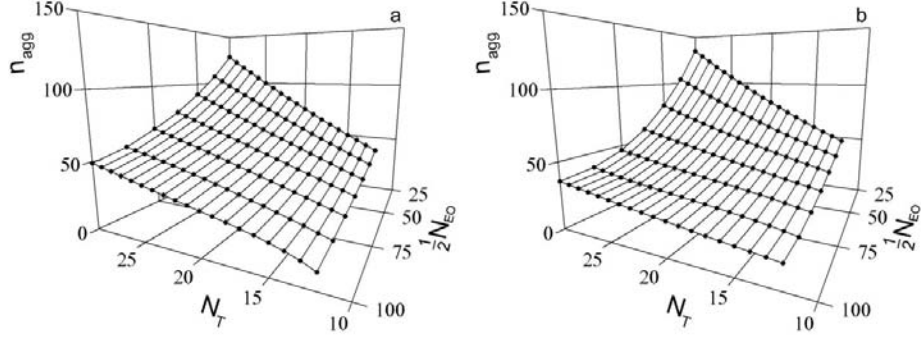


Figure 3.5: Aggregation numbers, at $\omega = 0$ for a mono-functional polymeric surfactant of type $C_{N_T}EO_{\frac{1}{2}N_{EO}}$ (a) and telechelic associative polymer of type $C_{N_T}EO_{N_{EO}}C_{N_T}$ (b) under theta conditions for the polymer backbone ($\tau = 0$).

In this set-up we consider a fixed total amount of material in micelles, hence an increase in aggregation number results in an equivalent decrease in the number of micelles.

In Fig.3.5 we show the calculated aggregation numbers as a function of N_{EO} and N_T under theta conditions for the backbone. We see that there are no large differences between the aggregation numbers of the mono-functional chains (Fig.3.5a) and the telechelic chains (Fig.3.5b). Unlike the case for the *CMC*, loop formation does not influence the results here. Since the total number of chains in micelles is fixed we do not take into account the free energy change associated with transfer of a unimer into a micelle, but only look at the most favorable distribution of a given number of chains over a variable number of micelles. We therefore do not see the influence of loop formation, as the entropy loss per chain due to loop formation is independent of the size of the micelle.

The decrease of the aggregation number with N_{EO} is the result of increasing elastic stress on the coronal chains with increasing backbone length. The increase in aggregation number with N_T results from geometrical effects of packing the tails in the core. Similar observations as shown in Fig.3.5b were recently reported by Meng and Russel [9].

The Daoud-Cotton model, that we have introduced above, is based on the stacking of stretching blobs, each containing an equal amount of elastic energy, in concentric layers around the grafting centre. The number of blobs per layer is constant and equals the number of arms in the polymer star f . The size of the blobs increases with increasing distance from the centre. In this way they account for the fact that stretching is strongest in proximity of the grafting centre. In our

micellar approach the aggregation number n_{agg} is equivalent to the number of arms f .

The size of a blob follows from geometric considerations;

$$\xi(z) = \frac{z}{f^{1/2}} = \frac{z}{n_{agg}^{1/2}} \quad (3.11)$$

where z is the radial distance from the centre of the coordinate system. We can obtain the free energy of stretching of the coronal chains, in an approach similar to Halperin [29], by integrating the osmotic pressure in the corona over the total corona volume. The osmotic pressure Π is given by $\frac{1}{\xi^3}$. The free energy of stretching (F^s) is given by

$$F^s = \int \Pi dV_{corona} = 4\pi \int_{r_{core}}^r \frac{z^2}{\xi^3} dz \quad (3.12)$$

The radius of the core r_{core} equals the cubed root of the dimensionless volume of the core. By assuming that the volume fraction of alkyl tails in the core is unity, we find that

$$r_{core} = n_{agg}^{1/3} N_T^{1/3} \quad (3.13)$$

In the Daoud-Cotton model the radius of the star-polymer scales as $N_B^\nu n_{agg}^b$, where $\nu = \frac{1}{2}$ and $b = \frac{1}{4}$ for theta conditions and $\nu = \frac{3}{5}$ and $b = \frac{1}{5}$ for chains in a good solvent. To apply this DC argument to predict the size of the micelle we must account for the finite volume of the micellar core. We can do this by extending the actual backbone with a number of virtual backbone segments, N_B^* , that together correct for the size of the core, such that $r_{core} = n_{agg}^{1/3} N_T^{1/3} = (N_B^*)^\nu n_{agg}^b$. Rewriting gives $N_B^* = (n_{agg}^{\frac{1}{3}-b} N_T^{\frac{1}{3}})^{1/\nu}$. With this correction the size of the micelle is given by

$$r = (N_B + N_B^*)^\nu n_{agg}^b \quad (3.14)$$

Inserting these expressions and the blob size, as defined in Eqn.3.11, into Eqn.3.12 gives

$$F^s \propto \int_{r_{core}}^r \left(\frac{n_{agg}^{1/2}}{z} \right)^3 z^2 dz = n_{agg}^{3/2} \ln \left[\frac{(N_B + N_B^*)^\nu n_{agg}^{b-\frac{1}{3}}}{N_T^{1/3}} \right] \quad (3.15)$$

As a first-order approximation we can balance this elastic energy in the corona with the excess free energy at the interface of the hydrophobic core and its surroundings (F^σ), to obtain n_{agg} .

Although the micellar core cannot be considered as a homogeneous macroscopic phase, we assume that there is some sort of interfacial tension γ , between the core

and its surroundings. If we assume that γ is a constant, the excess free energy of the interface then follows

$$F^\sigma = \gamma A_{core} \propto n_{agg}^{2/3} N_T^{2/3} \quad (3.16)$$

where the surface area of the spherical core is given by $A_{core} = (n_{agg} N_T)^{2/3}$. By balancing

$$\frac{\partial F^s}{\partial n_{agg}} = \frac{-\partial F^\sigma}{\partial n_{agg}} \quad (3.17)$$

and inserting the exponents ν and b as given above, we find the following result

$$n_{agg}^{-5/6} \propto f(n_{agg}) = \begin{cases} N_T^{-2/3} \ln \left[\frac{(N_B + N_B^*)^{1/2} n_{agg}^{-1/12}}{N_T^{1/3}} \right] & \text{if } \tau = 0 \\ N_T^{-2/3} \ln \left[\frac{(N_B + N_B^*)^{3/5} n_{agg}^{-2/15}}{N_T^{1/3}} \right] & \forall \tau > 0 \end{cases} \quad (3.18)$$

where

$$N_B^* = \begin{cases} n_{agg}^{1/6} N_T^{2/3} & \text{if } \tau = 0 \\ n_{agg}^{4/15} N_T^{2/3} & \forall \tau > 0 \end{cases} \quad (3.19)$$

The agreement between the scaling argument and the numerical results is satisfying both for the N_T - and N_B -dependence of n_{agg} , as shown in Fig.3.6a and b. Upon varying the alkyl chain length, for fixed values of N_B under theta conditions for the polymer backbone, the numerical results give a slope that is equal or close to the predicted slope (on double logarithmic scale) of $-5/6$ (Fig.3.6a). This indicates that even for the smallest backbone length considered here ($N_{EO} = 50$) the micelles can be seen as star-like structures and are not yet in the crewcut regime.

When we change the backbone length under theta conditions, for fixed N_T , we also find a good agreement between the model and SCF results (Fig.3.6b). However, if we do the same under good solvent conditions for the backbone the agreement is significantly less. We attribute this to the fact that the value $\frac{3}{5}$ for the swelling exponent ν is valid in the limit of infinite chain lengths and might not be accurate for the finite chain lengths chosen here.

In this Chapter our interest is in the scaling behavior of the aggregation number, analyzed using the scaling argument above. However, using our numerical results we can determine the arbitrary prefactor needed to convert the proportionality in

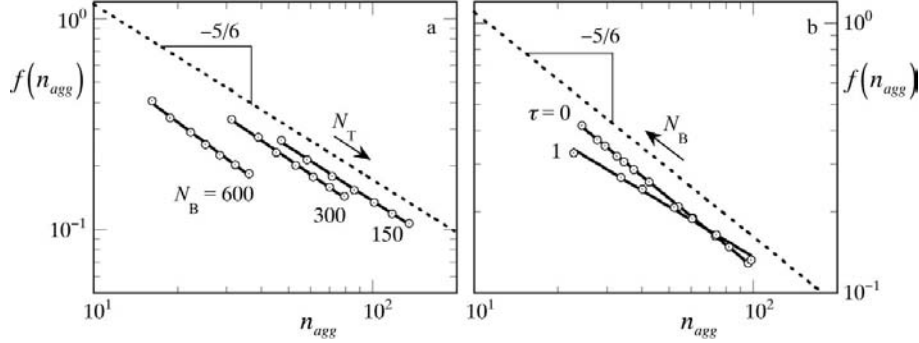


Figure 3.6: Comparison of the numerically calculated aggregation numbers and the scaling model $f(n_{agg})$ in Eq.3.18. Open symbols are numerical results, solid lines are corresponding power-law fits and dotted lines indicate the exponent of $-\frac{5}{6}$, as predicted by Eq.3.18. a) For fixed values of N_B (600, 300 and 150) as a function of alkyl length N_T , under theta conditions for the polymer backbone and b) For $N_T = 20$ as a function of backbone length N_B , which increases in the direction of the arrow, for theta ($\tau = 0$) and good solvent conditions ($\tau = 1$) for the polymer backbone.

Eqn.3.18 into an equality. For theta conditions, where the model describes the numerical scaling best, we find a prefactor of 0.17.

For the same flowerlike micelles Francois and co-workers have predicted that $n_{agg} \propto N_T^{4/5}$ [4]. It is easily shown that by neglecting the logarithmic term, Eqn.3.18 returns to this result. Although this is a good approximation and gives reasonable correspondence with our numerical results, we cannot neglect the logarithmic correction to find the exact dependence of the aggregation number on the hydrophobe length.

3.4 Conclusions

We have studied the micellization of telechelic associative polymers and their monofunctional analogues focussing on the proportionality of e.g. the CMC and the aggregation number on the size of the hydrophilic and hydrophobic block(s). The numerical results from the self-consistent field calculations are compared to approximate, but insightful, scaling arguments. We have shown that the scaling of the CMC with the hydrophilic backbone length could be explained with a simple model based on the entropic penalty for loop formation. We also found that coronal density profiles are reasonably described by the Wijmans-Zhulina and Li-

Witten model, which are elaborations on the Daoud-Cotton model that could only describe the coronal density decay in a limited part of the corona. Furthermore we have shown that the proportionality of the aggregation number with the length of the hydrophobic tail and hydrophilic backbone is well described by an expression based on the same Daoud-Cotton model, taking into account the finite volume of the core. In summary we conclude that simple scaling arguments can be used to predict the various aspects of the micellization of telechelic associative polymers in reasonable detail.

References

- [1] Xu, B.; Yekta, A.; Winnik, M. A. *Colloids Surf. A* **1996**, *112*, 239.
- [2] Pham, Q. T.; Russel, W. B.; Thibault, J. C.; Lau, W. *Macromolecules* **1999**, *32*, 2996.
- [3] Semenov, A. N.; Joanny, J. F.; Kokhlov, A. R. *Macromolecules* **1995**, *28*, 1066.
- [4] Francois, J.; Beaudoin, E.; Borisov, O. *Langmuir* **2003**, *19*, 1011.
- [5] Halperin, A. *Europhys. Lett.* **1989**, *8*, 351.
- [6] Halperin, A.; Alexander, S. *Macromolecules* **1989**, *22*, 2403.
- [7] ten Brinke, G.; Hadzioannou, G. *Macromolecules* **1987**, *20*, 486.
- [8] Balsara, N. P.; Tirrel, M.; Lodge, T. P. *Macromolecules* **1991**, *24*, 1975.
- [9] Meng, X. X.; Russel, W. B. *Macromolecules* **2005**, *38*, 593.
- [10] Li, H.; Witten, T. A. *Macromolecules* **1994**, *27*, 449.
- [11] Wijmans, C. M.; Zhulina, E. B. *Macromolecules* **1993**, *26*, 7214.
- [12] Dan, N.; Tirrel, M. *Macromolecules* **1992**, *25*, 2890.
- [13] Daoud, M.; Cotton, J. *J. Physique* **1982**, *43*, 531.
- [14] Fleer, G. J.; Cohen Stuart, M. A.; Scheutjens, J. M. H. M.; Cosgrove, T.; Vincent, B. *Polymers at Interfaces*; Chapman and Hall (London), 1993.
- [15] Jodar-Reyes, A. B.; Ortega-Vinuesa, J. L.; Martin-Rodriguez, A.; Leermakers, F. A. M. *Langmuir* **2002**, *18*, 8706.
- [16] Hill, T. L. *Thermodynamics of Small Systems, Parts 1 and 2*; Dover Pub. Inc. (New York), 1994.
- [17] Hall, D. G.; Pethica, B. A. In *Nonionic Surfactants*; Marcel Dekker Inc.: New York, 1967; chapter 16.
- [18] Scheutjens, J. M. H. M.; Fleer, G. J. *J. Phys. Chem.* **1979**, *83*, 1619.
- [19] Scheutjens, J. M. H. M.; Fleer, G. J. *J. Phys. Chem.* **1980**, *84*, 178.
- [20] Evers, O. A.; Scheutjens, J. M. H. M.; Fleer, G. J. *Macromolecules* **1990**, *23*,

- 5221.
- [21] Jodar-Reyes, A. B.; Leermakers, F. A. M. *J. Phys. Chem. B* **2006**, *110*, 6300.
 - [22] Flory, P. J. *Principles of polymer chemistry*; Cornell University Press (Ithaca), 1953.
 - [23] de Bruijn, V. G.; van den Broeke, L. J. P.; Leermakers, F. A. M.; Keurentjes, J. T. F. *Langmuir* **2002**, *18*, 10467.
 - [24] Tanford, C. *The hydrophobic effect: formation of micelles and biological membranes*; Wiley (New York), 1980.
 - [25] van Os, N.; Haak, J.; Rupert, L. *Physico-chemical properties of selected anionic, cationic and nonionic surfactants*; Elsevier, Amsterdam, 1993.
 - [26] Jacobson, H.; Stockmayer, W. H. *J. Chem. Phys.* **1950**, *18*, 1600.
 - [27] des Cloizeaux, J. *Phys. Rev. A* **1974**, *10*, 1665.
 - [28] Semenov, A. N. *Sov. Phys. JETP* **1985**, *61*, 733.
 - [29] Halperin, A. *Macromolecules* **1987**, *30*, 2943.

Chapter 4

Phase behavior of flowerlike micelles

We study the interactions between flowerlike micelles, self-assembled from telechelic associative polymers, using a molecular self-consistent field (SCF) theory and discuss the corresponding phase behavior. Adopting a SCF cell model, we calculate the free energy of interaction between a central micelle surrounded by others. Based on these results, we predict the binodal for coexistence of dilute and dense liquid phases, as a function of the length of the hydrophobic and hydrophilic blocks. In the same cell model we compute the number of bridges between micelles, allowing us to predict the network transition. Several quantitative trends obtained from the numerical results can be rationalized in terms of simple scaling arguments.

This chapter was published as:

J. Sprakel, N.A.M. Besseling, M.A. Cohen Stuart and F.A.M. Leermakers: *Phase behavior of flowerlike micelles in a SCF cell model*, Eur. Phys. J. E 25 (2008), 163.

4.1 Introduction

Telechelic associative polymers are solvophilic linear polymers modified with a solvophobic group or block at both ends of the chain. The central block can, e.g., be a neutral polymer such as poly(ethylene oxide) [1] and poly(acryl amide) [2] or a polyelectrolyte [3]. Also for the end-groups a wide variety of choices exist, such as alkyl tails [1, 2], perfluoroalkyl tails [4], pyrene groups [5], hydrophobic polymer blocks such as poly(propylene oxide)s [6] and even buckminsterfullerenes [7].

When two layers of end-adsorbed telechelic polymers (also known as telechelic brushes), are brought close to each other, bridges between the two surfaces will form. As chains gain conformational freedom when they can form bridges in addition to forming loops, an entropic attraction between the brushes results. Early numerical investigations by Milner and Witten [8] revealed that the overall interaction potential between these types of brushes is a balance between steric repulsion and a weak bridging attraction, both appearing at distances of the order of twice the brush thickness. A recently published study, using density-functional theory, substantiates these conclusions [9]. There is also experimental evidence of bridge formation between end-adsorbed layers of telechelic polymers [10, 11].

Bridging also occurs between micelles of telechelic associative polymers and leads to the formation of transient networks, but can also cause a demixing into a dilute and a more concentrated liquid phase [12]. The depth of the attractive well in the pair potential between these flowerlike micelles is reported to depend primarily on the aggregation number and on the degree of stretching of the coronal chains [13]. For ideal chains, the possibility to form bridges increases the conformational possibilities with a factor of 2 per chain. This leads to an increase in the entropy per chain of $k_B \ln 2 = 0.69k_B$, hence a change in free energy of $-0.69k_B T$ per chain. For chains with excluded volume, steric effects also come into effect, and as a result the effective contribution, per chain, to the attraction is reduced [14].

Based on theoretical predictions for the pair potential, several descriptions are available that link the compositions in the dilute and the dense coexisting phases to the molecular architecture [15, 16]. For associative polymers bearing many associating groups per chain it is predicted that, in the absence of excluded-volume interactions, all solutions are unstable above the network threshold and therefore must phase separate [17]. For telechelic associative polymers, with only 2 associating groups per chain, we will show that formation of a transient network is not necessarily accompanied by phase separation. This is also suggested by experiments on alkyl end-capped poly(ethylene oxide)s [16].

In a previous study we have used the self-consistent field theory of Scheutjens and Fler in combination with scaling arguments to investigate some important aspects of the self-assembly of telechelic associative polymers into spherical flowerlike micelles [18], such as the entropic penalty associated with the formation of loops in the corona. In this Chapter we extend this work in studying the interactions between flowerlike micelles, and two of the macroscopic consequences of these interactions; phase separation and network formation. Our method differs from previous efforts to model the interactions between these micelles. We choose a more '*ab initio*' approach; we do not make *a priori* assumptions on the micellar structure and aggregation number, instead these follow from our analysis.

We will start from the free energy of interaction between a central micelle surrounded by others, calculated in a so-called cell model. Subsequently, we use these results to predict the coexistence curves for dilute and dense micellar phases. Finally, we briefly discuss the threshold where intermicellar bridging leads to the formation of a transient network, which can also be predicted from the self-consistent field calculations. Several trends from the numerical results will be explained using scaling arguments based on the molecular architecture of the telechelic polymers.

4.2 Self-consistent field cell model for micelles

Our calculations are based on the discrete self-consistent field theory developed by Scheutjens and Fler (SF-SCF) [19, 20]. In SF-SCF theory the same length a is used to divide chains into segments and space into lattice sites. We consider telechelic chains, with segments $s = 1, 2, \dots, N$, and a spherical lattice consisting of h concentric layers with reflecting boundary conditions. The spherical lattice will be referred to as the "cell" in the remainder of this Chapter. The mean-field approximation is applied to each layer z with $z = 1, 2, \dots, h$, hence the micelles are spherical. The key lattice parameters are the number of sites $L(z)$ in each layer, for our spherical geometry $L(z) = \frac{4}{3}\pi(z^3 - (z-1)^3)$, and the *a priori* step probabilities $\lambda_{\Delta z}(z)$. These step probabilities are given by the fraction of all neighboring sites of a site in layer z that are located at $z + \Delta z$ ($\Delta z = -1, 0, +1$) and reflect the probability that a segment $s - 1$, linked to a segment s located at z , is in layer $z + \Delta z$. In a curved geometry, the step probabilities are a function of z and obey the internal balance: $\lambda_{-1}(z)L(z+1) = \lambda_1(z)L(z)$ [21]. Nearest-neighbor interactions are taken into account in terms of the Flory-Huggins interaction energy that is parameterized by the interaction parameters χ_{xy} , where x and y represent any two different segment species [22].

In the context of this model we can define a molecular state c of a species i , by the subsequent z -positions of all chain segments z_{is}^c . The number of possible conformations ω_i^c of a chain i in state c is, within a Markov approximation, given by

$$\omega_i^c = L(z_{i1}^c) \prod_{s=2}^{N_i} \lambda_{\Delta z}(z_{is}^c) Z \quad (4.1)$$

where z_{is}^c is the layer in which segment s of molecule i in state c is found, $L(z_{i1}^c)$ is the number of sites in layer z , where the first segment of species i in conformation c is located, and Z is the number of neighbors of each site. $\prod_{s=2}^{N_i} \lambda_{\Delta z}(z_{is}^c)$ is the multiple product of the step probabilities of the subsequent steps, going from the layer where segment 1 is located to the layer where segment 2 is located, etc. up to the last segment N_i , all according to the conformation c .

The Helmholtz energy of the inhomogeneous system can be written as a functional of the distribution of molecular states;

$$\frac{F(\{n_i^c\}, T)}{k_B T} = \sum_{i,c} n_i^c \ln \left(\frac{n_i^c}{\omega_i^c} \right) + \frac{F^{int}}{k_B T} \quad (4.2)$$

The first term accounts for the configurational entropy. The Flory-Huggins interaction energy is given by the second term, and can be written as

$$\frac{F^{int}}{k_B T} = \frac{1}{2} \sum_{z,x,y} n_x(z) \langle \phi_y(z) \rangle \chi_{xy} + u'(z) \left[\sum_x n_x(z) - L(z) \right] \quad (4.3)$$

in which $n_x(z)$ is the number of segments of segment species x in layer z . The factor $\langle \phi_y(z) \rangle$ is the average fraction of y segments among the nearest neighbors of a segment in layer z and is found with $\langle \phi_y(z) \rangle = \sum_{\Delta z} \lambda_{\Delta z}(z) \phi_y(z)$ where $\phi_y(z) = n_y(z)/L(z)$. The second term in Eqn.4.3 is coupled to the incompressibility of the system, in which $u'(z)$ is the Lagrange parameter.

The abundance of each molecular state in terms of a molecular field is obtained by evaluating $\partial \Omega / \partial n_i^c = 0$ ($\forall i, c$), with the grand potential

$$\Omega = F - \sum_i \mu_i n_i \quad (4.4)$$

where $\mu_i = (\partial F / \partial n_i)_{T, n_{j \neq i}}$. The number of molecules of species i in state c , n_i^c , is found from a Boltzmann weight of the potential fields for that species u_i^c , and follows

$$n_i^c \propto \omega_i^c \exp \left[\frac{-u_i^c}{k_B T} \right] \quad (4.5)$$

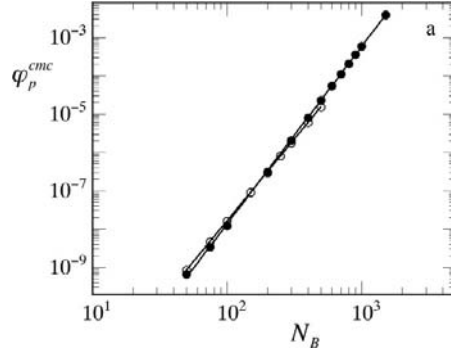


Figure 4.1: Comparison between the numerical results for the critical micelle concentration for A₂₀-B_N-A₂₀ chains using the present coarse-grained model for telechelic polymers (filled symbols) and the molecularly realistic model used in Chapter 3 (open symbols).

The potential field for a species i in conformation c , follows from summation over the segment potentials $u(z_{is}^c)$ for all segments in the chain;

$$u_i^c = \sum_{s=1}^{N_i} u(z_{is}^c) \quad (4.6)$$

The segment potential for a segment s of type x in layer z is obtained by differentiating the interaction term in the free energy (Eqn.4.3) to the number of segments of type x in that layer; $u_x(z) = \partial F^{int} / \partial n_x(z)$.

A solution for the complete distribution of molecular states $\{n_i^c\}$ should satisfy the following incompressibility constraints: $\sum_x n_x(z) = L(z)$ for all z , which fixes $u'(z)$, and $\sum_c n_i^c = n_i$ for all i , which gives the normalization constant for Eqn.4.5.

It turns out that the segment density distributions, that determine the molecular field, can be found using the propagator scheme developed by Scheutjens en Fler [19] without explicitly evaluating all n_i^c . In this way both the molecular fields and the segment density distributions can be efficiently calculated in a numerical iteration procedure, until self-consistency is reached [23]. A more detailed description of SF-SCF theory and its applications to self-assembly can be found elsewhere [24]

In a previous study on the micellization of telechelic polymers we have used a molecularly realistic model to predict the self-assembly of a specific class of telechelic associative polymers, i.e. alkyl end-capped poly(ethylene oxide)s, in which hydrogenated carbon atoms and ether oxygens of poly(ethylene oxide) were treated as different segment types [25]. Here we choose a coarse-grained version

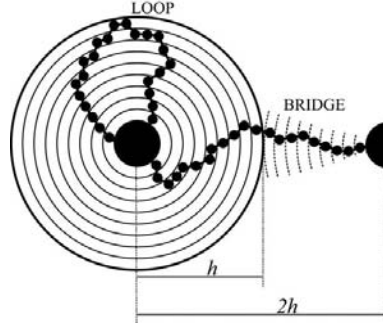


Figure 4.2: Schematic representation of the self-consistent field cell model, at a cell size h , with reflecting boundary conditions. Coronal chains, departing from the micellar core, have two 'dominant' configurations: i) loops, for all values of h , the one shown here just reaches the outer layer and ii) bridges, that cross the cell boundary, for not too large values of h .

of that model, in which the solvophilic, middle-block segments are represented by one "average" segment type B , and the solvophobic, end-block segments are represented by segment type A , such that the present study is applicable to a wide variety of telechelic associative polymers. Freely jointed A - B - A chains are placed on the spherical lattice together with a monomeric solvent S . The A -blocks are oligomeric (N_A between 10 and 35) and strongly segregate with the monomeric solvent. The central B -blocks are polymeric (N_B between 100 and 10,000). The interactions between the three segment species are quantified by the corresponding χ parameters. All calculations are carried out under θ -conditions for the polymer backbone, i.e. $\chi_{BS} = 0.5$. For example for poly(ethylene oxide), one of the most used neutral backbones in associative polymers, it is known that the Flory interaction parameter between the polymer and water at room temperature is very close to 0.5 [26]. The other two parameters were chosen such that the results for the critical micelle concentrations (CMC) of the molecularly realistic model in [25] are reproduced. The results from the earlier model could be reproduced, with an error of less than 10% for the investigated range of block lengths, with $\chi_{AS} = 1.9$ and $\chi_{AB} = 1$ in the present coarse-grained model. The correspondence between the results for the CMC from the molecularly realistic model [18] and the current model is illustrated in Fig.4.1.

4.2.1 Isolated, non-interacting micelles

Isolated micelles are studied in the self-consistent field cell model for large values of h , such that the central object cannot interact with any neighbors. For large h , no bridges can form, and all chains form loops (see Fig.4.2).

According to the thermodynamics of small systems [27, 28], the work associated with the formation of micelles \mathcal{E} must vanish, i.e. $\mathcal{E} = 0$. In a real system, the number of micelles \mathcal{N} is adjusted by the system until this condition is met, i.e. $\partial F / \partial \mathcal{N} = \mathcal{E} = 0$. In this sense, the number of micelles is not a controlled variable (i.e. it is not an external variable). In the self-consistent field modeling of flowerlike micelles, however, one studies a small system that contains a single micelle. Indeed, for such an analysis the number of micelles is exactly controlled. This implies that the thermodynamic analysis of micellization in a SCF model requires special attention.

The micellar object in the SCF model is translationally restricted to the center of the coordinate system. The grand potential Ω of such a micelle is readily available from the SCF calculations (see Eqn.4.4). For dilute solutions one can estimate the translational entropy per micelle as $S_{trans} = -k_B \ln \varphi_p^m$, where φ_p^m is the volume fraction of micelles in the system. The overall work of formation of a micelle in the SCF model is therefore

$$\mathcal{E} = k_B T \ln \varphi_p^m + \Omega = 0 \quad (4.7)$$

which gives the connection between the microscopic model to the macroscopic thermodynamics [27, 28]. In the SCF model, Eqn.4.7 is used as follows. Typically from the calculations the relation $\Omega(n_{agg})$ is known, where n_{agg} is the excess number of amphiphiles per micelle. From Eqn.4.7 we then find $\varphi_p^m(n_{agg})$. As $0 < \varphi_p^m < 1$, it is clear that relevant micelles have $\Omega > 0$.

It can be shown that the Gibbs-Duhem equation for micellization in the small system reads

$$\partial \Omega / \partial \mu_p = -n_{agg} \quad (4.8)$$

As the fluctuations in (micellar) aggregation numbers are related to $\partial n_{agg} / \partial \mu_p$, and because this is necessarily a positive number, we find from Eqn.4.8 that relevant micellar systems obey to $\partial \Omega / \partial n_{agg} < 0$ (stability constraint).

In the context of this SCF model, the critical micelle concentration is defined as the concentration where $\partial \Omega / \partial n_{agg} = 0$. The aggregation number n_{agg} is defined as the number of polymer chains in the micelle, and is related to the total number of polymer chains n_p in the system and the number of micelles \mathcal{N} with $n_p =$

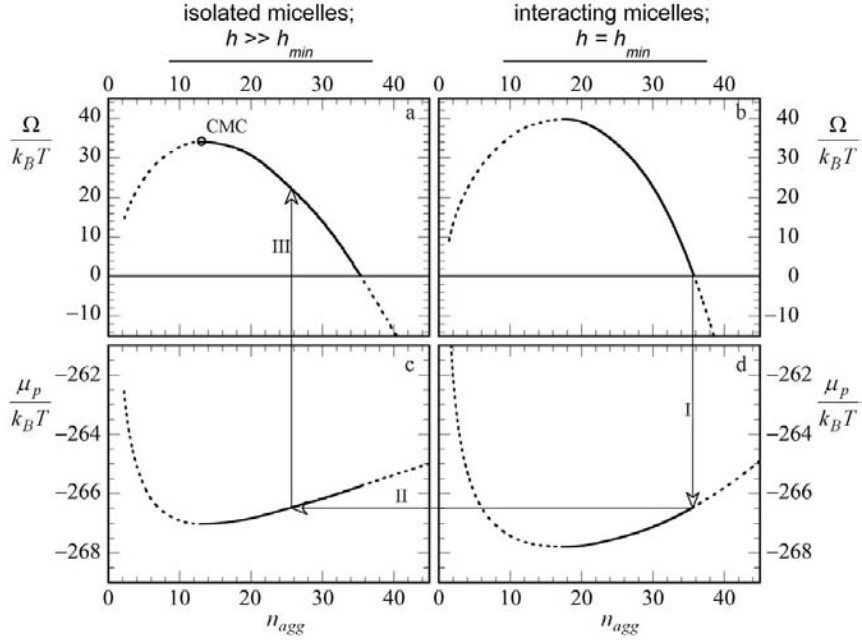


Figure 4.3: Typical results from the SF-SCF calculations for isolated and non-interacting micelles ($h \gg h_{min}$, a & c) and for interacting micelles at the minimum of the interaction energy between the micelles with respect to h ($h = h_{min}$, b & d). Results shown are for systems of A₂₀-B₅₀₀-A₂₀ polymers, dotted lines represent solutions that are not macroscopically stable.

$\mathcal{N}n_{agg} + V\varphi_p^b/N$, where V is the volume of the system, φ_p^b is the bulk unimer concentration and N is the total chain length of the polymer. For the calculations, where $\mathcal{N} = 1$, the appropriate volume is the cell volume $V^{cell} = \frac{4}{3}\pi h^3$.

In Fig.4.3a we see the grand potential as a function of aggregation number, due to the stability constraint we only consider the solutions for which $\partial\Omega/\partial n_{agg} < 0$. In Fig.4.3 all solutions from the self-consistent field calculations, which correspond to situations that are not macroscopically stable, i.e. when $\partial\Omega/\partial n_{agg} > 0$, or which are physically not meaningful, i.e. when $\Omega < 0$, are indicated with dotted lines.

4.2.2 Interacting micelles in concentrated systems

The interactions between micelles are studied in the cell model by decreasing the cell size h to the same order of magnitude as the size of the micelle. Typical results for this situation are shown in Fig.4.3b and 4.3d. Here again we only consider those

solutions for which $\partial\Omega/\partial n_{agg} < 0$. By decreasing the cell size, which is equivalent to increasing the concentration of micelles, the central object can interact with its neighbors by way of the reflecting boundary conditions. In essence the idea of a reflecting, i.e. mirroring, boundary, is straightforward. In a flat geometry, the reflecting boundary is a plane of symmetry; for each chain configuration that leaves the system volume through the boundary, a complementary chain enters the volume through the same boundary. Mathematically this is implemented by forcing the segment densities, as well as the segment potentials, in a given layer outside the boundary to assume the same (known) value as its mirror-image inside the volume. The mathematical implementation of the boundary condition in the current spherical geometry is the same. An intuitive understanding of the resulting situation is, however, somewhat troublesome. Again, for each chains that leaves the cell through the outer boundary a complementary chain enters the volume as if it comes from a neighboring micelle. The exact position of all neighbors is however not realistically accounted for. The distance between the center of the central micelle and its mirror images is $2h$. For small enough values of h we distinguish two dominant types of conformations of the coronal parts of the polymers upon interaction; bridges and loops. This is illustrated schematically in Fig.4.2.

We compute the thermodynamic quantities for these interacting micelles at $\Omega = 0$ as a function of h . As discussed in the previous section the grand potential is directly coupled to the translational entropy of the micelles (Eqn.4.7). Setting the condition $\Omega = 0$ implies that we consider the translational entropy to be negligible. At high concentrations, where the micelle interacts with many neighbors, this assumption is reasonable. It is known that under experimental conditions a structured and highly interconnected micellar network is formed, in which the translational freedom of the micelles is obviously suppressed [29]. One of the consequences of the cell model is that the distances between all micelles in the system are approximated to be equal. We can argue that this approximation should be reasonable for concentrated systems where the micelles are closely packed, and for systems where the micelles are trapped in an attractive well that is many times larger than the thermal energy $k_B T$, such that fluctuations around the equilibrium position are small. This issue is evaluated in somewhat more detail in the Discussion at the end of this Chapter.

The free energy difference of a micelle surrounded by neighbors with respect to an isolated micelle (for which $\Omega = 0$), is defined as $\Delta F^m(h) = F^m(h) - F^m(\infty)$. Note that this free energy difference is not a pair potential, rather the interaction free energy between a central micelle and all its neighbors. The cell size value where ΔF_m is minimal is denoted h_{min} .

4.2.3 Computing biphasic coexistence

The attractive interactions between flowerlike micelles can cause macroscopic demixing [12]. To determine the coexistence in the context of this SCF model we make two approximations. The first is that in the dilute phase the micelles have no intermicellar interactions, such that we can use the results for isolated micelles to predict the properties of this phase. The second approximation is that in the dense phase the micelles have no translational entropy, such that we can use the results from the cell model for intermicellar interactions for this phase. These approximations are likely to be valid away from the critical point. Close to the critical point however, the micelles will interact with each other in both phases as well as have significant translational entropy in both the dense and the dilute phase. The true position of the critical point is therefore not obtained in this approach.

In the coexisting liquid phases (denoted *dense* and *dilute*) both the osmotic pressures ($\Pi^{dense} = \Pi^{dilute}$) and the chemical potential of the polymer ($\mu_p^{dense} = \mu_p^{dilute}$) should be equal. For the dilute phase we can argue that, as the concentration of micelles is very low, the osmotic pressure will be negligible. Here we approximate the osmotic pressure to be zero. Consequently, the osmotic pressure in the dense phase will also be zero. Although the concentration of micelles is significant in the dense phase, we can argue that the attraction between the micelles, resulting in a negative second virial coefficient, can strongly reduce the osmotic pressure to negligible values. To predict coexistence we need to find solutions to the self-consistent field model for both isolated and interacting micelles, that have the same chemical potential of the polymer μ_p .

Our approach is schematically illustrated in Fig.4.3. We start with the typical result of the grand potential versus aggregation number for interacting micelles (dense phase). Above we discussed the choice for approximating the osmotic pressure to be zero in both phases. For an incompressible system, as is the case in these SCF calculation, we can find the osmotic pressure by differentiating the free energy to the cell volume, that is given by $\frac{4}{3}\pi h^3$, hence;

$$\Pi = \frac{-\partial F^m(h)}{\partial V} = \frac{-\partial F^m(h)}{4\pi h^2 \partial h} = 0 \quad (4.9)$$

Since $4\pi h^2$ is always finite positive, $\partial F^m / \partial h$ must be zero. As a consequence, we will regard the minimum of the free energy of interaction with respect to h to be the equilibrium situation. In other words, we find the solutions to the self-consistent field model for $h = h_{min}$ and for which $\Omega = 0$. These requirements are met, as indicated in Fig.4.3b, for a given aggregation number (here $n_{agg} = 34$). In the plot of the chemical potential of unimers μ_p versus aggregation number (Fig.4.3d) we

can now find the corresponding chemical potential of the polymer chains in the bulk phase (here $-266.5k_BT$, arrow I).

The volume fraction in the dense phase (φ_p^{dense}), given by the composition in the cell, can be split up into two contributions: that of polymer chains that are associated in the central micelle (φ_p^m) and that of free unimers (φ_p^b). The contribution of chains in the micelle, φ_p^m , is obtained by dividing the total number of polymer segments (each occupying 1 lattice site) in the micelle by the cell volume $V^{cell} = \frac{4}{3}\pi h_{min}^3$;

$$\varphi_p^m = \frac{N_p n_{agg}}{\frac{4}{3}\pi h_{min}^3} \quad (4.10)$$

where $N_p = 2N_A + N_B$ is the total chain length of the *ABA* polymer. The bulk volume fraction of free unimers follows from μ_p , using the Flory-Huggins expression for the chemical potential for a system composed of species *S* (solvent) and *ABA* (polymer) and segments *S*, *A* and *B*;

$$\begin{aligned} \frac{\mu_p - \mu_p^*}{k_BT} = & -\ln \varphi_p^b + (1 - \varphi_p^b)(1 - N_p) + \\ & + \frac{1}{2}N_p \sum_i \sum_j (\varphi_i^b - \Phi_i) \chi_{ij} (\varphi_j^b - \Phi_j) \end{aligned} \quad (4.11)$$

in which μ_p^* is the reference state of the chemical potential of the polymer, defined such that Eqn.4.11 returns zero for $\varphi_p^b = 1$. φ_i^b and φ_j^b are the bulk volume fractions of segment types *i* and *j*, with *i* or *j* = *A*, *B*, *S*. Φ_i and Φ_j are the fractions of segments in *ABA* the polymer that are of type *i* and *j* respectively. Hence, Φ_S is zero, $\Phi_A = 2N_A/N_p$ and $\Phi_B = N_B/N_p$.

Now that we have all ingredients to compute the composition of the dense phase, we proceed to calculate the composition of the dilute phase. We now start from the chemical potential of the unimers found in Fig.4.3d (arrow I). As the chemical potential of the unimers must be equal in both phases, we can find the coexisting configuration of a system of isolated non-interacting micelles. In Fig.4.3c we see that at the given chemical potential, the isolated micelles have an average aggregation number of 25 (arrow II). For the dilute system we can now also see, in Fig.4.3a, that at this chemical potential and corresponding configuration, the micelles have a finite, non-zero grand potential (arrow III), in this case $\Omega \approx 20 k_BT$. This indicates that in the dilute phase the micelles do have significant translational entropy, since $\Omega = -S_{trans}T$.

With the chemical potential and the grand potential known for the dilute phase, we can also calculate its overall composition. Again, the overall polymer volume

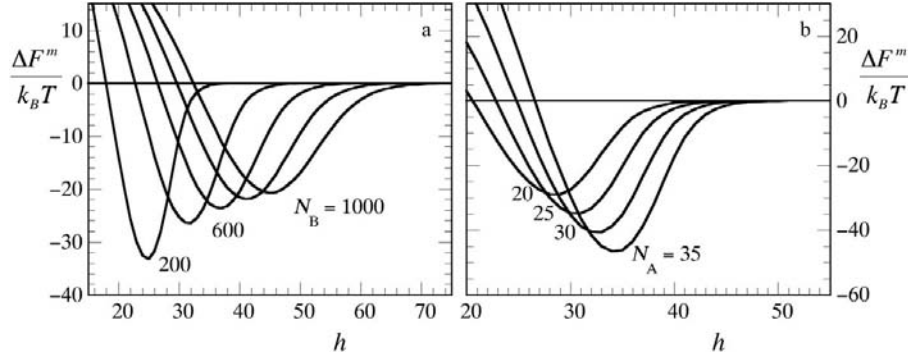


Figure 4.4: Free energy of interaction $\Delta F^m(h)$ between a central flowerlike micelle and all its neighbors, calculated in the self-consistent field cell model; a) for $A_{20}-B_N-A_{20}$ polymers with $N_B = 200, 400, 600, 800$ and 1000 and b) for $A_N-B_{500}-A_N$ with $N_A = 20, 25, 30$ and 35 .

fraction is given by $\varphi_p^{dilute} = \varphi_p^b + \varphi_p^m$. The bulk volume fraction φ_b^b again follows from Eqn.4.11, and must be the same as in the dense phase since the chemical potentials are also equal. The volume fraction of polymer in micelles in the dilute phase can be obtained from Ω (Eqn.4.7).

4.2.4 Computing the number of bridging chains

In this SCF cell model it is also possible to obtain the number of bridges n_b that are formed by a micelle. To find n_b we start by defining the lattice parameters for the central object and its mirror image. The system now contains twice as many layers; $z = 1, 2 \dots h, h+1 \dots 2h$. The number of sites per layers $L(z)$ is given by $L(z) = \frac{4}{3}\pi(z^3 - (z-1)^3) \forall z < h+1$ and $L(z) = L(2h-z+1) \forall z > h$. Consequently, we need to mirror the step probabilities, such that for $z > h$: $\lambda_{\Delta z}(z) = \lambda_{-\Delta z}(2h-z+1)$ ($\Delta z = -1, 0, 1$), and the segment potentials, with $u_x(z) = u_x(2h-z+1)$ for all $z > h$ and x . By defining a bridge as a chain that has its first segment in a layer with $z < h+1$ and its last segment in $z > h$, we can calculate n_b using the propagator scheme of Scheutjens and Fleer.

4.3 Intermicellar interactions

Several results for the interactions between flowerlike micelles, calculated in the SCF cell model, are shown in Fig.4.4, as a function of backbone length (Fig.4.4a)

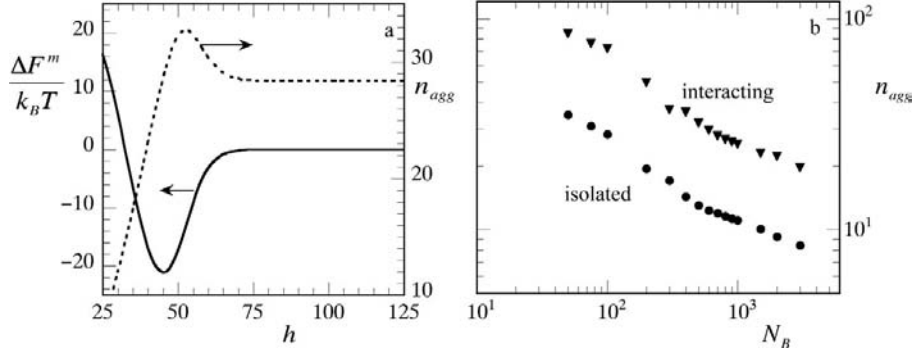


Figure 4.5: a) Effect of interactions in the cell model on the aggregation number (n_{agg}), in comparison to the interaction free energy ΔF^m for $A_{20}-B_{500}-A_{20}$ polymers and b) dependence of the aggregation number on the backbone length for isolated micelles ($h \gg h_{min}$, circles) and micelles at the minimum of the interaction potential ($h = h_{min}$, triangles).

and end-block length (Fig.4.4b). We can recognize some clear trends: the interactions decrease in strength and increase in range with increasing backbone length and with decreasing length of the associating end blocks.

For end-adsorbed layers of telechelic polymers it has been predicted that the *range* of both steric and bridging interactions is proportional to the brush thickness [8]. For micelles this suggests that the interaction range is characterized by the radius of the micelle (R) [13]. We have previously shown [18] that

$$R \propto \left(N_B + n_{agg}^{\frac{1}{6}} N_A^{\frac{2}{3}} \right)^{\frac{1}{2}} n_{agg}^{\frac{1}{4}} \quad (4.12)$$

This follows from the Daoud-Cotton model [30], adjusted for the non-zero size of the micellar core. When the concentration of micelles is increased, or, in other words, when the typical distance between the micelles is decreased, the chemical potential changes. This also leads to a change in aggregation number. In Fig.4.5a the change in aggregation number with h is shown (dotted curve). We see a significant change of the number of chains per micelle with decreasing h that is equivalent to increasing the concentration of micelles. This implies that, to properly apply Eqn.4.12 we must use $n_{agg}(h)$ rather than a fixed n_{agg} . In Fig.4.5b it is shown that although the absolute value of n_{agg} depends on the concentration, the same dependence between aggregation number and backbone length is found for isolated micelles and micelles that interact with multiple neighbors. The change in aggregation number with a variation in the molecular architecture has been discussed previously [18].

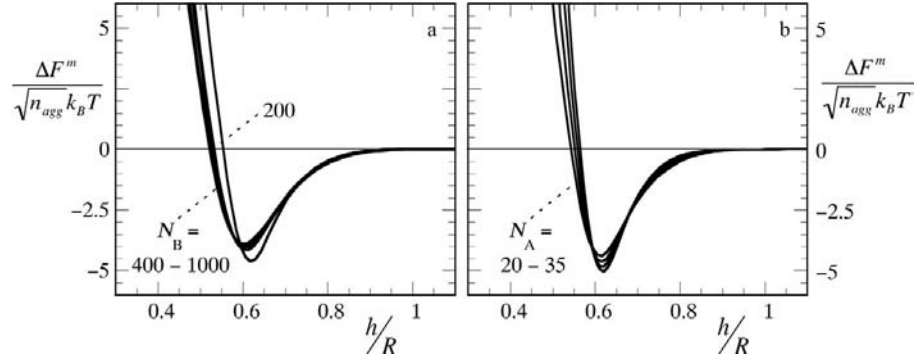


Figure 4.6: Rescaled free energy of interaction between a central flowerlike micelle and all its neighbors, calculated in the self-consistent field cell model, plotted versus the rescaled cell size h/R ; a) for $A_{20}-B_N-A_{20}$ polymers with N_B ranging from 200 to 1000 and b) for $A_N-B_{300}-A_N$ with N_A ranging from 30 to 35.

Adopting a Derjaguin approximation, Meng and Russel calculate the interactions between flowerlike micelles starting from the results for flat telechelic brushes. Within this approximation, the *strength* of the interaction is governed by two parameters only; the aggregation number n_{agg} and the degree of stretching of the coronal chains $RN_B^{-1/2}$. They derive that $\Delta F^m \propto n_{agg} N_B R^{-2}$. For R we can use Eqn.4.12. Here we can approximate R by $N_B^{1/2} n_{agg}^{1/4}$, since N_B is generally much larger than $n_{agg}^{1/6} N_A^{2/3}$. Rewriting gives

$$\Delta F^m(h) \propto n_{agg}(h) \frac{N_B}{R^2} \approx n_{agg}(h)^{\frac{1}{2}} \quad (4.13)$$

With Eqns 4.12 and 4.13 as predictions for the range and strength of the interactions respectively, we can plot the curves in Fig.4.4 on rescaled coordinates. We plot the normalized interaction energy $\Delta F^m / \sqrt{n_{agg}}$ versus the normalized distance between the centers of the micellar objects h/R , where R is found from Eqn.4.12. The result is shown in Fig.4.6.

We see that the curves, with the exception of the curves for $N_B = 200$ in Fig.4.6a, now almost collapse onto a master curve. This confirms that the range of the interactions is determined by the size of the micelles and that the strength of the interactions is a function of the aggregation number and chain stretching only. The curve for the smallest middle block length ($N_B = 200$) in Fig.4.6a does not coincide with the other curves because the assumption that $n_{agg}^{1/6} N_A^{2/3}$ is negligible compared to N_B (see derivation of Eqn.4.13) is not valid for this short chain length.

If we take the value of the interaction energy at h_{min} and divide this by the aggregation number, we find the contribution per chain to the depth of the attractive well. In the range of molecular parameters investigated here, we find an average contribution per chain to the attraction of 0.6 - 0.7 $k_B T$. This is of the same order of magnitude as the predicted value of $k_B T \ln 2 = 0.69 k_B T$ for ideal chains [13]. We must note that, although we are at θ -conditions for the polymer backbone ($\chi_{BS} = 0.5$), the chains do show stretching in the micellar corona. This is also reflected in the fact that for micelles of ideal chains the depth of the minimum would depend solely on the aggregation number, whereas here we need to account for chain stretching as well in order to collapse the curves in Fig.4.6. We can attribute this apparent importance of excluded volume effects for chains in a θ -solvent, to crowding in the corona of the micelle.

The interactions start when h/R is approximately unity, which corresponds to a separation between the centers of the interacting objects of roughly twice the micellar radii. This has also been predicted previously [8].

4.4 Biphase Coexistence

In Fig.4.7 we show the numerically calculated coexisting compositions (Eqns 4.7, 4.10 and 4.11) in systems of flowerlike micelles, both as a function of the length of the middle B -block and as a function of the length of the A -end-blocks. We can immediately see that the phase diagrams are strongly asymmetric with respect to the volume fraction of polymer at the extrapolated critical point.

In the concentrated phase the amount of unimers is negligible compared to the chains assembled in the micelle, hence $\varphi_p^{dense} \approx \varphi_p^m$. Also $N_p \approx N_B$ as the end-block length is small compared to the middle block in the molecular architectures investigated here. We already argued that $h_{min} \propto R$. Using Eqn.4.10 we can derive

$$\varphi_p^{dense} \propto \frac{n_{agg} N_B}{R^3} \quad (4.14)$$

The proportionality $\varphi_p^{dense} \propto R^{-3}$ was already predicted by Francois et al. [16]. The radius of the micelle R can again be approximated by $N_B^{1/2} n_{agg}^{1/4}$. The aggregation number is intricately linked to molecular architecture, as discussed in [18]. As a first order approximation we can use $n_{agg} \propto N_A^{4/5}$, in which the logarithmic dependency of the aggregation number on N_B has been omitted as it is much weaker than the power-law proportionality between N_A and n_{agg} . We now find

$$\varphi_p^{dense} \propto N_B^{-\frac{1}{2}} N_A^{\frac{1}{5}} \quad (4.15)$$

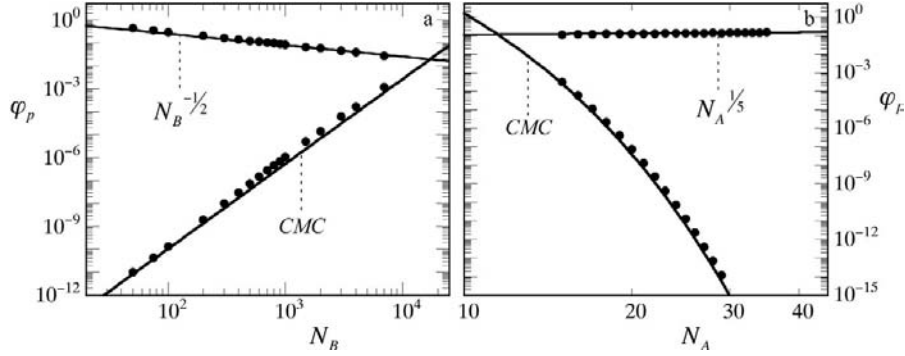


Figure 4.7: Numerically obtained binodals (symbols) as a function of a) backbone length (N_B) in a system of $A_{20}-B_N-A_{20}$ polymers and b) end-block length (N_A) in a system of $A_N-B_{500}-A_N$ polymers. Solid lines are numerically calculated critical micelle concentrations (CMC) and fits to the scaling relation in Eqn.4.15, with $\varphi_p \propto N_B^{-1/2}$ in a) and $\varphi_p \propto N_A^{1/5}$ in b).

To test this scaling relation, we have fitted the dense branches of the binodals in Fig.4.7 to $\varphi_{dense} \propto N_B^{-1/2}$ (Fig.4.7a) and $\varphi_{dense} \propto N_A^{1/5}$ (Fig.4.7b), respectively. An excellent correspondence is found between the scaling argument and the numerical results.

For the dilute branch of the binodal we find that the compositions are close to the critical micelle concentrations (CMC). This can be seen in Fig.4.7, where the lower solid lines are the critical micelle concentrations. For the parameters chosen here, that imply strong segregation of the end-blocks, we have previously [18] discussed the dependency of the CMC on the molecular architecture. Combining $\varphi_{dilute} \approx CMC$ with the result found in [18] gives:

$$\varphi_p^{dilute} \propto N_B^{\frac{3}{2}+g} \exp\left(-\frac{3}{2}N_A\right) \quad (4.16)$$

where the exponential decay of the CMC with the end-block length N_A is similar to that of ordinary surfactants, but twice as strong because there are 2 hydrophobic moieties attached to a single chain. The factor N_B^g is the dependency of the CMC on the length of the hydrophilic block for equivalent diblock copolymers (in these calculations $g \approx 2$), and the factor $N_B^{3/2}$ accounts for the entropy loss due to loop formation of non-interacting telechelic chains in isolated flowerlike micelles [31].

Using the scaling relations for both branches of the binodal in Eqns 4.15 and 4.16 we can also derive expressions for the point where these branches meet. This intersection point can be considered to be an upper limit for the critical value of

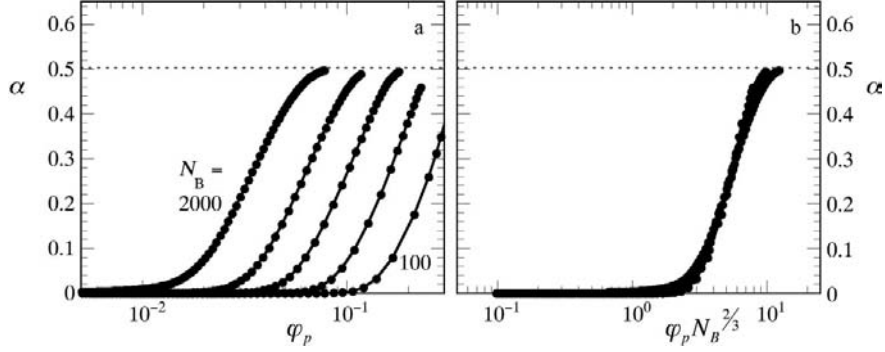


Figure 4.8: a) fraction of the total chains in the micelle that have formed a bridge $\alpha = n_b/n_{agg}$ as a function of polymer volume fraction ϕ_p for various values of N_B (100, 200, 400, 1000, 2000) in systems of A_{20} - B_N - A_{20} polymers. b): same results as in a) plotted as α versus $\phi_p N_B^{2/3}$.

N_B or a lower limit for the value of N_A at the critical point. For example, to find the upper limit for the critical backbone length (N_B^*), for a given end-block length N_A , we start with $\phi_p^{dense} = \phi_p^{dilute}$. Rewriting then gives:

$$N_B^* \propto N_A^{\frac{1}{10g}} \exp\left(\frac{3}{4g} N_A\right) \quad (4.17)$$

As the latter, exponential, term grows much faster than the first, power-law, term, we can neglect the first term and find; $N_B^* \propto \exp\left(\frac{3}{4g} N_A\right)$. Here $g \approx 2$, giving; $N_B^* \propto \exp\left(\frac{3}{8} N_A\right)$. This gives a quasi-Traube's rule [32] for the minimal length of a middle block, for a given end-block length, that assures that the system is homogeneous at all concentrations, which could be used as a design rule, e.g., for the development of novel associative thickeners, where the occurrence of demixing is undesired.

In the explanation of the approach to compute biphasic coexistence, we have mentioned that the model can be expected to be only valid far enough away from the critical point. As explained in more detail in the Discussion-section of this Chapter, we expect all data points shown in Fig.4.7 to lie within the validity of our model.

4.5 Transient network threshold

From the self-consistent field cell model we have also obtained the number of bridges, n_b , formed by the central micelle with its neighbors. As stated in the

introduction we expect bridging to be an entropic phenomenon, driven by the gain in conformational freedom when chains have the possibility to form bridges in addition to forming loops. For a chain, of which at least one segment is located at the symmetry plane, the probability to form a loop and the probability to form a bridge are equal. As a result, we expect that at high concentrations exactly half of all chains have formed a bridge, whereas the other half is present in loops. In Fig.4.8a the fraction of chains that have formed a bridge $\alpha = n_b/n_{agg}$ is plotted versus polymer concentration. It shows that in the limit of high concentrations this value indeed levels off at a plateau value of $\frac{1}{2}$. From the same plot we can also conclude that the onset and saturation of bridging occurs at lower volume fractions for chains with larger middle blocks.

Now that we have obtained the number of bridges as a function of polymer concentration we can estimate at what concentration a macroscopic association cluster of micelles is formed. Above this concentration, where we have a percolated structure in our system, we can expect the mechanical properties of the system to change from fluid-like to viscoelastic. The concentration φ_p^{net} where this transition occurs is denoted the transient network threshold

To find the network threshold we need to define a criterion for the average number of bridges per micelle that are required for the formation of a macroscopic network (n_b^{net}). Here we will consider two estimates for this transition. The first is the so-called Flory gel point criterion [22], that takes into account the functionality n_{agg} of the nodes;

$$\alpha^{net} = \frac{n_b^{net}}{n_{agg}} = \frac{1}{n_{agg} - 1} \quad (4.18)$$

where $\alpha^{net} = n_b/n_{agg}$ is the fraction of the total number of possible bridges that must form to obtain a macroscopic network. In these systems $n_{agg} \gg 1$, hence n_b^{net} goes to unity. The Flory criterion does not take into account non-effective bridges, e.g. the formation of rings of nodes (micelles) connected by bridges.

The second criterion is derived from classical bond percolation theory. For a 3-dimensional cubic lattice, Monte Carlo simulations have shown that the fraction of bonds formed should equal 0.25 to reach the bond percolation threshold [33]. As the functionality of the nodes in a 3D cubic lattice is 6 by definition, on average 1.5 bonds/node are required for percolation. In our model we can use this same value for n_b^{net} . This percolation approach does not take into account the functionality of the nodes, rather assumes a fixed value (6 for a 3D cubic lattice), but does account for the formation of non-effective bonds.

The two different criteria are compared in Fig.4.9. We see, as expected from the

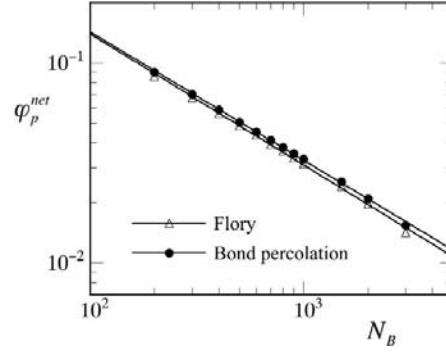


Figure 4.9: Comparison between transient network threshold φ_p^{net} , as predicted by the Flory-criterion and the bond percolation criterion by Stauffer et al. [33] as a function of central block length N_B , for $A_{20}-B_N-A_{20}$ polymers.

definitions of the two criteria, that the predicted transient network thresholds are very close, with the bond percolation criterion giving a slightly higher predicted threshold concentration.

As for the other properties discussed in previous sections, we can investigate how the network threshold changes with variations in the molecular architecture. For the proportionality of φ_p^{net} with the backbone length N_B , we can take a closer look at Fig.4.9. The solid lines are power-law fits to the results from the self-consistent field calculations. We empirically find that $\varphi_p^{net} \propto N_B^{-2/3}$. Using this relation to rescale the volume fraction-axis of Fig.4.8a, as is done in Fig.4.8b, we see superposition of all curves of the fraction of bridging chains versus concentration. This indicates again that the quantity $N_B^{-2/3}$, for a given N_A , determines the bridge formation throughout the concentration range.

Qualitatively we can understand that the transient network is formed at lower concentrations when the middle block is longer. First of all, the minimal distance required between micelles to allow bridge formation, is larger for larger middle blocks, as the chains can reach over longer distances compared to smaller values of N_B . Secondly, we know from [25] and Fig.4.5b that the aggregation number is a decreasing function of N_B . If we distribute the same amount of polymer material over many micelles, with a smaller aggregation number, the typical distance between the micelles will be smaller than when we have few micelles with a large aggregation number. Both effects will contribute to the observed scaling of φ_p^{net} with N_B . At this time however, we do not have a more quantitative explanation for this dependency.

The proportionality of the concentration where a network is formed with the end-block length N_A is more complicated. From our calculations we find that $\varphi_p^{net} \propto N_A^k$, where the scaling exponent k itself is a function of N_B . For the current choice of parameters $k \propto N_B^{0.7}$. The increase in φ_p^{net} with increasing N_A is again attributed to effect that a change in associative block length has on the aggregation number, as we know that $n_{agg} \propto N_A^{4/5}$. How this translates into the intricate relation that is found, is not clear at present.

In classical transient network theories, such as the generalized Green-Tobolsky theory of Tanaka and Edwards [34], rheological parameters such as the zero-shear viscosity and plateau modulus are related directly to the number of elastically active chains per unit volume. In these theories a linear relation is expected between the overall polymer concentration and the plateau modulus. Experimental results however, predict a much stronger increase. According to Annable *et al.* this must be attributed to the fact that not only the number of micelles increases with concentration, but that also the fraction of chains per micelle that forms a bridge (i.e. α) is a strong function of concentration [35]. This is exactly what we see in Fig.4.8.

4.6 Discussion

With the predictions for the critical micelle concentrations [18], the coexistence curves, and the transient network thresholds, we can construct phase diagrams for our telechelic associative polymers. In Fig.4.10 we show two examples of phase diagrams, for two values of the end-block length N_A .

In comparing the phase diagrams for $N_A = 20$ and $N_A = 16$, the depression of the upper limit of the critical value of N_B (Eqn.4.17) and the shift in the micellization threshold are clearly distinguishable. The volume fractions, corresponding to either the *CMC* (line 1) or the dilute branch of the binodal (line 2), decrease exponentially with a change in the end-block length N_A (Eqns 4.16 and 4.17), explaining the large effect for a relatively small change in N_A . For the network formation threshold (line 3), that is proportional to a power-law of N_A , the change is hardly visible.

From Fig.4.10 and the discussion of the various scaling arguments above, it is clear that there are large differences in how volume fractions, at which the various transitions occur, depend on the molecular architecture. As a result it is not possible to superimpose these phase diagrams by rescaling the volume fraction axis with respect to the volume fraction at the critical point, which is a technique commonly employed when studying phase diagrams.

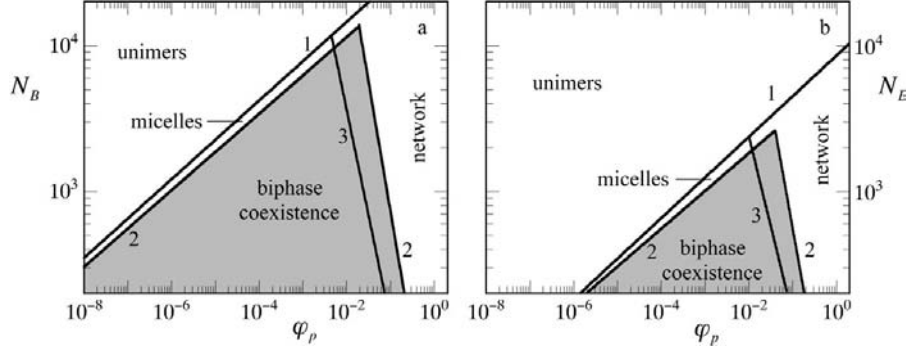


Figure 4.10: Phase diagram for $A_{20}-B_N-A_{20}$ (a) and for $A_{16}-B_N-A_{16}$ polymers (b). Indicated transitions are; 1) micellization threshold, 2) the binodal for biphase coexistence and 3) the transient network threshold. Note that the intersect of the two binodal branches is not the actual critical point, it is an upper limit for the actual critical point.

There is a regime, above the intersection of the micellization threshold with the transient network threshold, where any micelle formation of the associative polymers immediately leads to the formation of a network. This is the case when the middle B block is very long and as a result n_{agg} will typically be very low and the CMC relatively high. As the corona chains can span large distances, any self-assembly will then be accompanied by formation of bridges, leading to a dilute network with nodes, i.e. micelles, of low functionality.

As discussed above, we cannot obtain the true critical point in our approach, due to the approximations that were needed to determine coexistence. Of course the binodal should be continuous at the critical point; the true binodal will have a different shape around the critical point compared to what is shown in Fig.4.10. We can roughly estimate where our approach is no longer valid. Phase separation no longer occurs when the depth of the attractive minimum in $\Delta F^m(h)$ becomes smaller than the thermal energy $k_B T$. In other words, conditions where the depth of the attraction is of order $k_B T$ must be close to the critical point. Due to technical issues, it is difficult, in this SF-SCF model, to calculate points close to the critical point. For all points that we have calculated, as shown in Fig.4.7, we find that the attraction is at least several $k_B T$. This indicates that for all these results our approach is valid.

In-depth comparison of our results with existing experimental data, such as in [12, 16], is difficult as the experimentally studied range and number of block lengths is too limited to verify the scaling behavior that we predict here. This

calls for a systematic experimental investigation of the properties discussed in this Chapter, over a larger range of both end- and middle block lengths. On a more qualitative level, we find that the experimental studies [12, 16] show the tendency for phase separation to increase when the hydrophobic blocks become longer and/or the hydrophilic blocks smaller. This agrees with our model, e.g. see Eqn.4.17 and Fig.4.10.

4.7 Conclusions

Using a self-consistent field cell model, and explicitly accounting for the self-assembled character of the interacting objects, we have mapped out the self-assembly and phase behavior of telechelic associative polymers with their soluble blocks at θ -conditions. Based on the calculations of intermicellar interactions, co-existence curves were predicted. From the numerical results, the concentration where a transient network is formed, was also predicted. Together with the results for the micellization threshold, phase diagrams were constructed.

Nearly all trends found from the numerical results could be rationalized using relatively simple scaling arguments. With these scaling arguments, a quantitative understanding of how the phase behavior depends on the molecular architecture of the telechelic associative polymers is easily accessible.

References

- [1] Kaczmariski, J. P.; Glass, J. E. *Macromolecules* **1993**, *26*, 5149.
- [2] Grassl, B.; Billon, L.; Borisov, O.; Francois, J. *Polym. Int.* **2006**, *55*, 1169.
- [3] Kimerling, A. S.; Rochefort, W. E.; Bhatia, S. R. *Ind. Eng. Chem. Res.* **2006**, *45*, 6885.
- [4] Cathebras, N.; Collet, A.; Viguiet, M.; Berret, J. *Macromolecules* **1998**, *31*, 1305.
- [5] Duhamel, J.; Yekta, A.; Hu, Y. Z.; Winnik, M. A. *Macromolecules* **1992**, *25*, 7024.
- [6] Ortona, O.; D'Errico, G.; Paduano, L.; Vitagliano, V. *J. Colloid Interface Sci.* **2006**, *63*, 301.
- [7] Huang, X. D.; Goh, S. H.; Lee, S. Y. *Macromol. Chem. Phys.* **2000**, *201*, 2660.
- [8] Milner, S. T.; Witten, T. A. *Macromolecules* **1992**, *25*, 5495.
- [9] Cao, D.; Wu, J. *Langmuir* **2006**, *22*, 2712.
- [10] Courvoisier, A.; Isel, F.; Francois, J.; Maaloum, M. *Langmuir* **1998**, *14*, 3727.

- [11] Kim, S.; Lau, W.; Kumacheva, E. *Macromolecules* **2000**, *33*, 4561.
- [12] Pham, Q. T.; Russel, W. B.; Thibeault, J. C.; Lau, W. *Macromolecules* **1999**, *32*, 2996.
- [13] Meng, X. X.; Russel, W. B. *J. Rheol.* **2006**, *50*, 169.
- [14] Bhatia, S. R.; Russel, W. B. *Macromolecules* **2000**, *33*, 5713.
- [15] Semenov, A. N.; Joanny, J. F.; Kokhlov, A. R. *Macromolecules* **1995**, *28*, 1066.
- [16] Francois, J.; Beaudoin, E.; Borisov, O. *Langmuir* **2003**, *19*, 1011.
- [17] Semenov, A. N.; Rubinstein, M. *Macromolecules* **1998**, *31*, 1373.
- [18] Sprakel, J.; Besseling, N. A. M.; Leermakers, F. A. M.; Cohen Stuart, M. A. *J. Phys. Chem. B* **2007**, *111*, 2903.
- [19] Scheutjens, J. M. H. M.; Fleer, G. J. *J. Phys. Chem.* **1979**, *83*, 1619.
- [20] Scheutjens, J. M. H. M.; Fleer, G. J. *J. Phys. Chem.* **1980**, *84*, 178.
- [21] Leermakers, F. A. M.; Sprakel, J.; Besseling, N. A. M.; Barneveld, P. A. *Phys. Chem. Chem. Phys.* **2007**, *9*, 167.
- [22] Flory, P. J. *Principles of polymer chemistry*; Cornell University Press (Ithaca), 1953.
- [23] Evers, O. A.; Scheutjens, J. M. H. M.; Fleer, G. J. *Macromolecules* **1990**, *23*, 5221.
- [24] Leermakers, F. A. M.; Lyklema, J. *Colloids Surf.* **1992**, *67*, 239.
- [25] Sprakel, J.; van der Gucht, J.; Cohen Stuart, M. A.; Besseling, N. A. M. *Phys. Rev. Letters* **2007**, *99*, 208301.
- [26] Zaslavsky, B. Y.; Bagirov, T. O.; Borovskaya, A. A.; Gulaeva, N. D.; Miheeva, L. H.; Mahmudov, A. U.; Rodnikova, M. N. *Polymer* **1989**, *30*, 2104.
- [27] Hill, T. L. *Thermodynamics of Small Systems, Parts 1 and 2*; Dover Pub. Inc. (New York), 1994.
- [28] Hall, D. G.; Pethica, B. A. In *Nonionic Surfactants*; Marcel Dekker Inc.: New York, 1967; chapter 16.
- [29] Francois, J.; Maitre, S.; Rawiso, M.; Sarazin, D.; Beinert, G.; Isel, F. *Colloids Surf. A* **1996**, *112*, 251.
- [30] Daoud, M.; Cotton, J. *J. Physique* **1982**, *43*, 531.
- [31] ten Brinke, G.; Hadziioannou, G. *Macromolecules* **1987**, *20*, 486.
- [32] Tanford, C. *The hydrophobic effect: formation of micelles and biological membranes*; Wiley (New York), 1980.
- [33] Stauffer, D.; Zabolitzky, J. G. *J. Phys. A: Math. Gen.* **1986**, *19*, 3705.
- [34] Tanaka, F.; Edwards, S. F. *Macromolecules* **1992**, *25*, 1516.
- [35] Annable, T.; Buscall, R.; Ettelaie, R.; Whittlestone, D. *J. Rheol.* **1993**, *37*, 695.

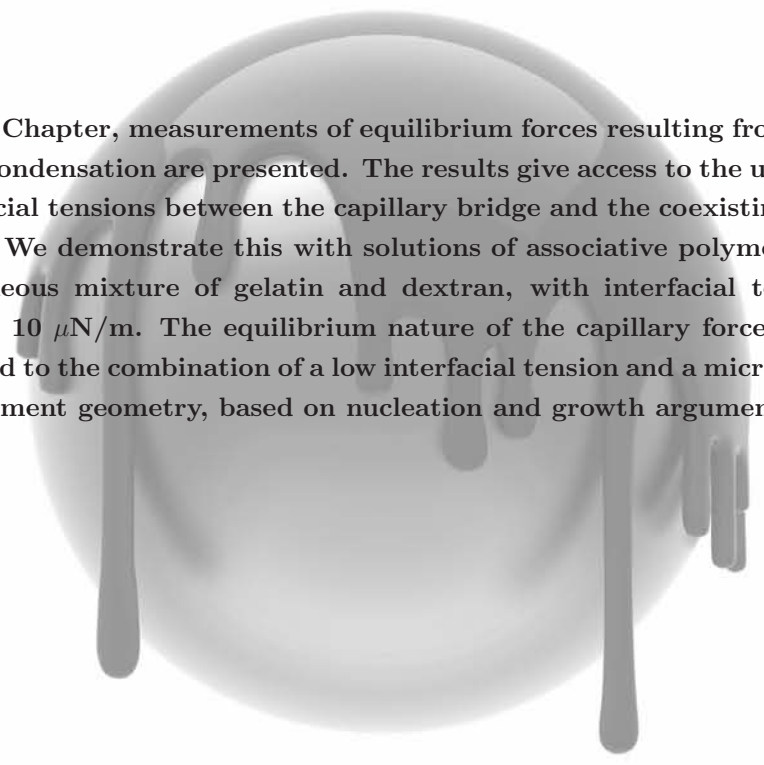
Part II

Associative Polymers at Surfaces



Chapter 5

Equilibrium capillary forces with Colloid Probe AFM



In this Chapter, measurements of equilibrium forces resulting from capillary condensation are presented. The results give access to the ultralow interfacial tensions between the capillary bridge and the coexisting bulk phase. We demonstrate this with solutions of associative polymers and an aqueous mixture of gelatin and dextran, with interfacial tensions around $10 \mu\text{N/m}$. The equilibrium nature of the capillary forces is attributed to the combination of a low interfacial tension and a microscopic confinement geometry, based on nucleation and growth arguments.

This chapter was published as:

J. Sprakel, N.A.M. Besseling, F.A.M. Leermakers and M.A. Cohen Stuart: *Equilibrium capillary forces with atomic force microscopy*, Phys. Rev. Letters 99 (2007), 104504.

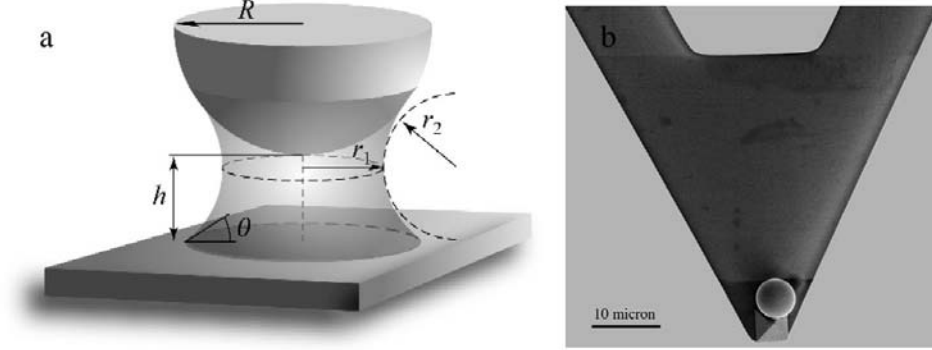


Figure 5.1: a) Artist impression of a capillary bridge between a spherical probe with radius R and a flat substrate, where r_1 and r_2 are the principal radii of curvature at the minimal thickness of the bridge, θ is the contact angle at the three-phase boundary and h is the separation between the two surfaces. b) SEM image of a colloidal probe particle ($R = 3 \mu\text{m}$) glued to a standard contact mode AFM cantilever.

5.1 Introduction

Interfaces are ubiquitous in soft matter and biological systems. The corresponding phase equilibria are often characterized by weak, tunable interactions and large length scales ξ . As a result, the interfacial tensions, $\gamma \propto k_B T / \xi^2$, are typically ultralow (i.e. $\ll 1 \text{ mN m}^{-1}$).

Measurement of ultralow interfacial tensions is notoriously difficult. Many available techniques, such as drop shape [1] or interfacial profile analysis [2], rely on optical visualization. However, in weakly segregated and near-critical systems, the optical contrast between the phases is generally small. Moreover, density differences are also small, because of which it is difficult to obtain accurate information from drop shape analysis under normal gravity. To induce larger deformations, the spinning drop method is commonly used [3]. However, it was recently reported that the centrifugal field that is applied in this method, significantly affects the compositions of coexisting liquid phases. Demixed systems can even be brought into the one-phase regime [4].

The method that is presented in this Chapter does not rely on optical contrast, density differences or strong external fields. We use Colloidal Probe Atomic Force Microscopy (CP-AFM), introduced independently by Ducker et al. [5] and Butt [6], to measure equilibrium forces originating from capillary, liquid bridges between two surfaces. We analyze the resulting force-separation profiles to extract ultralow

interfacial tensions. In Fig.5.1a we show a schematic representation of a capillary liquid bridge between a sphere and a flat substrate, the characteristic configuration in the CP-AFM experiment.

When a homogeneous phase, in which one of the components is near its saturation point, is confined between two surfaces, a new phase can be formed by either condensation or evaporation. It is well known that, e.g., water condenses between hydrophilic surfaces in humid air [7]. Between hydrophobic surfaces at close separation, immersed in pure water, a capillary bridge of water vapor is formed, a process known as capillary evaporation or cavitation [8]. Capillary condensation is also reported for systems that show liquid-liquid coexistence, e.g., demixed ternary polymer-solvent systems [9]. Because the curvature of the capillary bridge is negative with respect to the inner phase, a negative pressure difference is present across the interface, leading to an attractive force between the surfaces. In almost all experimental studies on capillary forces, non-equilibrium behavior is observed, i.e. there is hysteresis in the measured forces in a cycle of decreasing (approach) and increasing (retract) the separation between the surfaces.

5.2 Materials & Methods

In this Chapter we consider aqueous solutions of telechelic associative polymers (hydrophilic polymers end-modified with hydrophobic tails); we use poly(ethylene oxide) (PEO) of various sizes that has been modified at both ends of the chain with C_{12} , C_{14} , C_{16} or C_{18} alkyl tails. In bulk, these systems weakly segregate into a dilute micellar phase (typically ~ 0.1 wt% polymer) and a phase relatively rich in polymer consisting of interacting micelles that are connected through bridges (typically ~ 3 wt%) [10], of which the latter wets the hydrophobic surfaces used in this study. The demixing is the result of an entropic attraction between the flowerlike micelles, due to bridge formation. Upon decreasing the distance between two hydrophobic surfaces immersed in a dilute, and homogeneous, solution of these polymers, we expect the formation of a condensed, polymer-rich capillary bridge.

For the CP-AFM measurements a silica sphere ($R = 3.0 \mu\text{m}$) is glued to the tip of a triangular AFM cantilever (see Fig.5.1b). The spherical probe, attached to the cantilever, and an oxidized silicon wafer (i.e. the flat substrate) are hydrophobized in the vapor of hexamethyl disilazane [11]. In a liquid cell, filled with aqueous solutions of the telechelic polymers, the distance between the hydrophobic probe particle and hydrophobic substrate (h) is varied. The deflection of the cantilever Δx at a given h can be converted into an interaction force F using Hooke's law

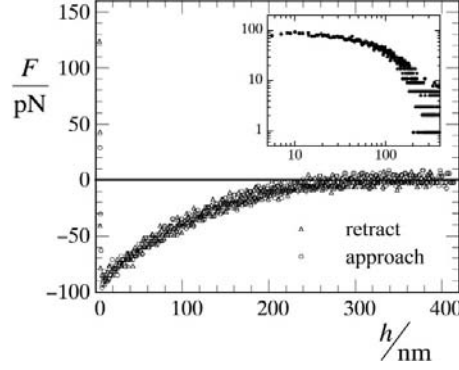


Figure 5.2: Interaction force, in picoNewtons, between hydrophobic surfaces immersed in a 50 mg L^{-1} solution of C_{18} end-modified PEO of 33 kg mol^{-1} (750 EO-units, $M_W/M_N = 1.1$). Inset: absolute values of the force-distance curve plotted on a double logarithmic scale.

$F = k \cdot \Delta x$, where k is the spring constant of the cantilever. We use cantilevers with a spring constant between 0.07 and 0.12 N m^{-1} as determined using the thermal fluctuations method of Hutter and Bechhoefer [12].

5.3 Results & Discussion

A typical force-distance curve is given in Fig.5.2. It shows a long ranged and weak attractive force, coming in at approximately 200 nm , and increasing in strength with decreasing h . The force curves we observe, share two remarkable features: i) approach and retract curves coincide (no hysteresis), and ii) there is no dependence on the approach and retract velocity (in the range of $100 - 1000 \text{ nm s}^{-1}$).

Various possible origins of this attraction can be considered, but most of them must be rejected. Depletion interactions are not a viable explanation, as we observe adsorption of the polymers onto these surfaces in optical reflectometry experiments and because the range of the attraction is many times larger than what is expected for depletion interactions [13]. For polymeric, i.e. molecular, bridging one would expect the range of the interactions to depend on the chain length of the polymer, which is not found in our experiments at all. We find the same range of attraction ($\approx 200 \text{ nm}$) for a C_{12} end-capped PEO of 5 kg mol^{-1} (110 EO-units) with a contour length of only 40 nm . For van der Waals interactions, the attractive force between a sphere and a flat surface should decay with h^{-2} [14]. The inset in Fig.5.2 shows a force curve plotted on a double logarithmic scale, showing that we do not find

the power-law behavior as expected for van der Waals interactions. We note that van der Waals forces are almost never found in AFM force measurements between silica surfaces in water, e.g. [15]. In the absence of polymers, the expected strong and long-ranged hydrophobic attraction [8] between the surfaces is observed (not shown). In the presence of associative polymer however, cavitation cannot occur because of the wetting layer that effectively changes the polarity of the surfaces. We therefore attribute the observed attractive forces to the action of a liquid bridge formed from a 'dense' polymer phase.

The hysteresis-free nature of the force-distance measurements allows us to use equilibrium thermodynamics to analyze the results. The total capillary force can be divided into two components. The first contribution originates from the pressure difference across the interface, given by the Laplace equation; $\Delta P = \gamma(r_1^{-1} + r_2^{-1})$, where γ is the interfacial tension and r_1 and r_2 are the principle radii of curvature of the interface between the capillary bridge and the reservoir. The second contribution is due to the component of the interfacial tension normal to the substrate. To predict the capillary force as a function of distance for the sphere-plate geometry, one must find the optimal radii of curvature for given h . The solution should obey the constraint that the mean curvature $J = (r_1^{-1} + r_2^{-1})$ is constant for all positions along the hyperboloid shape, as the Laplace pressure must be homogeneous within the capillary bridge. A well-known approximate solution to this problem is $F \approx 4\pi R\gamma \cos \theta$ (see e.g. [14]), where R is the radius of the spherical particle and θ is the contact angle at the three-phase boundary. The accuracy of this expression is however limited due to the many approximations in the derivation.

Instead, we prefer to use the more accurate solution of Willett and co-workers [16], who developed a solution to the Laplace equation for the sphere-plate geometry in the toroidal approximation, i.e. assuming that the shape of the capillary bridge matches the void in the centre of a torus. The critical assumption in their work is that the volume of the liquid bridge V_b remains constant at all h , which could become less accurate when the systems are very close to their critical point. We numerically fit Willett's model to our experimental data, by inserting the known values for h and F and assuming a small contact angle ($\theta < 10^\circ$), to find both V_b and the interfacial tension between the phase relatively rich in polymer and the dilute micellar phase. In Fig.5.3a we compare the experimental results with the best fit to the theoretical model for two different telechelic polymers. The agreement between model and experiment is good. The slight, yet systematic, deviations that are observed between the prediction by Willett *et al.* and our experimental data can be attributed to the non-exact nature of this theoretical description of

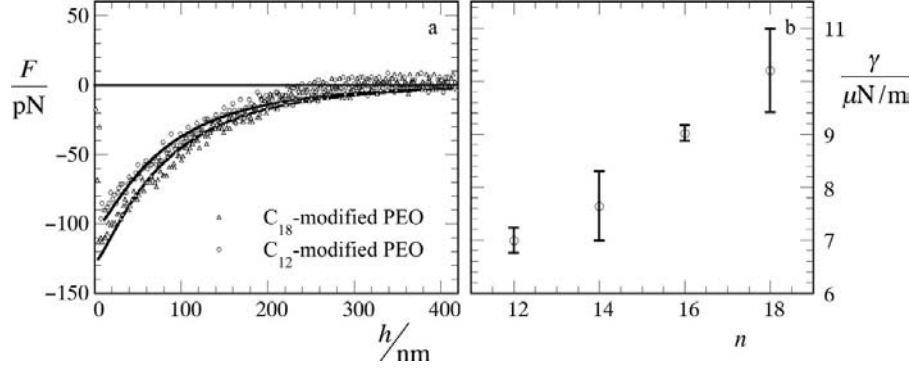


Figure 5.3: a) Experimental force curves between hydrophobic surfaces in 50 mg L^{-1} aqueous solutions of C_{12} - and C_{18} -modified PEO of 33 kg mol^{-1} (750 EO-units) (symbols), and curve fits to the model by Willett et al. [16] (drawn lines). b) Interfacial tensions versus the number of carbon atoms n in the hydrophobic alkyl tails at both ends of the PEO chain, for PEO of 33 kg mol^{-1} (750 EO-units). Each point, with indicated error, is the average of at least 5 measurements.

equilibrium capillary forces, as implied by the approximations that were discussed above.

The interfacial tensions obtained for the associative polymer systems are plotted in Fig.5.3b as a function of the number of carbon atoms n in the alkyl tails at both ends of the PEO chains. From the indicated error we can conclude that the accuracy of the present method is excellent.

Experimental results on the bulk phase behavior of these polymers indicate that decreasing the size of the hydrophobic tails, at a given PEO length and concentration, moves the weakly segregated system towards the critical point [10]. In Fig.5.3b we see that γ decreases with decreasing n as expected. However, we must note that the experimentally accessible n -range is too small to investigate the expected scaling behavior of the interfacial tension.

Often, capillary condensation phenomena are accompanied by hysteresis. It is therefore remarkable that we find no hysteresis in the force-distance curves, as shown in Fig.5.2. This may be explained as follows: the formation of a capillary bridge consists of two steps; nucleation and growth. For heterogeneous nucleation, the energy barrier (ΔG^*) associated with the formation of a nucleus of critical dimensions, is proportional to γ [17]. The rate of nucleation is proportional to $\exp(-\Delta G^*/k_B T) \propto \exp(-\gamma A^*/k_B T)$, where A^* is the surface area of the critical nucleus. For systems with ultralow interfacial tensions, nucleation is very fast, as

the nucleation rate increases exponentially with decreasing interfacial tension. This explains why capillary condensation of water, or cavitation of water vapor, does give rise to pronounced hysteresis [7, 8], as the interfacial tension (between water and vapor) is a factor of 10^4 higher than that of the system considered here.

The rate of growth of the condensate is determined by the diffusion of polymer chains towards the capillary bridge. We can define a characteristic diffusion time (τ_D) as $\tau_D \approx L^2/D$, where D is the diffusion coefficient and L the mean diffusive path. From the Stokes-Einstein relation we estimate that the diffusion constant of a poly(ethylene oxide) chain of 750 EO-units, which is the largest polymer considered in this Chapter, is $4 \cdot 10^{-11} \text{ m}^2 \text{ s}^{-1}$ in water at room temperature. The value of L depends strongly on the geometry of the experimental set-up. From fitting the experimental data we have, in addition to the interfacial tension, also obtained the volume of the capillary bridge, which was consistently found to be in the order of $0.1 \text{ } \mu\text{m}^3$. Hence, the diameter of the capillary bridge is of the order of $0.1 \text{ } \mu\text{m}$ at the onset of the capillary attraction ($h = 200 \text{ nm}$). If we take 10 times this value as a rough estimate of the mean diffusive path (i.e. $L = 1 \text{ } \mu\text{m}$), we find that $\tau_D = 25 \text{ ms}$, whereas the experimental timescale is of the order of seconds. This may explain why transport towards the condensed phase is also not rate limiting, in this specific geometry.

Experiments in the Surface Force Apparatus (SFA) on other demixed polymeric systems show pronounced non-equilibrium behavior, even when experimental timescales are many times larger than in our experiments [9]. In these experiments the interfacial tensions are of the same order of magnitude, hence the nucleation rate is expected to be similar to our case. However, the geometry in the SFA, i.e. crossed cylinders with a curvature of the order of millimeters, gives a much larger characteristic timescale of diffusion. If the size of the capillary bridge is also of the order of millimeters in the SFA set-up, τ_D increases from milliseconds in the CP-AFM experiment to several hours in the SFA geometry.

Clearly it is the specific combination of a microscopic geometry and a weakly segregated system that leads to the observation of equilibrium capillary forces. This implies that we should find equilibrium forces for many systems with ultralow interfacial tensions. As a further test we have therefore carried out measurements on a biphasic system of which the interfacial tension is reported in literature. We use a demixed mixture of fish gelatin and dextran in water, for which the interfacial tension has been reported to be $9 \pm 3 \text{ } \mu\text{N m}^{-1}$ [18]. After formation of two macroscopic phases, one enriched in gelatin, the other in dextran, we fill the liquid cell of the AFM set-up with the dextran-rich phase and repeat the experiment as described above with hydrophilic silica surfaces. It is known that the gelatin-

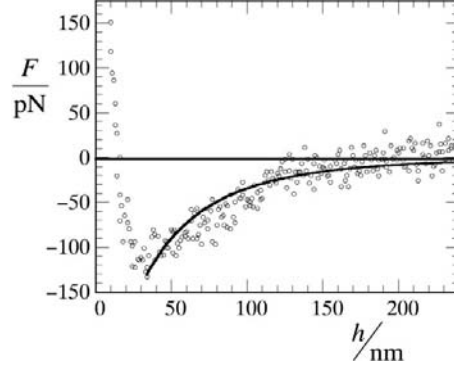


Figure 5.4: Experimental force curve between hydrophilic surfaces in the dextran-rich phase of the demixed aqueous mixture of fish gelatin and dextran (overall polymer concentration of 9 wt%) (symbols), and curve fits to Willett's model (drawn line).

enriched phase preferentially wets the silica surface (with $\theta = 0$) [19], we therefore expect condensation of a gelatin-rich phase between the silica sphere and substrate. The resulting force curve is shown in Fig.5.4; the result is very similar to what is observed for the associative polymers. After fitting the data in the same manner as above, we find an interfacial tension of $15 \pm 3 \mu\text{N m}^{-1}$, which is in agreement with the value reported in literature.

For the gelatin-dextran system we observe a repulsion coming in at approximately 25 nm, for the associative polymers this did not show until $h = 5$ nm (Fig.5.3a). We must realize that the primary requirement for capillary condensation to occur, is the presence of a wetting layer. For polymeric systems this entails adsorption of the polymer, forming various structures at the solid surface. At small h compression of these surface layers will result in a repulsion, that precedes the hard-wall repulsion at $h = 0$. For every experimental systems the details of this phenomenon are different, as well as the timescales on which these effects are reversible. The short-ranged repulsion, found for both experimental systems, is thus fundamentally linked to the capillary condensation that causes the long-ranged attraction.

Finally, we have attempted to visualize the capillary bridges, for the associative polymer system, using confocal microscopy. The same methylated silica particles used as colloidal probe in the CP-AFM experiments were placed on a glass cover slip, and subsequently immersed in a 50 mg/L solution of a C_{18} modified telechelic polymer, dyed by solubilizing Nile Red in the hydrophobic cores of the flowerlike micelles. In Fig.5.5 we show an image, in which a capillary bridge (with an increased

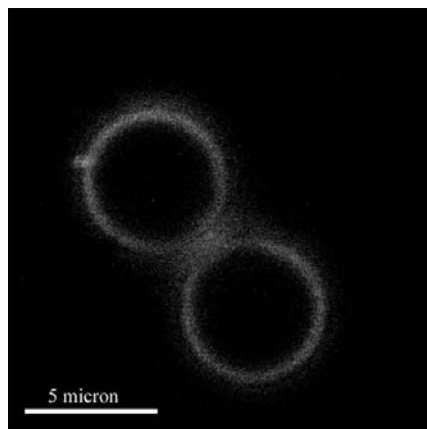


Figure 5.5: Fluorescence micrograph of two methylated silica particles immersed in a 50 mg/L solution of a C_{18} -modified PEO, in which the micellar cores are dyed with Nile Red.

density of polymer thus increased fluorescence intensity) seems to appear between two neighboring particles. We can roughly identify the characteristic pendular shape as sketched in Fig.5.1. Note the clearly observable adsorbed/wetting layer around the entire circumference of the particles.

5.4 Conclusions

We have measured equilibrium capillary forces between a microscopic spherical probe and a flat substrate. This was possible due to a combination of a very small interfacial tension between condensate and the bulk phase and a sufficiently small geometry. By analysis of the resulting force-separation profiles we have directly obtained the ultralow interfacial tensions between the weakly segregated phases. In the next Chapter we will derive a simple thermodynamic argument for the capillary adhesion force and compare this to calculations using the self-consistent field theory of Scheutjens and Fleer.

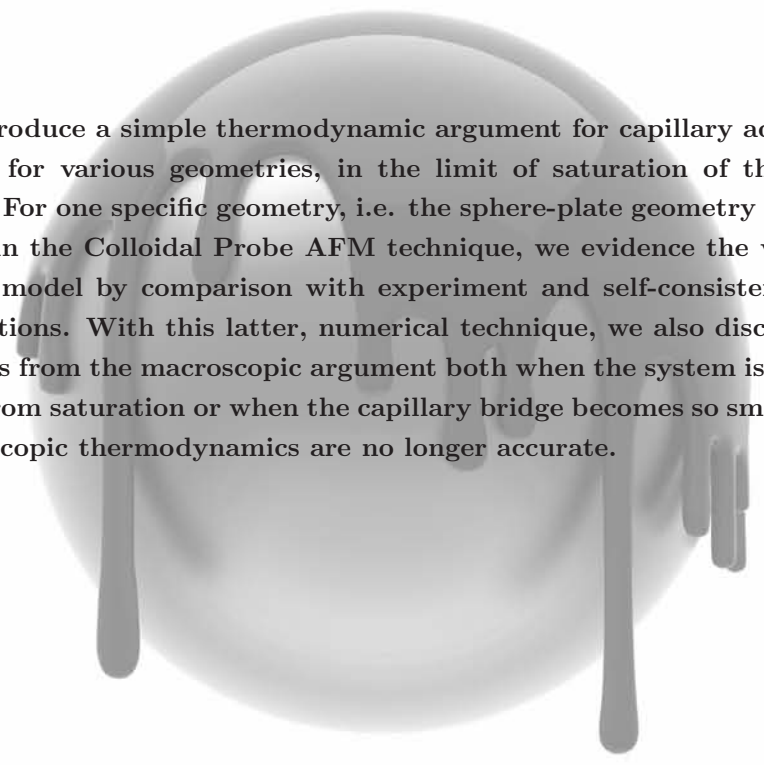
References

- [1] Butler, J. N.; Bloom, B. H. *Surf. Sci.* **1966**, 4, 1.
- [2] Aarts, D. G. A. L. *J. Phys. Chem. B* **2005**, 109, 7407.
- [3] J. L. Cayias, R. S. Schechter, W. H. W. *Adv. Chem. Ser.* **1975**, 8, 234.

- [4] Scholten, E.; Sagis, L. M. C.; van der Linden, E. *Biomacromolecules* **2006**, *7*, 2224.
- [5] Ducker, W. A.; Senden, T. J.; Pashley, R. M. *Nature* **1991**, *353*, 239.
- [6] Butt, H. J.; Farshchi-Tabrizi, M.; Kappl, M. *J. Appl. Phys.* **2006**, *100*, 024312.
- [7] Christenson, H. K. *J. Phys. Chem.* **1993**, *97*, 12034.
- [8] Bremond, N.; Arora, M.; Ohl, C. D.; Lohse, D. *Phys. Rev. Letters* **2006**, *96*, 224501.
- [9] Wennerstroem, H.; Thuresson, K.; Linse, P.; Freyssingeas, E. *Langmuir* **1998**, *14*, 5664.
- [10] Pham, Q. T.; Russel, W. B.; Thibault, J. C.; Lau, W. *Macromolecules* **1999**, *32*, 2996.
- [11] Marinova, K. G.; Christova, D.; Tcholakova, S.; Efremov, E.; Denkov, N. D. *Langmuir* **2005**, *21*, 11729.
- [12] Hutter, J. L.; Bechhoefer, J. *Rev. Sci. Instrum.* **1993**, *64*, 1868.
- [13] Knoben, W.; Besseling, N. A. M.; Cohen Stuart, M. A. *Phys. Rev. Letters* **2006**, *97*, 068301.
- [14] Israelachvili, J. *Intermolecular & Surface Forces*; Academic Press (London), 1985.
- [15] Ducker, W. A.; Senden, T. J.; Pashley, R. M. *Langmuir* **1992**, *8*, 1831.
- [16] Willett, C. D.; Adams, M. J.; Johnson, S. A.; Seville, J. P. K. *Langmuir* **2000**, *16*, 9396.
- [17] Turnbull, D. *J. Chem. Phys.* **1950**, *18*, 198.
- [18] Scholten, E.; Sprakel, J.; Sagis, L. M. C.; van der Linden, E. *Biomacromolecules* **2006**, *7*, 339.
- [19] Tromp, R. H.; Lindhoud, S. *Phys. Rev. E* **2006**, *74*, 031604.

Chapter 6

Capillary adhesion in the limit of saturation



We introduce a simple thermodynamic argument for capillary adhesion forces, for various geometries, in the limit of saturation of the bulk phase. For one specific geometry, i.e. the sphere-plate geometry such as found in the Colloidal Probe AFM technique, we evidence the validity of our model by comparison with experiment and self-consistent field calculations. With this latter, numerical technique, we also discuss deviations from the macroscopic argument both when the system is moved away from saturation or when the capillary bridge becomes so small that macroscopic thermodynamics are no longer accurate.

This chapter was published as:

J. Sprakel, N.A.M. Besseling, M.A. Cohen Stuart and F.A.M. Leermakers: *Capillary adhesion in the limit of saturation: Thermodynamics, self-consistent field modeling and experiment*, *Langmuir* 24 (2008), 1308.

6.1 Introduction

The adhesion between particles mediated by liquid bridges, commonly known as capillary adhesion, is of significant technological and scientific interest. In some cases capillary adhesion is undesired, such as when it causes dry powders to agglomerate when stored in humid environments, or when it causes dispersions to phase separate [1]. In other cases the adhesion forces are specifically employed, e.g., for micro-manipulation [2] or to create larger structures, such as in granulation of pharmaceutical powder formulations before tableting [3] and in creating the appropriate mixture of sand and water for building sand-castles [4]. Capillary adhesion is even debated to be partly responsible for the strong adhesion of some types of geckos with walls, enabling them to walk up-side-down [5]. These are just a few examples of the wide variety of cases where capillary adhesion is important.

Recently, we have shown that it is possible to measure fully equilibrated capillary forces using Colloidal Probe Atomic Force Microscopy (CP-AFM) [6]. The absence of hysteresis in these experiments, which is a rare feature in this type of measurements, could be attributed to the combination of having a system with an ultralow interfacial tension (fast nucleation) and a microscopic geometry (limited diffusion lengths). Because of the equilibrium nature of the capillary condensation that leads to these forces, the results can be used to determine thermodynamic properties such as the interfacial tension between the phase that forms the capillary bridge and the outer bulk phase it coexists with. To do so, one needs to have a relation that describes the capillary force for that specific geometry as a function of, e.g., the interfacial tension and the contact angle. In the CP-AFM method a solid sphere interacts with a planar wall. We will refer to this situation as the sphere-plate geometry. Several options exist for analyzing the capillary forces in the sphere-plate geometry. A well known solution is that derived by Orr et al. [7, 8], who gave a simple expression for the pull-off force, i.e. the adhesion force at contact of the sphere with the flat wall. The result is often stated to be valid only for large spheres and far enough from saturation of the outer bulk phase, or in terms of water-vapor coexistence at not too high relative humidities. Another solution is that of Willett et al. [9], who predicted the full force-separation curve for this geometry, again with some significant approximations. In the previous work [6] we have shown that this latter model agrees well with our experimental data, and when used to extract the interfacial tension from the force-distance curves returns approximately the same interfacial tension as measured independently with another technique.

In this Chapter we will introduce a simple thermodynamic approach to find

the capillary adhesion force at zero separation (i.e. pull-off force), which has its validity close to saturation (high relative humidity). Although this Chapter will focus mainly on the sphere-plate geometry, we will extend the argumentation to the geometry of two spheres. The final results of this approach look similar to what can be found in literature (e.g. [7, 8]) but differ fundamentally in their physical background. Subsequently we will compare the theoretical considerations with a recent experimental result, and show that the experimental data corresponds very well with the thermodynamic model. Finally, we will present numerical results from self-consistent field calculations to evidence our reasoning and to discuss what happens when we move away from saturation and away from the macroscopic limit where the theoretical argumentation is valid.

6.2 Macroscopic model

In this section we will discuss some thermodynamic arguments that can be used to predict capillary adhesion forces, based on macroscopic considerations. Hence the width of the interface is negligible compared to the size of capillary bridge, therefore the position of the interface is unambiguously defined. This also implies that the interfacial tension is a constant and that curvature corrections to the interfacial tension are negligible. Self-consistent field calculations, using a similar technique as we will use in a following part of this Chapter, have revealed that curvature corrections to the interfacial tension are very small, both for binary systems of simple liquids [10] and for ternary polymer/polymer/solvent mixtures [11].

We consider two solid surfaces, one of which is a flat wall and the other a solid sphere with radius R , separated by a distance h (see Fig.6.1). When these surfaces are immersed in a fluid mixture having a miscibility gap, a new phase can be formed between the two surfaces that is thermodynamically stable, even when the liquid mixture is undersaturated. When the bulk phase is not saturated, the condensate cannot be stable in absence of these surfaces. This process of formation of a new and stable phase between two surfaces is called capillary condensation. Capillary condensation only occurs when the condensing phase preferentially wets the surfaces, i.e. a contact angle θ measured through the condensed phase of less than 90° , and when the separation distance between the surfaces h is small enough.

The phenomenon of capillary condensation is in essence captured by the Kelvin equation [12]:

$$\mu - \mu^* = v_m \Delta P \quad (6.1)$$

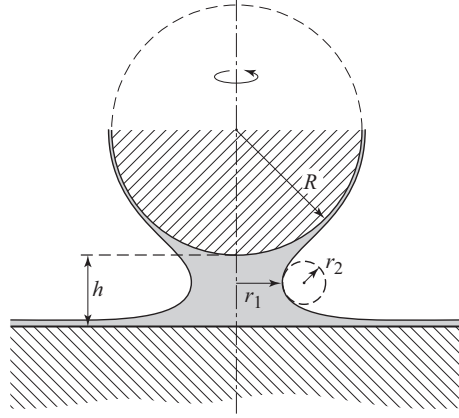


Figure 6.1: Schematic representation of a capillary bridge between a sphere of radius R and a flat wall, indicated are the principal radii of curvature r_1 and r_2 , chosen at the waist of the capillary bridge, and the surface separation h . The entire system is rotationally symmetric around the central axis. The situation shown here is for the case of complete wetting, i.e. the contact angle $\theta = 0$ and an undersaturated bulk phase.

that relates the relative under- or oversaturation of the outer bulk phase, given by the difference in the actual chemical potential μ and the chemical potential at saturation μ^* , to the pressure difference between the bulk phase and the condensate, ΔP . The coefficient v_m is the molecular volume. The difference in pressure between the condensate and the outer bulk phase is given by the Young-Laplace equation [12]:

$$\Delta P = \gamma J = \gamma \left(\frac{1}{r_1} + \frac{1}{r_2} \right) \quad (6.2)$$

where γ is the interfacial tension between the condensate and the bulk phase and $J = (r_1^{-1} + r_2^{-1})$ is the mean curvature, defined by the two principal radii of curvature r_1 and r_2 , as indicated in Fig.6.1. With these two basic thermodynamic equations we can already derive the main premises of capillary condensation. If we have a condensed liquid in a bulk phase below its saturation point we can see from the Kelvin equation that this would require a negative Laplace pressure to meet equilibrium. From the Laplace equation we can deduce that a spherical droplet of the condensed phase, in which r_1 is equal to r_2 by definition, cannot have a negative Laplace pressure. In other words, this situation will not be thermodynamically stable. For a capillary condensate however, which in a sphere-plate geometry has a characteristic hyperboloid shape, the two radii of curvature are not equal. By

definition r_1 is always positive and r_2 is negative, hence when $-1/r_2$ is larger than then $1/r_1$ a net negative curvature results and the condensed phase can be thermodynamically stable. Note that, as the Laplace pressure must be homogeneous within the capillary condensate, the mean curvature J must be constant over the entire surface of the capillary bridge, r_1 and r_2 however may vary from point to point along the interface. In the following we conveniently choose r_1 and r_2 at the waist of the capillary bridge, i.e. the point where the bridge has its smallest diameter, because this is the only position where the interfacial tension acts in the same direction as the total adhesion force between the two surfaces.

In a grand-canonical ensemble, that is when the total system volume V , the temperature T and the chemical potentials μ are fixed, the interaction energy between the two surfaces (G^{int}) in presence of a capillary condensate is given by:

$$G^{int}(h) = \gamma A_c(h) - \Delta P V_c(h) \quad (6.3)$$

where A_c and V_c are the surface area and the volume of the capillary bridge, respectively. The interaction force $F(h)$ between the surfaces is found by differentiating with respect to the separation distance h

$$F(h) = \frac{-\partial G^{int}(h)}{\partial h} = -\gamma L_b(h) + \Delta P A_b(h) \quad (6.4)$$

where L_b is the circumference of the capillary bridge at its waist and A_b is the surface area of the cross-section at this same position. As the capillary bridge is rotationally symmetric, we find $L_b = 2\pi r_1$ and $A_b = \pi r_1^2$. With Eqn.6.2, we can rewrite Eqn.6.4 as

$$F = -2\pi r_1 \gamma + \pi r_1^2 \left(\frac{1}{r_1} + \frac{1}{r_2} \right) \gamma \quad (6.5)$$

For capillary condensation, in full thermodynamic equilibrium, the Laplace pressure is smaller than or equal to zero, hence both terms in the above equation give a zero or negative contribution to the force; in other words capillary condensation necessarily leads to attraction between the two surfaces. Although the result in Eqn.6.5 for the adhesion force seems fairly simple, the difficulty is in predicting the values of r_1 and r_2 for a given situation. For certain specific situations this can be dealt with exactly, as we will show below.

One frequently used solution has been given by Orr et al. [7], who derived the adhesion force between a sphere and a flat wall at contact ($h = 0$) due to the presence of a capillary bridge. Their result $F(0) = -4\pi R\gamma \cos \theta$ is found after some severe approximations [7, 8]. The derivation starts by neglecting the γA term in

the interaction energy (given in Eqn.6.3), leaving only the ΔPV term. The second main step in their derivation is a geometric approximation, i.e. $-r_2 \ll r_1$, to eliminate one of the two radii of curvature from the equations, which only holds for large enough spheres. Finally, the result as stated above is obtained. However, if we consider Kelvin's law (Eqn.6.1), we must realize that this approach is invalid in the limit of saturation, where the chemical potential of the component that wets the surfaces μ becomes equal to the chemical potential of that component at saturation μ^* , as the Laplace pressure should vanish exactly at saturation;

$$\lim_{\mu \rightarrow \mu^*} \Delta P = 0 \quad (6.6)$$

Hence, the assumption that the γA term becomes negligible compared to the Laplace pressure term is fundamentally incorrect when the bulk phase is close to saturation. Of course this is recognized by other researchers in the field (see, e.g., [13]).

Here we will introduce a simple thermodynamic approach to describe the capillary adhesion force at contact in the limit of saturation, which does not contain severe approximations. Starting from Eqn.6.2 and Eqn.6.6 we easily find that in the limit of saturation the mean curvature must be zero, hence

$$\lim_{\mu \rightarrow \mu^*} r_1 = -r_2 \quad (6.7)$$

For the capillary bridge, the condition in Eqn.6.7 can be satisfied due to the hyperboloid shape of the condensate. In this limit the interaction force between the surfaces can be simplified to

$$\lim_{\mu \rightarrow \mu^*} F = -2\pi r_1 \gamma \quad (6.8)$$

as the Laplace pressure term in Eqn.6.5 must vanish at saturation.

Now let us focus on the adhesion force, which is the force that holds the sphere and the wall together when they are at contact, i.e. at $h = 0$. For this condition in the limit of saturation, a schematic representation is given in Fig.6.2.

For the case of complete wetting in the limit of saturation, the minimal width of the neck is found at the meridian of the sphere, as this is the only solution for which r_1 equals $-r_2$ while satisfying the boundary condition $\theta = 0$. This means that in the limit of saturation and for the case of complete wetting $r_1 = -r_2 = R$. For non-zero contact angles, smaller than 90° , $r_1 = -r_2 = R \cos \theta$, which follows from simple geometric arguments, as illustrated in Fig.6.2. Combining this result with Eqn.6.8, we find an exact expression for the capillary adhesion force between a sphere and a plate in the limit of saturation:

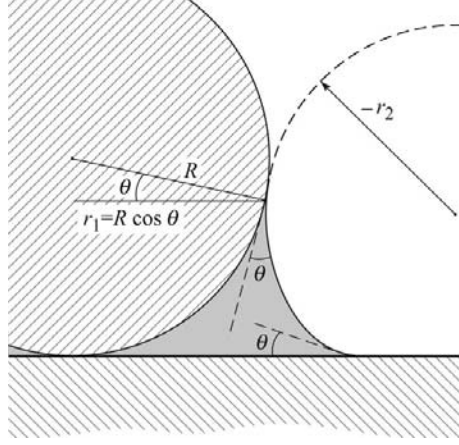


Figure 6.2: Schematic representation of a capillary bridge between a sphere of radius R and a flat wall at contact ($h = 0$) at saturation of the surrounding bulk phase and with a finite contact angle θ . In this specific conditions the Laplace pressure must be zero (Eqn.6.6), hence $r_1 = -r_2$. From geometric arguments we derive that $r_1 = R \cos \theta$.

$$\lim_{\mu \rightarrow \mu^*} F(h = 0) = -2\pi R\gamma \cos \theta \quad \text{sphere-plate} \quad (6.9)$$

Note that our result differs only by a factor of 2 from the well known result of Orr et al., as discussed above, yet the derivation of our result is significantly different and contains no severe approximations.

The result in Eqn.6.9 is analogous to the expression used in the Wilhelmy plate method for measuring interfacial tensions [14]. The underlying physical arguments are different however; in the Wilhelmy-plate equation the hydrostatic pressure in the capillary bridge balances the finite Laplace pressure, whereas here we neglect gravitational effects and have a vanishing Laplace pressure. An assessment of the effect of gravity on these types of capillary bridges is given in [15]. One way of estimating the relative importance of gravity is by means of the dimensionless Bond number, which is the ratio of the body forces (gravity) to the interfacial tension forces:

$$Bo = \frac{\Delta\rho g l^2}{\gamma} \quad (6.10)$$

For our problem $\Delta\rho$ is the difference in density between the phase forming the capillary bridge and the surrounding bulk phase, g the gravitational acceleration and l the characteristic dimension of the capillary bridge. For large Bond numbers

($\gg 1$) the body forces dominate and for small Bond numbers ($\ll 1$) the surface tension forces are most important. In the CP-AFM set-up, where the sphere is typically micrometers large, l will also be of order μm or smaller. For a capillary bridge of water, in coexistence with its vapor, the Bond number is of order 10^{-7} , and for the system discussed in the experimental part of this Chapter, which demixes into two liquid phases with only minor density differences and an ultralow interfacial tension, we find a Bond number of around 10^{-4} . This means that in both cases gravitational effects are completely negligible.

For complete wetting ($\theta = 0$) and at saturation, the wetting layers on the flat surface can grow infinitely large and a macroscopic bulk phase that swallows the particle will be formed instead of the mesoscopic capillary bridge between the two surfaces. For systems with a non-zero contact angle this is not the case, as the adsorption layers will always have finite, microscopic, dimensions even exactly at saturation. This implies that defining capillary forces *at* saturation for the latter type of wetting is useful, but it has no meaning when we are dealing with complete wetting. As a consequence, we formulate our results *in the limit of* saturation such that the analysis is valid both for complete and partial wetting situations.

In the introduction we mentioned the model of Willett and co-workers [9], who gave a numerical solution for the capillary force as a function of the separation distance h in the toroidal approximation, i.e. assuming that the shape of the capillary bridge matches the void in the center of a torus, and by assuming that the volume of the liquid bridge remains constant at all h . If we numerically take the limit to zero separation of the adhesion force predicted with the model of Willett et al., we find a pull-off force that approximately, within 5%, equals $-2\pi\gamma R$, which is in accordance with Eqn.6.9. We must note that Willett's model does not account at all for the relative undersaturation under which the capillary condensation occurs. The fact that the limit of Willett's model to $h = 0$ gives approximately the same result as Eqn.6.9, seems to indicate that it is valid in the limit of saturation, although this does not become apparent from the derivation of their model.

We can extend the model for the adhesion force in the limit of saturation towards the case of two spheres of equal radius R . For this case again Eqns 6.7 and 6.8 must apply. However, the geometry of the capillary bridge is different, see Fig.6.3. With the triangle drawn between the center of one of the solid spheres, the point of contact between the spheres and the center of the circle that describes the outer radius of curvature, we find $r_1 = -r_2 = \frac{2}{3}R$ using Pythagoras' theorem. This is valid for complete wetting, and for the same reasons as above we can extend this to partial wetting by correcting with the cosine of the contact angle. The adhesion force between two spheres of equal size in the limit of saturation is thus given by

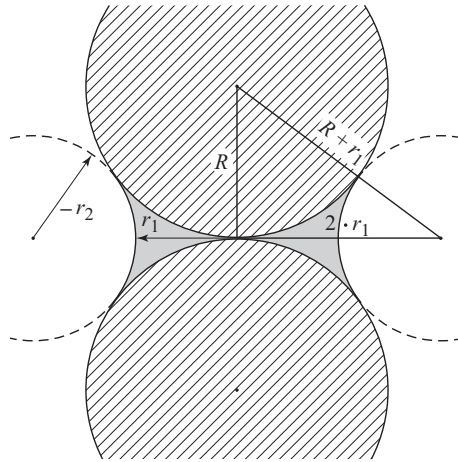


Figure 6.3: Schematic representation of a capillary bridge between two spheres of equal radius R , at contact ($h = 0$) and at saturation of the surrounding bulk phase. At saturation $r_1 = -r_2$, as the Laplace pressure must be zero (Eqn.6.6). Using Pythagoras' theorem we find that $r_1 = \frac{2}{3}R \cos \theta$.

$$\lim_{\mu \rightarrow \mu^*} F(h=0) = -\frac{4}{3}\pi R\gamma \cos \theta \quad \text{equal spheres} \quad (6.11)$$

Also for this geometry an approximate argument is given in [8], based on the same reasoning as explained above, i.e. neglecting the γA term in the interaction energy and with significant geometric approximations. As in the previous case for the sphere-plate geometry, the result again differs from our Eqn.6.11 by a numerical constant; in this case the difference is a factor of $\frac{2}{3}$.

We can also derive a more general geometric argument that is not limited to the two specific cases (sphere-plate and equal spheres) discussed above. For the case of two spheres, with arbitrary radii R_1 and R_2 we can construct a geometry, an example of which is shown in Fig.6.4. The following considerations are only valid for the case of complete wetting, i.e. a zero contact angle. Again we start with the fact that $r_1 = -r_2$ (Eqn.6.7). Below we express all radii of curvature in terms of r_1 .

First we must define the quantity f that represents the fraction of the vertical line, which connects the two centers of the spheres, belonging to the upper triangle. Hence, $(1 - f)$ is the fraction of that same vertical line that belongs to the lower of the two adjacent triangles. The total length of this vertical line is $R_1 + R_2$.

Using Pythagoras' theorem we find the following relations:

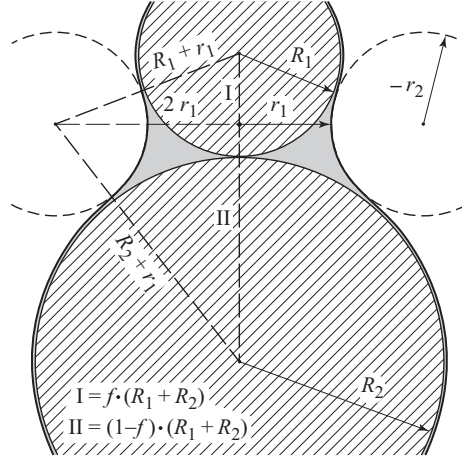


Figure 6.4: Schematic representation of a capillary bridge between two spheres with arbitrary radii R_1 and R_2 respectively, at zero separation ($h = 0$), at saturation of the surrounding bulk phase ($\mu = \mu^*$) and for complete wetting ($\theta = 0$). Eqn.6.7 dictates that $r_1 = -r_2$, as the Laplace pressure must be zero at saturation (Eqn.6.6). The quantity f is the fraction of the vertical line between the centers of the spheres that is part of the upper triangle, hence $(1-f)$ is the fraction of the line that is part of the lower adjacent triangle.

$$f^2(R_1 + R_2)^2 + (2r_1)^2 = (R_1 + r_1)^2 \quad (6.12)$$

for the upper triangle, that is linked to the sphere with radius R_1 , and

$$(1-f)^2(R_1 + R_2)^2 + (2r_1)^2 = (R_2 + r_1)^2 \quad (6.13)$$

for the lower triangle, linked to the sphere with radius R_2 . Combining these two equations leads to the following expression for f :

$$f = \frac{1}{2} \left(\frac{(R_1 + r_1)^2 - (R_2 + r_1)^2}{(R_1 + R_2)^2} + 1 \right) \quad (6.14)$$

For the two specific geometries that we have discussed above, we can find numerical values for f . For the case of two spheres of equal radius $f = \frac{1}{2}$. This value reflects the symmetry of the system with respect to the plane of contact between the two spheres. For the sphere-plate geometry, in which $R_2 \rightarrow \infty$, we find that $f = 0$. This latter case of course is the strongest case of asymmetry as one of the surfaces has lost its curvature. To use these considerations in predicting the capillary adhesion force, based on Eqn.6.8, we need to express r_1 as a function of f , R_1 and R_2 . We

can do so, e.g., by solving Eqn.6.12. This gives a quadratic equation in terms of r_1 , which logically leads to two possible solutions. With the boundary condition $r_1 > 0$, we find the proper solution:

$$r_1 = \frac{1}{3}R_1 + \frac{1}{3}\sqrt{4R_1^2 - 3f^2(R_1 + R_2)^2} \quad (6.15)$$

For the geometry of two equal spheres ($R_1 = R_2 = R$), for which $f = \frac{1}{2}$, we can show that Eqn.6.15 returns $r_1 = \frac{2}{3}R$, which is the same result that we have derived above, leading to Eqn.6.11. For the sphere-plate geometry ($R_1 = R$, $R_2 \rightarrow \infty$ and $f = 0$) Eqn.6.15 returns $r_1 = R$, which is again exactly the same as the result leading to Eqn.6.9.

6.3 Measurements with CP-AFM

In the previous Chapter we have shown that it is possible to measure fully equilibrated forces using the Colloidal Probe AFM technique developed by Ducker et al. [16], in systems with ultralow interfacial tensions. Here we show one example of such an experiment, in a system for which an independent experimental result for the interfacial tension is available.

Silica spheres with a radius of $3\ \mu\text{m}$ (gift from Philips Laboratories, the Netherlands) are attached to large narrow-legged AFM contact-mode cantilevers, using the method of Giesbers [17], and oxidized silicon wafers (WaferNet, Germany) are used as the flat substrate. The attached probes and substrates are washed with water and ethanol and cleaned in a plasma-cleaner (Harrick PDC-32G). The spring constant of the cantilever was determined to be $0.07 \pm 0.005\ \text{N/m}$, using the method of Hutter and Bechhoefer [18].

The force measurements are performed on a Nanoscope 4 instrument equipped with a PicoForce scanner (Digital Instruments). The separation between the surfaces is found by determining zero-distance position, i.e. where the slope of the cantilever deflection versus vertical piezo movement reaches unity (constant compliance regime). It is known that there is some uncertainty in this method [19] that is generally of $O(1\ \text{nm})$, which is not significant in the context of the long-ranged forces discussed here.

High molecular weight fish gelatin (Norland Products Inc.) and dextran (500 kDa, Sigma) are dissolved in 50 mM KCl (to suppress electrostatic interactions between the silica surfaces and to aid dissolution) at an overall polymer concentration of 100 g/l. Due to the miscibility gap between these biopolymers, two aqueous macroscopic phases are formed, one enriched in dextran, the other enriched in

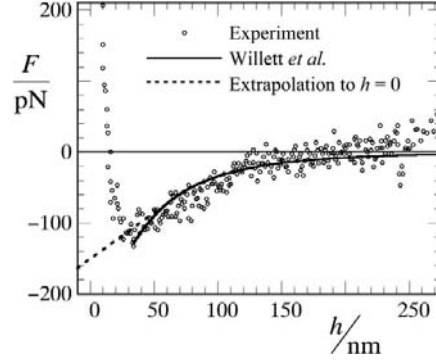


Figure 6.5: Experimental force-separation curve for capillary condensation in a system of gelatin and dextran between a silica sphere ($R = 3 \mu\text{m}$) and a silica substrate, measured with CP-AFM. Symbols are the experimental data, the solid line is a fit to the model of Willett *et al.* [9] and the dotted line is a graphical extrapolation of the attractive force to $h = 0$.

gelatin. Microscopy has revealed that, when these 2-phase systems are brought in contact with silica surfaces, the gelatin rich phase completely wets the surface ($\theta \approx 0$) [20], hence it is expected that when we bring the dextran-rich phase between two silica surfaces at close separation, a capillary bridge of the gelatin enriched phase is formed. We fill the liquid cell of the Atomic Force Microscope with the dextran-rich phase at its binodal composition, meaning that this phase is at its saturation point; $\varphi_{gelatin}^b / \varphi_{gelatin}^* = 1$.

The force-distance curve that results from bringing together the two surfaces in the Atomic Force Microscope is shown in Fig.6.5. We see a long-ranged, weak (≈ 100 pN) attractive force due to the capillary condensation of a gelatin-rich phase between the surfaces. Van der Waals forces can be excluded as a possible origin of the attraction, as the force measured here decays much slower than what is predicted for van der Waals attraction between a sphere and a flat surface, i.e. $F_{vdW} \propto h^{-2}$. We should also point out that van der Waals forces are almost never found in CP-AFM measurements between silica surfaces in aqueous systems, e.g. [21], although theory predicts that it should be possible to measure them in the CP-AFM set-up. At small separation distances (< 25 nm) we see steric effects of the material in the gap and of the material adsorbed onto the silica surfaces that is compressed, which gives rise to a repulsion that precedes the infinitely large repulsion at $h = 0$. In order to properly distinguish the weak attractive force, the y -axis is scaled to small values of the attractive and repulsive surface force, hence

the large repulsion close to $h = 0$ cannot be seen in this plot. For a more elaborate analysis of this and other experiments on capillary forces in systems with ultralow interfacial tensions as measured with Atomic Force Microscopy we refer to [6].

Interfacial tensions in the same system of fish gelatin and dextran, have been determined using a method based on the relaxation of droplets, deformed by shear flow, to their spherical shape after cessation of the flow. For the same overall composition, i.e. 10 wt% biopolymers and 90 wt% solvent, an interfacial tension of $9 \pm 3 \mu\text{N/m}$ has been found [22].

The volume of the capillary bridge formed from the gelatin-rich phase, is extremely small, i.e. of order picoliters, compared to the total volume of the dextran-rich phase in the liquid cell ($\approx 1 \text{ ml}$). Although the bulk phase will be slightly depleted from gelatin by the formation of a gelatin-rich capillary bridge, we can still reasonably assume the bulk phase to be at or very close to its saturation point. This allows application of Eqn.6.9. For this we need to extrapolate the attractive force to $h = 0$. Graphical extrapolation of the attractive force, shown as the dotted line in Fig.6.5, yields $F(h = 0) = -150 \pm 20 \text{ pN}$. Using Eqn.6.9 we find an interfacial tension of $8 \pm 1 \mu\text{N/m}$, which is in excellent agreement with the result from literature.

If we use the model of Willett et al. [9] to fit our experimental data (solid line in Fig.6.5), using all points on the force-distance curve up to $\approx 25 \text{ nm}$, in a least sum of squares procedure, we find an interfacial tension of $14 \pm 3 \mu\text{N/m}$. Above we have discussed that, for the same parameters, Willett et al. would extrapolate to the same value of the adhesion force as our result in Eqn.6.9. Here however we find a different result, which can be explained by the fact that the shape of the force-distance curve predicted by Willett et al., which was the best fit of the model to our data, does not accurately match our experimental data. The stronger downward curvature of the force-distance curve predicted by this model also leads to a higher extrapolated adhesion force at contact, than is found by graphically extrapolating the data, which in turn leads to a higher value for the interfacial tension.

The deviations in the shape of $F(h)$ as predicted by Willett et al. compared to our experimental results could possibly be explained by the fact that the model contains several major approximations. It is, e.g., assumed that the shape of the capillary bridge is that of the void in a torus, i.e. the toroidal approximation. Another assumption made by Willett and co-workers is that the volume of the capillary bridge remains constant over all distances at which it is present. This is also not always accurate, and becomes less reasonable for systems with low interfacial tensions, i.e. weakly segregated systems. It is possible that for the

system discussed above, with an ultralow interfacial tension, the volume of the liquid bridge is not constant during the whole compression and decompression cycle.

The capillary forces measured in the CP-AFM set-up, for this and other systems with ultralow interfacial tensions, do not show signs of hysteresis [6]. The ultralow interfacial tension strongly reduces the nucleation barrier and with that exponentially increases the nucleation rate, such that nucleation is no longer a limiting step. It is the microscopic geometry in this experimental technique, and the resulting microscopic dimensions of the capillary bridge, which ensures that transport (i.e. diffusion) of material for formation of the bridge is also much faster than the experimental time scales. Previously we estimated that the characteristic diffusion time for the polymers is of the order of tens of milliseconds, whereas the experiment takes place on the scale of several seconds.

6.4 Self-consistent field calculations

The description of the interface between two immiscible fluids was first given by van der Waals more than a century ago [23]. The famous hyperbolic tangent shape of the density profiles of both liquids across the interface can be retrieved in a simple lattice model with monomeric species [24]. Applications of the same procedure to more complicated geometries are not frequently found in literature, but are at least in principle straightforward. A unique feature of this method is that the position and shape of the interface is a result of the free energy minimization. In this method we can easily, compared to, e.g., experiments, vary parameters such as the relative undersaturation, size of the sphere, and contact angle, to investigate the effect these parameters have on the capillary adhesion force. This makes the self-consistent field method a useful additional tool, next to the thermodynamic model in the first section and the experiments in the second section of this Chapter.

We use the discretization scheme of Scheutjens and Fleer as the machinery of this self-consistent field method. The details of this technique are described elsewhere [25, 26, 27, 28]. Here we will only address the choices made in the present model. In the calculations two monomeric species A and B are placed on a two-gradient cylindrical lattice (see Fig.6.6), each monomer filling exactly one lattice site of volume b^3 , with b the discretization length. All sites must be filled by one of the two species, thus the system is fully incompressible. In the calculations inhomogeneities are allowed in the radial, z -direction as well as in the x -direction along the length of the cylinder. The system consists of M_z layers

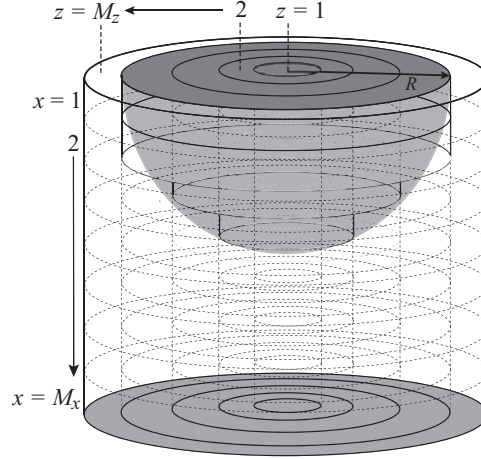


Figure 6.6: Schematic representation of our SCF geometry; a 2-gradient cylindrical lattice, allowing inhomogeneities in the x - (with M_x layers) and z -direction (with M_z layers) only. The flat surface is placed at $x = M_x$ and the centre of the sphere (with radius R) is placed at $(x, z) = (1, 1)$. Note that in the calculations $M_z \gg R$.

in the z -direction and M_x layers in the x -direction. The interactions between all species and the densities of all species are averaged in one direction. As a result, all properties of the system are rotationally symmetric around the length axis of the cylinder. A flat, rigid, surface, constructed of segments of type S , is located on one side of the system (at $x = M_x$). On the other side of the system a rigid quasi-hemisphere is constructed of the same segments S . Due to the discrete nature of our model and the cylindrical geometry of the lattice, this object does not have a perfectly smooth hemispherical surfaces, rather it is slightly terraced on the scale of the discretization length b (see Fig.6.8). In all calculations the other length scales in the problem, such as the interfacial width ξ , are kept several times larger than the discretization length, so that any roughness effects can be neglected.

In this self-consistent field theory nearest neighbor interactions are accounted for using a Flory-Huggins interaction energy, which is parameterized by the Flory-Huggins interaction parameters χ , that must be defined between all pairs of unlike segment species in the system. Here χ_{BS} is set to 0 in all cases. χ_{AB} sets the strength of the segregation between monomers A and B . The critical interaction parameter for two monomers A and B $\chi_{AB}^c = 2$, below which no demixing occurs. The distance to the critical point $\Delta\chi_{AB}$ is defined here as $\chi_{AB} - \chi_{AB}^c$, and sets the interfacial tension γ between the A-rich and the B-rich phase and determines

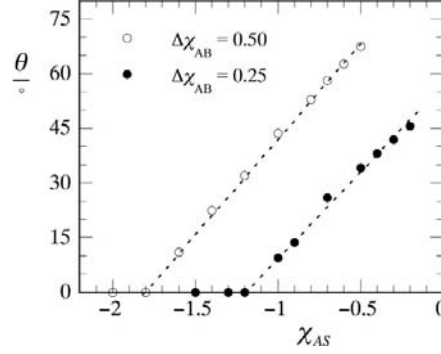


Figure 6.7: Contact angle θ (in degrees) versus the adsorption energy χ_{AS} as a function of the distance to the critical point, from one-gradient self-consistent field calculations for flat interfaces. Dotted lines are drawn to guide the eye.

the width ξ of the interface between the two phases. The wetting behavior is set with χ_{AS} . For negative values of χ_{AS} , as chosen here, the A -rich phase wets the surfaces.

The combination of the adsorption energy set by means of χ_{AS} (for $\chi_{BS} = 0$) and the distance to the critical point of the A and B mixture ($\Delta\chi_{AB}$) together determine the contact angle at the three phase contact line between, e.g., an A -rich droplet on a solid surface (S segments) in coexistence with a bulk phase rich in B . For this situation we can write Young's law [12] as:

$$\cos \theta = \frac{\gamma_{sb} - \gamma_{sa}}{\gamma_{ab}} \quad (6.16)$$

where indices s represents the solid surface, a the phase forming the droplet enriched in component A and b the bulk phase rich in species B . Of course, there is adsorption of component A at the sb -interface. For partial wetting the thickness of this adsorption layer is always microscopic. All three interfacial tensions in Eqn.6.16 can be easily obtained in one-gradient self-consistent field calculations for flat interfaces, which allows calculation of the contact angle for a given combination of χ_{AB} and χ_{AS} . In Fig.6.7 we show two examples of results for the contact angle from these simple SCF calculations in a flat geometry. We see that at small adsorption energies the contact angle goes towards 90° , which we can logically expect for the case where neither of the two components shows a preference for the substrate. At high enough adsorption energies we see the transition from partial to complete wetting. We also see that the point where this transition occurs depends strongly on χ_{AB} , as this sets the interfacial tension between the liquid phases γ_{ab} , which is

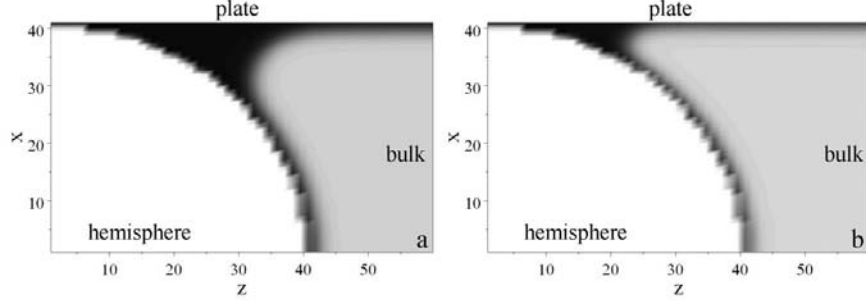


Figure 6.8: Volume fraction profile plots of a capillary bridge at contact between a sphere ($R = 40b$) and a flat plate in a binary mixture of monomers with $\Delta\chi_{AB} = 0.5$, $\theta = 0$ ($\chi_{AS} = -2$) and the interfacial width $\xi \approx 4b$, for two values of relative undersaturation: a) $\varphi_A^b/\varphi_A^* = 0.95$ and b) $\varphi_A^b/\varphi_A^* = 0.85$. The greyscale reflects the local volume fraction of component A , which forms the minority phase that condenses: black indicates the volume fraction of component A in the A -rich phase at bulk coexistence and white indicates a volume fraction of component A equal to zero. The two axes are the radial direction z and the height x of our cylindrical lattice, both in units b .

one of the three ingredients in Eqn.6.16.

The following calculations are conducted in a grand canonical ensemble, i.e. the free energy is minimized for a given separation between the surfaces while the chemical potential of monomers (μ), volume of the system (V) and the temperature (T) are fixed. Setting the chemical potential of A is equivalent to setting the relative undersaturation of this component in the bulk phase. From classical thermodynamics we know that we can write the quantity $\mu_A - \mu_A^*$, which was introduced in the previous section, as the natural logarithm of the ratio of the actual activity α_A^b of component A in the bulk phase to the activity α_A^* of component A at saturation; $\mu_A - \mu_A^* = k_B T \ln(\alpha_A^b/\alpha_A^*)$. For ideal systems the activity may be replaced by the volume fraction φ . Although the system here is clearly not ideal, we will present some results as a function of φ_A^b/φ_A^* , as this quantity is most closely related to experimentally accessible properties such as the relative humidity or undersaturation. Of course at saturation $\varphi_A^b/\varphi_A^* = \alpha_A/\alpha_A^* = 1$.

From the self-consistent field calculations we obtain the volume fraction profiles of all components. When we plot, e.g., the volume fraction profiles of component A in a 2 dimensional contour plot, the capillary bridge is visualized. Examples of such plots at $h = 0$ are shown in Fig.6.8 for the case of complete wetting ($\theta = 0$), and in Figures 6.9a and 6.9c, for the case of a contact angle of 32° . In both plots

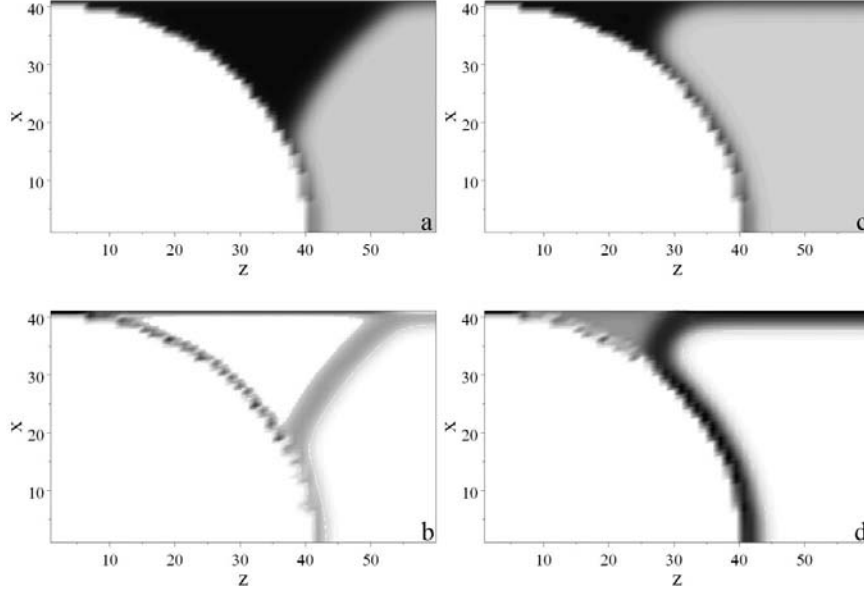


Figure 6.9: Contour plots of the volume fraction profile (a & c) and grand potential density ω (b & d) of a capillary bridge between a sphere ($R = 40b$) and a flat plate ($h = 0$) in a binary mixture of monomers with $\Delta\chi_{AB} = 0.5$, $\theta = 32^\circ$ ($\chi_{AS} = -1$), at saturation $\varphi_A^b/\varphi_A^* = 1$ (a & b) and with a relative undersaturation of $\varphi_A^b/\varphi_A^* = 0.9$ (c & d). a & c) coloring reflects the local volume fraction $\varphi_A(x, z)$ of component A: black indicates the volume fraction of component A in the A-rich phase at bulk coexistence ($\varphi_A = 0.85$) and white indicates $\varphi_A = 0$, b & d) coloring reflects the local grand potential density $\omega(x, z)$, where white equals the grand potential density of the bulk phase and black is the maximum value of the grand potential density in the system ($0.13 k_B T/b^3$ for b) and $0.06 k_B T/b^3$ for d)). The two axes are the radial direction z and the height x of our cylindrical lattice, both in units b .

we see the effects of a slight change in the relative undersaturation on the shape and total curvature of the capillary bridge.

The density contour plot in Fig.6.9a shows the situation at saturation, where we would expect the Laplace pressure to be zero (Eqn.6.6). In the context of these self-consistent field calculations, the Laplace pressure is found from the difference between the grand potential density ω inside the capillary bridge and that in the surrounding bulk phase;

$$\Delta P = \omega_{bulk} - \omega_{bridge} \quad (6.17)$$

where the grand potential density is the local grand potential Ω per unit volume, with

$$\Omega = G - \sum_i \mu_i n_i \quad (6.18)$$

in which G is the Helmholtz energy of the system and n_i the number of molecules of component i with chemical potential μ_i . In an incompressible system, where there is no bulk pressure term, the grand potential is thus closely linked to interfacial quantities such as the interfacial tension and the Laplace pressure.

The grand potential density profiles, as obtained from the calculations, are plotted in a similar way as the volume fraction profiles. These 2D contour plots of $\omega(x, z)$ are shown in Figures 6.9b and 6.9d. In these graphs we can see that at saturation, $\varphi_A^b/\varphi_A^* = 1$, the grand potential density is the same in the center of the capillary bridge as on the outside in the bulk phase (Fig.6.9b), implying a zero Laplace pressure, whereas they are clearly different for a slight undersaturation, $\varphi_A^b/\varphi_A^* = 0.9$, as shown in Fig.6.9d. This is consistent with classical thermodynamics, as expressed in Eqn.6.1.

We also see that the Laplace pressure is homogeneous inside the capillary bridge, as we should expect, but that the grand potential density ω is locally enhanced at the interface between the capillary neck and adjacent bulk phases, either liquid or solid. This is consistent with finite values of the interfacial tension that acts there. In the context of these SCF calculations the interfacial tension is defined as the integral of the grand potential density per unit area across the interface.

The interaction curves between the hemisphere and plate are calculated by systematically varying the separation h between the surfaces, while all other properties (μ_A , χ_{AB} and χ_{AS}) are fixed. The free energy of interaction $G^{int}(h)$ is defined as the actual free energy of the system with respect to the reference state which is the free energy of the system at infinite separation of the surfaces; $G^{int}(h) = G(h) - G(\infty)$.

A few examples of the results for the free energy of interaction versus surface separation that we obtain in the two-gradient self-consistent field calculations are given in Fig.6.10. Firstly we must mention that these results were obtained by systematically decreasing the surface separation h , but that the results were the same for the calculations in which the surface separation was increased stepwise. This indicates that at least for these cases hysteresis is absent, or occurs on length scales that are small or equal to the discretization length. This is in contradiction with the results that are often found for capillary forces between two parallel walls, where hysteresis is generally very pronounced [29]. Further investigations using

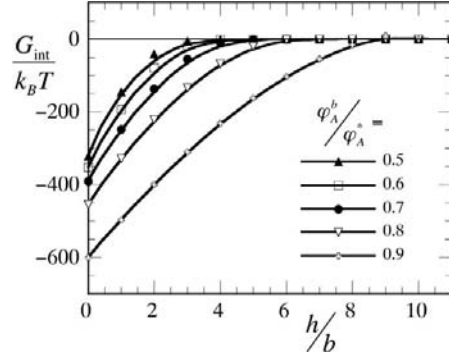


Figure 6.10: Interaction free energy $G^{int}(h)$ in units $k_B T$ versus surface separation h in units of the discretization length b for various values of the relative undersaturation φ_A^b/φ_A^* of component A in the bulk phase, for a system with $\Delta\chi_{AB} = 0.5$ and $\chi_{AS} = -2$ ($\theta = 0$). The geometry is a hemisphere of radius $40b$ interacting with a planar wall.

our self-consistent field model, for sake of brevity not shown here, indicate that hysteresis becomes more pronounced when we increase the size of the sphere (going towards two parallel plates), when we increase the distance to the critical point, i.e. increase the interfacial tension and when we increase the relative undersaturation of component A in the bulk phase. A first indication of this latter conclusion can already be seen in Fig.6.10 as the small overshoot found at $h = 9$, for the case of $\varphi_A^b/\varphi_A^* = 0.9$, which seems to be a first indication of the presence of hysteresis, although very limited for the example shown here. In the plots we also see that both the total adhesive energy due to the capillary bridge and the range of the attractive interaction increase significantly with moving the bulk phase closer to saturation. Note that for the case of complete wetting, i.e. zero contact angle, the calculations cannot be performed exactly at saturation, because the system will completely fill with the condensed phase, as was also discussed above.

With existing experimental techniques the interaction energy versus surface separation cannot be determined directly. With the Surface Force Apparatus, the Atomic Force Microscope or, e.g., optical trapping techniques the force-separation curve is, in theory, directly accessible. In reality however, non-equilibrium aspects often make this impossible. In special cases, as we have recently shown, it is possible to measure force-distance curves in full equilibrium [6]. A experimental measures that is relatively easily obtained, and which is often used to quantify the strength of capillary adhesion, is the so-called pull-off force. This is the force needed to pull apart the surfaces from contact ($h = 0$). In our calculations this quantity can be

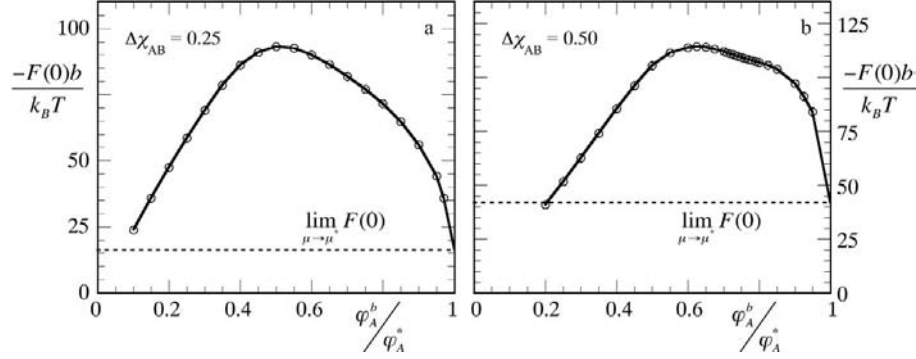


Figure 6.11: Effect of relative undersaturation φ_A^b/φ_A^* on the capillary adhesion force at contact $-F(h=0)$, between a sphere ($R = 40b$) and a flat plate, for a system with a zero contact angle ($\chi_{AS} = -2$), and distance to the critical point $\Delta\chi_{AB}$ of 0.25 ($\xi \approx 7b$) (a) and 0.5 ($\xi \approx 4b$) (b), respectively. The value of $-F(h=0)$ as predicted with Eqn.6.9 is indicated with the dotted line.

found, by taking the forward derivative of the interaction free energy from $h = 0$, as stated in Eqn.6.4.

For the system investigated in Fig.6.10 the pull-off forces versus the relative undersaturation are shown in Fig.6.11b, and are compared to a system closer to the critical point, i.e. with a lower interfacial tension, in Fig.6.11a. Let us first focus on the results close to saturation, i.e. where $\varphi_A^b/\varphi_A^* \rightarrow 1$. In this graph the limiting pull-off force at saturation is indicated by the dotted line. As stated before, the calculations cannot be carried out exactly at saturation for a system with zero contact angle. Extrapolation of the numerical results towards saturation however clearly show that the pull-off force approaches the value predicted by the macroscopic thermodynamic model, as described in Eqn.6.9, even for these calculations on mesoscopic length scales. The ratio between the radius of the sphere and the interfacial width ξ gives a qualitative idea of the importance of microscopic effects. In the calculations presented here this ratio is approximately equal to 10. In the real macroscopic limit, where the width of the interface is negligible compared to the size of the sphere and the size of the capillary bridge, this ratio is many times larger. Unfortunately, this domain is difficult to access in these calculations due to divergence of the computational time when scaling up the system. But even though we are not yet in the true macroscopic domain with the calculations, we do find a good correspondence between the model in the first section of this Chapter and the numerical results.

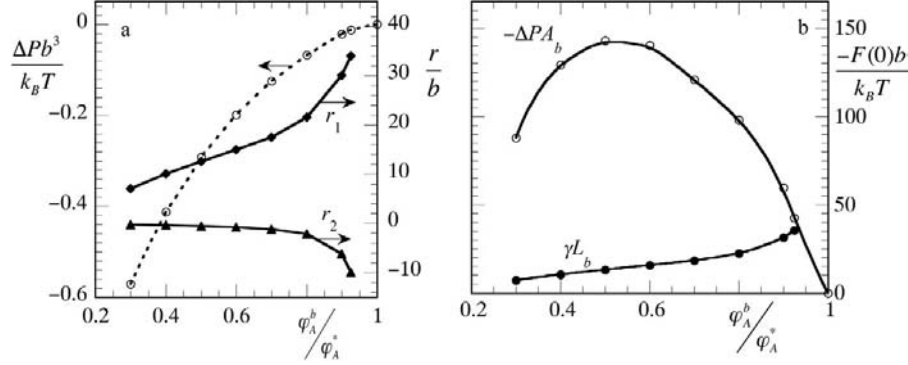


Figure 6.12: Laplace pressure ΔP and principal radii of curvature r_1 and r_2 (a) and the absolute values for the resulting terms in Eqns 6.4 and 6.5 (b) for the same system and configuration as in Fig.6.11b ($h = 0$, $R = 40b$, $\Delta\chi_{AB} = 0.5$, $\chi_{AS} = -2$) as a function of the relative undersaturation ϕ_A^b/ϕ_A^*

When moving away from saturation we see the non-monotonous behavior of the pull-off force. A maximum in the pull-off force as a function of the undersaturation is also seen in experiments with Atomic Force Microscopy, e.g. [30]. The precise effect that relative humidity has on the adhesion force is thought to depend very specifically on the geometry in which the measurements are carried out, such that the shape of the resulting curve of pull-off force versus relative humidity can be used to deduce the geometry of the measurements [31]. Very recently, Jang et al. have proposed that the non-monotonous behavior, for the sphere-plate geometry such as found in the Colloid Probe AFM technique, can be fully explained by the susceptibility of the capillary bridge to volume change upon the separation distance [32]. In that paper two counteracting structural effects on the volume of the liquid bridge are separately described: i) the liquid bridges tends to increase its volume upon increasing the surface separation because of the larger height that the bridge must span, ii) the liquid bridge tends to decrease its volume upon increasing the separation by narrowing the size of the waist. The specific combination of these two effects, which are both argued to depend differently on the relative humidity, gives the type of behavior also seen here.

We can investigate this non-monotonous behavior of the pull-off force in some more detail using some thermodynamic quantities obtained from the calculations. Inspection of the expression for the capillary adhesion force in Eqn.6.4 reveals two terms; the first, $-\gamma L_b$, corresponding to the interfacial work term in the free energy and the second, $\Delta P A_b$, that is derived from the volume term in Eqn.6.3.

As stated above, we can directly obtain the Laplace pressure from the calculations. To apply Eqn.6.5, we also need to find the value of r_1 as a function of the relative undersaturation. As above, we take the value of r_1 at the waist of the capillary bridge using the density profiles, as shown, e.g., in Fig.6.8. In these systems, where the interfacial width is significant compared to the width of the capillary bridge, we position the interface at the plane where the densities of components A and B have the steepest decay in the direction normal to the interface. This should, in first order, gives us a realistic estimate of r_1 . Combination of the values of ΔP , r_1 and a known interfacial tension γ , also leads us to the value of r_2 , using Eqn.6.2. We have carried out these steps for the same system and configuration as considered in Fig.6.11b. Fig.6.12a shows how the Laplace pressure and the principal radii of curvature of the capillary bridge change with relative undersaturation. First of all, we note that the Laplace pressure goes to zero with the logarithm of the quantity φ_A^b/φ_A^* , as is of course dictated by Kelvin's law (Eqn.6.1). We also see that r_1 and r_2 diverge when $\varphi_A^b/\varphi_A^* \rightarrow$ goes to unity.

We now combine these quantities to calculate the two terms in our thermodynamic model for capillary adhesion forces, as given in Eqn.6.5. The individual contribution of both terms to the total adhesion force is shown in Fig.6.12b. It becomes apparent that the γL_b becomes increasingly important when approaching saturation, which was of course our main argument in the derivation of the macroscopic model in the limit of saturation. We also see that the non-monotonous behavior must be attributed to the Laplace pressure term in the adhesion force. This also becomes clear when looking at the ingredients of both terms. In the γL_b -term there are only constants and one term r_1 , which we have seen to monotonously increase when approaching saturation. In the $\Delta P A_b$ -term we however have r_1 and r_2 , that both change with the undersaturation, one becoming more positive, the other more negative with increasing φ_A^b/φ_A^* . This leads to the maximum in the contribution of the Laplace pressure term, and in turn leads to the maximum in the total pull-off force versus undersaturation.

In the first section of this Chapter we have discussed the approximate model by Orr et al. [7, 8], in which the γL_b -term is considered negligible compared to the $\Delta P A_b$ -term, which is exactly the opposite approach as we have chosen here. In Fig.6.12b we can see that this approximation is only reasonable for relatively low undersaturations, although extrapolation of the curves seems to indicate that at very low undersaturations ($\varphi_A^b/\varphi_A^* < 0.2$) both terms again become of the same order of magnitude. We also see that the second assumption by Orr and co-workers, i.e. $-r_2 \ll r_1$, is not accurate over the entire range of undersaturations, for this mesoscopic model. This assumption can be expected to be more reasonable for

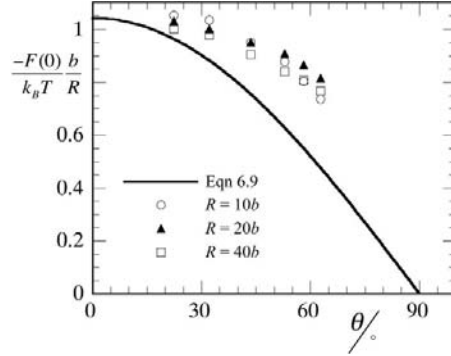


Figure 6.13: Effect of contact angle θ on the capillary adhesion force at contact $F(h = 0)$ (in units $k_B T b^{-1}$) normalized with the sphere radius R in units b , for a system with a distance to the critical point $\Delta\chi_{AB} = 0.5$, at saturation ($\varphi_A^b/\varphi_A^* = 1$). Symbols are numerical results from self-consistent field calculations. Drawn line is the prediction from our macroscopic model, expressed in Eqn.6.9.

macroscopic systems. The values found for the pull-off force between $\varphi_A^b/\varphi_A^* = 0.8$ and 0.4 , where the first assumption discussed above is reasonable, are of the same order of magnitude as what is predicted by Orr et al. (i.e. two times the value indicated by the dotted line). The deviations between our SCF result and the approximate predicted are smaller for the system in Fig.6.11b as this system is closer to the macroscopic limit.

According to our macroscopic model, summation of the two terms in Eqn.6.5, should give the total adhesion force. However if we add the values found in Fig.6.12b, we do not return to the exact values found by direct differentiation of the free energy to h , as given in Fig.6.11b. We must also note that the discrepancy is small for large values of φ_A^b/φ_A^* but increases in magnitude when moving away from saturation. This seems to indicate that the macroscopic considerations work well close to saturation, but that other effects come into play farther away from $\varphi_A^b/\varphi_A^* = 1$. We attribute this to the fact that the capillary bridge, beyond some point, becomes of the same dimensions as the width of the interface. For this specific case $\xi = 4b$, and in Fig.6.12a we can see that the diameter of the capillary bridge r_1 becomes of this order of magnitude when decreasing φ_A^b/φ_A^* to well below 1. In these cases an additional length scale ξ becomes important and we can expect that the macroscopic considerations are no longer fully accurate.

Finally we want to show some results of calculations exactly at saturation, for systems with non-zero contact angles. These calculations are technically challeng-

ing as the systems have the tendency to fill completely with the condensed phase at saturation, as a result of the reflecting boundary conditions. In Fig.6.13 we find the comparison between the prediction based on macroscopic thermodynamics (Eqn.6.9) and the results from our mesoscopic self-consistent field calculations. We see that the numerical results are close to the macroscopic prediction and that normalization of the adhesion force with the radius of the sphere R has almost collapsed the numerical data onto one curve. This latter observation indicates that the linear proportionality of the pull-off force with the sphere radius as predicted, is retrieved in the SCF results. Although the numerically found pull-off forces are close to the theoretical prediction, there are deviations, that become more pronounced for larger contact angles. We believe that this must again be attributed to the mesoscopic dimensions of the system in the calculations, such that we are not dealing with a truly macroscopic system. The fact that the deviations decrease for small contact angles is due to the fact that the width of the capillary bridge increases with decreasing contact angle, and hence we are approaching the macroscopic limit for these systems with small contact angles.

6.5 Conclusions

In this Chapter we have introduced a simple and intuitive model for capillary adhesion in the limit of saturation, that we have worked out in more detail for one specific and experimentally relevant geometry, i.e. the case of a sphere interacting with a planar wall. We have shown one example of a measurement of equilibrium capillary forces using this technique, to further evidence the reasoning deployed in the thermodynamic model. In the last part of this Chapter we have applied a numerical self-consistent field method to study capillary condensation and capillary forces, both in the limit of the validity of our macroscopic model and in cases where this model can be expected to lose its validity. In some cases deviations of the numerical results with the thermodynamic consideration could be attributed to finite size effects of the system under consideration.

References

- [1] Olsson, M.; Joabsson, F.; Picullel, L. *Langmuir* **2005**, *21*, 1560.
- [2] Rollot, Y.; Regnier, S.; Guinot, J. C. *Int. J. Adhes. Adhes.* **1999**, *19*, 35.
- [3] Thiel, W. J.; Nguyen, L. T.; Stephenson, P. L. *Powder Technology* **1983**, *34*, 75.

- [4] Nowak, S.; Samadani, A.; Kudrolli, A. *Nature Physics* **2005**, *1*, 50.
- [5] Huber, G.; Mantz, H.; Spolenak, R.; Mecke, K.; Jacobs, K.; Gorb, S. N.; Arzt, E. *Proc. Nat. Acad. Sci.* **2005**, *102*, 16293.
- [6] Sprakel, J.; van der Gucht, J.; Cohen Stuart, M. A.; Besseling, N. A. M. *Phys. Rev. Letters* **2007**, *99*, 208301.
- [7] Orr, F. M.; Scriven, L. E.; Rivas, A. P. *J. Fluid Mech.* **1975**, *67*, 723.
- [8] Israelachvili, J. *Intermolecular & Surface Forces*; Academic Press (London), 1985.
- [9] Willett, C. D.; Adams, M. J.; Johnson, S. A.; Seville, J. P. K. *Langmuir* **2000**, *16*, 9396.
- [10] Oversteegen, S. M.; Blokhuis, E. M. *J. Chem. Phys.* **2000**, *112*, 2980.
- [11] Leermakers, F. A. M.; Barneveld, P. A.; Sprakel, J.; Besseling, N. A. M. *Phys. Rev. Letters* **2006**, *97*, 006103.
- [12] Lyklema, J. *Fundamentals of Interface and Colloid Science. Volume I: Fundamentals*; Academic Press Ltd., London, 1991.
- [13] Pakarinen, O. H.; Foster, A. S.; Paaajanen, M.; Kalinainen, T.; Katainen, J.; Makkonen, I.; Lahtinen, J.; Nieminen, R. M. *Modell. Simul. Mater. Sci. Eng.* **2005**, *13*, 1175.
- [14] Heertjes, P. M.; Smet, E. C. D.; Witvoet, W. C. *Chem. Eng. Sci.* **1971**, *26*, 1479.
- [15] Adams, M. J.; Johnson, S. A.; Seville, J. P. K.; Willet, C. D. *Langmuir* **2002**, *18*, 6180.
- [16] Ducker, W. A.; Senden, T. J.; Pashley, R. M. *Nature* **1991**, *353*, 239.
- [17] Giesbers, M.; Kleijn, J. M.; Cohen Stuart, M. A. *J. Colloid Interface Sci.* **2002**, *248*, 88.
- [18] Hutter, J. L.; Bechhoefer, J. *Rev. Sci. Instrum.* **1993**, *64*, 1868.
- [19] McKee, C. T.; Mosse, W. K. J.; Ducker, W. A. *Rev. Sci. Instrum.* **200**, *77*, 053706.
- [20] Tromp, R. H.; Lindhoud, S. *Phys. Rev. E* **2006**, *74*, 031604.
- [21] Ducker, W. A.; Senden, T. J.; Pashley, R. M. *Langmuir* **1992**, *8*, 1831.
- [22] Scholten, E.; Sprakel, J.; Sagis, L. M. C.; van der Linden, E. *Biomacromolecules* **2006**, *7*, 339.
- [23] van der Waals, J. D. *Thermodynamische theorie der capillariteit in de onderstelling van een continue dichtheidsverandering*; Verhand. Kon. Akad. v Wetensch., 1893.
- [24] Safran, S. A. *Thermodynamics of Surfaces, Interfaces and Membranes*; Addison-Wesley (Reading), 1994.
- [25] Scheutjens, J. M. H. M.; Fleer, G. J. *J. Phys. Chem.* **1979**, *83*, 1619.

- [26] Scheutjens, J. M. H. M.; Fleer, G. J. *J. Phys. Chem.* **1980**, *84*, 178.
- [27] Evers, O. A.; Scheutjens, J. M. H. M.; Fleer, G. J. *Macromolecules* **1990**, *23*, 5221.
- [28] Fleer, G. J.; Cohen Stuart, M. A.; Scheutjens, J. M. H. M.; Cosgrove, T.; Vincent, B. *Polymers at Interfaces*; Chapman and Hall (London), 1993.
- [29] Hill, T. L. *J. Chem. Phys.* **1947**, *15*, 767.
- [30] Xiao, X.; Qian, L. *Langmuir* **2000**, *16*, 8153.
- [31] Butt, H. J.; Farshchi-Tabrizi, M.; Kappl, M. *J. Appl. Phys.* **2006**, *100*, 024312.
- [32] Jang, J.; Yang, M.; Schatz, G. *J. Chem. Phys.* **2007**, *126*, 174705.

Chapter 7

Dynamics of polymer bridge formation and disruption

In this Chapter we show that the formation and subsequent disruption of polymer bridges between two solid surfaces is characterized by slow relaxation times, due to the slowing-down of polymer dynamics near a surface. For colloidal particles, that are in constant (Brownian) motion, kinetic aspects should not be overlooked. To understand these effects, we develop a mean-field model of polymer bridging and bridge disruption that agrees quantitatively with our experiments.

This chapter was published as:

J. Sprakel, E. Bartscherer, G. Hoffmann, M.A. Cohen Stuart and J. van der Gucht:
Dynamics of polymer bridge formation and disruption, Phys. Rev. E 78 (2008), 040802.

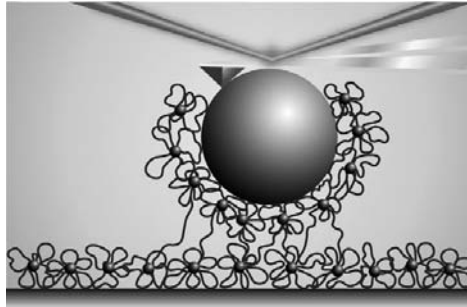


Figure 7.1: Impression of of the colloidal probe AFM set-up, with adsorbed layers of flowerlike micelles forming polymer bridges between the solid surfaces.

7.1 Introduction

Polymers can induce attractive interactions between two surfaces [1]. Best known examples are perhaps the depletion attraction for non-adsorbing polymers [2] and bridging attraction for adsorbing polymers [3, 4]. Theories of bridging interactions often focus on thermodynamic equilibrium [1, 5]. However, the dynamics of polymers near surfaces is often very slow [6], so that an equilibrium state may not be reached in practical cases. This can have great consequence for the interactions between colloidal particles that are in constant motion with respect to each other. To investigate such effects, we study the kinetics of bridge formation and disruption with colloidal probe atomic force microscopy. A simple kinetic model is developed that quantitatively describes the data and elucidates the molecular processes underlying the observed forces.

7.2 Methods

With the Colloidal Probe AFM technique [7], the interaction force F between a spherical particle and a planar solid surface is measured as a function of the separation distance h (Figure 7.1). An oxidized silicon wafer is employed as the flat substrate and a $3\text{ }\mu\text{m}$ radius silica sphere as the colloidal probe, which is glued to a standard contact mode cantilever with a nominal spring constant of 0.06 N/m . The measurements are carried out on the ForceRobot (JPK-Instruments), which is an automated AFM set-up with built-in active vibration reduction. Actual spring constants of the cantilevers are measured with the thermal noise method [8]. Measurements consist of three stages: I) compression (approach), II) a contact (surface)

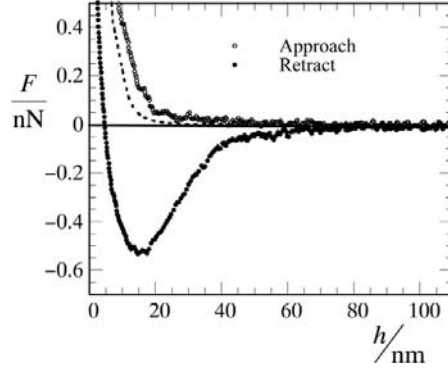


Figure 7.2: Typical force-separation curve for a full scan, showing the approach (\circ) and retract (\bullet) trace, with $v = 500$ nm/s, $t_s = 1$ s for 0.1 g/L C16-20k. Dotted line shows an averaged approach trace for measurements in pure solvent (10^{-2} M NaCl).

delay of t_s seconds (ranging between 0 and 10s), III) decompression (retract). The velocity of (de)compression is set to $v = \pm 500$ nm/s, unless stated otherwise. For $t_s > 0$, step II is activated with a repulsive trigger force on approach of 500 pN.

We study the bridging forces between adsorbed layers of telechelic associative polymers. The equilibrium bridging interactions between such layers have been predicted theoretically quite extensively, e.g., using the Milner-Witten-Cates self-consistent field formalism [5]. These telechelic polymers consist of a hydrophilic polymer (polyethylene oxide, PEO), modified on both ends with an alkyl tail. In dilute aqueous solutions they form micelles, that are often called flowerlike micelles, due to the petal-like structure of the looped corona chains. When these micelles are brought close enough, polymeric bridges between them will be formed (see Chapter 4). We use the following nomenclature for the polymers: $Cm-pk$, where m is the number of carbon atoms in the alkyl tails and p is the molecular weight (in kg/mol) of the water-soluble backbone, e.g., C14-20k is a PEO chain of 20 kg/mol modified with tetradecyl tails at both ends. The preparation of these polymers has been described elsewhere [9]. Prior to the measurements, the surfaces are submerged in a 0.1 g/L polymer solution in 10^{-2} M NaCl, and left to equilibrate for at least 1h. During equilibration the PEO corona of the micelles adsorbs onto the surfaces [10]. For these polymeric surfactants, the large headgroup (PEO part) leads to a large preference for spherically symmetric micelles. We can thus expect this shape to be retained at the surface [11].

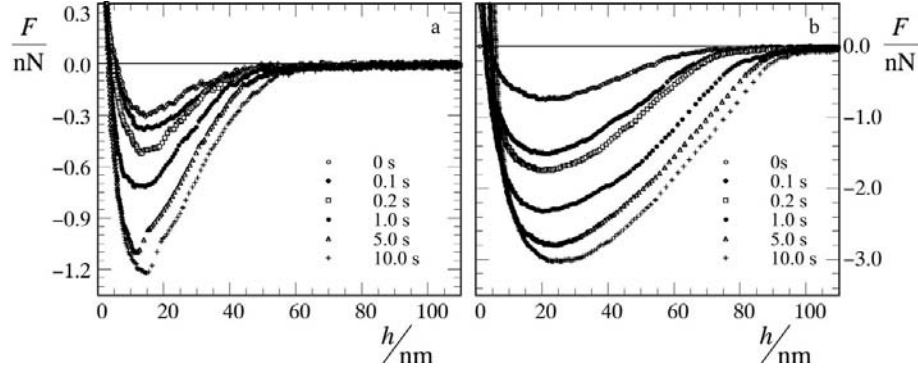


Figure 7.3: Retract traces with varying surface delay times t_s , as indicated in the plots, recorded at $v = 500\text{nm/s}$ for C16-20k (a) and C18-20k (b).

7.3 Results and Discussion

All measured $F(h)$ curves share two common features (Fig.7.2): i) on approach a purely repulsive force is found and ii) on retract an attractive well appears due to the formation of polymer bridges between the surface layers. The repulsive interaction on approach is partly electrostatic and partly steric in origin. In pure solvent, only the electrostatic component is observed (solid curve in Fig.7.2), for which the Debye length $\kappa^{-1} = 3\text{ nm}$. The additional repulsion in the polymer solutions is due to compression of the adsorbed polymers. It starts around 20 nm, corresponding to twice the hydrodynamic radius of the flowerlike micelles $R_h = 9.9 \pm 0.5\text{ nm}$, as found from light scattering. This indicates that the micellar structure is indeed largely preserved at the surface.

The hysteresis observed between approach and retract in Fig.7.2 already shows that the bridging process occurs on relatively long timescales. This is further confirmed when we change the time t_s that the surfaces are kept in contact (Fig.7.3). We see that at the shortest surface delay time of $t_s = 0$, corresponding to an effective contact time of approximately 40 milliseconds, there is already a significant bridging attraction. When we increase the contact time, up to 10 s, the bridging force continues to increase. Longer delay times are not accessible due to physical limitations of the technique.

In Fig.7.4, we plot the maximum attractive force F_m as a function of the surface delay time t_s . Assuming that the force, at a given surface separation h , is proportional to the number of bridges n_b , which we will justify below, Fig.7.4 reflects the kinetics of bridge formation.

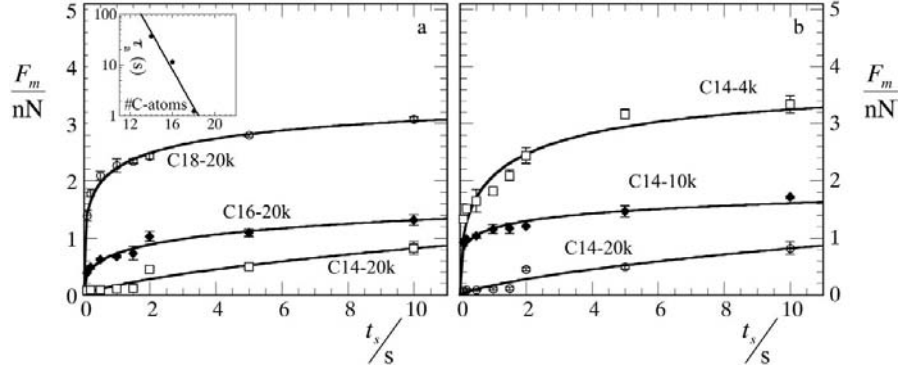


Figure 7.4: Absolute values of the maximum attractive force F_m versus surface delay times t_s , recorded at $v = 500\text{nm/s}$ for a) 20 kg/mol PEO end-capped with alkyl-tails of increasing length (C₁₄, C₁₆, C₁₈) b) tetradecyl end-capped PEO of varying molar weight (4, 10 and 20 kg/mol). Drawn lines are fits to Eqn.7.1. Insets shows the corresponding values of τ_a as a function of the number of carbon atoms in the alkyl tails (a) and polymer chain length (b).

Fig.7.4 does not show a single exponential relaxation, hence the bridge formation is not a first-order process with a single relaxation time. The data can be fitted with a stretched exponential relaxation (Fig.7.4):

$$F_m = F_{m,\infty} \left(1 - \exp \left[- \left(\frac{t_s}{\tau_a} \right)^\beta \right] \right) \quad (7.1)$$

where τ_a is the average bridging timescale, $F_{m,\infty}$ is the final plateau in F_m and β the stretch exponent, here found to be approximately 1/2. The values of τ_a found by fitting the data to Eqn.7.1 are shown in the insert in Fig.7.4 and are between 1 and 50 s. This is several decades larger than the bulk relaxation time for these polymers, which is on the order of a millisecond [12]).

The reason for this slow bridge formation is that the PEO chains are partly adsorbed onto the silica surface. In order to form a bridge, segments must desorb, which is a slow process. Moreover, depending on the position of a chain with respect to the surface, the number of adsorbed segments, and consequently also the desorption rate, can vary. This would lead to a distribution of relaxation times, which explains the stretched exponential form (Eqn.7.1).

The typical association timescale increases with polymer length (insert in Fig.7.4b). For polymer desorption, the energy barrier for desorption scales with the number of binding sites, which increases approximately as the radius of gyration of the

polymer. We also find that τ_a decreases with the length of the alkyl tails (insert Fig.7.4a). We attribute this to the fact that longer alkyl tails give a stronger driving force for micelle formation [13], hence the micelles will be less deformed at the surface. This leads to a reduction of the number of segments per chains that are adsorbed onto the surface. As a result desorption will be faster for adsorbed layers formed from telechelic polymers with longer alkyl tails. Note that in bulk the relaxation time is an increasing function of alkyl length [12].

The total number of bridges formed at very long contact times, represented by $F_{m,\infty}$, is found to decrease with polymer length and to increase with alkyl tail length. This is thought to be caused by changes in the surface coverage. Larger alkyl tails and shorter polymer backbones, give larger micellar aggregation numbers [13], leading to increasing number of chains adsorbed per unit area.

Upon increasing the separation between the surfaces (retract phase) the bridges that are present will be disrupted. To describe this process, we assume that the dissociation of bridges is a first-order reaction and that pulling on the chains enhances dissociation. Assuming that bridge disruption is an activated process, the dissociation rate is expected to increase exponentially with the pulling force f_b :

$$\frac{\partial n_b}{\partial t} = -k_d n_b = -k_{d,0} n_b \exp\left(\frac{f_b \delta}{k_B T}\right) \quad (7.2)$$

where $k_{d,0}$ is the rate constant when there is no force on the polymers and δ is the length over which the force acts (here the length of the alkyl tails). For the force per bridge we use a Gaussian spring approach: $f_b = 3vt k_B T / N l_K^2$, where $h = vt$ and N is the number of statistical segments in the chain with Kuhn-length l_K . The total force $F = f_b n_b$ can then be calculated as a function of the distance h :

$$F = \frac{3k_B T h n_{b,0}}{N l_K^2} \exp\left[\frac{k_{d,0} N l_K^2}{3v\delta} \left(1 - \exp\left(\frac{3\delta h}{N l_K^2}\right)\right)\right] \quad (7.3)$$

where $n_{b,0}$ is the number of bridges at the beginning of the retraction. This result implies that the curves shown in Fig.7.3 all have the same shape and differ only in $n_{b,0}$. Upon rescaling the curves with F_m , which is directly proportional to $n_{b,0}$, we can collapse all curves measured at a given v for various t_s , as shown in the insert in Fig.7.5b for one data set.

To compare Eqn.7.3 with our experiments, we enter realistic parameters in our model for the Kuhn-length of PEO ($l_K = 0.9$ nm [14]), the number of statistical segments ($N = 225$ for PEO20k) and the alkyl contour length ($\delta \approx 2$ nm, for C₁₆H₃₃). To describe our data, we have now 2 remaining parameters, i.e. $n_{b,0}$ and $k_{d,0}$. In Fig.7.5a we see that the model describes the experimental data very well.

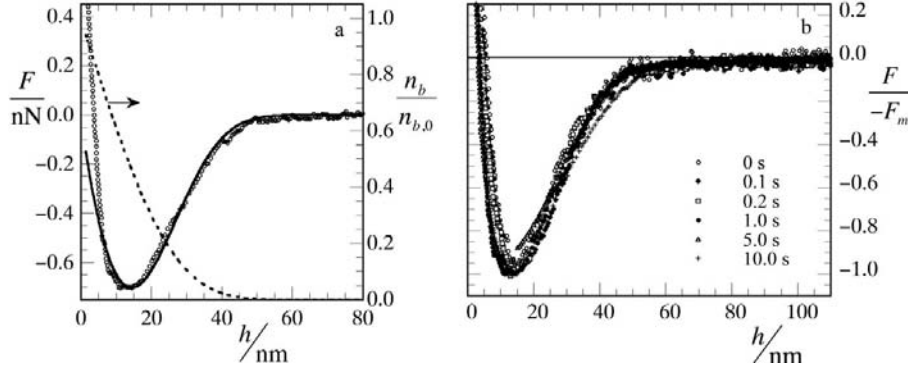


Figure 7.5: a) Comparison between the model (drawn line, Eqn.7.3) and experimental data (\circ , as in Fig.7.3a for $t_s = 1$ s). Fixed model parameters: $N = 225$, $l_K = 0.9$ nm, $\delta = 2$ nm and $v = 500$ nm/s. Fitted parameters: $n_B = 1600$ and $k_{d,0} = 20.1$ s $^{-1}$. Dotted line shows the corresponding change in the number of bridges $n_b/n_{b,0}$. b) Same data as in Fig.7.3a, with the force F scaled to the maximum attractive force F_m , collapsing $F(h)$ for various t_s onto a single curve.

For this example, i.e. a C16-20k polymer and $t_s = 1$ s, we find $n_{b,0} = 1600$ and $k_{d,0} = 20$ s $^{-1}$.

During the retract stage the force per bridge increases, while the number of bridges decreases (dotted line in Fig.7.5a), giving rise to the minimum in the force. Note that in the measurements, a short-ranged repulsive force is present, as discussed above, which is not accounted for in the model. This explains the deviations between experiment and model for short distances. We also assumed that all chains are elongated by the same amount; this is an approximation since the bead surface is curved.

We can estimate the total number of polymer chains between the interacting surfaces by assuming that bridges can only form in the region where the separation is < 25 nm (i.e. $< 5R_g$). The surface area of a spherical cap, with base radius $3\mu\text{m}$ and height 25 nm, is approximately $0.5\mu\text{m}^2$. From optical reflectometry measurements, we find an adsorbed amount of 1.8 mg/m^2 . Combining these numbers leads to a estimated total of 10^4 polymer chains in the area of interaction. For a contact time of $t_s = 1$ s, we found that 1600 bridges had been formed, which is roughly $\frac{1}{5}$ of the total number of polymer chains.

From Fig.7.3 it can be seen that the range of the bridging attraction is larger for C₁₈-modified polymers than for those with C₁₆ tails. The reason for this is that longer alkyl tails dissociate more slowly from the micelles than do short ones

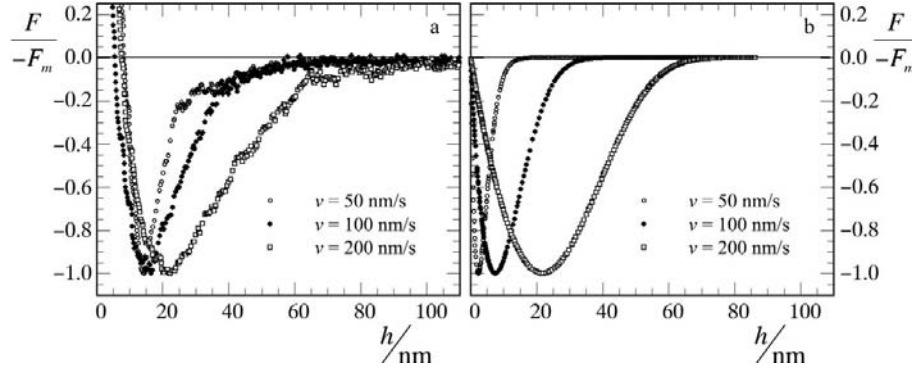


Figure 7.6: a) Effect of retract velocity v on the force-distance profile, for C16-20k and $t_s = 0$, b) shows the corresponding prediction of our model (Eqn.7.3), with the same parameters as in Fig.7.5.

($k_{d,0}$ is smaller and δ is larger), so that the chains can be stretched further before the bridges are disrupted. Similarly, the range is longer for polymers with a longer PEO spacer, because longer chains can be stretched further (data not shown).

The characteristic disruption timescale for the polymer in the example (C16-20k, Fig.7.5), $\tau_{d,0} = 1/k_{d,0} \approx 0.05$ s, whereas the timescale for association τ_a for the same polymer is 11.5 s. In bulk solution, the relaxation times for these processes are around 1 ms, again showing the large retardation of the polymers near solid surfaces. There clearly is an asymmetry between the timescales for bridge formation and disruption. Two reasons for this asymmetry come to mind. First of all, formation of the bridges takes place in a compressed configuration, leading to a high density of polymers in the gap between the surfaces that slows down the chain dynamics. Secondly, it is not hard to imagine that a loop-configuration of the chain allows more segments to adsorb onto the surfaces than a bridge conformation, that in principle is directed normal to the surfaces. This also causes the kinetics of bridge disruption to be faster than that of bridge formation.

In colloidal systems, the velocity with which particles move is governed by their size and the viscosity of the surrounding medium. The relative velocity between two particles can therefore vary over many decades. We see that the separation velocity has a strong influence on the shape of the bridging attraction force (Fig.7.6a). When the separation velocity is increased, the position of the maximum attraction shifts to larger separations and the overall range of the bridging force increases. Both features are also predicted by our model (Eqn.7.3), as shown in Fig.7.6b.

7.4 Conclusion

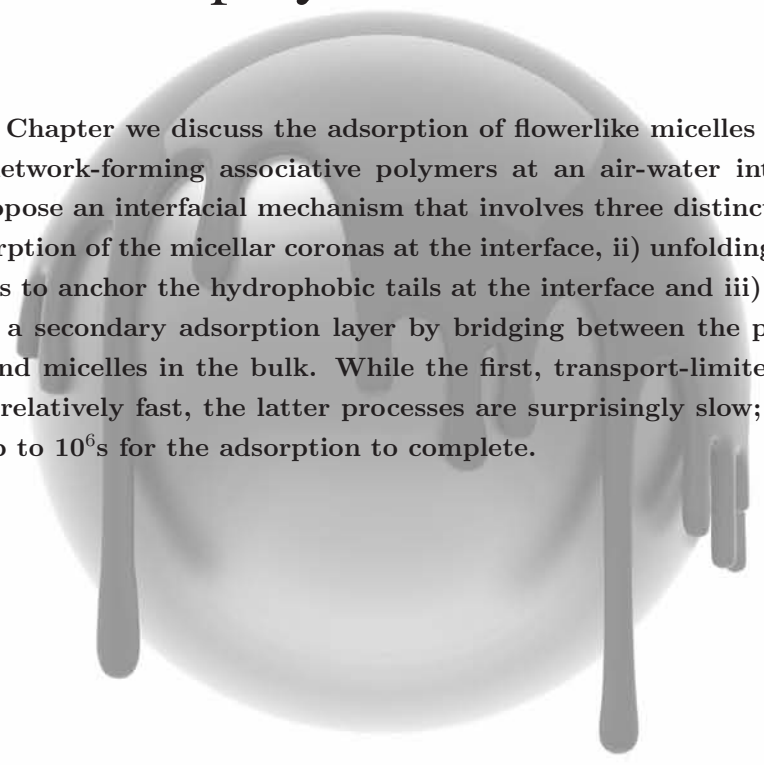
We conclude that the dynamics of polymer bridging can be understood with first-order association/dissociation reactions. Bridge formation is governed by a distribution of rate constants, while the disruption rate is increased by pulling the surfaces apart. The slow time constants for these processes indicate that these kinetic considerations are important for understanding the effect of polymer bridging on the interactions between 'real' colloidal particles. Modeling the dynamics of these systems with a simple argument based on activated sticker extraction is a very versatile strategy. In Chapter 10, we have shown that it can also predict the non-linear shear rheology of macroscopic networks of the same polymers.

References

- [1] Fleer, G. J.; Cohen Stuart, M. A.; Scheutjens, J. M. H. M.; Cosgrove, T.; Vincent, B. *Polymers at Interfaces*; Chapman and Hall (London), 1993.
- [2] Wijting, W. K.; Knoben, W.; Besseling, N. A. M.; Leermakers, F. A. M.; Cohen Stuart, M. A. *Phys. Chem. Chem. Phys.* **2004**, *6*, 4432.
- [3] Giesbers, M.; Kleijn, J. M.; Fleer, G. J.; Cohen Stuart, M. A. *J. Colloid Interface Sci.* **1998**, *142*, 343.
- [4] Cohen-Tannoudji, L.; Bertrand, E.; Bressy, L.; Goubalt, C.; Baudry, J.; Klein, J.; Joanny, J. F.; Bibette, J. *Phys. Rev. Lett.* **2005**, *94*, 038301.
- [5] Milner, S. T.; Witten, T. A. *Macromolecules* **1992**, *25*, 5495.
- [6] Sukhishvili, S.; Chem, Y.; Muller, J. D.; Gratton, E.; Schweizer, K. S.; Granick, S. *Macromolecules* **2002**, *35*, 1776.
- [7] Ducker, W. A.; Senden, T. J.; Pashley, R. M. *Nature* **1991**, *353*, 239.
- [8] Hutter, J. L.; Bechhoefer, J. *Rev. Sci. Instrum.* **1993**, *64*, 1868.
- [9] Sprakel, J.; van der Gucht, J.; Cohen Stuart, M. A.; Besseling, N. A. M. *Phys. Rev. Letters* **2007**, *99*, 208301.
- [10] Postmus, B. R.; Leermakers, F. A. M.; Koopal, L. K.; Cohen Stuart, M. A. *Langmuir* **2007**, *23*, 5532.
- [11] Ligoure, C. *Macromolecules* **1991**, *24*, 2968.
- [12] Berret, J. F.; Calvet, D.; Collet, A.; Viguier, M. *Curr. Opin. Colloid Interface Sci.* **2003**, *8*, 296.
- [13] Sprakel, J.; Besseling, N. A. M.; Leermakers, F. A. M.; Cohen Stuart, M. A. *J. Phys. Chem. B* **2007**, *111*, 2903.
- [14] Kawaguchi, S.; Imai, G.; Suzuki, J.; Miyahara, A.; Kitano, T. *Polymer* **1997**, *38*, 2885.

Chapter 8

Hierarchical adsorption of associative polymers



In this Chapter we discuss the adsorption of flowerlike micelles formed from network-forming associative polymers at an air-water interface. We propose an interfacial mechanism that involves three distinct steps; i) adsorption of the micellar coronas at the interface, ii) unfolding of the micelles to anchor the hydrophobic tails at the interface and iii) formation of a secondary adsorption layer by bridging between the primary layer and micelles in the bulk. While the first, transport-limited, process is relatively fast, the latter processes are surprisingly slow; it may take up to 10^6 s for the adsorption to complete.

This chapter is published as:

J. Sprakel: *Hierarchical adsorption of network-forming associative polymers*, *Langmuir in press* **2009**.

8.1 Introduction

Hierarchical self-assembly is a versatile route to create large structures from small building blocks. Nature has developed numerous routes to exploit soft and tunable interactions for the creation of superstructures. One might think of the subsequent assembly of actin and crosslinker proteins into filaments, bundles and networks [1] and the assembly of caseins into supermicelles [2]. Through the development of block copolymers of widely varying architecture, these routes are now also actively pursued with synthetic building blocks.

A well-studied class of polymers that shows such hierarchical self-assembly is that of telechelic associative polymers. These macromolecules, consisting of a water-soluble middle block (the spacer) and associating, hydrophobic stickers at both chain ends, spontaneously assemble into so-called flowerlike micelles, where the spacer loops in the micellar corona. These micelles subsequently connect through intermicellar bridges, leading to the formation of sample-spanning transient networks [3]. The formation of flowerlike micelles occurs only above a critical micelle concentration (see Chapter 3). A similar threshold concentration can be identified for the formation of bridges between the micelles that ultimately drives the network formation (Chapter 4).

In this Chapter we demonstrate that an air-water interface can trigger a secondary assembly process, while there are only isolated micelles in the bulk solution. By means of drop shape tensiometry we study the kinetics of adsorption of flowerlike micelles, their unfolding at the air-water interface and the subsequent formation of bridges between the adsorbed layer and micelles in the bulk. Interestingly, the latter two processes are very slow.

Networks formed from telechelic associative polymers are widely used as rheology modifiers in, e.g., paints and cosmetics. In many of these applications, the polymer networks are filled with colloidal particles (e.g., the latex and pigment particles in a paint). For this reason, many experimental studies have set out to understand the interactions between associative polymers and surfaces [4], and the effects of these polymers on the interactions between colloids (see [5] and Chapters 5 and 7). The results presented in this Chapter, especially the extremely long times needed to reach a full adsorption equilibrium, shed new light on the observations reported so far.

8.2 Experimental

The polymers under study are polyethylene oxide (PEO) chains of 4, 10 and 20 kg/mol (Fluka), to which tetradecyl ($C_{14}H_{29}$) tails have been covalently attached by means of a urethane linker (see Chapter 10 for the synthesis procedure). Samples are coded based on the molecular weight of the PEO spacer, e.g., $C_{14}20k$ corresponds to the tetradecyl-modified PEO of 20 kg/mol. Solutions of these polymers are made in MilliQ water. DLS measurements confirm the presence of micelles in the solutions used here, with hydrodynamic radii of approximately 7-10 nm.

Adsorption is studied by means of tensiometry on an automated drop tensiometer (ITConcept), at 25 °C. In this technique the shape of an air bubble, suspended at the tip of a flat-ended needle in the solution of interest, is analyzed to yield the interfacial tension. The droplet shape is a balance between buoyancy and interfacial tension forces so that the interfacial tension can be extracted when the density difference between the two phases is known [6]. The optical cells, syringes and needles are thoroughly cleaned in a plasma cleaner (Harrick) to remove any traces of unwanted surface active compounds. The optical cell was covered with parafilm after insertion of the needle, to prevent evaporation during the measurements.

The main advantage of this technique for the present study is that it has a stable signal, i.e. no baseline drift, over long times, seen from the constant interfacial tension of pure water over more than $2 \cdot 10^5$ s (approximately 2.5 days) (Fig.8.1a). This allows us to perform long adsorption measurements, revealing very slow adsorption processes.

8.3 Results and Discussion

In Fig.8.1a we see that the adsorption of the telechelic associative polymers occurs in 3 distinct steps, indicating three consecutive processes that lead to the interfacial tension decrease. We can describe the decrease of the interfacial tension in time with a triple exponential function:

$$\gamma(t) = \gamma_0 - \sum_{i=1}^3 \Delta\Pi_i \left(1 - \exp \left[-\frac{t}{\tau_i} \right] \right) \quad (8.1)$$

where γ_0 is the interfacial tension of the pure air-water interface (72 mN/m), τ_i is the characteristic relaxation time of step $i=1, 2$ or 3 , and $\Delta\Pi_i$ the corresponding surface pressure increase. These parameters are also illustrated in Fig.8.1b. The surface pressure is defined as $\Pi = \gamma_0 - \gamma$. In Fig.8.1b we see that such a triple

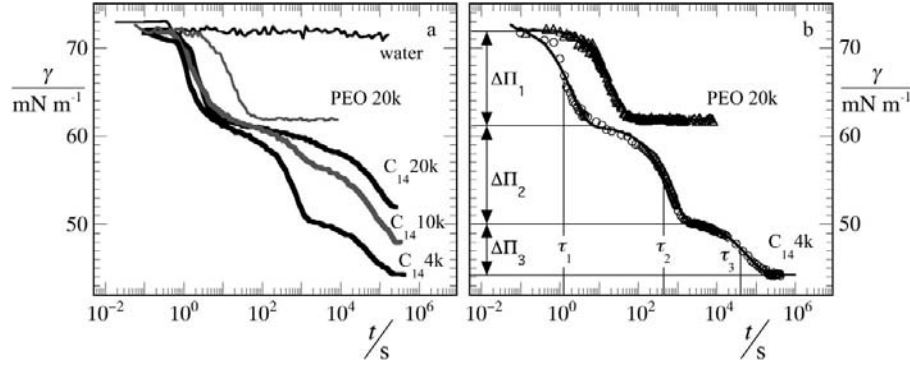


Figure 8.1: a) Interfacial tension γ versus time t of a newly formed interface between air and i) water, ii) an aqueous solution of PEO (20 kg/mol at 10 mg/mL) and iii) aqueous solutions of tetradecyl end-capped PEO of varying molecular weight (20, 10 and 4 kg/mol at 20 mg/mL). b) Two data sets from a) fitted (drawn lines) with a single exponential for unmodified PEO of 20 kg/mol, and a triple exponential (Eqn.8.1) for telechelic C_{14} 20k. Illustrated are the three relaxation times τ_1 , τ_2 and τ_3 and corresponding surface pressure differences $\Delta\Pi_1$, $\Delta\Pi_2$ and $\Delta\Pi_3$ for the three stages of telechelic polymer adsorption.

exponential function describes the measured decrease in interfacial tension very well.

The adsorption of unmodified PEO homopolymer (see Fig.8.1a) shows a single decay and reaches a steady plateau relatively fast. The adsorption of polymeric surfactants with a single associating group, which are able to form micelles but can not form bridges, shows 2 distinct stages before reaching a steady plateau, as for example discussed in [7]. The 3rd adsorption stage that we observe for the telechelic polymers, is a new feature likely to be related to the bridge-forming nature of these bifunctional polymers. We will now take a closer look at these three processes separately.

8.3.1 1st stage

Starting from a pristine interface (Fig.8.2a), material needs to be transported towards and along the interface, in order to accomplish an fully covered interface. In these experiments, with no active flow, transport is necessarily diffusive. Mohrbach [8] describes two possibilities for the initial kinetics of diffusive adsorption from a micellar solution. When the transport kinetics in the bulk towards the interface is rate limiting, the adsorbed amount Γ increases with $t^{1/2}$, this case is known as diffusion-limited adsorption (DLA). In the first stage of adsorption, where the

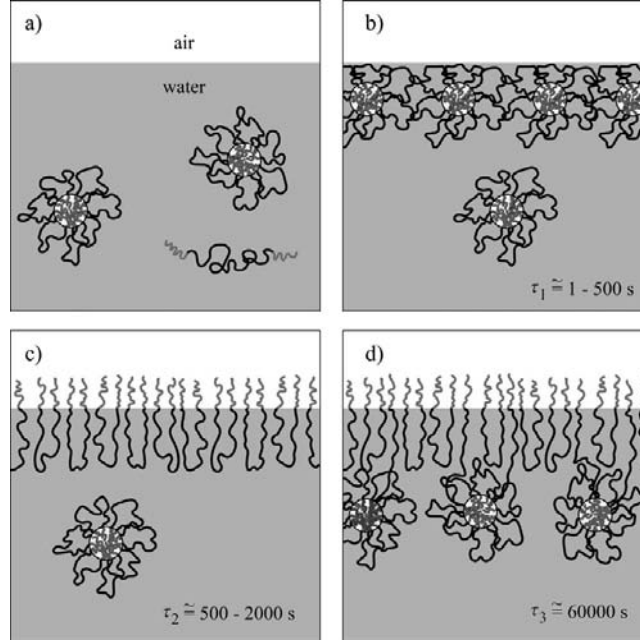


Figure 8.2: Illustration of the three stages of telechelic polymer adsorption in time. Starting from a clean, newly formed interface in a solution of flowerlike micelles (a), micelles diffuse towards the surface and adsorb with their corona chains (step 1, b). Once the micelles have attached to the surface, they unfold to expose the alkyl tails in the micellar core to the air-water interface (step 2, c). Finally, the telechelic polymers in the adsorbed layer form bridges with micelles in the bulk phase, giving rise to a secondary adsorbed layer (step 3, d).

adsorbed layer is still dilute, we can expect the surface pressure to increase proportional to Γ . For DLA the decrease of the surface tension is thus expected to follow $\gamma(t) \propto t^{-1/2}$ [9].

When, on the other hand, the kinetics at and near the interface are rate determining, the adsorbed amount, and thus the surface pressure, approaches its limiting value exponentially. This is known as kinetically-limited adsorption (KLA). As is shown in Fig.8.3a, we find a clear exponential decay of the interfacial tension in time, indicative of KLA.

For both transport-limited regimes (DLA and KLA) of micellar adsorption, it is predicted that the characteristic relaxation time τ_1 scales with polymer bulk concentration as $\tau_1 \propto c^{-2}$ [8]. In Fig.8.3a, we clearly see the effect of polymer concentration on the kinetics of the initial adsorption mechanism. Indeed, the

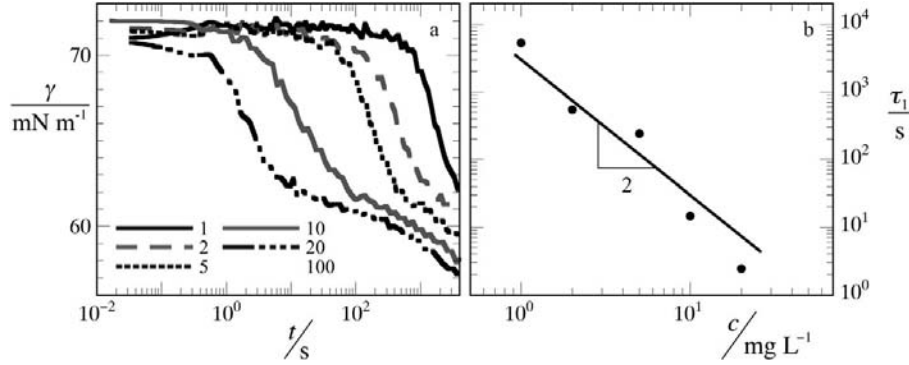


Figure 8.3: a) Kinetics of the first adsorption stage as a function of the polymer bulk concentration c (given in mg/L) for aqueous solutions of a C_{14}k telechelic associative polymer. b) Corresponding relaxation time τ_1 of the first adsorption stage, determined by fitting $\gamma(t)$ to Eqn.8.1. Drawn line corresponds to $\tau_1 \propto c^{-2}$, as expected for kinetically-limited adsorption (KLA).

characteristic relaxation time τ_1 scales with c^{-2} (Fig.8.3b).

The surface pressure reached during this first stage is around 12 mN/m (Fig.8.4), corresponding to the surface pressure of a fully covered PEO layer at the air-water interface (see Fig.8.1). This indicates that during this first stage, micelles adsorb onto the interface with their PEO coronas (Fig.8.2b) until the interface is fully saturated with EO segments. The limiting surface pressure reached after the first stage does not depend on the polymer bulk concentration as polymers generally have a very high affinity adsorption isotherm. Moreover, the surface pressure during this step is independent of the chain length of the PEO spacer in the telechelic polymers. This corresponds to what is found for homopolymer adsorption, and is explained as the formation of a 'semi-dilute' surface layer whose compressibility no longer depends on the chain length of the original polymers but only on the mesh ('blob') size of the network of interpenetrating coils [10]. Apparently, for this first stage of the adsorption process, it does not matter that the PEO chain is part of a micelle, as we find the same behavior as is found for PEO homopolymer adsorption.

8.3.2 2nd stage

The second adsorption stage, also found for polymeric surfactants with only one associating end-block [7], can be attributed to reorganizations of the adsorption layer. The micelles 'unfold' in order to expose their alkyl tails to the air (Fig.8.2c), allowing more material to be adsorbed onto the interface and further decreasing

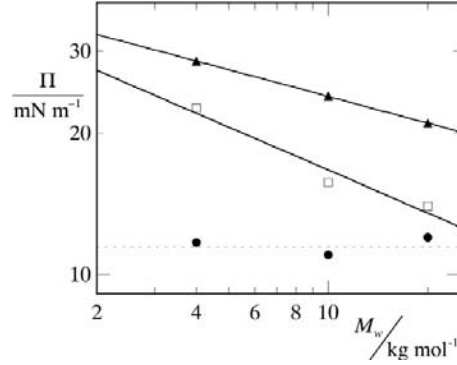


Figure 8.4: Surface pressure versus molecular weight of the telechelic polymer (all for 20 mg/L), after the first ($\Delta\Pi_1$, ●), the second ($\Delta\Pi_1 + \Delta\Pi_2$, □) and the third and final ($\Delta\Pi_1 + \Delta\Pi_2 + \Delta\Pi_3$, ▲) adsorption stage. Drawn lines are power-law fits and the dotted horizontal line is to guide the eye.

the interfacial tension.

The 'plateau' value of the surface pressure after the second step, i.e. $\Delta\Pi_1 + \Delta\Pi_2$, decreases with the chain length M_w of the polymers (Fig.8.4). The adsorption into a brush-like layer is, in first order, a balance between the adsorption energy, determined by the alkyl tails, and the stretching energy in the spacers. Since the alkyl tails for these polymers are the same, we can assume that the total stretching energy per chain is also the same for all these polymers. The surface pressure can be estimated by counting the number of stretching blobs, i.e. chain units for which the stretching energy is $1 k_B T$, per unit area. As the stretching energy per chain is the same, the differences in surface pressure between the various polymers are proportional to the differences in the number of adsorbed chains per unit area $\sigma \propto \Pi$. In the brush model of Milner, Witten and Cates, the stretching energy per chain scales as $F_s \propto M_w \sigma^{2/3}$ [11]. As F_s is the same for the different polymers, we can deduce that $\sigma \propto \Pi \propto M_w^{-3/2}$. This argument is only valid for end-adsorbed chains, i.e. when the alkyl tails adsorb and the PEO spacer does not. In the opposite case, where only the PEO spacers adsorb and the alkyl tails do not, the surface pressure does not depend on the molecular weight of the polymer, as we have seen above. Here we find (Fig.8.4) that $(\Delta\Pi_1 + \Delta\Pi_2) \propto M_w^{-0.5}$. Apparently, the adsorbed layer after the second adsorption step is a mix between adsorbed alkyl tails and remaining PEO segments. It is possible that, rather than a homogeneous brush layer as sketched in Fig.8.2c, a inhomogeneous layer of hemimicelles is formed, due to the highly asymmetric shape of the polymers. A similar scaling of the surface

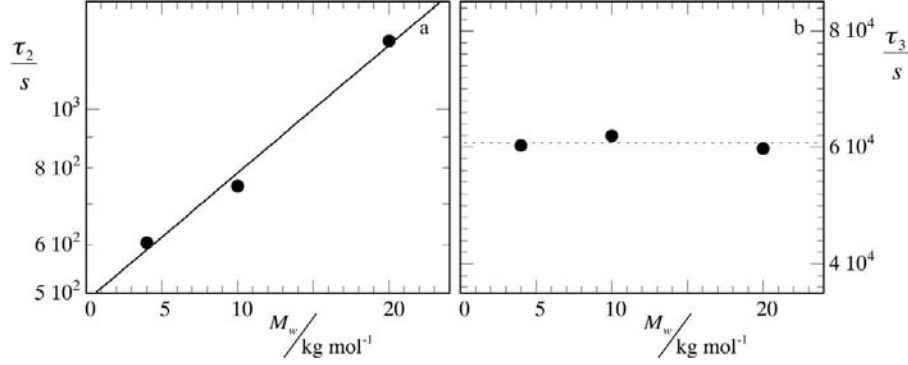


Figure 8.5: Molar mass dependence of the characteristic time scales τ_2 (a) and τ_3 (b) for the second and third adsorption stage, respectively, obtained by fitting the data shown in Fig.8.1a with Eqn.8.1. Drawn line in a) illustrates $\tau_2 \propto \exp(M_w)$, dotted line in b) is to guide the eye.

pressure of a brush-like layer of telechelics with the length of the spacer is reported in [4].

This stage is also characterized by an exponentially decaying interfacial tension, with which a relaxation time τ_2 can be associated. In Fig.8.5a we see that this relaxation time, between 600 and 2000 seconds, increases exponentially with the length of the PEO spacer.

A likely explanation for this exponential relation is that the dynamics are governed by an energy barrier (E_A) between the initial micellar configuration (Fig. 8.2b) after the first adsorption step and the end-adsorbed configuration (Fig.8.2c) towards which the layer is transitioning. For a process with first-order kinetics, the typical timescale follows $\tau_2 \propto \exp(E_A/k_B T)$. For the exposure of the alkyl tails to the air-water interface, the micellar corona that is in between the core and the interface, needs to be removed from the interface. An estimation for the free energy barrier associated with this process is ΠA , with A the area of the part of the layer that needs to be removed. The pressure Π in the layer of adsorbed corona chains is independent of chain length, as shown above. The area of the PEO layer that needs to be removed for a micellar core to reach the interface is approximately the cross section of the micelle, which is linear in M_w (Chapter 2). This reasoning thus predicts $\tau_2 \propto \exp(M_w)$, corresponding to our observations in Fig.8.5.

8.3.3 3rd stage

The third, and final, stage of the adsorption process is not found for either homopolymers or monofunctional polymeric surfactants. This suggests that this step is related to the fact that these telechelic polymers can form bridges between the adsorbed brush-like layer and micelles in the bulk. The further decrease of the interfacial tension during this stage indicates that additional material is collected at the interfacial layer. We propose that this step reflects the creation of bridges between the primary layer and free micelles in the bulk solution, leading to a secondary layer of weakly-bound micelles below the primary adsorbed layer (Fig.8.2d).

In bulk, bridging between micelles assembled from telechelic polymers is purely driven by entropy. For an isolated micelle, both chain ends must reside in the same micellar core and the flexible linker is forced to form a loop. When two of these micelles are close enough, the chains can now choose to form either a loop or a bridge, for which both chain ends reside in different cores. For symmetry reasons, there is no free energy difference between the bridge and the loop configuration. This gives an entropic attraction between micelles of $\ln 2 = 0.7 k_B T$ per bridge and a total attraction that is proportional to the aggregation number (Chapter 4).

In the bulk, no clustering was found for the polymer solutions used here. The fact that clustering does seem to occur at the interface in this third adsorption stage, suggests that the attractive potential between a bulk micelle and surface layer is significantly larger than that between two bulk micelles, which is probably due to the higher local concentration of chains near the interface.

To verify this hypothesis, we have carried out some calculations using the self-consistent field theory of Scheutjens and Fleer [12, 13, 14]. In Chapters 3 and 4 we used the same numerical method to study the self-assembly of telechelic polymers in bulk systems. For the calculations here, polymer chains are placed on a two-gradient cylindrical lattice (see Fig.8.6), that is divided into isometric lattice sites with discretization length b . Inhomogeneities in density are only allowed in the radial (x-) direction and along the length of the cylinder (y-direction). As a result, all properties of the system are rotationally symmetric around the axis of the cylinder. Here we define three segment types: S, a monomeric solvent, segments A, representing the insoluble (hydrophobic) tail segments and species B, for the segments of the soluble (PEO) backbone. The system is fully incompressible, i.e. all lattice sites must be filled with one of the segments species. The $A_{14}B_{100}A_{14}$ telechelic polymer in these calculations mimics the $C_{14}10k$ polymer used in the experiments, which consists of a water-soluble PEO chain of approximately 100 statistical segments [15], capped on both ends with an alkyl tail of 14 carbon atoms. The calculations

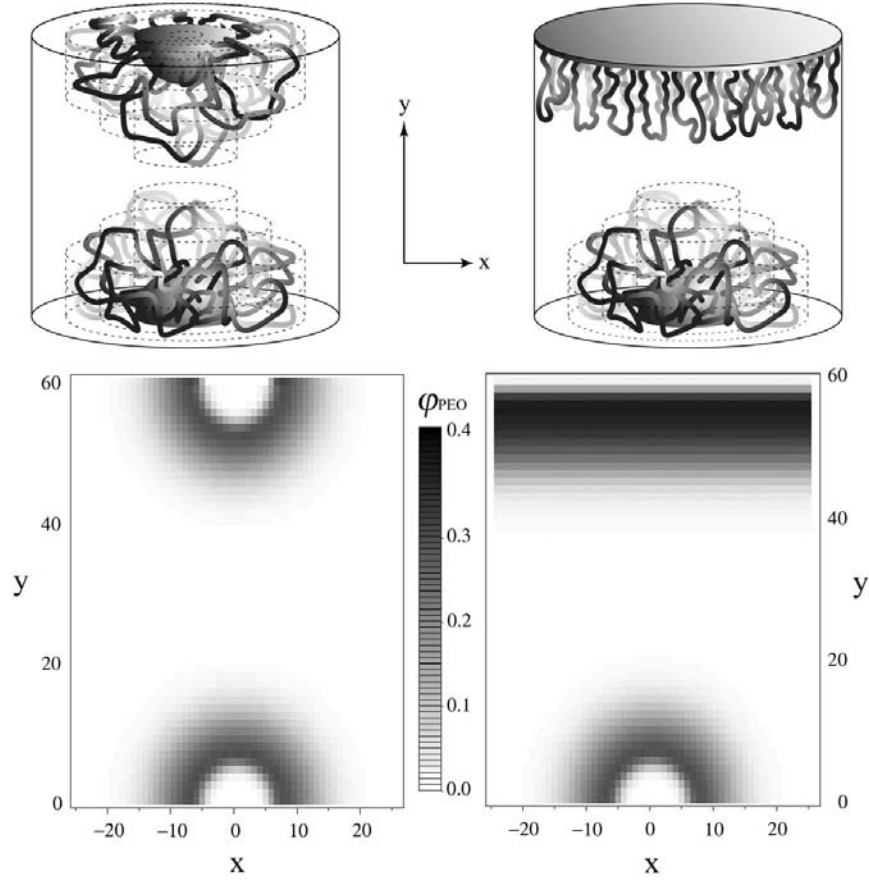


Figure 8.6: Top: illustration of the two scenarios in the SCF calculations on a 2-gradient cylindrical lattice, i.e. micelle-micelle (left) and micelle-adsorbed layer (right) interaction. Bottom: corresponding density profiles (at a separation of $h = 60b$) as obtained from the SCF calculations for the 2 scenarios, showing the volume fraction ϕ_{PEO} of the soluble polymeric backbone in a cross-section of the lattice (x and y in units b). The surface is located at $y = 60$ in the left image. The pixelated appearance of these density profiles is due to the discretization the SCF approach.

are carried out in a grand canonical ensemble (μ, V, T constant), for which the characteristic thermodynamic potential is the grand potential. All results correspond to thermodynamic equilibrium. The dynamics of the self-assembly process are not accessible.

Interactions between the segments are accounted for, on a nearest-neighbor level, with a Flory-Huggins interaction energy that is parameterized by the inter-

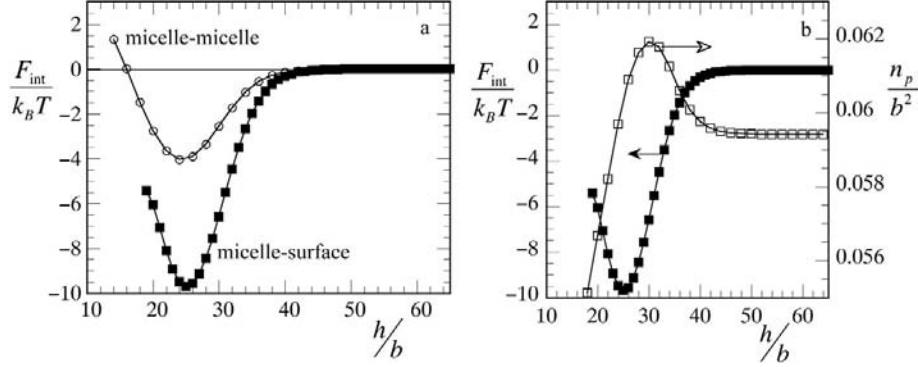


Figure 8.7: a) Free energy of interaction F_{int} versus separation distance h between two micelles in bulk (\circ) and between a bulk micelle and an adsorbed layer of telechelic polymers (\blacksquare). b) $F_{int}(h)$ between a bulk micelle and the surface layer as in a) (\blacksquare) and corresponding response of the adsorbed amount in the primary surface layer (\square) given as the number of polymer chains n_p per unit area.

action parameters χ_{ij} between any pair of unlike segments in the system. Here we use the same parameters as defined in Chapter 4, i.e. $\chi_{AS} = 1.9$ (strong segregation of the tails with the solvent), $\chi_{BS} = 0.5$ (theta conditions for the backbone) and $\chi_{AB} = 1$ (insolubility of the PEO chain in the hydrocarbon micellar core). For the calculations with the adsorbed layer, an adsorption energy $\chi_{ads} = -2$ was set between the A-segments and the surface (placed at the upper boundary of the cylindrical lattice), giving a homogeneous layer of end-adsorbed polymers, and an adsorbed amount that is equivalent to approximately 1 mg/m^2 .

We considered two situations: the pair interaction between two bulk micelles and the interaction between a bulk micelle and a layer of telechelic polymers adsorbed onto a hydrophobic surface. A cross-section of the density profile (of the PEO chains) for both configurations is shown in Fig.8.6, together with an illustration of these scenarios.

The resulting free energy of interaction F_{int} , as a function of the separation distance h between the two micelles, or between the micelle and the surface, is shown in Fig.8.7a. Indeed we observe that already for moderate adsorbed amounts, the attractive potential between a bulk micelle and an adsorbed layer is significantly, i.e. several $k_B T$, larger than that between two identical micelles. This explains the interface-triggered clustering observed in our experiments, while clustering is absent in the bulk.

The kinetics of the interfacial bridging process is remarkably slow; irrespective

of the chain length of the PEO spacer we find $\tau_3 \approx 6 \cdot 10^4$ s. In bulk networks of these polymers, where each micelle is surrounded by many others, the kinetics of the bridging process is governed by the energy barrier of transferring a hydrophobic sticker from one micellar core to another through the aqueous phase, leading to relaxation times of order 1 millisecond [16]. Note that this relaxation time is also relatively insensitive to the length of the spacer.

Clearly, the situation is very different for the interfacial bridging process as it is more than 10^7 times slower. The main difference between these two cases is in finding a micellar core once a sticker has escaped from its original position. In a bulk network, micelles are in close contact, and finding a neighboring micelle is thus not rate limiting. The polymer concentration in the present study (20 mg/mL for the data in Fig.8.5b) is a factor 1000 lower than a typical concentration where these polymers form networks (≈ 20 g/L). This significantly decreases the probability that an escaped sticker finds a micelle with which it can form a bridge. Forming a bridge thus requires the *simultaneous* release of a sticker from the interface and the nearness of a bulk micelle. This could explain the extremely slow kinetics observed here. Moreover, the crowding at the interface might also slow down the sticker escape.

Since both the sticker length, determining the escape frequency, and the polymer concentration, determining the probability that an escaped sticker finds a micelle to bridge with, are equal for the cases investigated here, we should not see any big difference in τ_3 with changes in spacer length, which is the case as shown in Fig.8.5b. Investigating these effects in more detail is subject for future study.

A weakly bound layer of micelles will not cause large changes in the surface pressure, as this dilute second layer is highly compressible. Nevertheless, we observe a further increase in surface pressure ($\Delta\Pi_3$) during this third stage of 6 - 8 mN/m (Fig.8.4). The formation of bridges releases some of the stretching energy in the primary adsorbed layer, so that new chains can be added to the primary layer in order to restore the balance between adsorption energy and stretching energy. The adsorbed amount increases only slightly due to bridging (Fig.8.7b), but as the adsorbed layer is already rather dense, small changes in the number of adsorbed chains per unit area, can have a relatively large effect on the compressibility of this layer.

8.4 Conclusions

In this Chapter we have shown that the adsorption of telechelic, network-forming, polymers can be very slow. In all of the experimental studies, including previous work of the present author, on the interactions between colloidal particles in solutions of these polymers (see Chapters 5 and 7 and, e.g., [5]) such long equilibration times have not been accomplished. When the adsorption of the PEO corona (i.e. our step 1) is the final state, expected, e.g., for hydrophilic silica surfaces that have a high affinity for PEO (Chapter 7), this is probably irrelevant. However, for those experiments on hydrophobic surfaces [5] and Chapter 5, the slow adsorption kinetics might have resulted in non-equilibrated surface layers. Therefore, special care should be taken that a true equilibrium is reached when working with adsorbed layers of polymeric micelles.

References

- [1] Bausch, A. R.; Kroy, K. *Nature Physics* **2006**, *2*, 231.
- [2] Noble, R. W.; Waugh, D. F. *J. Am. Chem. Soc.* **1965**, *87*, 2236.
- [3] Serero, Y.; Aznar, R.; Porte, G.; Berret, J. F.; Calvet, D.; Collet, A.; Viguier, M. *Phys. Rev. Letters* **1998**, *81*, 5584.
- [4] Barentin, C.; Muller, P.; Joanny, J. F. *Macromolecules* **1998**, *31*, 2198.
- [5] Courvoisier, A.; Isel, F.; Francois, J.; Maaloum, M. *Langmuir* **1998**, *14*, 3727.
- [6] Benjamins, J.; Cagna, A.; Lucassen-Reynders, E. H. *Colloids Surf. A* **1996**, *114*, 245.
- [7] Díez-Pascual, A. M.; Compostizo, A.; Crespo-Colín, A.; Rubio, R. G.; Miller, R. *J. Colloid Int. Sci.* **2007**, *307*, 398.
- [8] Mohrbach, H. *J. Chem. Phys.* **2005**, *123*, 126101.
- [9] Diamant, H.; Ariel, G.; Andelman, D. *Colloids Surf. A* **2001**, *183*, 259.
- [10] des Cloizeaux, J.; Jannink, G. *Polymers in Solution. Their modelling and structure.*; Oxford University Press, New York, 1991.
- [11] Milner, S. T.; Witten, T. A.; Cates, M. E. *Macromolecules* **1988**, *21*, 2610.
- [12] Scheutjens, J. M. H. M.; Fleer, G. J. *J. Phys. Chem.* **1979**, *83*, 1619.
- [13] Scheutjens, J. M. H. M.; Fleer, G. J. *J. Phys. Chem.* **1980**, *84*, 178.
- [14] Fleer, G. J.; Cohen Stuart, M. A.; Scheutjens, J. M. H. M.; Cosgrove, T.; Vincent, B. *Polymers at Interfaces*; Chapman and Hall (London), 1993.
- [15] Kawaguchi, S.; Imai, G.; Suzuki, J.; Miyahara, A.; Kitano, T. *Polymer* **1997**, *38*, 2885.

- [16] Annable, T.; Buscall, R.; Ettelaie, R.; Whittlestone, D. *J.Rheol.* **1993**, *37*, 695.

Part III

Rheology of Associative Polymer Networks



Chapter 9

Brownian particles in transient polymer networks

We discuss the thermal motion of colloidal particles in transient polymer networks. For particles that are physically bound to the surrounding chains, light scattering experiments reveal that the sub-millisecond dynamics changes from diffusive to Rouse-like upon crossing the network formation threshold. Particles that are not bound, do not show such a transition. The typical Rouse scaling of the MSD with the square root of time, as found in the experiments at short time scales, is explained by developing a bead-spring model of a large colloidal particle connected to several polymer chains. The resulting analytical expressions for the MSD of the colloidal particle are shown to be consistent with experimental findings.

This chapter was published as:

J. Sprakel, J. van der Gucht, M.A. Cohen Stuart and N.A.M. Besseling: *Brownian particles in transient polymer networks*, Phys. Rev. E 77 (2008), 061502 and as J. Sprakel, J. van der Gucht, M.A. Cohen Stuart and N.A.M. Besseling *Rouse dynamics of colloids bound to polymer networks*, Phys. Rev. Letters 99 (2007), 208301.

9.1 Introduction

Microrheology is a growing field of science, founded on the pioneering work of researchers such as Weitz and Mason [1, 2] and MacKintosh and Schmidt [3, 4]. In microrheology, the thermal motion of probe particles is interpreted in terms of the mechanical properties of the medium in which they are suspended. The motion of the particles can be quantified with a variety of techniques, such as diffusing wave spectroscopy [5], dynamic light scattering [6], and various microscopy-based techniques [7] often in combination with tools such as optical tweezers [8]. Besides the study of synthetic model systems, such as polymer solutions [9], associative polymer networks [10] and living polymer systems [6], the field has found connection with biology, in the numerous publications on biological materials such as actin networks [11], microtubule solutions [12] and membranes [13].

In order to relate measurements of particle dynamics to the macroscopic viscoelastic moduli, Mason and Weitz assumed that the Stokes drag for viscous fluids can be extended to describe the viscoelastic drag at all frequencies [1]. The generalized Stokes-Einstein relation that they proposed assumes furthermore that the medium is homogeneous around the particle and that it can be considered as a viscoelastic continuum. This seems justified if the particle radius R is much larger than the bulk correlation length ξ of the medium. Nevertheless, significant differences between bulk rheology and microrheology have been observed even for $R > \xi$ [10, 6]. It has been argued that such discrepancies could be related to depletion layers around the particles [14, 15, 16]. The occurrence of depletion should be very sensitive to specific interactions between the particles and the medium. In this Chapter we analyze in detail how such interactions affect the dynamics of colloidal particles embedded in transient polymer networks, in particular at short times.

Since Einstein's famous paper on Brownian motion [17], it is known that the mean square displacement $\langle \Delta r^2 \rangle$ of colloidal particles in purely viscous fluids increases linearly with time, the diffusion coefficient being the proportionality constant. The motion of colloids in viscoelastic media however, is more complex. Most types of motion show scaling behavior,

$$\langle \Delta r^2 \rangle \propto t^\alpha \tag{9.1}$$

For diffusion $\alpha = 1$. All dynamics for which the exponent α is smaller than unity, are denoted subdiffusive. According to the generalized Stokes-Einstein relation used in microrheology, such subdiffusive behavior can be related to the viscoelastic response of the medium at the corresponding frequencies [1]. For example, for particles in elastic media with $G^*(\omega) = G_0$, caging is observed ($\alpha = 0$), i.e. the

particles are restricted to displacements for which the elastic deformation energy of the surrounding matrix is smaller than the thermal energy $k_B T$, leading to a plateau in the mean square displacement [18]. Another example of subdiffusive behavior was observed for particles in solutions of F-actin, where $\alpha = 0.75$ is found at short times. This can be related to the $G^*(\omega) \propto \omega^{3/4}$ behavior predicted for semi-flexible polymers at high frequencies [11]. For beads covalently bound to microtubules, α was found to depend on the flexibility of the chains; 'relaxed' chains yield $\alpha = 0.8$, whereas pre-stretched, hence more rigid, microtubules gave significantly lower values of α [12]. Finally, subdiffusive behavior may also be caused by local structural inhomogeneities in the medium, unrelated to the bulk rheology. For example, particles in F-actin networks were seen to 'hop' between distinct pores in the network, giving $0 < \alpha < 1$ depending on the ratio R/ξ [19].

In this chapter we report evidence of a Rouse-like motion ($\alpha = \frac{1}{2}$) of colloidal particles that are physically bound to flexible polymer networks. We present a detailed analysis of this type of submillisecond dynamics of colloids in transient polymer networks. The experimental results are rationalized by constructing an analytical model for the motion of a large colloidal particle connected to a surrounding polymer network. We also discuss the motion of the probe particles at intermediate (milliseconds) and longer (seconds) time scales, and compare these to predictions based on the bulk rheological behavior of the solutions.

9.2 Experimental

9.2.1 Materials

Hydroxyl-terminated polyethylene oxide (PEO), with a nominal M_W of 35 kg/mol and $M_W/M_N = 1.2$, was used as purchased from Fluka. Part of it was converted into a telechelic associative polymer by attaching hexadecyl ($C_{16}H_{33}$) groups at the chain ends, as follows. The PEO was reacted in toluene with hexadecyl isocyanate (Sigma) in presence of DBTDL (Sigma), at 60°C for 12h. After 3 cycles of dissolution in toluene and precipitation in heptane, the polymer was further purified by dissolution in ethyl acetate, filtration over 0.2 μm syringe filters, evaporation of the solvent and drying. Critical chromatography indicated that approximately 85% of all chain ends have been modified with a hexadecyl tail, i.e. on average 1.7 hydrophobic groups are attached per chain.

Silica particles (Monospher M100, Merck) with a hydrodynamic radius of 70 nm are used either without further treatment (denoted plain silica particles), and after a pre-adsorption step with a high molecular weight PEO (referred to as PEO-

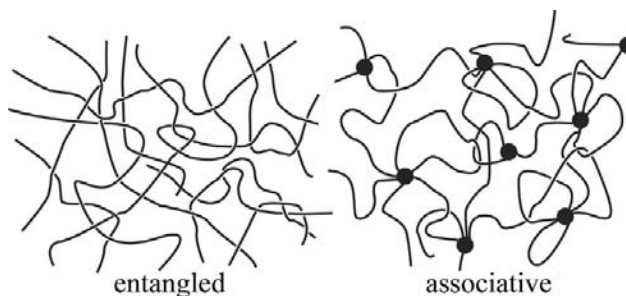


Figure 9.1: Schematic representation of the two types of networks that are discussed in this Chapter. On the left a solution of flexible polymers above the overlap concentration, in which the junction points are formed by entanglements. On the right a micellar, associative network of telechelic polymers. In these associative networks the junction points are formed by flowerlike micelles, that are interconnected by polymer bridges.

covered silica in the remainder of this Chapter). This treatment involved diluting the silica particles to a 1 wt% dispersion, adding 10 mg/L of polyethylene oxide (Polymer Source) with a molecular weight of 1000 kg/mol, and stirring for 72h. Highly monodisperse, charge stabilized core-shell latex particles ($R_h = 110\text{nm}$), polymerized from styrene and some acidic acrylate monomers, were kindly supplied by Akzo Nobel Coatings (Sassenheim, the Netherlands). The silica particles (plain and PEO-covered) are used at a volume fraction of 10^{-4} and the latex particles at a volume fraction of 10^{-5} , such that particle-particle interactions are negligible and multiple scattering is avoided.

The dynamic light scattering experiments are carried out on 3 different set-ups; 1) a home-built set-up equipped with a solid-state (DPSS) laser ($\lambda = 532\text{nm}$), a PMT detector and hardware correlator, with a fixed detection angle of 90° , 2) an ALV5000, equipped with an argon laser ($\lambda = 514.5\text{nm}$), ALV/SO-SIPD fiber detector mounted on a goniometer and a hardware correlator and 3) a Malvern Nano-S, with a He-Ne laser ($\lambda = 632.8\text{ nm}$), an avalanche photodetector at a detection angle of 173° . In all experiments the temperature was controlled at 20°C .

Rheological measurements are conducted on a Paar Physica MCR301 rheometer. The viscosity measurements are carried out in a couette (concentric cylinder) geometry, at shear rates well within the Newtonian regime of the corresponding system. The viscoelastic properties of the networks are characterized in oscillatory experiments, in a cone-plate set-up, with a cone diameter of 75 mm. In these experiments the frequency of deformation is varied, at a fixed strain of 0.1%, which

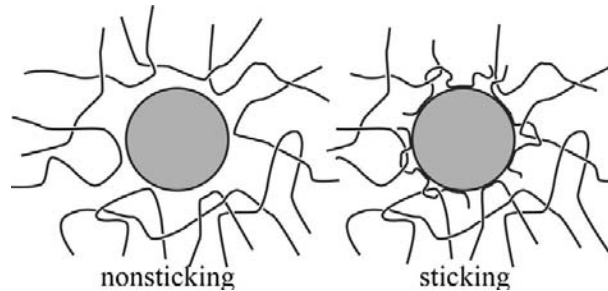


Figure 9.2: Schematic illustration of the two types of particle-network interactions. On the left the "nonstick" situation, in which no chains of the matrix adsorb onto the particle. This situation also applies when adsorbed chains are not entangled or associated with the matrix. On the right "sticking" between particle and matrix as a result of adsorption of polymer chains onto the particle surface. These adsorbed chains are connected to the transient network, either through entanglements or through associative interactions.

was checked to be in the linear regime. For both geometries the temperature was kept at 20 °C with integrated peltier elements.

9.2.2 Classification of systems

We study the motion of colloidal particles in two classes of transient polymer networks, see Fig.9.1. The first are entangled systems of flexible homopolymers. We use aqueous solutions of polyethylene oxide (PEO). The second class of networks are associative networks formed from the $C_{16}H_{33}$ -modified telechelic associative polymers described above. These types of polymers are known to form transient networks, in which the nodes are flowerlike micelles, interconnected by polymer bridges [20].

In this study we distinguish two types of particle-matrix interactions, as illustrated in Fig.9.2. i) Sticking particles; the polymer chains in the network can adsorb onto the particle surface. In this study we use plain silica particles; it is well-known that PEO strongly adsorbs onto silica surfaces [21]. ii) Nonsticking particles; when the polymer chains in the network cannot adsorb onto the particles surface. For the entangled polymer networks these are the latex particles, and in the associative networks these are the PEO-covered silica particles, in this case the high molecular weight PEO layer adsorbed onto the particles ensures that the chains in the network cannot adsorb [22]. The high molecular weight polymers that are adsorbed onto these particles can however participate in entanglements, that

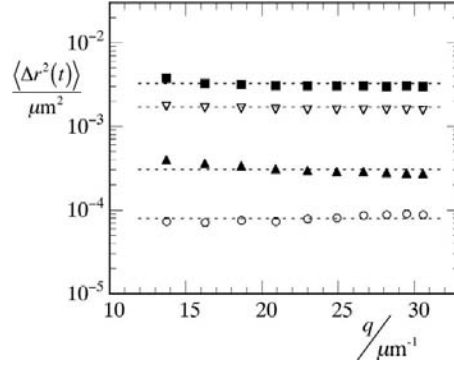


Figure 9.3: Angular dependence of the MSD of plain silica particles ($R_h = 70\text{nm}$) in a 80 g/L aqueous solution of PEO ($M_W = 35\text{kg/mol}$) at a given correlation time t . The angle of detection was varied between 50° and 140° and is expressed here as the scattering vector q . Shown are $t = 10^{-2}$ ms (\circ), $t = 10^{-1}$ ms (\blacktriangle), $t = 1$ ms (∇) and $t = 2$ ms (\blacksquare).

will also become important in the associative networks at higher concentrations.

9.2.3 Dynamic Light Scattering

The mean square displacement $\langle \Delta r^2 \rangle$ (MSD) of monodisperse spherical particles can be measured directly with Dynamic Light Scattering (DLS) [23]. The intensity correlation function $g^{(2)}(t)$ evaluates fluctuations in the intensity I of light scattered by the particles;

$$g^{(2)}(t) = \frac{\langle I(\tau)I(\tau+t) \rangle}{\langle I(\tau) \rangle^2} \quad (9.2)$$

From $g^{(2)}(t)$ one obtains the normalized field autocorrelation function $g^{(1)}(t)$ from

$$g^{(2)}(t) = 1 + A(g^{(1)}(t))^2 \quad (9.3)$$

where $0 < A \leq 1$ is an instrumental constant. Assuming Gaussian statistics, $g^{(1)}(t)$ gives direct access to the mean square displacement (MSD) of the particles using

$$\langle \Delta r^2(t) \rangle = \frac{-6}{q^2} \ln [g^{(1)}(t)] \quad (9.4)$$

where $q = 4\pi n_m \sin(\theta/2)/\lambda$ is the length of the scattering vector, with θ the angle of detection measured with respect to the incident beam, n_m the refractive index of the medium and λ the wavelength of the light in vacuum. Use of Eqn.9.4 is justified when the scattering of the polymer matrix is negligible with respect to

that of the particles and when particle-particle interactions can be ignored. The particle concentrations in our experiments are chosen such that both requirements are obeyed.

In Fig.9.3 we have plotted the MSD, at several fixed times, versus the measurement angle in the light scattering set-up, expressed as the scattering vector q . We see that the MSD (Eqn.9.4) is almost constant over the investigated q -range, which indicates that non-gaussian contributions to the particle displacement are small. The small deviations from the dotted horizontal lines, as seen in Fig.9.3, must be attributed to minor errors in the alignment of the optical train in the light scattering set-up. These errors however do not influence the results shown below, as these are obtained at fixed scattering angles.

In the set-ups used here, the shortest available correlation time is 200 ns. Our data, which was recorded during 2h or more per sample, starts at 10 μ s and ends at 100s, hence well within the borders of the accessible range of correlation times. The accuracy of the normalized correlation function $g^{(2)}(t) - 1/A$ can be estimated using an approximation given by Berne and Pecora [24]. For a measurement of 2h, which is the minimum here, the standard deviation in the correlation function is approximately $1 \cdot 10^{-5}$ % for $\tau = 10\mu$ s and 0.1 % for $\tau = 100$ s. Hence, the data presented here is accurate over the entire time range investigated. Note that this DLS technique offers a significantly higher short-time resolution than video-based particle tracking methods [25].

9.3 Results and Discussion

9.3.1 Linear rheology of polymer solutions

For both polymer classes we have measured the low shear viscosity η as a function of polymer concentration in the absence of particles. The results are shown in Fig.9.4. At low polymer concentrations the viscosity increases very weakly with polymer concentration. At a certain concentration, the increase in viscosity becomes much stronger. We will loosely denote this concentration as the network formation threshold (where the network can be formed by micellar junction points in the case of the telechelic polymers or by entanglements in the case of unmodified PEO). For the unmodified PEO, this occurs at approximately 25 g/L, and the cross-over from the dilute to the entangled regime is rather gradual. For the associative polymers this occurs at a significantly lower concentration of 5 g/L and the transition is much sharper. Fig.9.4 also shows that the viscosity increase beyond this network threshold is stronger for the associative networks than for the

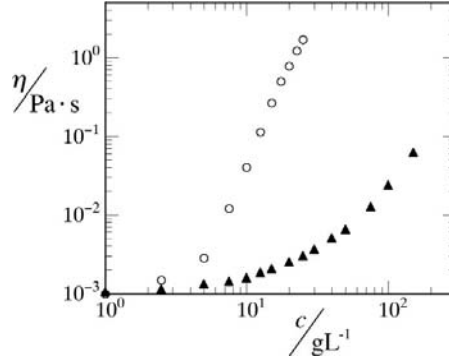


Figure 9.4: Low shear viscosities of aqueous solutions of PEO ($M_W = 35\text{kg/mol}$, \blacktriangle) and aqueous solutions of hexadecyl ($\text{C}_{16}\text{H}_{33}$)-modified PEO of the same molecular weight (\circ).

entangled systems. This is due to the difference in network structure and strength of the junction points.

In rheological oscillation measurements the viscoelastic properties of a system can be determined. In these measurements, the storage (G') and loss (G'') moduli are determined as a function of the angular deformation frequency ω . For the associative system, a typical result is shown in Fig. 9.5a. The simplest description of a viscoelastic fluid is the spring-dashpot model, or so-called Maxwell model, that is governed by a single relaxation time τ_0 [26]. The Maxwell model leads to the following expressions for the storage modulus

$$G' = \frac{G_0 \tau_0^2 \omega^2}{1 + \omega^2 \tau_0^2} \quad (9.5)$$

and loss modulus

$$G'' = \frac{G_0 \tau_0 \omega}{1 + \omega^2 \tau_0^2} \quad (9.6)$$

where G_0 is the plateau modulus. The mechanical response of the associative networks is described well by the Maxwell model, as seen from the fit to Eqns 9.5 and 9.6 in Fig. 9.5a. The Maxwell behavior of associative polymer systems has been established extensively in literature [27].

The values of G_0 and τ_0 , obtained in this manner for the associative polymer system, are plotted in Fig. 9.5b as a function of polymer concentration. In classical transient network theories, such as the generalized Green-Tobolsky theory of Tanaka and Edwards [28], the plateau modulus is linearly proportional to the num-

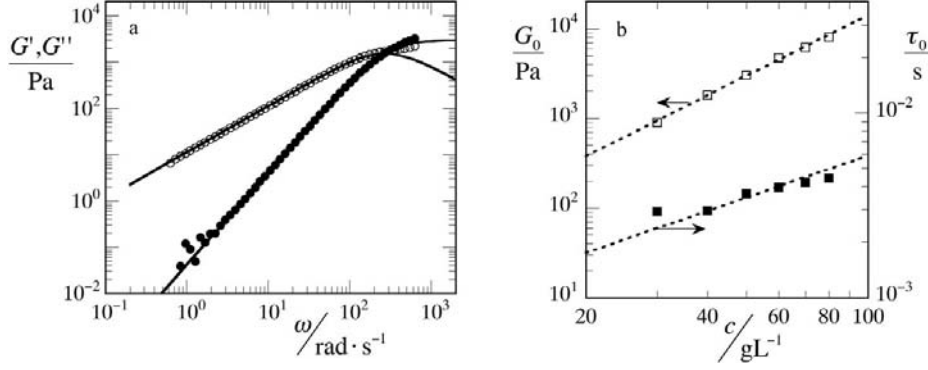


Figure 9.5: a) Frequency dependence of storage (G' , ●) and loss modulus (G'' , ○) of a 50 g/L aqueous solution of associative polymers. Drawn lines are fits to the Maxwell model (Eqns 9.5 and 9.6). b) Plateau modulus (G_0 , □) and relaxation time (τ_0 , ■) versus associative polymer concentration. Drawn lines are powerlaw fits to the data, with $G_0 \propto c^{2.3}$ and $\tau_0 \propto c^{0.75}$.

ber of elastically active chains. When the fraction of all chains that is elastically active is constant, we would also expect a linear relation between plateau modulus and concentration. We observe a much stronger increase in G_0 with concentration however; $G_0 \propto c^{2.3}$. Annable *et al.* gave an explanation in terms of structural changes of the network, i.e. not only the total number of chains in the system increases with concentration but also the fraction of those chains that is mechanically active.

9.3.2 Motion of particles in polymer solutions

The primary result of the light scattering experiments are the intensity correlation functions (Eqn.9.2). In Fig.9.6 we show a set of such correlation functions for plain silica particles in associative networks. For particles in pure water, we see a mono-exponential decay, which is indicative of purely diffusive motion of monodisperse particles. With increasing polymer concentration the main relaxation time shifts to higher values, as a result of the increasing viscosity of the medium (as shown in Fig.9.4). At higher polymer concentrations the correlation functions start to deviate from a simple mono-exponential decay. This complex behavior will become more apparent when the results are converted into the MSD $\langle \Delta r^2(t) \rangle$, using Eqn.9.4.

In Fig.9.7 some typical results are shown. For particles in pure water, here

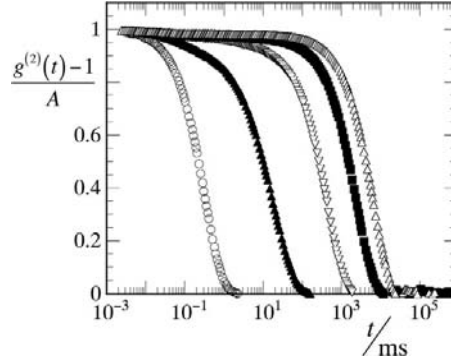


Figure 9.6: Normalized intensity correlation functions, as obtained with DLS, for plain silica particles ($R_h = 70\text{nm}$) in aqueous solutions of associative polymers as a function of polymer concentration; 0 g/L (\circ), 9.6 g/L (\blacktriangle), 30.1 g/L (∇), 49.5 g/L (\blacksquare) and 77.1 g/L (\triangle). Each curve consists of approximately 250 datapoints.

shown for both plain silica particles (Fig.9.7a) and for PEO-covered silica particles (Fig.9.7b), the mono-exponential decay in the correlation curves corresponds with a linear relation between the MSD and time. This is the sign of pure diffusion, where the exponent α in Eqn.9.1 is 1. The proportionality constant in this relation is $6D$, where D is the diffusion coefficient [17].

When the pure water that surrounds the particles is replaced by a polymer network, the behavior becomes more complex. For nonsticking particles in a polymer solution that has formed a transient network, as shown in Fig.9.7b, we see at short times a diffusive behavior, again with $\alpha = 1$. At intermediate time scales we see the appearance of a plateau in the MSD ($\alpha \approx 0$). At a certain MSD, the energy associated with elastic deformation of the network becomes of the order of the thermal energy. As a result the particles will be restricted to motion within this typical length scale, resulting in the plateau in the MSD. At longer time scales, due to the non-permanent nature of the crosslinks in these transient networks, we find a diffusive motion again. Similar experiments in covalently cross-linked polymer networks showed a plateau persisting up to the highest correlation times investigated (10^6 s) [29]. For sticking particles, as shown in Fig.9.7a, the same changes in the MSD at intermediate and long time scales are observed when the medium crosses the network formation threshold. However, we see an additional effect occurring at short correlation times (< 0.1 ms). For these short times and for sticking particles we do not find diffusive motion, but a subdiffusive dynamics with $\langle \Delta r^2 \rangle \propto t^{1/2}$.

In the following sections we separately discuss the behavior in the three different

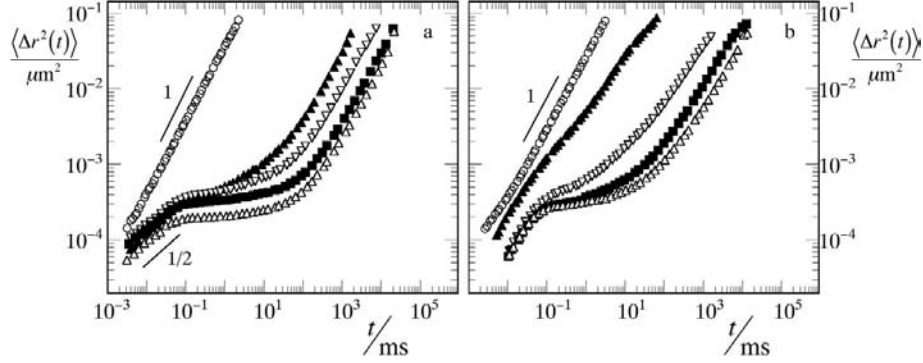


Figure 9.7: MSD of colloids in associative networks, as measured with DLS (Eqn.9.4). a) Sticking conditions: plain silica particles ($R_h = 70\text{nm}$) in associative polymer solutions of 0 (\circ), 20.0 g/L (\blacktriangle), 30.1 g/L (∇), 49.9 g/L (\blacksquare) and 60.2 g/L (\triangle), b) nonstick conditions; silica particles pre-treated with a high molecular weight PEO in associative polymer solutions of 0 (\circ), 10.0 g/L (\blacktriangle), 19.9 g/L (∇), 30.1 g/L (\blacksquare) and 40.0 g/L (\triangle).

regimes that can be distinguished in the dynamics of colloidal particles in transient networks; i) the diffusive (nonsticking) and subdiffusive (sticking) motion at short time scales ($t < 10^{-4}$ s), ii) the caging plateau at intermediate time scales (10^{-4} s $< t < 10^{-1}$ s) and iii) the long time diffusive behavior ($t > 1$ s).

9.3.3 Short time scales

In Fig.9.8 we have plotted the exponent α , for the short time ($t < 10^{-4}$ s) dynamics of various combinations of particles and networks, as a function of polymer concentration. We see that under sticking conditions (for plain silica particles) there is a transition from diffusive ($\alpha = 1$) to subdiffusive motion with $\alpha = \frac{1}{2}$. This transition is found, both for the unmodified and the associative polymer systems, at approximately twice the threshold concentration for network formation. For particles that are not bound to the surrounding network this transition is absent. This is shown in Fig.9.8 for the nonstick latex particles in entangled networks. For these particles the short-time motion remains diffusive over the entire concentration regime. These results strongly suggest that the typical exponent of $\frac{1}{2}$, is related to the binding of particles to the surrounding matrix and the presence of a network.

One special situation is also shown in Fig.9.8 (squares), for particles with a preadsorbed layer of a high molecular weight PEO in associative networks. The associative polymer chains forming the network cannot adsorb onto these particles, so that we expect the particle not to show signs of the subdiffusive behavior.

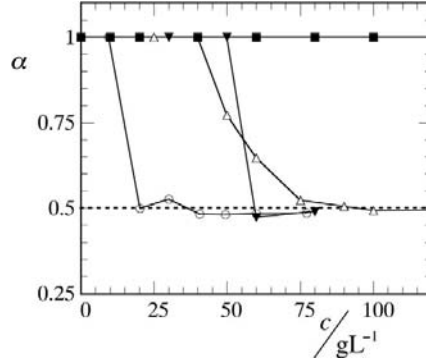


Figure 9.8: Effect of polymer concentration c on the exponent α (Eqn.9.1) for the short-time motion of particles in polymer networks. 4 different combinations of probe particles and polymer are shown: silica particles (sticking) in solutions of unmodified PEO (\triangle), silica particles (sticking) in solutions of hydrophobically modified, associative, polymer (\circ), PEO-covered silica particles (special conditions, see text) in associative polymer solutions (\blacktriangledown) and nonstick latex particles in regular PEO solutions (\blacksquare). The dotted line indicates $\alpha = 0.5$, for Rouse-like motion.

However, at higher concentrations entanglements also become important in the associative networks, in addition to the associative "crosslinks" (i.e. micelles) between the chains. The adsorbed layer at the surface of the particle, can probably take part in entanglements, and as a result we see that the transition from diffusive to subdiffusive motion is delayed from twice the network threshold of the associative system (≈ 20 g/L) to a higher concentration where entanglements also become important (≈ 60 g/L). The transition for this special situation is found close to that of sticking particles in unmodified polymer solution. This indicates that entanglements become important at roughly the same concentration in the unmodified and in the modified systems.

A similar transition from diffusive to subdiffusive behavior upon changing the surface chemistry has been observed for particles in F-actin solutions by Chae *et al.* [14]. These authors observed diffusive motion for non-sticky polystyrene probes pre-adsorbed with bovine serum albumin, while bare polystyrene beads displayed a mean square displacement proportional to $t^{3/4}$. The exponent of $3/4$ is related to the bending (or Rouse) modes of the semi-flexible actin polymers. As we will show in the next section, the analogous Rouse modes for flexible chains lead to the $t^{1/2}$ scaling in the present work.

A physical interpretation of the short time diffusive motion observed for non-

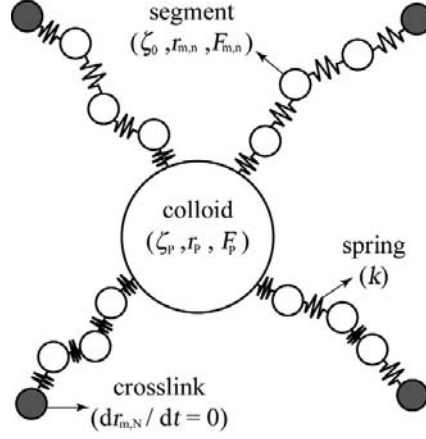


Figure 9.9: Illustration of the proposed model of a colloidal particle (the large central bead) bound to several surrounding polymer chains (the bead-spring chains attached to the particle) that are part of a polymer network through the crosslinks, here represented by the gray beads at the ends of the chains. In this illustration the number of adsorbed chains f is equal to 4, and the length of each chain part $N = 4$.

sticking particles over the entire concentration range, even when there is a transient network surrounding the particles, is for example given in [6]. The nonsticking particles are surrounded by a depletion layer. At short times, when the particle displaces over small distances, the particles do not feel the surrounding network and exhibit a diffusive motion, with a corresponding diffusion coefficient that is of the same order of magnitude as the diffusion coefficient of these particles in the pure solvent. The short time diffusion coefficient is slightly smaller than its pure solvent counterpart, though, because the flow field arising from the particle's Brownian motion is weakly perturbed by the surrounding network. A detailed analysis of such effects has been given by others [15, 16, 30, 31].

In the following section we will develop a model, that gives a physical interpretation of the subdiffusive short-time dynamics observed for sticking particles in transient networks.

9.3.4 Rouse model for colloids bound to polymer networks

The exponent $\alpha = \frac{1}{2}$ found for the short-time motion of sticking particles is indicative of Rouse-like behavior. Here we propose a bead-spring model for the motion of a large particle anchored to a set of polymer chains to explain this scaling.

We consider a particle connected to f adsorbed polymer chains that are elastically active, i.e. connected to both the particle and a junction point in the polymer network (Fig.9.9). The first segment in every chain m is connected to the particle, and the last segment N_m is fixed in a cross-link. For simplicity, we assume that $N_m = N$ is the same for all chains. The equation of motion for a polymer segment in one of the adsorbed chains reads, neglecting inertia [32]:

$$\zeta_0 \frac{dr_{m,n}}{dt} = -k(2r_{m,n} - r_{m,n-1} - r_{m,n+1}) + F_{m,n} \quad (9.7)$$

where ζ_0 is the friction coefficient of a polymer segment, k is the spring constant of a bond between two monomers (related to the Kuhn length l_K by $k = 3k_B T / l_K^2$), $r_{m,n}$ denotes the position of segment n in chain m , and $F_{m,n}$ is the random force acting on that segment due to collisions with the solvent molecules. The colloidal particle is connected to f chains, so that its motion is described by:

$$\zeta_P \frac{dr_P}{dt} = -k \sum_{m=1}^f (r_P - r_{m,1}) + F_P \quad (9.8)$$

where $\zeta_P \gg \zeta_0$ is the friction coefficient of the particle and r_P its position. We assume that the chain ends can be considered fixed in space at the short time scales that we are interested in here: $dr_{m,N}/dt = 0$. The random forces acting on the polymer segments and on the particle are assumed to be Gaussian and uncorrelated in time: $\langle F_{m,n}(t) \rangle = 0$ and $\langle F_{m,n}(t) F_{m',n'}(t') \rangle = 2k_B T \zeta_{m,n} \delta_{mm'} \delta_{nn'} \delta(t - t')$ according to the fluctuation dissipation theorem [32]. Equations 9.7 and 9.8 constitute a set of coupled differential equations that can be written in matrix form: $\dot{\mathbf{R}} = -\mathbf{A} \cdot \mathbf{R} + \mathbf{F}$. The solution is obtained by determining the eigenvalues and eigenvectors of the Rouse connectivity matrix \mathbf{A} [33]. These can be obtained numerically, but for sufficiently long chains we can also obtain analytical expressions by taking a continuum limit. In [34], we derived the mean square displacement of the particle:

$$\langle \Delta r^2(t) \rangle = \frac{12k_B T \chi^2 f}{k} \sum_{p=1}^N \frac{1 - \exp(-(\omega_p^2 k / \zeta_0)t)}{\omega_p^2 (N\omega_p^2 + N\chi^2 f^2 + \chi f)} \quad (9.9)$$

where $\chi = \zeta_0 / \zeta_P \ll 1$ is the size ratio between a polymer segment and the probe particle and where ω_p is determined by the characteristic equation $\omega_p \tan(\omega_p N) = \chi f$. For very weakly coupled particles, $N\chi f \ll 1$, the motion is dominated by the particle friction and the motion is diffusive until a plateau is reached. On the other hand, for $N\chi f > 1$, the connection with the polymer becomes important, and the particle mean square displacement shows three different regimes. At very

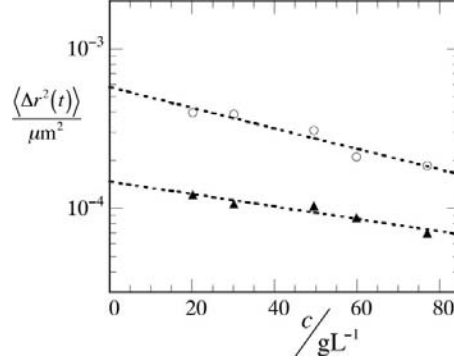


Figure 9.10: Comparison of the effect of polymer concentration on the MSD in the Rouse regime (at $t = 10^{-5}\text{s}$, \blacktriangle) and at the caging plateau where $\alpha(t)$ (Eqn.9.1) is minimal (\circ) for plain silica particles in associative networks. Dotted lines are drawn to guide the eye.

short times ($t < \zeta_P^2/\zeta_0 k f^2$) the particle friction dominates and the mean square displacement is diffusive: $\langle \Delta r^2(t) \rangle = 6D_P t$ with $D_P = k_B T/\zeta_P$. Interestingly, at short time scales the particle motion is indeed Rouse-like, as observed in the experiments:

$$\langle \Delta r^2(t) \rangle = \frac{12k_B T}{f(\zeta_0 k \pi)^{1/2}} t^{1/2} \quad (9.10)$$

In this limit the prefactor does not depend on the friction coefficient of the particle. Hence, the bead just follows the motion of the polymer segments. Note that the mean square displacement still depends on the particle radius R in this regime, as the number of adsorbed chains f is a function of R . At longer time scales $t \gg N\zeta_P/fk$, the mean square displacement reaches a plateau, which depends on the number of adsorbed chains f and their length N :

$$\delta^2 = \lim_{t \rightarrow \infty} \langle \Delta r^2(t) \rangle = \frac{6k_B T N}{fk} \quad (9.11)$$

This expression for the mean square plateau displacement δ^2 , is a balance between the thermal energy $k_B T$ of the probe particle and the elastic energy in the surrounding network of polymer chains. Note that in our model the cross-links were assumed to be fixed, so that the long-time diffusive regime observed experimentally is not accounted for in this model.

The model above gives a microscopic explanation of both the short time Rouse dynamics and the caging plateau at intermediate time scales. Relating these equations to measurable quantities is however somewhat troublesome due to the ingre-

dients that were used, such as the number of elastically active adsorbed chains f and their length N . From Eqns 9.10 and 9.11 we can see however, that for a given system, the mean square displacement for a given time t in the Rouse regime, and for the mean square plateau displacement, should both scale with $1/f$.

In Fig.9.10 we compare the MSD in the Rouse regime and at the caging plateau as a function of polymer concentration. We see that both quantities show approximately the same dependence on concentration. This implies that Eqns 9.10 and 9.11 are consistent with our experimental data, when we assume that all parameters in the model except f remain constant. The decrease in MSD with polymer concentration then indicates that the number of adsorbed chains that are active in the network f increases with polymer concentration, which is expected. When the total number of chains in the system, as well as the number of junction points, increases, the number of chains that are connected to both a particle and a junction point in the network will also increase.

9.3.5 Intermediate time scales

The previous section gave a microscopic explanation of the short and intermediate time dynamics of colloidal particles in polymer networks. A more macroscopic consideration is derived by Mason and Weitz [1], who derived a generalized Stokes-Einstein equation that relates the mean square displacement of a particle to the viscoelastic modulus $G^*(\omega)$ of the surrounding medium. In the plateau region, where $G^*(\omega) = G_0$, this gives for the plateau MSD δ^2 :

$$\delta^2 = \frac{k_B T}{6\pi R G_0} \quad (9.12)$$

This expression is a macroscopic analogue to Eqn.9.11.

The comparison between the true plateau displacement measured with DLS and the value predicted by Eqn.9.12, using the bulk plateau modulus as plotted in Fig.9.5b, is given in Fig.9.11. We clearly see that the correspondence is very poor. The predicted value of δ^2 is a much stronger function of concentration ($\delta^2 \propto c^{-2.2}$) than the measured plateau displacement of the colloids ($\delta^2 \propto c^{-0.6}$). This was also observed previously for living polymer networks [6], where it was tentatively attributed to the existence of a depletion layer around the particle, that increases the actual cage size as experienced by the particles. Levine and Lubensky [30] developed a shell model that takes into account the presence of a depletion layer consisting of pure solvent, which was successfully applied to actin and DNA solutions [14, 15, 16]. In the present case, however, depletion effects can not explain the deviations observed, as we find exactly the same plateau displacement for

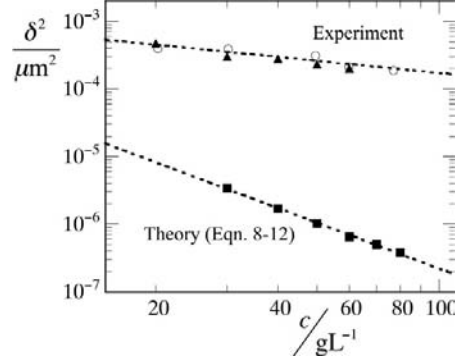


Figure 9.11: Effect of polymer concentration on the mean square plateau displacement δ^2 from the DLS measurements, for plain silica particles (\circ) and PEO-pretreated silica particles (\blacktriangle) in associative networks, and as obtained from Eqn.9.12 with the bulk plateau modulus shown in Fig.9.5b (\blacksquare). Drawn lines are power-law fits to the data.

particles which stick to the network (and therefore should not have a depletion layer) and for particles that do not (which do have a depletion layer around them) (see Fig.9.11).

Several other causes may be suggested to explain the strong deviations. First of all, as stated in the Introduction, it is the ratio of the dominant length scales R/ξ , that is believed to determine whether the particle experiences a homogeneous medium. For the systems studied here, R was either 70 or 110 nm. For polymer solutions above the overlap concentration (as used here), the correlation length must be smaller than the radius of gyration of the polymer coils, which is approximately 5 nm in this case. We therefore estimate $R/\xi \geq 10$. However, it is possible that the system shows structural and/or mechanical inhomogeneities on length scales larger than the particle size and/or particle displacement. If this is the case, the particles will preferentially probe the elastically weaker areas in the network, as there they are less restricted in their motion. The average elasticity that is experienced by the particles is then significantly smaller than the macroscopic elasticity, yielding a larger value of δ^2 than expected from Eqn. 9.12. This is exactly what we observe in Fig.9.11. Strangely, one would expect, when the bulk correlation length becomes smaller, i.e. with increasing polymer concentration, that the correspondence between the macroscopic prediction and the experimental results would also increase. However we see that the deviation between the two grows with increasing concentration. This has also been observed by van der Gucht *et al.* [6].

The deviations might also originate from our assumption of a Maxwellian fluid.

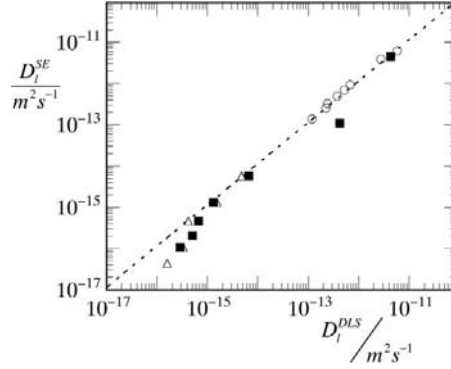


Figure 9.12: Stokes-Einstein diffusion coefficient D_l^{SE} , calculated with Eqn.9.14 and the bulk viscosity, versus the long time diffusion coefficient obtained from the DLS experiments D_l^{DLS} . For systems of 1) plain silica particles in entangled networks of unmodified PEO (\circ), 2) plain silica particles in associative networks (\triangle) and 3) silica particles, pre-treated with a high molecular weight PEO, in associative networks (\blacksquare). Drawn line represents a perfect agreement, i.e. $D_l^{SE} = D_l^{DLS}$.

In Fig.9.5a, we can see that the Maxwell model does not accurately describe the viscoelastic response of the system at high frequencies. The frequency range that corresponds to the time scales of the caging plateau is not accessible at all with conventional bulk rheometry. As a result we have to assume that the same parameters (G_0 and τ_0) that describe the experimentally accessible frequency range, describe the behavior at higher frequencies. It is conceivable that this assumption is not valid in this case, and as a result could explain why Eqn. 9.12 fails to describe our experimental data.

9.3.6 Long time scales

For the long time diffusive motion, at time scales beyond the caging dynamics ($t > 1$ s), we define a diffusion coefficient D_l , given by [17]

$$D_l = \frac{d\langle \Delta r^2(t) \rangle}{6dt} \quad (9.13)$$

The Stokes-Einstein equation predicts the diffusion coefficient of a spherical particles in a homogeneous liquid with viscosity η :

$$D = \frac{k_B T}{6\pi\eta R} \quad (9.14)$$

In Fig.9.12 we have plotted, for various combinations of particles and networks, the diffusion coefficient calculated with Eqn.9.14, using the bulk viscosity (as shown in Fig.9.4) versus the directly measured value of D_l (Eqn.9.13). Both approaches give, within the experimental uncertainty, the same value for the diffusion coefficient. This indicates that at these longer time scales the macroscopic properties of the networks dominate the particle dynamics.

9.4 Conclusions

The thermal displacement of colloidal particles in transient polymer networks shows 3 distinct regimes; a slow diffusive motion at long time scales, an elastic caging plateau at intermediate time scales and at short time scales either a fast diffusive motion for particles that do not stick to the surrounding network, or Rouse-like dynamics for particles that are physically bound to the surrounding network. We conclude that for short times, hence small displacements, the microscopic details of the medium and the interactions between medium and particles are very important, whereas at very long time scales the motion seems governed by the bulk viscosity. For the short time Rouse dynamics of particles bound to their surrounding polymer network we have proposed an analytical model, which is found to be at least qualitatively consistent with the experimental results. The findings in this Chapter indicate that both of the central assumptions often made in microrheology, i.e. that particle-matrix interactions can be neglected and that the particles displace through a homogeneous medium, must be made with caution.

References

- [1] Mason, T.; Weitz, D. A. *Phys. Rev. Letters* **1995**, *74*, 1250.
- [2] Gisler, T.; Weitz, D. A. *Curr. Opin. Colloid Interface Sci.* **1998**, *3*, 586.
- [3] Gittes, F.; Schnurr, B.; Olmsted, P. D.; Mackintosh, F. C.; Schmidt, C. F. *Phys. Rev. Letters* **1997**, *79*, 3286.
- [4] Mackintosh, F. C.; Schmidt, C. F. *Curr. Opin. Colloid Interface Sci.* **1999**, *4*, 300.
- [5] Harden, J. L.; Viasnoff, V. *Curr. Opin. Colloid Interface Sci.* **2001**, *6*, 438.
- [6] van der Gucht, J.; Besseling, N. A. M.; Knoben, W.; Bouteiller, L.; Cohen Stuart, M. A. *Phys. Rev. E* **2003**, *67*, 051106.
- [7] Tseng, Y.; Kole, T. P.; Lee, S. H. J.; Wirtz, D. *Curr. Opin. Colloid Interface Sci.* **2002**, *7*, 210.

- [8] Furst, E. M. *Curr. Opin. Colloid Interface Sci.* **2005**, *10*, 79.
- [9] van Zanten, J. H.; Amin, S.; Abdala, A. A. *Macromolecules* **2004**, *37*, 3874.
- [10] Lu, Q.; Solomon, M. J. *Phys. Rev. E* **2002**, *66*, 061504.
- [11] Schnurr, B.; Gittes, F.; Olmsted, P. D.; Mackintosh, F. C.; Schmidt, C. F. *Biophys. J.* **1997**, *72*, TU285.
- [12] Caspi, A.; Elbaum, M.; Granek, R.; Lachish, A.; Zbaida, D. *Phys. Rev. Letters* **1998**, *80*, 1106.
- [13] Levine, A. J.; Mackintosh, F. C. *Phys. Rev. E* **2002**, *66*, 061606.
- [14] Chae, B. S.; Furst, E. M. *Langmuir* **2005**, *21*, 3084.
- [15] Chen, D. T.; Weeks, E. R.; Crocker, J. C.; Islam, M. F.; Verma, R.; Gruber, J.; Levine, A. J.; Lubensky, T. C.; Yodh, A. G. *Phys. Rev. Lett.* **2003**, *90*, 108301.
- [16] Huh, J. Y.; Furst, E. M. *Phys. Rev. E* **2006**, *74*, 031802.
- [17] Einstein, A. *Ann. d. Phys.* **1905**, *17*, 549.
- [18] van Zanten, J. H.; Rufener, K. P. *Phys. Rev. E* **2000**, *62*, 5389.
- [19] Wong, I. Y.; Gardel, M. L.; Reichman, D. R.; Weeks, E. R.; Valentine, M. T.; Bausch, A. R.; Weitz, D. A. *Phys. Rev. Letters* **2004**, *92*, 178101.
- [20] Serero, Y.; Aznar, R.; Porte, G.; Berret, J. F.; Calvet, D.; Collet, A.; Viguier, M. *Phys. Rev. Letters* **1998**, *81*, 5584.
- [21] Dijt, J. C.; Cohen Stuart, M. A.; Fleer, G. J. *ACS Symp. Ser.* **1993**, *532*, 14.
- [22] Santore, M.; Fu, Z. *Macromolecules* **1997**, *30*, 8516.
- [23] Pecora, R. *Dynamic Light Scattering*; Plenum Press, New York, 1985.
- [24] Berne, B. J.; Pecora, R. *Dynamic Light Scattering*; Dover, Mineola, New York, 2000.
- [25] Savin, T.; Doyle, P. S. *Biophys. J.* **2005**, *88*, 623.
- [26] Larson, R. G. *The Structure and Rheology of Complex Fluids*; Oxford University Press (USA), 1998.
- [27] Annable, T.; Buscall, R.; Ettelaie, R.; Whittlestone, D. *J.Rheol.* **1993**, *37*, 695.
- [28] Tanaka, F.; Edwards, S. F. *Macromolecules* **1992**, *25*, 1516.
- [29] Dasgupta, B. R.; Weitz, D. A. *Phys. Rev. E* **2005**, *71*, 021504.
- [30] Levine, A. J.; Lubensky, T. C. *Phys. Rev. Lett.* **2000**, *85*, 1774.
- [31] T. H. Fan, J. K. G. Dhont, R. T. *Phys. Rev. E* **2007**, *75*, 011803.
- [32] Doi, M.; Edwards, S. F. *The Theory of Polymer Dynamics*; Clarendon Press (Oxford), 1986.
- [33] Zimm, B. H.; Kilb, R. W. *J. Pol. Sci.* **1959**, *37*, 19.
- [34] Sprakel, J.; van der Gucht, J.; Cohen Stuart, M. A.; Besseling, N. A. M. *Phys. Rev. E* **2008**, *77*, 061502.

Chapter 10

Shear banding in associative polymer networks

In this chapter, experimental evidence of an instability in the shear flow of transient networks formed by telechelic associative polymers is presented. Velocimetry experiments show the formation of shear bands, following a complex pattern upon increasing the overall shear rate. The occurrence of shear banding is explained on the basis of a microscopic constitutive equation following classical transient network theory.

This chapter was published as:

J. Sprakel, E. Spruijt, M.A. Cohen Stuart, N.A.M. Besseling, M.P. Lettinga and J. van der Gucht: *Shear banding and rheochaos in associative polymer networks*, Soft Matter **4** (2008), 1696.

10.1 Introduction

Physically crosslinked, micellar networks formed by telechelic associative polymers are popular model systems for studying the rheology of transient networks [1, 2, 3]. In dilute aqueous solutions these hydrophilic polymers, modified with a hydrophobic moiety at both chain ends, self-assemble into spherical, unconnected, micelles. The associative blocks (stickers) at both chain ends reside in the same micellar core, while the middle block (spacer) forms a loop in the corona. At higher concentrations (typically 0.1 - 1 wt%) bridging between the micelles leads to the formation of a sample-spanning network, where the spherical cores of the micelles form the junction points. This results in solutions that are characterized by a Maxwellian viscoelastic response with a single mechanical (zero-shear) relaxation time [1]. The reversible character of these systems can be tuned with the length and chemistry of the hydrophobic end blocks (stickers); the zero-shear relaxation time τ_0 can vary from tenths of milliseconds for small hydrocarbon tails to several hundreds of seconds for larger fluorocarbon tails [4].

At low shear rates, solutions of associative polymers show Newtonian behavior. When the reciprocal shear rate is on the order of the relaxation time or beyond, a rich variety of non-Newtonian responses is found. At moderate shear rates, shear thickening is observed, which is attributed to stretching of the polymer chains (bridges) due to the applied flow. At higher shear rates, strong shear thinning is found. This shear thinning is often explained as a decrease in the number of elastically active chains (bridges) in favor of the number of loops that do not contribute directly to the network [5].

Berret and co-workers have shown that, in systems of fluorocarbon end-capped poly(ethylene oxide) with relaxation times many decades larger than those of the systems employed here, the first region of the shear thinning regime is characterised by an inhomogeneous flow, that appeared to resemble the planar fracture of solids [6]. Others have suggested that the rheology of similar transient networks, formed by adding telechelic polymers to microemulsions, shows the sign of shear banding [5], but, so far, these conjectures have remained unsubstantiated. In this Chapter we present direct experimental evidence of such a shear banding transition in networks of telechelic associative polymers.

Shear induced inhomogeneities are found in a variety of soft materials, such as linear aggregates of small surfactants (wormlike micelles) [7, 8], linear supramolecular polymers [9], rod-shaped colloids [10], entangled polymers [11] and structures suspensions of spherical colloids [12]. The unstable flow in these systems leads to the formation of banded structures, either in the gradient direction (shear banding)

or in the vorticity direction (vorticity banding). Three-dimensional inhomogeneities can also occur in certain cases [13, 14]. Using model transient networks, consisting of physically crosslinked spherical micelles, we will argue that shear banding can be expected to be a common phenomenon in all networks with non-permanent cross links.

In rest, a phase transition driven by the entropy gain of bridge formation, can be found in some systems of telechelic polymers. Depending on the length of the stickers, the length of the spacer and the degree of functionalization, solutions of telechelic polymers can demix into a viscous (network) phase rich in polymer and a dilute phase [15]. Computer simulations [16, 17] and experiments [2, 18] have shown that shear can induce anisotropy in transient micellar networks, as the bridges perpendicular to the flow direction will be disrupted more strongly than those in the flow direction. This is expected to lead to the formation of strings and/or sheets of micelles that are aligned in the flow direction and held together by bridges. Recent simulations show that shear banding can occur in systems of spherical particles with soft interactions [19], which in essence is very similar to the systems used in this Chapter.

This Chapter focusses on the shear banding transition in networks of telechelic associative polymers, for which we present direct evidence using laser Doppler velocimetry. In connection we will address the transient response of these systems in the shear banding regime. Stress relaxation mechanisms are observed on time scales many decades larger than the zero-shear relaxation time. In some cases the stress, rather than reaching a steady value, is found to show erratic fluctuations. This phenomenon, often named rheochaos, is shown to be related to spatiotemporal fluctuations in the banded flow. Following Tanaka and Edwards [20] and Michel *et al.* [5], we will explain the occurrence of the inhomogeneous flow as a direct result of the reduction of the relaxation time of stickers in the micellar cores, due to shear-induced stretching of the spacers. This approach leads to a simple constitutive equation specific to the microstructure of these systems that is experimentally evidenced based on results from superposition rheometry.

10.2 Experimental

10.2.1 Materials

The telechelic associative polymers that are studied here consist of a polyethylene oxide (PEO) spacer with a nominal M_W of 20 kg/mol and an octadecyl end group at both chain ends connected by urethane linkers. The PEO (Fluka) was dissolved in

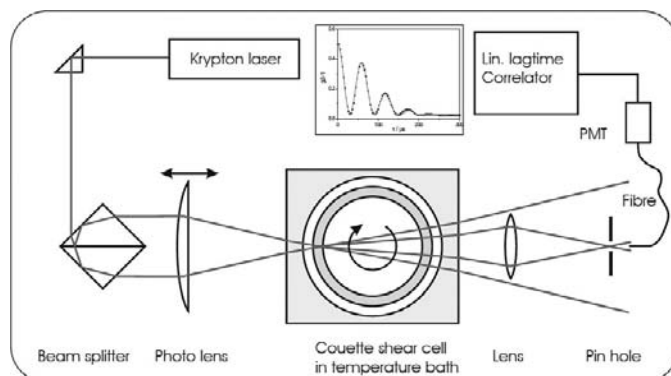


Figure 10.1: Schematic outline of the heterodyne dynamic light scattering set-up used to measure local fluid velocity profiles. Illustration courtesy of H. Kriegs and P. Lettinga.

dry toluene (Sigma-Aldrich) and reacted with octadecyl isocyanate (Sigma-Aldrich) for 40h at 80 °C in presence of dibutyl tindilaurate (Sigma-Aldrich) as a catalyst. The modified polymers were isolated during three cycles of dissolution in toluene and precipitation in low-boiling petroleum-ether. Further purification comprised dissolution in demineralized water, double filtration over paper and 450 nm cellulose acetate membrane filters and removal of the solvent through freeze drying. It was found with $^1\text{H-NMR}$ that on average 1.9 alkyl tails (i.e. 95% conversion) were attached to each PEO chain. All samples were prepared by dissolving the polymer in demineralized water yielding optically transparent solutions. By studying the excimer formation of pyrene with fluorescence spectroscopy [21], the critical micelle concentration for these polymers in water, was found to be approximately $1 \cdot 10^{-5}$ g/L.

10.2.2 Rheology

Rheological experiments were conducted on MCR300 and MCR301 rheometers (Paar Physica). Shear flow measurements were conducted in a couette (concentric cylinder) geometry with an inner diameter of 16.66 mm and a gap width of 0.71 mm. Samples were left for at least 30 mins after loading to equilibrate. Flow curves were recorded in various ways: i) fast scans from low ($\dot{\gamma} = 0.1 \text{ s}^{-1}$) to high shear rate ($\dot{\gamma} = 300 \text{ s}^{-1}$), recorded with 25, 50 and 200 data points, with a measurement time of 1 s per point and ii) slow scan from high ($\dot{\gamma} = 300 \text{ s}^{-1}$) to low ($\dot{\gamma} = 1 \text{ s}^{-1}$) shear rate, consisting of 50 data points in which the measured stress is averaged over 100 s. For the transient flow measurements, a fixed shear rate was

imposed at $t = 0$, without any pre-shear treatment. Oscillatory measurements, to determine the viscoelastic properties of the transient networks, were conducted in a cone-plate set-up with a cone diameter of 50 mm, and tilt angle of 1° . Frequency sweeps were performed between 1 and 600 rad/s. These frequency sweeps were fitted with a single relaxation time Maxwell model [1], to obtain the mechanical relaxation times τ and plateau moduli G . For the zero-shear properties, the strain was fixed at 5%, which was checked to be in the regime of linear response, giving access to the zero-shear relaxation time τ_0 and plateau modulus G_0 .

Standard rotational and oscillatory experiments were carried out under strain-controlled settings, which is realized with a feedback-loop in the rheometer hardware. Parallel superposition measurements, in which the oscillating frequency sweeps are superimposed on rotational shear flow, were carried out at controlled stress of 10 Pa for the oscillatory motion and a varying controlled stress to accomplish the desired average shear rate.

10.2.3 Laser-Doppler Velocimetry

Local velocity profiles of the shear flow of associative polymer networks were measured using heterodyne dynamic light scattering in combination with a differential Laser-Doppler velocimeter (see Fig.10.1). Note that these experiments are conducted on a different set-up as the rheometry measurements described above. The couette cell had an inner diameter of 44 mm and a gap width of 2 mm. The optical part of the setup consisted of a Kr laser beam (647 nm), split into two beams of equal intensity. These beams were focussed in a small volume of the gap of the transparent Couette cell. Scattered light was detected in the forward direction of the laser beam. The light scattered from each of the two beams, has a different Doppler shift and the resulting interference can be analyzed to yield a local velocity of the sheared liquid.

Wall positions were determined by measuring a velocity profile at a low shear rate, where the solutions are Newtonian and no slip or non-linear flow phenomena are expected. The size of the focal point of the two laser beams can be estimated from the diameter and divergence of the laser beam and the crossing angle at the focal point, resulting in a lower limit of about 100 μm . The temporal resolution is determined by the minimal time needed to measure an intensity autocorrelation function and was found to be on the order of 1 s, comparable to the limit found by Salmon *et al.* [23]. In these experiments the inherent scattering of the micellar networks was used, hence no probe particles were added. Each velocity profile consists of 18 points across the gap, each of which has been averaged over 3

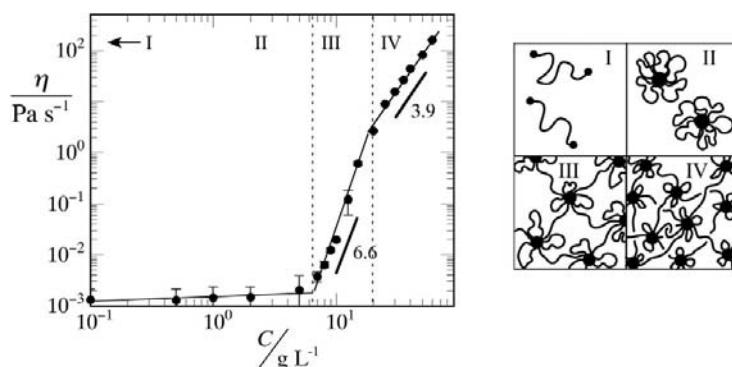


Figure 10.2: Low-shear viscosity of aqueous solutions of $C_{18}H_{37}$ -end capped PEO ($M_W = 20$ kg/mol) versus polymer concentration. 4 structural regimes are distinguished [22]: I) unimers, II) flowerlike micelles, III) associative network of micelles connected through bridges IV) associative network with entanglements. Drawn lines are power-law fits to the experimental data, exponents are indicated in the graph.

measurements of 10 s per datapoint.

10.3 Results and Discussion

The structure of solutions of telechelic associative polymers develops in 4 stages with increasing concentration, each with their own effect on the low-shear viscosity (Fig.10.2) [22]. At low concentrations the chains exist as unimers (stage I), and the viscosity is approximately that of the solvent (here water). Above the critical micelle concentration (here found at $1 \cdot 10^{-5}$ g/L) the chains associate into flowerlike micelles (stage II), and the viscosity increases slightly due to the added hydrodynamic volume of the micelles. Above a certain threshold the flowerlike micelles will form bridges, which leads to a sample-spanning transient network, with associative connections between the micellar cores (stage III). This is indicated by the sudden and steep increase in viscosity. The concentration threshold for network formation is found here at 6 g/L. All experiments are carried out well above this concentration. The dependence of the viscosity on concentration in this regime is discussed by Annable et al. [1]. At higher concentrations, entanglements of the flexible polymer spacer also become important (regime IV). We see this regime starting at roughly 20 g/L, which is around the overlap concentration for the unmodified analogue of the PEO spacer used here. Similar observations as shown in Fig.10.2 were made in [22].

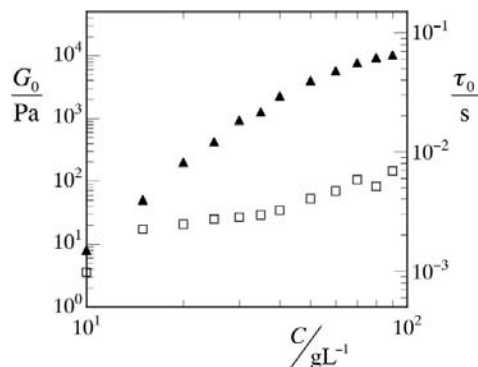


Figure 10.3: Zero-shear relaxation times τ_0 (\square) and plateau moduli G_0 (\blacktriangle) as a function of polymer concentration, as obtained from fitting frequency sweeps to a single element Maxwell model.

10.3.1 Steady-state rheology

The zero-shear viscoelasticity of these systems is known to be Maxwellian [1], thus characterized by a single mechanical zero-shear relaxation time τ_0 and plateau modulus. For the systems investigated, the relaxation times are between 2 and 7 milliseconds, and plateau moduli range from 10 Pa (10 g/L) up to 10^4 Pa (90 g/L) (Fig.10.3).

The results just mentioned are all recorded well within the regime of linear response. In this Chapter we focus however on the non-linear rheology of these transient networks. With increasing overall shear rate, 4 different regimes can be distinguished (Fig.10.4); at low shear rates the flow is Newtonian (regime A). At somewhat higher shear rates a modest shear thickening is found (regime B). This shear thickening has been studied in detail by others [24, 25], and is attributed to the stretching of the PEO middle blocks, without decreasing the number of bridges between micelles. At higher shear rates the flow curves reveal shear thinning behaviour, which is the main focus of this Chapter. We will show that in the first part of the shear thinning, in regime C, the flow becomes inhomogeneous. In regime D, even though still shear thinning, the flow becomes homogeneous again.

In Fig.10.5a we can see that the shape of the flow curve depends strongly on how it is obtained. Fast scans from low to high shear rate, reveal a characteristic loop-like structure in the shear thinning regime, which becomes more pronounced if the scan is carried out faster, i.e. when $d \ln(\dot{\gamma})/dt$ is increased. This non-monotonic behaviour is an indication that the flow can become inhomogeneous. In classical

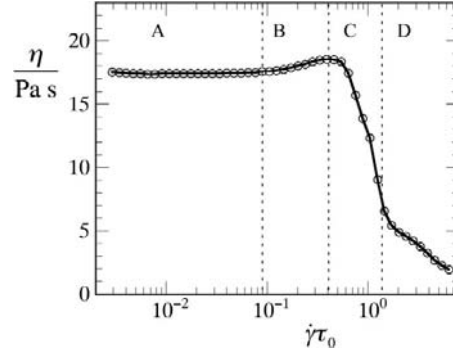


Figure 10.4: Static viscosity versus imposed shear rate for a 30 g/L associative polymer solution, showing 4 different flow regimes with increasing shear rate: A) Newtonian, B) shear thickening, C) and D) shear thinning. Recorded at a scan rate of $\partial \ln(\dot{\gamma})/\partial t = 0.16$

shear banding theory, this loop, in analogy with a van der Waals loop for equilibrium phase transitions, is a metastable path which can lead to the flow decomposing into a banded structure with a high shear rate band at the inner rotating wall and a low shear rate band at the outer stationary wall. This would, in the ideal case, give a plateau in the stress through this metastable loop. The physical interpretation of this ideal plateau, with $d \ln \sigma / d \ln \dot{\gamma} = 0$ is similar to tie-lines in classical fluid coexistence, as it connects the two conditions (here shear rates) that coexist with each other. If the imposed shear rate is changed within this plateau, both the compositions and the shear rates in the bands stay constant, only the widths of the bands adjust (similar to a lever rule for classical fluid coexistence).

Two procedures for obtaining the flow curve have been attempted, see section 10.2.2. The first is to start at high shear rates, and slowly decrease the shear rate into the Newtonian regime. This is shown as the thick drawn line in Fig.10.5a. Another approach is to look at the transient (i.e. time resolved) behaviour of the stress at a given imposed shear rate. It is expected that some time after switching on the shear flow, a stable stress value is obtained. The value of the stress at that point would correspond to the steady-state value. In our system however the stress does not reach a steady value, but continuously fluctuates after some initial relaxation. The magnitude of these fluctuations is indicated with the vertical bars in Fig.10.5a. We see that the transient points and the slow scan give approximately the same flow curve, in which the Newtonian regime is followed by strong shear thinning with $d \ln \sigma / d \ln \dot{\gamma} = 0.1$ (Fig.10.5b), which we will show to be the sign of a shear banding transition.

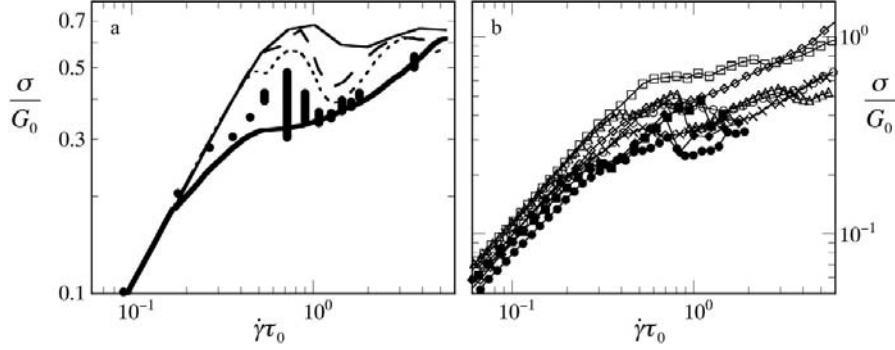


Figure 10.5: a) Flow curve ($c = 30$ g/L) obtained in various manners. Thin lines are scans from low to high shear rate with different scan speeds: $\partial \ln(\dot{\gamma})/\partial t = 0.32$ (solid), 0.16 (dashed) and 0.04 (dotted). Thick drawn line is a slow scan from high to low shear rate ($\partial \ln(\dot{\gamma})/\partial t = 0.01$). Vertical bars show the amplitude of the stress fluctuations, after the initial stress relaxation, during transient flow. b) Dimensionless stress σ/G_0 versus dimensionless shear rate $\dot{\gamma}\tau_0$ as a function of telechelic polymer concentration c : \diamond 15 g/L, \square 20 g/L, \circ 25 g/L, \times 30 g/L, \triangle 35 g/L, \blacklozenge 40 g/L, \bullet 50 g/L and \blacksquare 60 g/L.

In experiments on wormlike micelles, that also show a banding transition, a truly horizontal stress plateau is often found. Here we find a pseudo-plateau, with $d \ln \sigma / d \ln \dot{\gamma} = 0.1$. Two possible explanations for such a positive slope have been given. The first is that there is a coupling between concentration and flow, i.e. that the concentration of the two coexisting bands is not constant. Another explanation is found in the finite curvature of the Couette cell, leading to an inhomogeneous stress field across the gap [26]. The effect of cell curvature on the expected slope can be estimated with $d \ln \sigma / d \ln \dot{\gamma} \approx 2l/R_1$ [27], with l the gap width and R_1 the radius of the inner, rotating, cylinder. For the geometry in these experiments we find a predicted slope of 0.17. This suggests strongly that the finite slope of the shear banding plateau is caused by cell curvature effect. After this quasi-plateau, another shear thinning regime with $d \ln \sigma / d \ln \dot{\gamma} \approx 0.5$ is found, in which the flow becomes homogeneous again.

For Maxwellian fluids, which the systems under investigation here are, flow curves can be made to coincide by rescaling them with two parameters only: the zero-shear relaxation time τ_0 and the plateau modulus G_0 . We see that this approach works for low shear rates (Fig.10.5a), where the flow is Newtonian, but starts to deviate as soon as non-linear effects, such as the shear banding transition, come into play. This suggests that in the banded regime, secondary parameters become important such as the actual relaxation time(s) of the system rather than

τ_0 . We will discuss this in more detail in a following section. The minor deviations between the rescaled flow curves in the Newtonian regime might be explained by the experimental error associated with the determination of both G_0 and τ_0 and the fact that these parameters were measured in a different geometry (cone-plate) than the set-up used to determine the flow curves (couette).

10.3.2 Stationary velocity profiles

Previously there has been speculation that the flow curves discussed in the previous section, reveal signs of an inhomogeneous flow [5]. With laser Doppler velocimetry we can show directly that this is indeed the case (Fig.10.6a). At low shear rates, in the Newtonian regime, the velocity profiles are linear as expected for simple Couette flow. When we enter the shear thinning regime, for which the quasi-plateau is found in Fig.10.5, we see that the steady-state velocity profiles are no longer linear, but show a banded structure, with bands of different shear rates coexisting with each other.

When the overall shear rate is further increased to the regime where $d \ln \sigma / d \ln \dot{\gamma} \approx 0.5$, the banded flow disappears. We note that the velocity profiles in this regime are approximately linear. Strong shear thinning leads to curved profiles in couette flow [27], but for the present geometry this occurs for values of $d \ln \sigma / d \ln \dot{\gamma}$ significantly smaller than 0.5.

A closer view on the banded flow is given in Fig.10.6c-f, in a sequence of increasing overall shear rates. The banding regime starts with a decomposition of the sample into two bands (10.6c and d), as expected in the classical picture. At somewhat higher shear there is a transition to an apparent 3 banded flow (10.6e). When the shear rate is further increased, the slowest band disappears and again two bands coexist with each other (10.6f). This process is also visualized in Fig.10.7, where we see how the width of the three bands and their actual shear rates change throughout the shear banding regime. It is obvious that this complex progression of the banding is not in line with the classical picture, described in the previous section, where only the relative width of the bands changes with shear rate.

In Fig.10.7a we can also see that no significant wall slip occurs at all shear rates, as the overall measured shear rate and the applied shear rate are consistent.

For transient networks of telechelic polymers with fluorocarbon stickers, Berret and S  r  ro have shown a solid-like fracture zone in the flow profile [6]. In these fluorocarbon-modified systems the zero-shear relaxation times are many decades larger (up to a factor 10^6). It is conceivable that this fracture behavior and our shear banding observations are of similar origin, but differ in manifestation due to

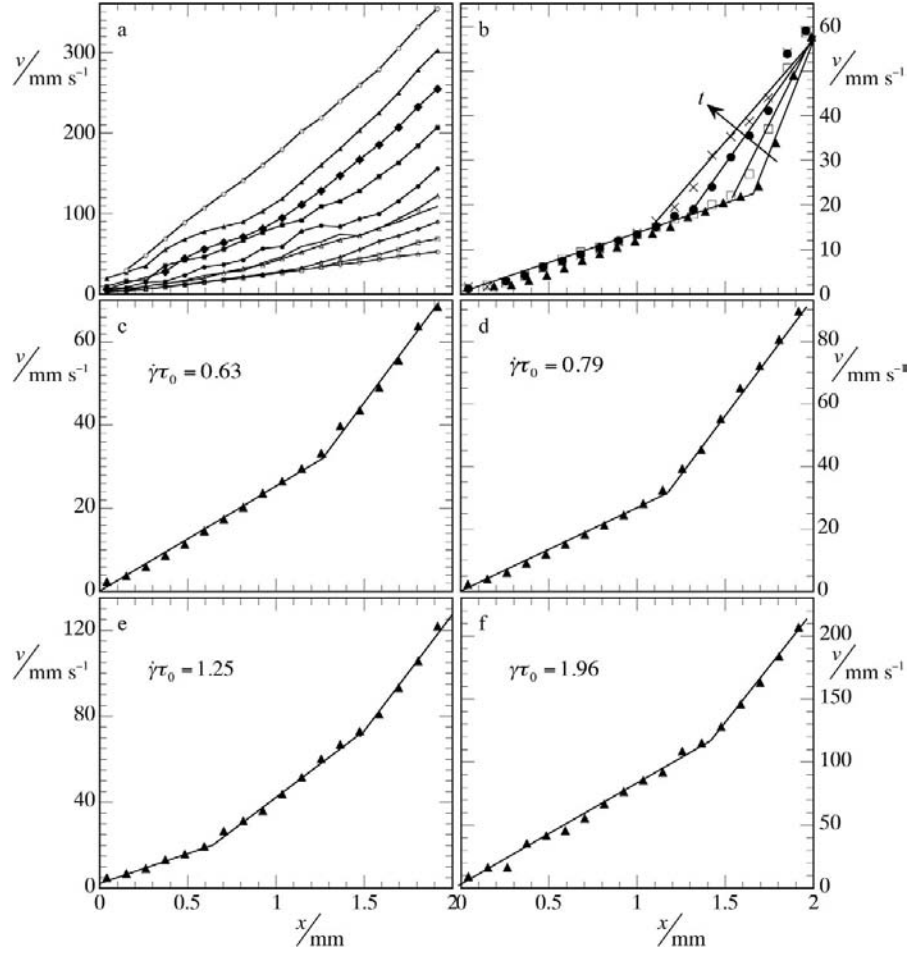


Figure 10.6: a) Overview of the velocity profiles for a 20 g/L telechelic polymer solution as a function of shear rate $\dot{\gamma} = 30$ \circ , 41 \square , 51 \diamond , 81 \triangle , 101 \bullet , 127 \blacksquare , 152 \blacklozenge , 177 \blacktriangle and 203 \circ . b) evolution of the velocity profile ($\dot{\gamma} = 30 \text{ s}^{-1}$, $C = 30 \text{ g/L}$) in time: 5 min \blacktriangle , 15 min \square , 35 min \bullet and 85 min \times after start of the shear flow. c)-f) same data as in a), shown separately for clarity.

this large difference in relaxation time.

10.3.3 Simple constitutive equation

Following Tanaka en Edwards [20, 28], Michel *et al.* [5] developed a simple model to rationalize the non-monotonic flow curves found for transient networks of physically crosslinked micro-emulsions. This model is based on the reduction of the residence

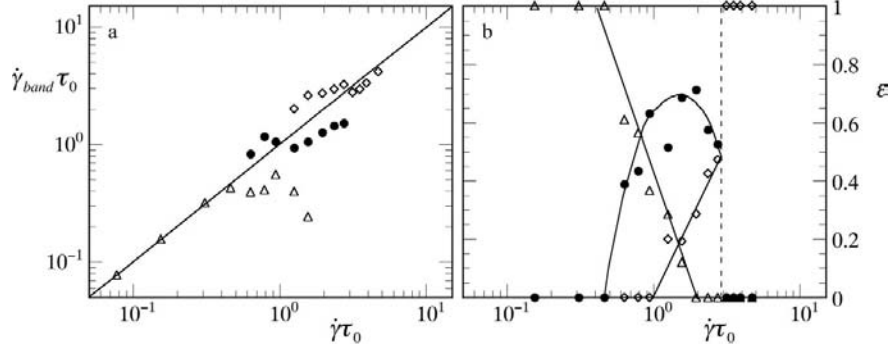


Figure 10.7: a) Average shear rate $\dot{\gamma}_{band}$ in the slow (\triangle), intermediate (\bullet) and the fast (\diamond) band as a function of the applied shear rate $\dot{\gamma}$. The solid line indicates Newtonian flow. b) Fraction of the gap (ϵ) occupied by the different shear bands as a function of the overall shear rate, showing the progression of the shear banded flow. Both for a 30 g/L telechelic polymer solution. The disappearance of the shear bands is found to occur suddenly, as indicated by the dashed vertical line. Solid lines are drawn to guide the eye.

time of a hydrophobic sticker in a junction point due to flow induced chain (spacer) stretching. In the following we describe a similar approach, that gives a microscopic view on why these transient networks show shear banding.

As stated in the introduction, the transient networks we study are formed from spherical micelles that are connected through polymeric bridges, i.e. the two stickers attached to a chain reside in different micellar cores. The chains that do not form a bridge are expected to form loops, i.e. both stickers are in the same micelle. In rest, the dynamics of the bridges can be described with a simple association-dissociation equilibrium:

$$\frac{\partial n_b}{\partial t} = k_a n_l - k_d n_b \quad (10.1)$$

where t is time, n_b the number of bridges, n_l the number of loops and $n = n_b + n_l$ is the total number of chains. The two reaction constants reflect the formation of bridges (k_a) and the dissociation of bridges (k_d). It is convenient to define an overall reaction constant as $K = k_a/k_d$. At steady-state the total number of bridges must be constant, $\partial n_b/\partial t = 0$, so

$$n_b = \frac{K n}{1 + K} \quad (10.2)$$

Under shear deformation, the chains that form the bridges are continuously stretched, which gives rise to an elastic restoring force that pulls on the stickers. This force

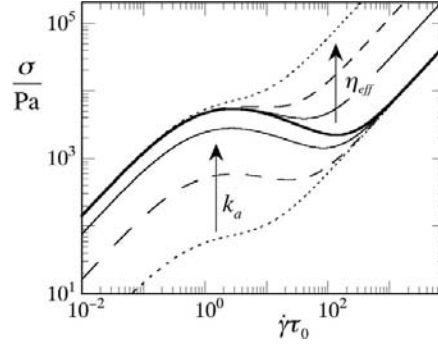


Figure 10.8: Flow curve predicted by Equations 10.5 and 10.7, for $\tau_0 = 0.017$ s, $\delta = 1.8$ nm, $\xi = 5$ nm, k_a increasing: 0.1, 1, 5 and 10 s^{-1} (for $\eta_{eff} = 0.1 \text{ Pa s}$) and η_{eff} increasing: 0.1, 0.5, 2 and 10 Pa s (for $k_a = 10 \text{ s}^{-1}$).

will enhance sticker dissociation. Here we assume an exponential relation between the lifetime of a bridge and the force [28]:

$$\tau = \tau_0 \exp\left(\frac{-f\delta}{k_B T}\right) \quad (10.3)$$

where τ_0 is the zero-shear residence time of the stickers, f the force acting on the chain ends associated with the stretching of the spacers and δ the length of the stickers. To calculate the force on the stickers, we assume that the chains are Gaussian; $f = r3k_B T/Na^2$, where r is the elongation of the chain and Na^2 is the square of the end-to-end distance of the undisturbed chain, with N the number of statistical segments and a their Kuhn length. In a time Δt at an imposed shear rate of $\dot{\gamma}$, the elongation is on the order of $r \approx \xi \Delta t \dot{\gamma}$, where $\xi = a\sqrt{N}$ is the end-to-end distance of the chain. During the lifetime of a bridge, the force then increases to approximately

$$f \approx \frac{3k_B T}{\xi} \Delta t \dot{\gamma} \quad (10.4)$$

By combining Equations 10.3 and 10.4, we can write for the average residence time

$$\langle \tau \rangle = \tau_0 \exp\left(-\frac{3\dot{\gamma} \langle \tau \rangle \delta}{\xi}\right) \quad (10.5)$$

The local stress, neglecting the contribution of the solvent, can be written as

$$\sigma = \frac{f}{\xi^2} \frac{n_b}{n} \quad (10.6)$$

where n_b/n is the fraction of chains that is involved in a bridge. This gives

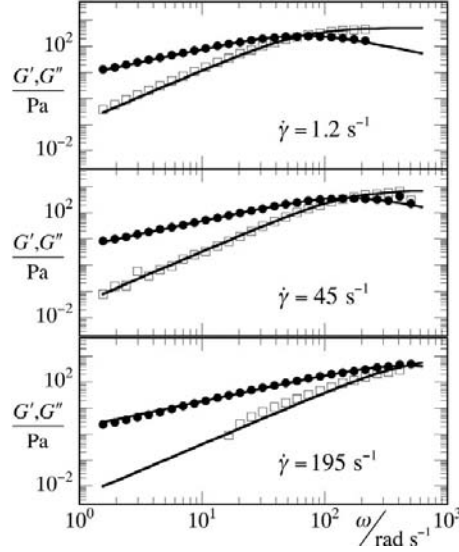


Figure 10.9: Frequency sweeps for various superimposed shear rates, for a 25 g/L associative polymer solution. Experimentally obtained storage (G' , \square) and loss (G'' , \bullet) moduli and fits to a single Maxwell model (drawn lines).

$$\langle \sigma \rangle = \frac{3k_B T \dot{\gamma} \langle \tau \rangle}{\xi^3} \frac{k_a \langle \tau \rangle}{1 + k_a \langle \tau \rangle} + \eta_{eff} \dot{\gamma} \quad (10.7)$$

where we have added the viscous contribution of the solvent $\eta_{eff} \dot{\gamma}$.

This constitutive equation predicts a non-monotonic flow curve (Fig.10.8), which is indicative of a mechanical instability leading to shear banding. Although this approach does not give any specific details about banded flow, it does offer a qualitative explanation on a microstructural level. For these systems the inhomogeneous flow is the result of the increased breakdown rate of bridges in favor of loops (that are not significantly stressed by the flow), leading to a more than proportional decrease in the number of "elastically active" chains.

10.3.4 Parallel superposition rheology

The model proposed in the previous section links the occurrence of inhomogeneous flow to the reduction of the 'relaxation' time of the stickers due to the applied shear flow. Using parallel superposition rheology, in which an oscillatory motion of the cone is superimposed on rotation, we can test this hypothesis.

In Fig.10.9 three frequency sweeps performed at various imposed shear rates are

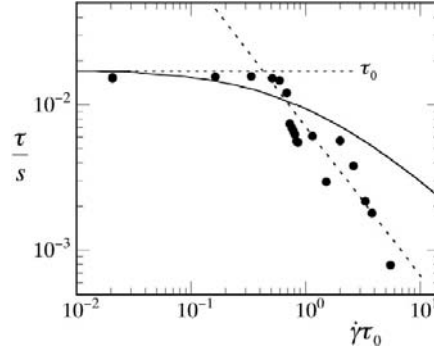


Figure 10.10: Mechanical relaxation time versus superimposed shear rate, from parallel superposition measurements on a 25 g/L polymer solution. Horizontal drawn line indicates the value of the zero-shear relaxation time τ_0 , curved drawn line is the decay of the relaxation time with shear rate as predicted by Eqn.10.5 for $\delta = 1.8$ nm, $\xi = 5$ nm and $\tau_0 = 0.017$ s. Dotted line is a power-law fit to the decay of the relaxation time with $\tau \propto \dot{\gamma}^{-1}$.

given. As expected from the model, we see that the frequency where the storage and loss modulus intersect, which is equal to the reciprocal of the mechanical relaxation time τ , shifts to higher values with increasing shear rate. In other words, we indeed observe that the relaxation time decreases with increasing shear rate. For other types of associative polymer networks, similar observations have been made by Mewis *et al.* [29].

At low shear rates the relaxation times are of the same order as the zero-shear relaxation time τ_0 , but at shear rates where we also find the onset of shear banding they start to decrease significantly (Fig.10.10). In the same Fig.10.10 the prediction by our model (Eqn.10.5) is shown, for which we have entered realistic estimates for the input parameters, such as $\xi = 5$ nm, which is the radius of gyration of the PEO spacer for which $a = 0.7$ nm [30], $\delta = 1.8$ nm which is the contour length of a $C_{18}H_{37}$ alkyl tail and $\tau_0 = 0.017$ s as obtained from rheology measurements.

Qualitatively, the model predicts a similar behaviour as found in the experiments, which supports the hypothesis posed above, that indeed reduction of the relaxation time due to shear flow is responsible for the inhomogeneous flow. On a quantitative level the model is not very accurate and predicts a weaker decrease of the relaxation time $\tau(\dot{\gamma})$ than what is measured. We propose three explanations for this difference. First of all, the $\langle \tau \rangle$, that is obtained with Eqn.10.5, is the average residence time of a sticker in a micellar junction point. This is of course not

necessarily the same as the mechanical relaxation time obtained with rheometry. Secondly, the model only contains few parameters and is intended for a qualitative explanation of the observed phenomena. It therefore might lack some important contributions, such as the effects of shear-induced structural changes in the network [16], non-Gaussian chain stretching due to the flow [18] and the directionality in the breaking of bridges, which will be stronger in the direction perpendicular to the flow. Perhaps the most important explanation is that the predictions of Eqn.10.5 assume the flow to remain homogeneous (i.e. follow the predicted, non-monotonic flow curve), whereas in the experiments the banding has most-likely already taken place, even in the cone-plate geometry used for these measurements.

10.3.5 Transient rheology

In a shear start-up experiment, a constant shear rate is imposed on the sample, starting at time $t = 0$, and the development of the stress, i.e. the transient stress response, is followed in time. For homogeneous flow it is expected that relaxation of the stress occurs on times scales on the order of the mechanical (Maxwell) relaxation time, here milliseconds. In the shear rate regime where shear banding is observed, in contrast, it can take tens of minutes for the stress to reach a steady plateau.

Various start-up stress responses are found when one goes through the shear banding regime. In some cases we find a classical stretched exponential decay (Fig.10.11a), with a characteristic time of 18 s, i.e. approximately $1000 \cdot \tau_0$, and a stretch exponent of 0.5. This type of stress decay, as studied in detail for wormlike micelles by Decruppe *et al.* [31], is explained as a nucleation process followed by a one-dimensional growth of the fast band from the slow band. This is consistent with the evolution of the banded structure in transient flow, as shown in Fig.10.6b. It starts with the formation of a thin band at the fast wall, which grows in width over approximately 90 minutes. Similar results are reported for systems of wormlike micelles [7].

These slow dynamics might be explained by transport of material across the gap, by a coupling between the banded flow and local polymer concentration. Fielding and Olmsted have shown that such a coupling results in a non-horizontal stress plateau in the flow curve [26], however curvature effects can also cause this same effect, as we discussed above.

In attempts to quantify the concentration of polymers in the coexisting bands, using confocal microscopy on fluorescently stained samples, we did not find any measurable difference in polymer concentration between the shear bands. This

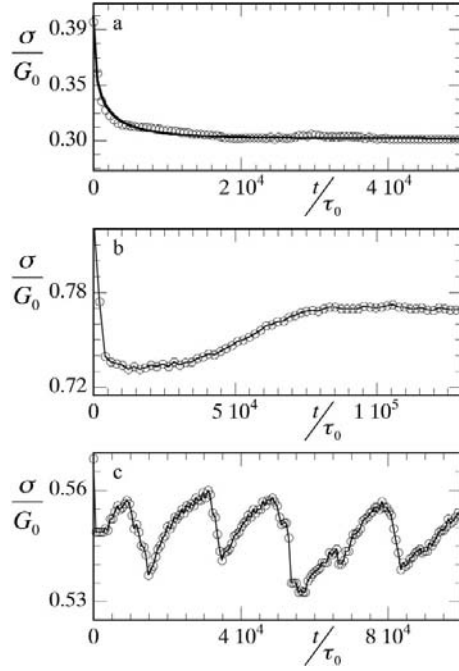


Figure 10.11: Typical examples of transient stress responses in shear start-up experiments: a) $c = 30$ g/L $\dot{\gamma}\tau_0 = 0.36$ b) $c = 20$ g/L $\dot{\gamma}\tau_0 = 3.09$ c) $c = 20$ g/L $\dot{\gamma}\tau_0 = 1.86$. In a) the drawn line shows a fit to a stretched exponential decay, with a characteristic time of 18 s ($\approx 1000\tau_0$) and a stretch factor of 0.5.

suggests that concentration differences between the bands, if any, are small. We therefore might speculate that it is transport of structure that is time limiting, rather than mass transport being the origin of the long relaxation times.

In the shear banding regime we find that after some initial relaxation of the stress, often no steady plateau is reached at all. The stress continuously fluctuates around a certain average (Fig.10.11c). These fluctuations are also indicated in the flow curves (Fig.10.5a). A true steady-state flow does not exist in this regime.

These apparently erratic fluctuations are often coined rheochaos. One explanation for rheochaos is a spatiotemporal dynamics of the structure of the banded flow and the resulting fluctuations in the shape and position of the interface between the bands. Instead of the ‘ideal’ picture of 2 concentric bands, with an interface parallel to the wall, now more and more evidence is being presented, both experimentally [13, 14] and theoretically [32, 33], of the occurrence a complex structure that changes in time.

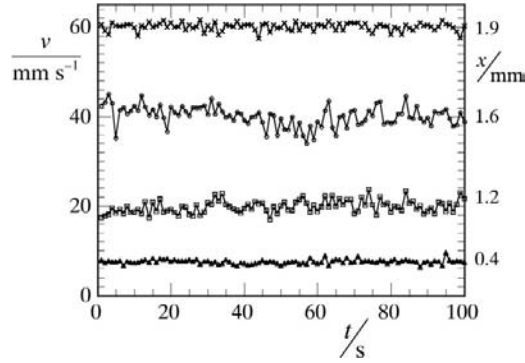


Figure 10.12: Time evolution of the local velocity ($c = 30$ g/L, $\dot{\gamma} = 30$ s $^{-1}$). The corresponding positions in the Couette gap are denoted on the right side of the figure. Note that the absolute fluctuations near the moving and stationary wall (1.9 and 0.4 mm respectively) are much smaller than the fluctuations in the slow band (1.2 mm) and near the interface between the two bands (1.6 mm).

Transient velocimetry experiments conducted at various positions in the gap of the Couette geometry (Fig.10.12) show that such a scenario might be the case here. In the centre of the gap, at and near the interface between the bands ($x = 1.2$ and 1.6 mm), there are significant fluctuations in the measured velocity, whereas the velocity is practically constant close to the stationary wall ($x = 0.4$ mm) or the rotating wall ($x = 1.9$ mm), with deviations on the order of the experimental accuracy of the technique,

These results suggest that the fluctuating stress is caused by the mechanical instability of the the interface between the coexisting bands. Note that we do not observe any signs of wall slip in the stationary velocity profiles, such that a boundary phenomenon (e.g. stick-slip at the couette walls) is not the origin of the fluctuating stresses. In Chapter 11 we analyze these anomalous fluctuations in more detail.

10.3.6 Rheological diagram of states

With the observations of shear banding we can draw the diagram of states of the complex rheology of these types of associative networks (Fig.10.13). It shows what type of behavior is found as a function of both polymer concentration and imposed shear rate. It had already been established that the Newtonian regime at low shear rates is followed by shear thickening, and subsequently changes into strong shear thinning. We have now shown directly, that the onset of the shear thinning

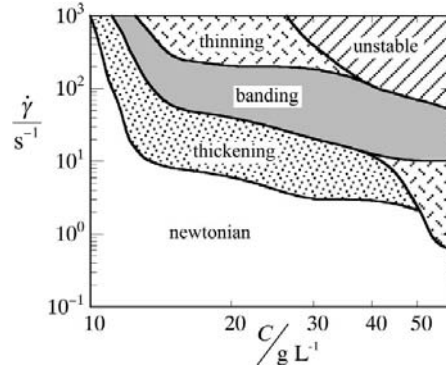


Figure 10.13: Rheological diagram of states for a C_{18} end-capped PEO of 20 kg/mol, indicating the type of rheological behavior as a function of concentration and imposed shear rate, as determined experimentally.

regime is characterised by a shear banding transition. As we could see in Fig.10.7, the upper and lower shear rate where shear banding occurs was experimentally accessible for this system. When we exit the shear banding regime by increasing the shear rate beyond this upper limit, the flow becomes homogeneous again, yet is still shear thinning (see also Fig.10.5).

However, at even higher shear rates the flow becomes macroscopically unstable and is accompanied by the sample being expelled from the measurement geometry. Visual inspection of the set-up under these conditions (Fig.10.14), reveals that the liquid climbs up the rotating axis of the rheometer. This rod-climbing, or Weissenberg, effect is often attributed to the development of large normal stress differences. This behavior is indicated in Fig.10.13 as ‘*unstable*’.

Other instabilities can be excluded here [34]. The inertial Couette-Taylor instability occurs at Taylor numbers larger than the critical value of 1712. This dimensionless Taylor number is defined as

$$Ta = \frac{l}{R_1} Re^2 = \frac{\rho^2 \dot{\gamma}^2 l^5}{\eta^2 R_1} \quad (10.8)$$

where Re is the Reynolds number, R_1 the radius of the inner cylinder (8.33 mm), l the gap width (0.71 mm) and ρ the density of the liquid ($\approx 1000 \text{ kg/m}^3$). For a 50 g/L solution of associative polymers, we find the instability to occur at $\dot{\gamma} = 60 \text{ s}^{-1}$ at a viscosity of $21 \text{ Pa} \cdot \text{s}$. This gives $Ta = 4 \cdot 10^{-8}$, hence inertial effects are completely negligible.

The purely elastic instability described for other shear banding systems [34],

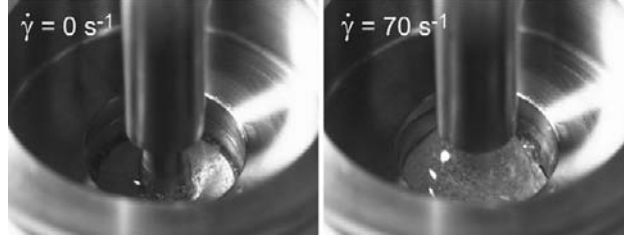


Figure 10.14: Photograph of a telechelic polymer solution in the Couette geometry in rest (left) and during shear (right), showing the Weissenberg effect

can also be excluded. It is expected to occur at a critical shear rate equal to

$$\dot{\gamma}^c = \frac{5.9}{\tau_0} \left(\frac{l}{R_2} \right)^{-\frac{1}{2}} \quad (10.9)$$

where R_2 is the radius of the outer cylinder (9.04 mm). For the same sample (50 g/L), with a zero-shear relaxation time of 25 ms, $\dot{\gamma}^c = 842 \text{ s}^{-1}$. The instability we observe appears at 60 s^{-1} and is therefore expected to be neither inertial nor elastic in origin, rather caused by normal stress differences, leading to a Weissenberg effect [35].

10.4 Conclusions

In this work we have shown direct evidence for a shear banding transition in transient networks of associative polymers under shear flow. Our results indicate that the banded flow does not obey the 'ideal' picture of shear banding. Deviations are found in the non-horizontal plateau, chaotic transient stress response and the unusual progression of the banded structure, as illustrated in Fig.10.7. A possible explanation can be found in the fact that there seems to be a time-limiting transport process, most likely being the transport of structure to form the final bands. We have also observed that the structure of the banded flow is strongly non-stationary both in time and in space, with structure fluctuations extending over macroscopic dimensions. As a result, no steady stress is reached in transient flow; the stress continuously fluctuates in a chaotic or intermittent manner.

The explanation of the observed banding transition, found in the facilitation of breaking elastically active junctions in the network due to the applied shear, has been verified experimentally using parallel superposition rheometry. We pose that shear banding is, in principle, the direct result of the influence of shear forces on

the lifetime of junction points in reversible networks, and can therefore be expected to occur in (almost) all transient networks.

With the direct evidence for complex shear banding in these model transient networks, new opportunities for investigating this phenomenon arise. With these systems the internal interactions, and hence the tendency for phase separation in rest, can be tuned by changing the molecular architecture, i.e. the length and chemistry of the hydrophobic stickers or soluble middle block. The importance of hydrodynamic and/or thermodynamic contributions to the observed flow-induced transition might be investigated systematically in this way [36]. Changing the end-blocks also drastically alters the mechanical relaxation time, which depends exponentially on the length of the stickers. This flexibility in designing these molecules, and their well-defined and understood structure, makes these model networks interesting alternatives to wormlike micelles for studying shear induced transitions.

References

- [1] Annable, T.; Buscall, R.; Ettelaie, R.; Whittlestone, D. *J.Rheol.* **1993**, *37*, 695.
- [2] Tam, K.; Jenkins, R.; Winnik, M.; Bassett, D. *Macromolecules* **1998**, *31*, 4149.
- [3] Berret, J. F.; Serero, Y.; Winkelman, B.; Calvet, D.; Collet, A.; Viguier, M. *J. Rheol.* **2001**, *45*, 477.
- [4] Berret, J. F.; Calvet, D.; Collet, A.; Viguier, M. *Curr. Opin. Colloid Interface Sci.* **2003**, *8*, 296.
- [5] Michel, E.; Appell, J.; Molino, F.; Kieffer, J.; Porte, G. *J. Rheol.* **2001**, *45*, 1465.
- [6] Berret, J. F.; Serero, Y. *Phys. Rev. Letters* **2001**, *87*, 048303.
- [7] Miller, E.; Rothstein, J. P. *J. Non-Newtonian Fluid Mech.* **2007**, *143*, 22.
- [8] Fischer, E.; Callaghan, P. T. *Phys. Rev. E* **2001**, *64*, 011501.
- [9] van der Gucht, J.; Lemmers, M.; Knoben, W.; Besseling, N. A. M.; Lettinga, M. P. *Phys. Rev. Letters* **2006**, *97*, 108301.
- [10] Kang, K. G.; Lettinga, M. P.; Dogic, Z.; Dhont, J. K. G. *Phys. Rev. E* **2006**, *74*, 026307.
- [11] Tapadia, P.; Ravindranath, S.; Wang, S. Q. *Phys. Rev. Letters* **2006**, *96*, 196001.
- [12] Imhof, A.; van Blaaderen, A.; Dhont, J. K. G. *Langmuir* **1994**, *10*, 3477.
- [13] Lopez-Gonzales, M. R.; Holmes, W. M.; Callaghan, P. T. *Soft Matter* **2006**,

- 2, 855.
- [14] Becu, L.; Anache, D.; Manneville, S.; Colin, A. *Phys. Rev. E* **2007**, *76*, 011503.
 - [15] Pham, Q. T.; Russel, W. B.; Thibault, J. C.; Lau, W. *Macromolecules* **1999**, *32*, 2996.
 - [16] Khalatur, P.; Khokhlov, A.; Mologin, D. *J. Chem. Phys.* **1998**, *109*, 9602.
 - [17] Khalatur, P.; Khokhlov, A.; Mologin, D. *J. Chem. Phys.* **1998**, *109*, 9614.
 - [18] Pellens, L.; Vermant, J.; Mewis, J. *Macromolecules* **2005**, *38*, 1911.
 - [19] van den Noort, A.; Briels, W. J. *Macromol. Theory Simul.* **2007**, *16*, 742.
 - [20] Tanaka, F.; Edwards, S. F. *Macromolecules* **1992**, *25*, 1516.
 - [21] Siu, H.; Duhamel, J. *Macromolecules* **2005**, *38*, 7184.
 - [22] Regalado, E.; Selb, J.; Candau, F. *Macromolecules* **1999**, *32*, 8580.
 - [23] Salmon, J.; Becu, L.; Manneville, S.; Colin, A. *Eur. Phys. J. E* **2003**, *10*, 109.
 - [24] Marrucci, G.; Bhargava, S.; Cooper, S. *Macromolecules* **1993**, *26*, 6483.
 - [25] Ma, S.; Cooper, S. *Macromolecules* **2001**, *34*, 3294.
 - [26] Fielding, S. M.; Olmsted, P. D. *Eur. Phys. J. E* **2003**, *11*, 65.
 - [27] Salmon, J.; Colin, A.; Manneville, S.; Molino, F. *Phys. Rev. Letters* **2003**, *90*, 228303.
 - [28] Tanaka, F.; Edwards, S. F. *J. Non-Newtonian Fluid Mech.* **1992**, *43*, 289.
 - [29] Mewis, J.; Kaffashi, B.; Vermant, J.; Butera, R. *Macromolecules* **2001**, *34*, 1376.
 - [30] Pattanayek, S. K.; Juvekar, V. A. *Macromolecules* **2002**, *35*, 9574.
 - [31] Decruppe, J.; Lerouge, S.; Berret, J. F. *Phys. Rev. E* **2001**, *63*, 022501.
 - [32] Aradian, A.; Cates, M. E. *Phys. Rev. E* **2006**, *73*, 041508.
 - [33] Fielding, S. M. *Soft Matter* **2007**, *3*, 1262.
 - [34] Manneville, S.; Colin, A.; Waton, G.; Schosseler, F. *Phys. Rev. E* **2007**, *75*, 061502.
 - [35] Kundu, P. T. *Soc. Rheol.* **1973**, *17*, 343.
 - [36] Dhont, J. K. G. *Phys. Rev. E* **1999**, *60*, 4534.

Chapter 11

Intermittent dynamics in shear-banded networks

In this Chapter we show an unusual behavior in the shear banded flow of a viscoelastic fluid. We report on an intermittent fracture and self-healing process in an apparently fluid material undergoing steady deformation, which causes large fluctuations in the measured stress. The statistical pattern of the fluctuations is indicative of self-organized criticality. We use a microscopic constitutive model to interpret the magnitude of these fluctuations.

This chapter was submitted as:

J. Sprakel, E. Spruijt, M.A.J. Michels, M.A. Cohen Stuart and J. van der Gucht:
Intermittent fracture and self-healing in a visco-elastic fluid, (2009).

11.1 Introduction

Visco-elastic materials are ubiquitous; both natural, such as the biopolymer networks that constitute the cellular cortex, as well as man-made, for example rheology modifiers found in foods, pharmaceuticals and coatings. When such materials are deformed at rates faster than they can structurally adapt, part of the structure in the quiescent state is broken down, which in most cases leads to shear thinning. Shear thinning can, when strong enough, make the flow macroscopically unstable, leading to the formation of two, or more, bands of differing shear rate; a phenomenon called shear banding [1, 2]. In the previous Chapter we have shown experimental evidence for such a transition in the shear flow of transient networks formed from telechelic associative polymers. In this Chapter we will show an intermittent fracture - healing process taking place around the interface between two shear bands in these visco-elastic fluids under steady deformation. A statistical analysis of the resulting stress fluctuations reveals a pattern that is characteristic of self-organized criticality [3], indicating that the system spontaneously reaches a critical point where its dynamics become scale invariant. Moreover, we can directly link the magnitude of the stress fluctuations to the size of the metastable loop in the constitutive relation underlying the flow instability.

11.2 Experimental

The rheological measurements are carried out on under strain rate control on an Anton Paar MCR501 rheometer, in a concentric cylinder geometry. The velocimetry measurements, with laser Doppler velocimetry, and rheological protocols are described in Chapter 10. The material under study is a water-soluble polymer (PEO, of 20 kg/mol) with a hydrophobic sticker (an octadecyl alkane) covalently attached to both chain-ends (see [1] for preparation procedure). Dissolved in water at sufficient concentration (in this letter at 25 g/L unless stated otherwise), it spontaneously associates into a transient network [4]. The network is composed of self-assembled micellar nodes, with a finite lifetime, interconnected by flexible polymer chains. These systems behave as visco-elastic Maxwell fluids, characterized by a single microscopic relaxation time τ_0 . This relaxation time represents the average lifetime of a polymer bridge between two nodes, and can be tuned with temperature [5].

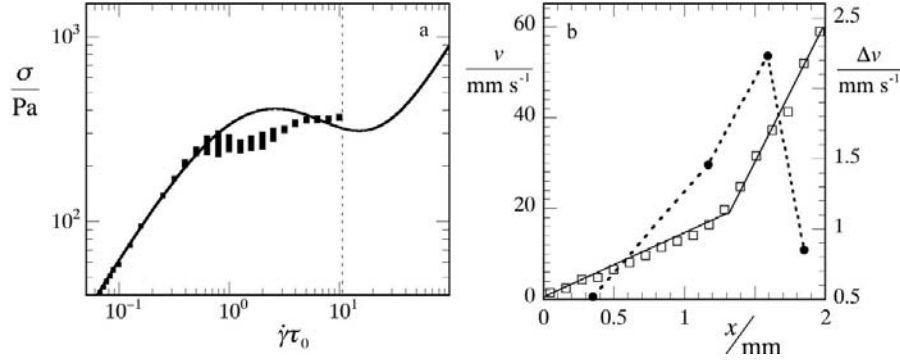


Figure 11.1: a) Shear stress σ versus dimensionless shear rate $\dot{\gamma}\tau_0$ for a transient polymer network at 25 g/L and 10°C ($\tau_0 = 36$ ms). The vertical bars indicate the range of stress fluctuations for a given shear rate. Drawn line is the flow curve predicted by the constitutive equation (Eqn.11.5). At shear rates beyond the dotted line another flow instability, a Weissenberg effect, occurs (see Chapter 10). b) Local fluid velocity v (\square) and standard deviation Δv of the time-averaged velocity (\bullet) as a function of the position x across the gap of the couette geometry, measured at $T = 20^\circ\text{C}$ and $\dot{\gamma}\tau_0 = 0.54$, for a 30 g/L associative polymer solution ($\tau_0 = 18$ ms).

11.3 Results & Discussion

Under constant shear, the tension on the stickers reduces the average lifetime of the polymer bridges, thus disrupting the network structure and producing a severe shear thinning, i.e. a viscosity that decreases strongly with applied shear rate. This makes the flow mechanically unstable [1, 6]. The result is that bands of different shear rate are spontaneously formed parallel to the flow direction (Figure 11.1b); a phenomenon known as shear banding [1, 2]. In the low-shear band the viscosity is high and there are still many junctions, while in the high-shear band many junctions are broken, resulting in a lower viscosity. A stress-plateau (see Fig.11.1a), the rheological signature for shear banding, has been observed before for similar telechelic polymers [6, 7], and in a recent paper we showed direct evidence for a shear-banded flow [1]. Such behavior is not unique to this material; it is observed in a wide variety of soft materials, such as solutions of wormlike micelles, colloidal suspensions and entangled polymer solutions [2]. For our system, this plateau occurs at shear rates $\dot{\gamma}$ on the order of the reciprocal relaxation time τ_0^{-1} . Velocity profiles measured in this regime (Figure 11.1b) indeed show bands of different shear rate. The flow is homogenous at lower shear rates, where the network can easily adjust to the deformation, and at high shear rates, where the network structure is

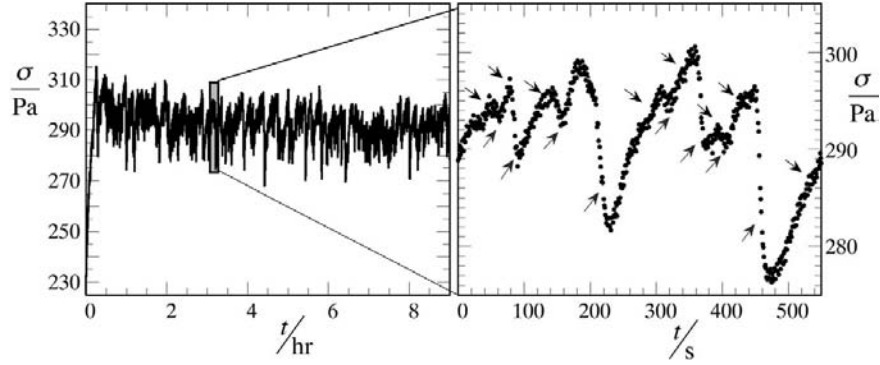


Figure 11.2: Typical transient stress response in the banded regime, at a steady shear rate of $\dot{\gamma}\tau = 1$, measured at $T = 10^\circ\text{C}$ ($\tau_0 = 36$ ms). Arrows in the right panel indicate the 2 different events constituting the fracture-healing behavior; healing (\searrow) and fractures (\nearrow). Note that at short time scales $O(\tau_0)$, at the start-up of the shear flow, the stress shows an overshoot, which is not visible here due to the longer sampling interval of 1 s ($\approx 30 \cdot \tau_0$).

almost entirely disrupted [1].

When the stress is measured as a function of time at a constant applied shear rate in the shear banding regime, it becomes clear that a true steady state is never reached: the stress keeps undergoing persistent fluctuations (top panel Fig.11.2). The magnitude of these stress fluctuations, indicated by the vertical bars in Fig. 11.1a, is on the order of 10 Pa, much larger than the experimental error (< 0.1 Pa). Such large fluctuations are only observed in the shear banding regime. At first glance, the signal may appear to be chaotic. Indeed the power spectrum (Fig.11.3a) shows no dominant frequencies. Chaotic stress responses have been studied in detail for solutions of wormlike micelles [8, 9].

In our case however, a distinct pattern appears when we zoom in on the signal (bottom panel Fig.11.2). Periods of more or less linear increase of the stress alternate with periods of rapid decrease of the stress. This pattern is reminiscent of the stick-slip motion of two bodies sliding past each other [10]. During a 'stick phase' an elastic force builds up, which is spontaneously released by a fracture that propagates between the two bodies, giving rise to a slip motion. After a fracture event, the bodies reconnect to start the stick motion again. A well-known example of stick-slip motion is the movement of tectonic plates in the earth's crust, where intermittent stress drops at the fault lines are responsible for earthquakes [11].

Velocimetry measurements (Fig.11.1b) in our system showed no slip at either

wall; the velocity close to both cylinder walls is constant and equal to the velocity of the wall. In the middle of the gap, however, we do observe significant velocity fluctuations (see Chapter 10). We argue therefore that the 'stick-slip-like' behavior that we observe in the stress response is due to repeated fracture-healing events in the material in the region around the interface between the two shear bands. During a healing stage structure builds up near the interface, which leads to an effective growth of the low-shear band and an increase of the stress. When the stress increases above a certain level, the low-shear band may become unstable, leading to a fracture and a break-down of the structure that was built up, with an associated drop in the stress. The repeated growth and shrinkage of the low-shear band leads to the large velocity fluctuations observed in the interfacial region (Fig.11.1b). Note that the localized fractures that we observe should not be confused with the macroscopic fracture observed by Berret and S  r  ro [12] for fluorocarbon telechelics. In contrast to what we find, these materials do not heal after a microscopic fracture so that the fracture can grow to macroscopic dimensions. This might be due to their much longer microscopic relaxation time, i.e. up to 170 times larger than τ_0 of our material.

While chaos may seem to reign, the dynamics of stick-slip processes are characterized by an underlying statistical pattern [10, 13]. In seismology, the Gutenberg-Richter law predicts the cumulative probability distribution $P(> m_o)$ of earthquakes larger than a given seismic moment m_o as $P(> m_o) \propto m_o^{-b}$ [13]. For earthquakes the exponent b is between 0.5 and 1.2 [14]. In our soft material we find the same power-law behavior for the distribution of the total stress drop $\Delta\sigma$ during a fracture (Fig.11.3b), although over a much smaller range, limited for small $\Delta\sigma$ by experimental noise. The exponent $b = 0.85$ we find is close to the value of 0.8 reported for pure stick-slip motion [10]. Attempts to explain such scaling behavior often involve the concept of self-organized criticality [3]. According to this theory, driven dissipative dynamical systems spontaneously reach a critical state that is characterized by a power-law distribution of events and power-law behavior in the power spectrum of the fluctuations. Our material obeys the same statistics.

The power-law behavior in the distribution of fracture moments is lost beyond amplitudes of roughly 10 Pa. For larger amplitudes the distribution decays very rapidly. The existence of such a cut-off implies that there is an upper limit to the stress fluctuations, which is obviously related to the bandwidth of the stress fluctuations in Fig.11.2. In Fig.11.4b, the difference S between the maximum and minimum stress, relative to the average stress $\bar{\sigma}$, is plotted as a function of the microscopic relaxation time. We see that the 'bandwidth' of the stress fluctuations increases with relaxation time.

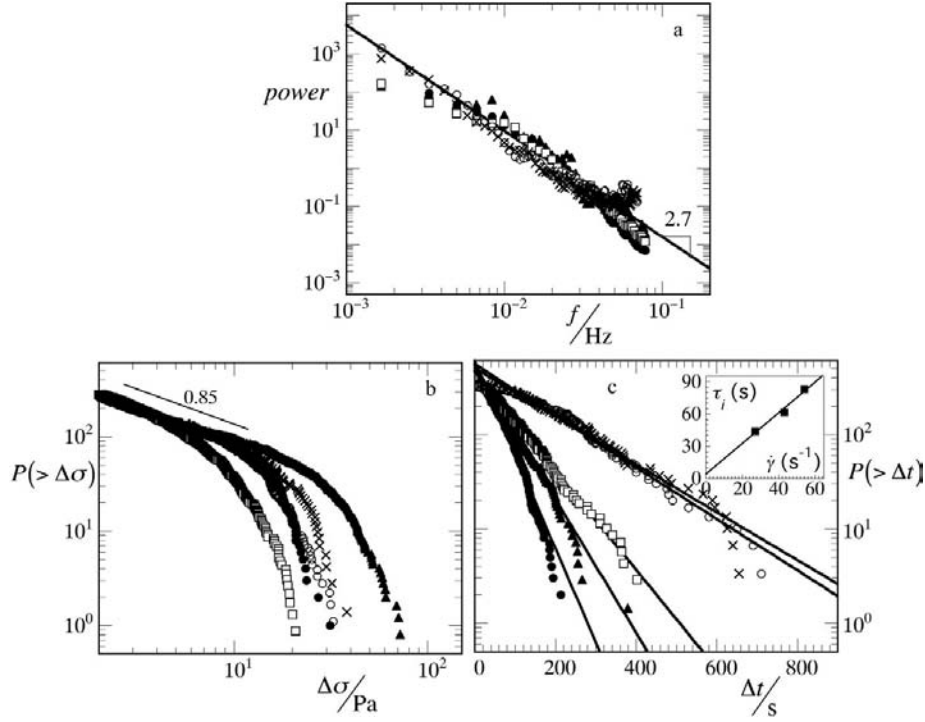


Figure 11.3: a) Power spectra obtained by Fourier transformation of the raw stress signal. b) Cumulative distributions of the stress-drop $\Delta\sigma$ of fractures. c) Cumulative distributions of the intervals Δt between fractures, drawn lines are fits to Poisson distributions. All for various shear rates and relaxation times: $\dot{\gamma}\tau_0 = 1.0$ and $\tau_0 = 37$ ms (i.e. $T = 10^\circ\text{C}$, \bullet), $\dot{\gamma}\tau_0 = 1.6$ and $\tau_0 = 37$ ms (\blacktriangle), $\dot{\gamma}\tau_0 = 2.0$ and $\tau_0 = 37$ ms (\square), $\dot{\gamma}\tau_0 = 1.0$ and $\tau_0 = 96$ ms (i.e. $T = 3^\circ\text{C}$, \circ), $\dot{\gamma}\tau_0 = 1.0$ and $\tau_0 = 107$ ms (i.e. $T = 2^\circ\text{C}$, \times) Insert in c) shows the dependence of the decay time τ_i for the interval distribution between fractures as a function of applied shear rate.

The limits on the stress fluctuations can be explained on the basis of the constitutive relation that underlies the shear banding behavior, which we presented in Chapter 10. The principal ingredient in this mean-field model is that flow enhances dissociation of the junctions. The reason for this is that the shear flow leads to elongation of the bridging chains, resulting in an elastic pulling force on the junctions:

$$f \simeq \frac{k_B T}{\xi} \tau \dot{\gamma} \quad (11.1)$$

Here ξ is the typical dimension of a chain in the flow gradient direction (we use $\xi = 2.5$ nm, estimated from the plateau modulus), so that the stretching rate is

roughly $\dot{\gamma}\xi$, while the entropic spring constant is $k_B T/\xi^2$. τ is the average lifetime of a junction, i.e. the typical time during which the chains are stretched before they dissociate. The lifetime τ is a function of the shear rate. Assuming that junction dissociation is an activated process [15], we can write

$$\tau = \tau_0 \exp\left(-\frac{f\delta}{k_B T}\right) = \tau_0 \exp\left(-\frac{\dot{\gamma}\tau\delta}{\xi}\right) \quad (11.2)$$

giving an implicit equation for τ , in which δ is the length over which the force acts, i.e. the length of the alkyl tail (here $\delta = 1.8\text{nm}$). We simplify this by expanding the exponential, which gives:

$$\tau = \frac{\tau_0}{1 + \delta\dot{\gamma}\tau_0/\xi} \quad (11.3)$$

For small shear rates, $\dot{\gamma}\tau_0 \ll 1$, sticker dissociation is unaffected by the shear rate, $\tau \approx \tau_0$. For high shear rates, $\dot{\gamma}\tau_0 \gg 1$, the average lifetime is equal to the time it takes to stretch the chain so far that the force becomes $k_B T/\delta$, i.e. $\tau \approx \xi/\delta\dot{\gamma}$.

As derived in Chapter 10, the steady-state concentration of bridges can be written as

$$n_b = \frac{Kn}{1 + K} \quad (11.4)$$

where n is the total concentration of chains (loops and bridges) and $K = k_a/k_d = k_a\tau$, with k_a and k_d the association and dissociation rate respectively. We assume that the equilibrium constant K_0 in rest is constant when τ_0 is varied ($k_a = K_0/\tau_0$), with $K_0 = 0.1$ found from the experimentally determined ratio of bridges to loops (results not shown). The shear stress is determined by the number of active bridges and the average force per bridge, which both depend on the shear rate:

$$\sigma = \xi n_b f + \eta_{eff} \dot{\gamma} = \left(\frac{k_a n \tau^2 k_B T}{1 + k_a \tau} \right) + \eta_{eff} \dot{\gamma} \quad (11.5)$$

with η_{eff} the high-shear viscosity, corresponding to the disrupted network (here $\eta_{eff} \approx 0.5 \text{ Pa s}$) and τ given by Eqn.11.3. In Fig.11.1a, this equation is plotted together with the experimental flow curve.

The decreasing part of this curve is mechanically unstable and corresponds to the regime where shear banding and the stress fluctuations are observed. Clearly, no matter how the two shear bands arrange themselves, the stress in this region is bounded by the maximum and the minimum in the stress-shear rate curve. Our microscopic model predicts that the loop becomes more pronounced if the microscopic relaxation time τ_0 increases (Fig.11.4a), which is in good agreement with the experimentally observed bandwidths of the stress fluctuations (Fig.11.4b).

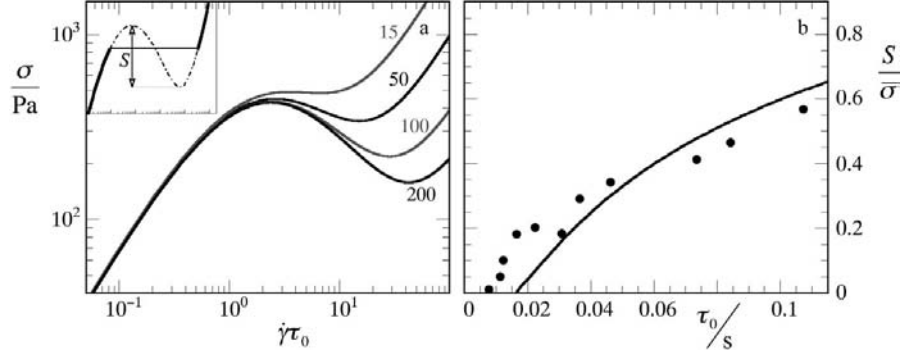


Figure 11.4: a) Flow curves predicted by the microscopic constitutive relation, Eqn.11.5, for various relaxation times τ_0 (given in ms). Inset illustrates the metastable loop (dotted line), the steady-state tie-line (horizontal plateau) and the definition of the predicted bandwidth S . b) Experimentally determined bandwidth of the stress fluctuations, given as the difference between maximum and minimum stress, relative to the average stress $\bar{\sigma}$. Drawn line is the prediction of our model. Note that the loop in the flow curve, and with that the shear banding behavior, disappears for $\tau_0 \ll 0.02\text{s}$.

The 'quiescent' intervals between two events show exponential (Poisson) distributions (Fig.11.3c) and display a cut-off at long interval times that is related to the cut-off in fracture magnitudes discussed above. The Poisson behavior implies that the intermittent fracture events occurring at different times are not correlated, in other words there is no memory of past fracture events. The reason for this lack of memory could be that the material quickly 'heals' once a fracture is terminated, since the microscopic relaxation time of the material is between 30-100 ms in this study, much shorter than the typical time between fracture events.

The average interval time τ_i between two fracture events is on the order of 10-100 seconds. This is roughly a thousand times longer than the microscopic relaxation time of the material, suggesting that the stress build-up is a process that involves the creation of many junctions. As seen in Fig.11.3c, an increase of the microscopic relaxation time (from 36 to 107 ms) leads to an increase in τ_i (from 40 to 170 s): as the formation of single connections is slowed down, the collective build-up process is also slower. Moreover, it can be seen that the interval time increases approximately linearly with the applied shear rate (inset of Fig.11.3c). The scenario that we propose is that the formation of new connections (association) across the gap is hindered by the velocity gradient between two neighboring fluid elements, as the average contact time between two nodes decreases.

11.4 Conclusion

In this Chapter we have presented a simple physical interpretation of a seemingly complex behavior in the banded flow of a transient polymer network. Previously, the apparently chaotic rheological responses of shear-banded soft materials were attributed to mechanical instabilities at or near the interface between the two bands [9, 16]. In this Letter we have shown that these fluctuating stresses can also be seen as the tell-tale of critical fluctuations, of a system in a self-organized critical state. This opens up new possibilities, as concepts known from the study of equilibrium critical phenomena now can be employed to understand these non-equilibrium phase transitions.

References

- [1] Sprakel, J.; Spruijt, E.; Cohen Stuart, M. A.; Besseling, N. A. M.; Lettinga, M. P.; van der Gucht, J. *Soft Matter* **2008**, *4*, 1696.
- [2] Olmsted, P. D. *Rheol. Acta* **2008**, *47*, 283.
- [3] Bak, P. *How Nature Works: The Science of Self-Organized Criticality*; Copernicus, New York, 1996.
- [4] Serero, Y.; Aznar, R.; Porte, G.; Berret, J. F.; Calvet, D.; Collet, A.; Viguier, M. *Phys. Rev. Letters* **1998**, *81*, 5584.
- [5] Annable, T.; Buscall, R.; Ettelaie, R.; Whittlestone, D. *J. Rheol.* **1993**, *37*, 695.
- [6] Michel, E.; Appell, J.; Molino, F.; Kieffer, J.; Porte, G. *J. Rheol.* **2001**, *45*, 1465.
- [7] Meins, J. F. L.; Tassin, J. F. *Macromolecules* **2001**, *34*, 2641.
- [8] Ganapathy, R.; Sood, A. *Phys. Rev. Letters* **2006**, *96*, 108301.
- [9] Fielding, S. M. *Soft Matter* **2007**, *3*, 1262.
- [10] Feder, H.; Feder, J. *Phys. Rev. Letters* **1991**, *66*, 2669.
- [11] Brace, W. F.; Byerlee, J. D. *Science* **1966**, *153*, 990.
- [12] Berret, J. F.; Serero, Y. *Phys. Rev. Letters* **2001**, *87*, 048303.
- [13] Gutenberg, B.; Richter, C. F. *Seismicity of the Earth and Associated Phenomena*; Princeton Univ. Press, Princeton, 1954.
- [14] Knopoff, L. In *Disorder and Fracture, NATO ASI Series B: Physics vol.235*; Charmet, J., Roux, S., Guyon, E., Eds.; Plenum, New York, 1990; chapter 4: The phenomenology of earthquake occurrence.
- [15] Tanaka, F.; Edwards, S. F. *Macromolecules* **1992**, *25*, 1516.
- [16] Eggert, M. D.; Kumar, S. *J. Colloid Int. Sci.* **2004**, *278*, 234.

Chapter 12

MR velocimetry of telechelic polymer networks

In this Chapter we discuss the construction of a home-built rheo-NMR set-up for studying the flow of fluids under controlled shear with Magnetic Resonance techniques. We also present some initial, non-trivial results for the flow profiles of a shear-banded telechelic polymer network. The rheometer consists of a highly-concentric couette geometry that is mounted in a low-field ($0.7 \text{ T} = 30.7 \text{ MHz}$) NMR device. Velocity profiles measured with a Pulsed Field Gradient Spin Echo (PFGSE) imaging sequence in shear-banded telechelic polymer networks show good agreement with results from laser Doppler velocimetry measurements on the same material (as shown in Chapter 10), confirming that the current set-up works properly. Moreover, as our MRI sequence gives access to absolute fluid velocities, we can unequivocally measure the amount of wall slip in these inhomogeneous flows.

The work presented in this Chapter is a collaboration with Frank Vergeldt, Henk van As & John Philippi of the Wageningen NMR Centre:

In the previous Chapters we have discussed the shear banding transition in associative thickener networks. Studying these types of shear-induced phase transitions relies mainly on two different approaches. The first is rheometry, in which the mechanical properties of the sample (e.g. viscosity) can be monitored as a function of the applied deformation rate or stress. Rheological data can give strong evidence for the occurrence of a mechanical instability, for example a plateau in the stress versus shear rate indicates shear banding. The second technique is velocimetry, which is the spatially-resolved measurement of the local fluid velocity, across the sample in the direction(s) of interest. Since shear banding is the formation of 2 (or more) zones in the sample that differ in shear rate (i.e., velocity gradient), velocimetry measurements are essential to prove the occurrence of such a flow instability.

A variety of velocimetry techniques is currently available for measuring fluid velocity profiles under controlled shear, such as Laser Doppler Velocimetry (LDV, see Chapter 10), Particle Imaging/Tracking Velocimetry (PIV/PTV) [1] and ultrasonic velocimetry (USV) [2]. Each of these techniques has its own merits and drawbacks in terms of spatial and temporal resolution and sample demands. While the optical techniques (LDV, PIV, PTV) generally have a very good spatial resolution, they require completely transparent samples. PIV and USV can record velocity profiles very quickly, allowing great temporal detail in, for example, start-up experiments, yet both techniques require the addition of probe particles, often several to tens of micron in diameter. This could seriously alter the local flow field, and in this way affect the manifestation of the instability of interest. For a comprehensive overview of velocimetry techniques, and other experimental probes of shear banding, we refer to a recent paper by Sebastien Manneville [3].

An alternative to these methods is Magnetic Resonance Velocimetry (MRV), in which NMR imaging (NMRi or MRI) techniques are used to measure velocity profiles of samples that are subjected to shear flow inside an NMR magnet [4, 5]. In a rheo-NMR set-up, in addition to performing velocimetry experiments, many other NMR techniques (spectral NMR, spin-relaxation measurements) may be employed to study for example inhomogeneities in density (spin-relaxation measurements) or changes in molecular structure (spectral NMR) in the sample of interest under shear. Moreover, the technique is non-invasive (no probe particles required), allows the analysis of even the most turbid samples and can be used to build up 2D or even 3D images of the flow field, while the velocimetry techniques discussed above are limited to 1 (LDV, ultrasonic velocimetry) or 2 dimensional (PIV) flow field visualization.

In this Chapter we discuss the development of, and preliminary results on, a

home-built rheo-NMR set-up. The main motivation for this venture is the fact that much of the rheological research carried out within Wageningen University concerns 'real' systems, such as paints and foods. Rheo-NMR offers a versatile new tool for the study of these very complex, and often opaque, systems.

The first report of performing NMR measurements on a sample under controlled shear flow, dates from 1990, when Nakatani, Polliks and Samulski [6] investigated broadening of the ^1H spectrum of a polymer melt subjected to shear flow in a cone-plate geometry. A year later, Xia and Callaghan [7] demonstrated that NMR imaging techniques could also be used to study the flow of complex fluids. In their experiments they related shear-thinning effects of an entangled polymer solution to deviations from Poiseuille flow when the sample was pumped through a narrow capillary. The MR velocimetry approach used in that paper formed the basis for a wide range of pioneering publications by the group of Paul Callaghan over the past 15 years, on a wide variety of systems, such as wormlike micelles [8], lamellar surfactant phases [9], suspensions of hard-spheres [10] and colloidal glasses [11]. In more recent years, several research groups have started participating in rheo-NMR research, leading to an ever-expanding range of NMR techniques and flow geometries for studying the flow of complex fluids under well-defined conditions. An overview of the (current) developments in this field can be found in [4, 5, 12].

12.1 Rheo-NMR set-up

The rheometer (see Figs. 12.1 and 12.2) consists of a concentric cylinder (couette) measuring cell, a driving shaft and a motor. Both the measuring cell and the driving shaft are constructed from PEEK (polyetheretherketon), which was chosen because of its high strength and durability, resistivity to almost any solvent and NMR transparency. The measuring cell consists of a solid inner cylinder with a diameter of 27.0 mm and a double-walled cup, with an inner diameter of 29.8 mm (gap size = 1.4 mm). The inner cylinder is driven by means of a driving shaft that is connected to the motor (Maxon RE30) via a gearbox. With the current combination of motor and gearbox, speeds between 1 and 1000 rpm are accessible, corresponding to a shear rate range of approximately $1\text{-}1000\text{ s}^{-1}$.

To prevent interference of the main magnetic field of the NMR set-up with the motor operation, it needs to be placed at a sufficient distance (in this case approximately 1 meter) from the center of the magnet. To accomplish a high concentricity of the couette cell with this long transfer distance, the driving shaft is guided by bearings of glass beads coated with a teflon layer on 4 positions along the

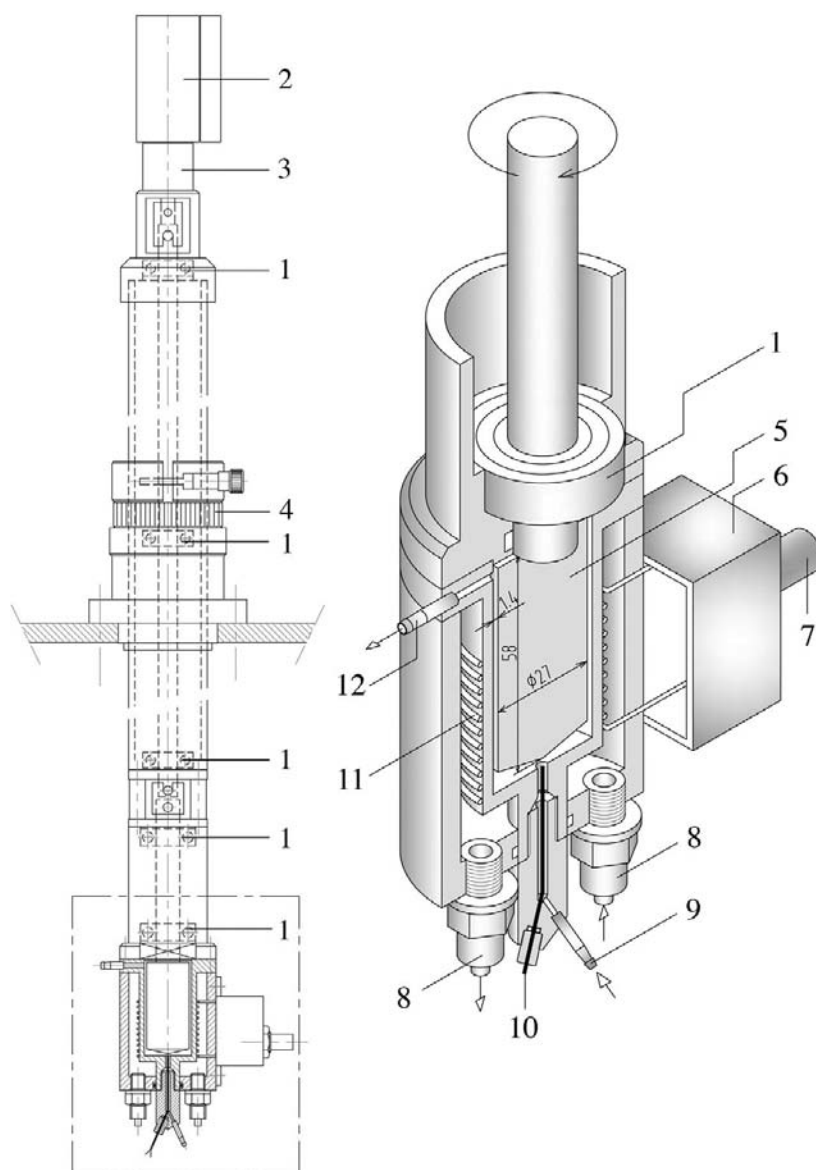


Figure 12.1: Schematic depiction of the rheo-MRI set-up (left) and detail image of the measuring cell (right); 1) tefflon-coated glass ball bearing, 2) motor, 3) gearbox, 4) position fine-tuning, 5) bob ($R = 13.5$ mm, gap size = 1.4 mm), 6) RF unit, 7) RF connector, 8) inlet/outlet cooling system, 9) fill tube, 10) thermocouple, 11) RF coil, 12) sample overflow.

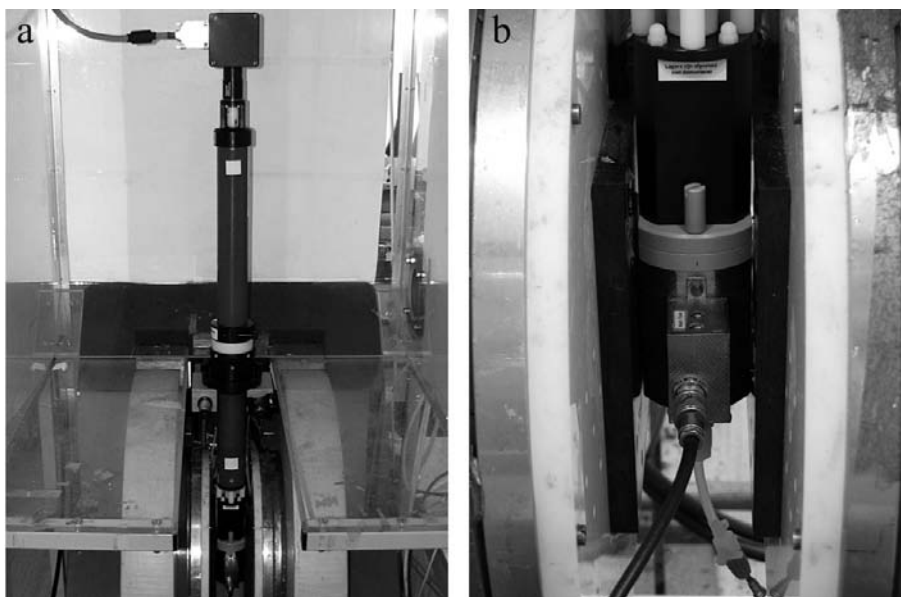


Figure 12.2: Photographs of a) the rheometer mounted in the NMR magnet and b) close-up of the measuring cell.

length of the rheometer. The concentricity of the Couette cell was measured to be 5 micrometers, which is similar to (or better than) the concentricity of commercially available rheometer cells.

The radio frequency (RF-) coil is wrapped around the outer wall of the couette cell, i.e. housed in the cavity in the double-walled measuring cup. It consists of 9 turns of a silver wire ($d = 1$ mm), over a length of 18 mm and with a total diameter of 32 mm. The RF-coil is connected to a control unit, for tuning and matching the RF-field to the resonance frequency of ^1H -nuclei.

To cool the sample, dried compressed air is guided through a heat exchanger immersed in a water bath at 2 °C and subsequently flushed through the hollow-walled measuring cup. As this cup also houses the RF-coil, no liquid cooling agents could be used. By adjusting the flux of cold air, the temperature of the sample could be controlled between 20 and 35 °C. The temperature of the sample can be monitored with a thermocouple, inserted through the bottom of the measuring cell.

The entire rheometer is mounted in the NMR magnet, by means of brackets attached to the NMR housing and a mounting system fixed to the rheometer shaft. Micro-manipulators in this mounting system allow accurate positioning of the cell to the center of the magnetic field. The rheometer set-up was constructed by

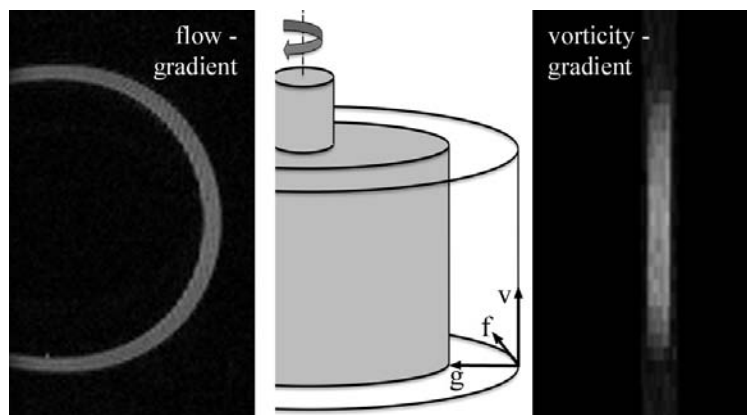


Figure 12.3: Two MRI cross-sections of the measuring cell, filled with water, in the flow-gradient (left) and vorticity-gradient (right) plane. In the schematic drawing of the measuring cell (center), the axes of the flow (f), gradient (g) and vorticity (v) direction are indicated.

Ontwikkelwerkplaats AFSG (Wageningen).

All MRI measurements were conducted on a 0.7 T, resulting in a Larmor resonance frequency for protons of 30.7 MHz, home-built NMR system consisting of a Bruker Avance console (Bruker BioSpin, Karlsruhe, Germany), a Bruker electromagnet stabilized by an external ^{19}F lock unit, and an actively shielded 1 T/m gradient set with planar geometry (Resonance Instruments Ltd, Witney, UK), providing a gap of 5 cm between the plates for housing the rheometer.

12.2 MR velocimetry

For NMR flow imaging a PFG-SE-TSE sequence is used. This sequence is a combination of a Pulsed Field Gradient (PFG) Spin Echo (SE) sequence for flow encoding (q -space imaging) and a Turbo Spin Echo sequence for fast imaging [13]. Typical parameters for flow encoding were gradient pulses of 1 ms, varied in 32 steps from -0.243 T/m to 0.228 T/m to sample the inverse displacement space (q -space), and a flow encoding time of 5 ms. Typical imaging parameters were a field-of-view of $2.6 \times 32 \text{ mm}^2$ of 32×32 pixels resulting in an in-plane resolution of $0.081 \times 1.0 \text{ mm}^2$ with the highest resolution in the gradient and the lower resolution in the vorticity direction (see Fig.12.3). A 1 mm slice was selected in the flow direction. Further relevant parameters are the turbo factor of 4, the echo time of 2.96 ms, the spectral width of 25 kHz, the number of averages of 4, and the repetition time

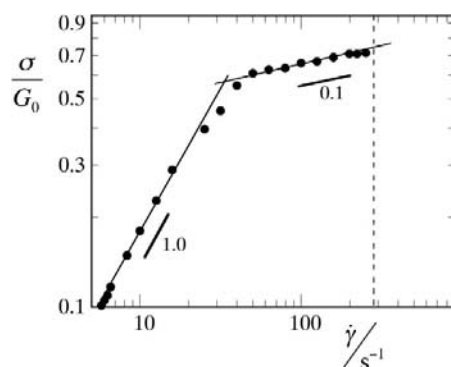


Figure 12.4: Shear stress σ , normalized by the plateau modulus G_0 , versus shear rate $\dot{\gamma}$ for a 25 g/L solution of C₁₈20k associative polymer in water at $T = 25^\circ\text{C}$. Drawn lines indicate the two main flow regimes; at low shear rates ($< 25 \text{ s}^{-1}$) the flow is Newtonian ($\sigma \propto \dot{\gamma}$), at higher shear rates ($> 50 \text{ s}^{-1}$) the system is strongly shear thinning ($\sigma \propto \dot{\gamma}^{0.1}$), indicative of a shear banding transition. The dotted line indicates where the Weissenberg instability (see Chapter 10) occurs.

of 3 s, resulting in a total experiment time of approximately 51 minutes.

For more information on the PFG-SE-TSE method, we refer to [13], and for more general information on NMR microscopy and rheo-NMR methods see [4, 14].

12.3 Experimental details

For the measurements presented below we have used the same material as in Chapter 11, i.e. a 25 g/L aqueous solution of an octadecyl-modified PEO of 20 kg/mol (abbreviated as C₁₈20k. The cell was filled with 8 ml of the sample and left to equilibrate for 1h. For each new measurement another 45 minutes were taken after setting the rheometer to the appropriate speed and before commencing the measurement, to allow the sample to reach a steady state. The flow curve was measured in a couette geometry on an Anton Paar MCR501 rheometer. All measurements are carried out at a temperature of 25°C .

12.4 Preliminary Results

In Fig.12.3 two MRI cross-sections of the measuring cell are shown. The MRI image in the flow-gradient plane, taken in the center of the vorticity direction shows the circular shape of the couette geometry. In the MRI image of the vorticity-gradient

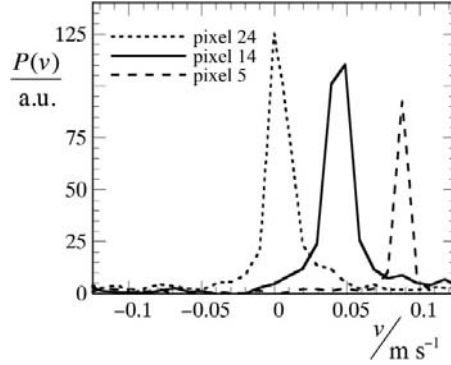


Figure 12.5: Examples of pixel propagators, the main output from the MRV measurements, showing the distribution of measured velocities in 3 pixels along the gradient direction, i.e. one close to the stationary wall (pixel 24), one in the center of the gap (pixel 14) and one close to the rotating bob (pixel 5), obtained at $\dot{\gamma} = 65 \text{ s}^{-1}$.

plane we can see the limits of the RF-coil, i.e. where the image quality starts to decrease at the top and bottom of the image. As the coil ($L = 18 \text{ mm}$) does not encase the entire length of the measuring cell (58 mm), accurate imaging is limited to a portion of the gap in the vorticity direction.

A flow curve, i.e. shear stress versus shear rate, for a telechelic polymer network at 25°C is shown in Fig.12.4. We can distinguish the two main flow regimes, discussed in more detail in Chapter 10, i.e. a Newtonian flow at low shear rates and strong shear thinning at higher shear rates. In the shear thinning regime we find that $\sigma \propto \dot{\gamma}^{0.1}$, rather than a true plateau in the stress as expected for shear banding. This is attributed to the curvature of the couette cell, giving a slightly inhomogeneous stress field across the gap. At even higher shear rates, a Weissenberg instability occurs (see Chapter 10).

The main output from the PFGSE-TSE velocimetry experiments are the so-called pixel propagators, i.e. the distribution of measured displacements over the sampling interval Δ for a given pixel in the field-of-view. Some examples of pixel propagators are shown in Fig.12.5, where the displacements have already been transformed into actual fluid velocities, for three different positions along the gap of the couette cell.

From the propagators, the fluid velocity profiles can be calculated. Here we take the average velocity from a pixel propagator at a given position along the gap, after proper baseline correction, and average this over 8 pixels (i.e. 8 mm) in the vorticity direction. In this approach, together with the chosen slice selection of 1

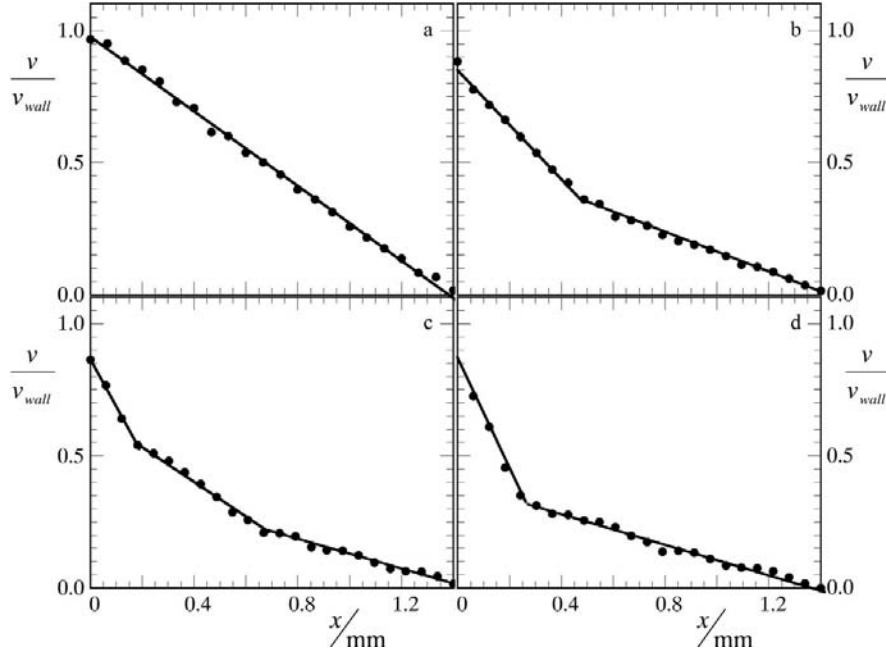


Figure 12.6: Local fluid velocity v , with respect to the applied wall velocity v_{wall} , versus position x across the gap of a couette cell, as measured with MR velocimetry. The sample is a 25 g/L solution of C₁₈20k associative polymers in water ($T = 25^\circ\text{C}$), at various shear rates; a) 40 s^{-1} , b) 70 s^{-1} , c) 90 s^{-1} and d) 120 s^{-1} . Lines are drawn to guide the eye.

mm in the flow direction and the measurement time of approximately 50 minutes, we obtain spatially and temporally averaged velocity profiles. This results in a good signal-to-noise ratio on the velocity profiles, but information on microscopic spatiotemporal dynamics (as discussed in Chapter 11) is lost.

Some velocity profiles measured with MRV on our associative polymer system, are shown in Fig.12.6. In agreement with the flow curve, we observe linear velocity profiles, indicative of Newtonian flow, at all shear rates $< 50\text{ s}^{-1}$ (Fig.12.6a), and kinked velocity profiles, the sign of shear banding, for shear rates $\geq 50\text{ s}^{-1}$ (Fig.12.6b-d), which is the regime where we also observe the (quasi)plateau in the flow curve (Fig.12.4). The progression of the banded flow with increasing shear rate, which is analyzed in more detail in Fig.12.7, looks very similar to what we measured with laser Doppler velocimetry, as discussed in Chapter 10. The banding starts with the decomposition of the flow into two bands (Fig.12.6b). At higher shear rates there is a transition to a 3-banded flow (Fig.12.6c) and when the shear rates is further increased, the high-shear band increases in size and shear rate

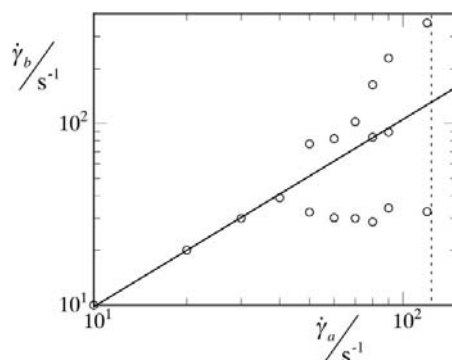


Figure 12.7: Applied shear rate $\dot{\gamma}_a$ versus measured shear rate(s) $\dot{\gamma}_b$ across the gap. Drawn line indicates $\dot{\gamma}_a = \dot{\gamma}_b$ as expected for homogeneous flows with stick boundary conditions. The dotted line indicates where the Weissenberg instability (see Chapter 10) occurs.

(Fig.12.6d).

With MR velocimetry absolute fluid velocities are measured. This allows us to unambiguously measure the amount of wall slip near the rotating inner wall. The velocity profiles show that the fluid velocity near the inner cylinder is a 100% of the applied wall velocity (stick boundary conditions) for Newtonian flows (Fig.12.6a), but decreases to approximately 80 - 90% (moderate slip) for the non-linear flows (Fig.12.6b-d). Other techniques, such as Laser Doppler Velocimetry, calibrate the fluid velocity to settings in which no slip is expected, yet are not able to give an absolute measure for the amount of wall slip, as is possible with MR velocimetry. Note that the observation of wall slip in shear-banded flows is not uncommon [15, 16].

12.5 Conclusion and Outlook

The initial results on our home-built rheo-NMR set-up look promising. Velocity profiles in shear-banded polymer networks, measured with MR velocimetry, show good agreement with velocity profiles on the same sample with laser Doppler velocimetry (see Chapter 10). Moreover, MR velocimetry measures the absolute magnitude of the local fluid velocities, which allows for more detailed studies of phenomena such as wall slip that often accompany shear-induced transitions.

12.6 Acknowledgements

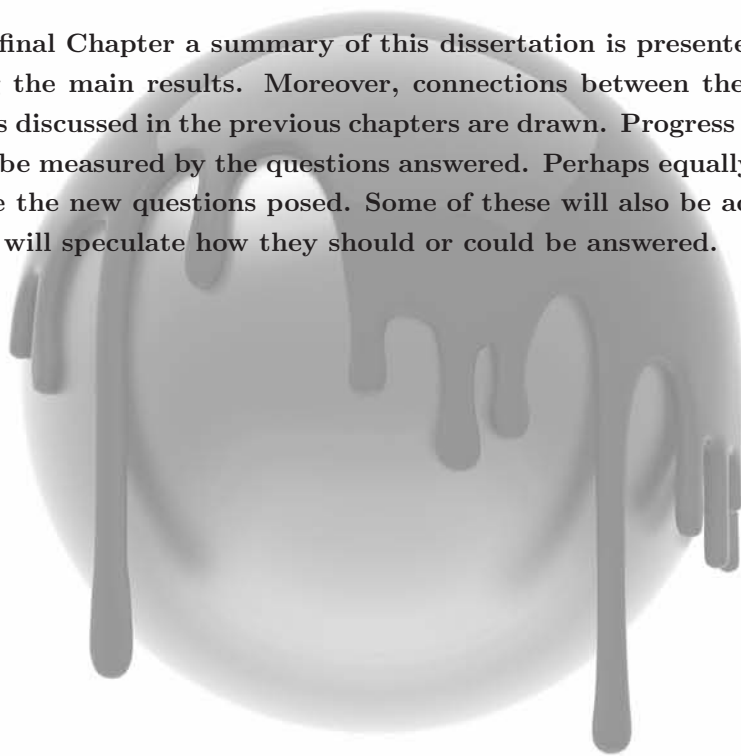
JS gratefully acknowledges Frank Vergeldt, Henk van As, John Philippi and Edo Gerkema of the Wageningen NMR Centre for their participation and pleasant co-operation in this project, and Hans de Rooij and Hans Meijer for designing and constructing the set-up.

References

- [1] Marin-Santibanez, B. M.; Perez-Gonzales, J.; de Vargas, L.; Rodriguez-Gonzalez, F.; Huelsz, G. *Langmuir* **2006**, *22*, 4015.
- [2] Sandrin, L.; Manneville, S.; Fink, M. *Appl. Phys. Lett.* **2001**, *78*, 1155.
- [3] Manneville, S. *Rheol. Acta* **2008**, *47*, 301.
- [4] Callaghan, P. T. In *Encyclopedia of Nuclear Magnetic Resonance. Volume 9*; Grant, D. M., Harris, R., Eds.; Wiley & Sons, Chichester, 2002; chapter Rheo-NMR; A New Window on the Rheology of Complex Fluids.
- [5] Bonn, D.; Rodts, S.; Groeninck, M.; Rafai, S.; Shahidzadeh-Bonn, N.; Coussot, P. *Annu. Rev. Fluid Mech.* **2008**, *40*, 209.
- [6] Nakatani, A. I.; Poliks, M. D.; Samulski, E. T. *Macromolecules* **1990**, *23*, 2686.
- [7] Xia, Y.; Callaghan, P. T. *Macromolecules* **1991**, *24*, 4777.
- [8] Lopez-Gonzales, M. R.; Holmes, W. M.; Callaghan, P. T. *Soft Matter* **2006**, *2*, 855.
- [9] Lutti, A.; Callaghan, P. T. *Eur. Phys. J. E* **2007**, *24*, 129.
- [10] Wassenius, H.; Callaghan, P. T. *Eur. Phys. J. E* **2005**, *18*, 69.
- [11] Rogers, S. A.; Vlassopoulos, D.; Callaghan, P. T. *Phys. Rev. Lett.* **2008**, *100*, 128304.
- [12] Callaghan, P. T. *Rep. Prog. Phys.* **1999**, *62*, 599.
- [13] Scheenen, T. W. J.; van Dusschoten, D.; de Jager, P. A.; van As, H. *J. Magn. Reson.* **2000**, *142*, 207.
- [14] Callaghan, P. T. *Principles of Nuclear Magnetic Resonance Microscopy*; Oxford University Press, New York, 1993.
- [15] Manneville, S.; Colin, A.; Waton, G.; Schosseler, F. *Phys. Rev. E* **2007**, *75*, 061502.
- [16] Holmes, W. M.; Callaghan, P. T.; Vlassopoulos, D.; Roovers, J. *J. Rheol.* **2004**, *48*, 1085.

Summary & General Discussion

In this final Chapter a summary of this dissertation is presented, highlighting the main results. Moreover, connections between the various subjects discussed in the previous chapters are drawn. Progress can only in part be measured by the questions answered. Perhaps equally important are the new questions posed. Some of these will also be addressed and we will speculate how they should or could be answered.



Coatings, although not always directly observable, play an important role in everyday life. They extend the lifetime of materials by protecting them against, e.g., corrosion, microbial attack and weathering, provide surfaces with specific properties (repellency, anti-fouling, etc.) and literally add color to our lives. The process of administering coatings often involves liquid carriers that allow transfer of coating-forming materials from a volume to a surface; such carriers are commonly known as paints.

In recent years, there has been a strong effort to replace traditional solvent-based coatings with water-based systems. Whereas solvent-based paints are (still) superior in performance compared to waterborne paints, they pose a serious threat to the environment and the health of the consumers using these product. The problem is the release of large amounts of volatile organic compounds (VOCs) into the atmosphere during the drying of such paints. The development of water-based paints with the same performance as solvent-based products is an important step towards accomplishing the further phasing-out of VOC-rich coatings.

One of the key ingredients in modern waterborne latex paints are associative thickeners, which are added as flow modifiers to establish the desired flow properties of such formulations. For this reason, industry has developed a strong interest in a thorough understanding and control of aqueous associative thickener systems.

Water-based paints typically are even more complex systems. In addition to water and thickeners they contain various particulate components, such as pigments and latex (binder) particles, and a wide range of additives, such as surfactants and co-solvents. With so many ingredients, the number of interaction pairs is very large. To accomplish a fundamental understanding of associative thickeners in these systems, we have adopted a bottom-up approach in this thesis. We started from pure thickener solutions in thermal and mechanical equilibrium, and along the way increased the complexity by bringing solid surfaces and non-equilibrium circumstances into play. In this way we have tackled some of the questions that emerged from industry. Moreover, we have tried to show that these systems are a true playground for soft matter¹ scientists, with interesting physics occurring on many time and length scales.

¹soft matter: a variety of states (for example colloidal suspensions or polymer solutions and gels) that are easily deformed by thermal stresses or fluctuations, with predominant physical behavior occurring on energy scales on the order of the thermal energy $k_B T$ ($\approx 4 \cdot 10^{-21}$ Joules at room temperature).

Associative Polymer Self-Assembly

The first part of this thesis dealt with the equilibrium supramolecular assembly of polymeric surfactants in general and telechelic polymers² in particular.

In Chapter 2 we proposed a comprehensive analytical model for the self-assembly of polymeric surfactants. This conceptually simple model consists of a driving force for micelle formation that comes from classical nucleation theory and an opposing force that hinders the same process described by polymer brush theory. A subtle balance between these two forces governs the micellization. With this model we are able to predict various properties such as critical micelle concentrations (i.e. the concentration at which micelles first start to appear), micellar aggregation numbers (i.e. the number of molecules per micelle) and their distributions. The main advantage of this analytical approach is that the physics behind the self-assembly remain transparent.

In Chapters 3 and 4 we turned to a numerical technique, the self-consistent field theory (SCFT) of Scheutjens and Fleer³, to solve the more complex problem of the self-assembly of telechelic polymers into micelles and networks, and to predict the phase separation boundaries in the regime in between these two states (see Figure 12.6 and section 1.2 for more details).

Once the phase behavior of these associative polymers was unravelled using this numerical tool, we developed several scaling arguments to further clarify the physics underlying the phase behavior of associative polymer systems. The essential features of the phase diagram of telechelic polymers were mapped out in this way. This enabled us to define design rules that can be employed to synthesize thickeners with a desired percolation threshold while being free of phase separation.

Interpreting the results obtained with self-consistent field models for self-assembly can be troublesome in the sense that the underlying physics are not always transparent. In Chapter 2 we have shown how the thermodynamic quantities found from self-consistent field calculations map onto the total free energy landscape, elucidating the thermodynamics behind SCFT for micellar systems. Several criteria that are often used in self-consistent field modeling, such as the 'stability constraint' used to predict the cmc and the use of the curvature of the free energy saddle points versus aggregation number to assess micelle polydispersity [1], could be justified in this way.

²telechelic associative polymer: water-soluble linear macromolecule with a water-insoluble, associating, block at both ends of the main polymer chain.

³Scheutjens-Fleer theory: a mean-field lattice-based method, developed in Wageningen in the 1980's by Jan Scheutjens and Gerard Fleer, in which thermodynamic properties are computed by numerically solving the governing statistical mechanical equations.

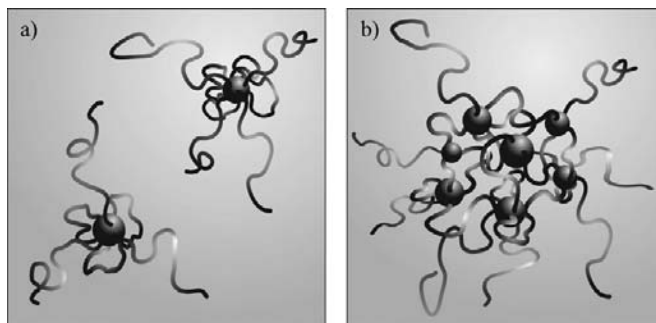


Figure S1: Illustration of the possible mechanisms in which monofunctional chains prevent phase separation in telechelic polymer solutions. a) the monofunctional chains enter the flowerlike micelles, and due to their extension outside the flowerlike corona they cause an additional repulsion between micelles that hinders phase separation. b) small domains of a demixed, condensed phase are stabilized on the outside by the monofunctional chains, forming supermicelles similar to casein micelles present in milk.

When micelles formed by the telechelic polymers are close enough together they will interact. Whereas simple surfactant micelles only experience a repulsive force arising from the compression of the micellar coronas⁴, micelles from telechelic polymers display a significant attraction. This attraction is the result of an increase in conformational entropy of the corona chains when they have the additional possibility to form bridges between the two micelles in addition to forming loops in the corona. When this attraction is strong enough, i.e. more than several $k_B T$, it can lead to a liquid-liquid phase separation (see Chapter 4).

Strangely, in experimental systems phase separation is much more rare than one might expect based on our calculations. Moreover, even different batches of the same polymer can vary in behavior whether phase separation is found or not. This raises the question what is causing these discrepancies. In our modeling, we assumed that all chains had exactly two hydrophobic stickers at their chain ends. In practice, the functionalization is never perfect and there is a distribution of di-, mono- and unfunctionalized chains present in each sample. We can think of two mechanisms in which the presence of monofunctional polymers prevents macroscopic phase separation, see Fig.S1.

First of all, the monofunctional chains might be part of individual flowerlike

⁴micelles are generally divided into two compartments: i) the core, that contains the insoluble blocks in the center of the micelle and ii) the corona, the outer layer of the micelle, that contains the soluble parts of the surfactants.

micelles and extend outside the flowerlike corona, as they are not able to form a loop (Fig.S1a). These extended arms give rise to an additional repulsive barrier between two micelles, hindering the micelles to cluster and eventually demix.

Another explanation, as illustrated in Fig.S1b, is that the combination of mono- and difunctional polymers leads to the formation of higher order assemblies. Finite sized domains of a phase-separated network structure might be stabilized on the outside by protruding chains of monofunctional polymers. A similar behavior is found in milk, where mixtures of various caseins (also diblocks and triblocks) spontaneously form supermicelles [2]. The size of these objects will depend on the ratio of mono- and difunctional chains. At high contents of monofunctional chains, one might find the structure illustrated in Fig.S1a.

Associative Polymers at Surfaces

In industry associative thickeners are often used as flow modifiers in products that also contain colloidal particles. This brings up the question, what effect telechelic polymers have on the stability of such colloidal suspensions. In practice, mixtures of associative polymers and colloids tend to be unstable, indicating the induction of attractive forces between the particles by the polymers. This is often attributed to bridging effects. In this thesis we have shown that, in dilute solutions of the polymers, indeed attractive interactions can be induced between two solid surfaces. However, the nature of this attractive force depends on the interactions between polymer and surface.

In Chapter 5 we demonstrated, with Colloid Probe (CP) -AFM experiments⁵, that the phase separation boundary for solutions of telechelic polymers can be shifted when they are confined between two very hydrophobic surfaces, leading to capillary condensation⁶. The attractive force resulting from this confinement-induced phase transition is due to the interfacial tension between the condensate and the dilute bulk liquid. The interfacial tension between the polymer-rich condensate and the polymer-poor bulk phase could be extracted from the experimental

⁵Colloid Probe AFM: a technique in which a micrometer-sized particle is glued onto an Atomic Force Microscopy (AFM) cantilever and is brought in vicinity of a flat surface, both immersed in the solution of interest. In the AFM, changes in the reflected light from a laser beam aimed at the top of the cantilever reveal small deflections of the cantilever. Because the cantilever acts as a spring, this deflection can be transformed into the interaction force between the particle and the flat surface.

⁶capillary condensation: the spontaneous condensation of a phase from an (under)saturated bulk phase, e.g., water from water vapor, induced by confining the bulk phase between two surfaces.

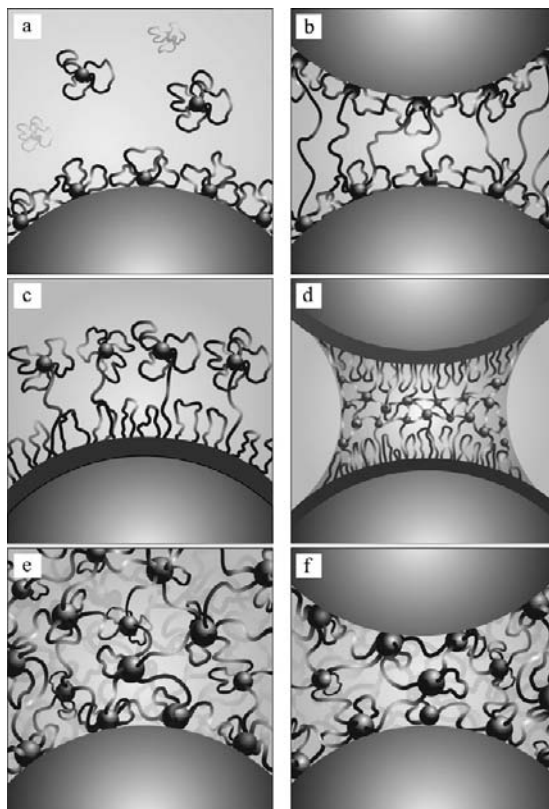


Figure S2: Illustration of the effect of polymer-particle interactions on the colloidal interactions induced by associative polymers. Weakly adsorbing associative polymer form a micellar layer on the particle surface (a), inducing a bridging attraction between two particles at close proximity (b). Associative polymers that strongly adsorb with their hydrophobic stickers form a wetting layer at the surface (c) causing a long-ranged capillary attraction between two of these particles (d). A particle dispersed in a network phase of the associative polymers (e), experiences repulsion due to hydrodynamic effects when a second particle approaches (f), and could also feel a short-ranged attraction due to depletion or bridging effects.

force curves and was found to be ultralow, i.e. 10^4 times smaller than the interfacial tension between water and air. Due to a combination of this ultralow interfacial tension and the small geometry of the experiments, we were able to measure capillary forces in full thermodynamic equilibrium for the first time.

Motivated by these experiments, we proposed a thermodynamic argument for capillary forces at saturation (i.e. 100% relative humidity in terms of water vapor)

in Chapter 6. The final expressions look very similar to what was derived by others previously [3], yet differ fundamentally in the arguments on which the derivation is based. In our approach, we simplified the thermodynamics by realizing that the Laplace pressure⁷ vanishes close to saturation. This was confirmed by SCF calculations and by a comparison with our earlier experiments.

This capillary effect is notably different from the molecular bridging attraction that we observed between hydrophilic surfaces in Chapter 7 of this thesis, and that has also been demonstrated for mildly hydrophobic surfaces by others [4]. A bridging attraction occurs when polymers are partly adsorbed on both of the opposing surfaces, which can only occur when the surfaces are close enough. Pulling the surfaces apart causes the polymer bridges to stretch out like springs, giving rise to a force that opposes the further increase of the separation between the surfaces. Since adsorption strongly decreases the dynamics of the polymers, these bridging processes were found to be significantly slower than the dynamics of bridge formation between two micelles in bulk solution, and also much slower than the capillary phenomena discussed above. With a simple kinetic model, we were able to describe the dynamics of bridge formation and disruption quantitatively, taking into account both molecular detail (size of the polymer backbone and length of the stickers) and macroscopic variables (the velocity with which the surfaces move with respect to each other).

The two types of attraction that we have studied in this dissertation have a significantly different manifestation. While the capillary forces are relatively weak, $O(10 \text{ pN})$, and long ranged (200-300 nm), the bridging forces are stronger, $O(1 \text{ nN})$, but significantly shorter ranged (10-50 nm).

So why do we observe capillary forces in one case and bridging forces in another? We believe that the answer lies in the differences in structure of the adsorbed polymer layer on different solid surfaces (see Fig.S2). As elaborated by Ligoure [5], the adsorption of micelles onto a surface can be considered as a wetting problem, which is modified by the presence of the micellar corona.

In general, these associative polymers have a strong tendency to form micelles with a spherical morphology, due to their highly asymmetric shape (small stickers and a long soluble backbone). When the interaction between the polymer and the surface is not particularly strong, the adsorbed layer will consist of admicelles (when the corona chains adsorb, Fig.S2a) or hemimicelles (when the hydrophobic tails adsorb). However, when the adsorption energy between the stickers and the surface is large enough, e.g., for the very hydrophobic surfaces used in Chapter 5,

⁷Laplace pressure: the pressure difference between the inside and the outside of a droplet caused by the interfacial tension acting between the two phases.

a flat brush-like layer may be formed by the telechelic polymers (Fig.S2c). Preliminary calculations using the self-consistent field theory (also used in Chapters 3, 4 and 6), show that such a transition between an inhomogeneous layer of adsorbed micelles and a homogeneous flat adsorption layer is indeed found already for small differences in adsorption energy between the alkyl tails and the solid surface.

For the brush-like layer formed on very hydrophobic surfaces, the local concentration of polymer chains at the interface can be high enough to induce clustering between the adsorbed layer and micelles in the bulk. In this way the formation of bridges between the surface layer and free micelles can result in a secondary adsorption layer (see Fig.S2c). Experimental evidence for such a process was given in Chapter 8. In other words, we can expect the local density of micelles to be enhanced close to a hydrophobic surface with respect to the bulk density. Such an increase in density extending out from the surface is called a (pre)wetting layer. When two of these wetting layers are brought in proximity, capillary condensation is inevitable (Fig.S2d and Chapter 5.).

On the other hand, when adsorption occurs in a micellar configuration (Fig.S2a), as is expected for the silica surfaces used in Chapter 7, the local concentration of telechelic polymer sticking out in the solution is not so strongly enhanced. As a result, the formation of a secondary layer of weakly bound micelles is less likely and capillary condensation does not occur. In this case we only observed the short-ranged bridging attraction (Fig.S2b).

In Chapter 8 we have studied the adsorption mechanism of telechelic polymer micelles from dilute solution onto an air-water interface, mimicking the adsorption of these polymers onto a very hydrophobic substrate. Kinetic tensiometry experiments showed three distinct stages of adsorption. In the first transport-limited process, flowerlike micelles diffuse towards and along the newly formed interface, while attaching onto the interface with their polymeric coronas. In the second, desorption-limited, step the micelles unfold and the micellar core spreads onto the interface. In the final stage, bridges between the adsorbed layer and bulk micelles are formed, leading to a secondary adsorption layer (see Fig.S2c). From dilute solution, this latter process is extremely slow (with a characteristic relaxation time of 60,000 seconds) as bridging requires the simultaneous release of a sticker from the adsorbed layer and the nearby presence of a bulk micelle. These experiments suggest that, as speculated above, a secondary adsorption layer can indeed be formed on very hydrophobic surfaces.

The above mentioned results apply to dilute polymer solutions, i.e. well below the threshold for network formation. In practical systems, such as paints, the polymer is always present in concentrations above this threshold. This makes one

wonder how results obtained in dilute polymer solutions translate into effects in a more concentrated regime. Unfortunately, performing CP-AFM measurements in concentrated systems is difficult, as the high viscosity of the associative thickener networks induce large drag forces on the cantilever that obscure the forces of interest. As a result, we must turn to other ways to study colloidal interactions.

A classical way to assess interactions between colloidal particles is viscosimetry. For a suspension of undeformable and impenetrable spheres, the relative viscosity η_r , i.e. the actual viscosity of the sample over that of the suspending medium can be written as a virial expansion⁸:

$$\eta_r = 1 + 2.5\phi + k_2\phi^2 + \dots \quad (12.1)$$

where the term linear in the volume fraction ϕ is a single particle term that is due to the deformation of the flow field around the particle, as derived by Einstein. The higher order terms are due to particle-particle interactions. For hard spheres, the second virial coefficient k_2 , according to Batchelor, is equal to 6.3, accounting for hydrodynamic interactions between two particles in a Newtonian medium [6]. When other interactions come into play, the value of k_2 will change; repulsive interactions lead to increased excluded volume, thus higher values of k_2 and weak attractive interactions result in the opposite. Strong attractive interactions that lead to clustering of the particles also tend to increase the viscosity of the sample, as the effective volume fraction of aggregates, which entrap part of the solvent, is larger than the volume fraction of these particles prior to aggregation.

Now let's look at the results from a relatively simple experiment (Figure S3), where we compare the increase in relative viscosity of latex particles suspended in water and in a solution of associative polymers that has formed a transient network. The latex particles in pure water, already show some additional electrostatic repulsion. When the medium is changed to the transient polymer network, rather than observing a decrease in virial coefficient due to bridging interactions, we see that the polymer matrix creates a significantly larger repulsion between the particles. We can rescale the measurements onto the classical Einstein-Batchelor prediction for hard spheres to extract the effective hard sphere volume fraction, and the corresponding effective particle radius. In this specific case, we find an increase in effective radius, between the latex particles suspended in water and in a telechelic polymer solution, of approximately 30 nm, which is much larger than a single adsorbed layer of these polymers. This might be explained by the fact that

⁸virial expansion: expressing a property (e.g., pressure or viscosity) of an ensemble of particles as a power series in the density. The proportionality constants of the various terms, the virial coefficients, are related to interactions between the particles.

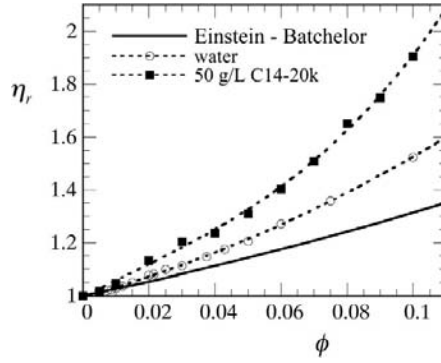


Figure S3: Relative viscosity η_r of 100 nm polystyrene latex particles, thoroughly cleaned by dialysis, dispersed in either water (open symbols) or in an associative polymer network (filled symbols). Solid line is the prediction by the classical Einstein-Batchelor equation for hard spheres.

hydrodynamic interactions are relatively long ranged in viscoelastic fluids, compared to hydrodynamic interactions in purely viscous fluids. Note that we did not observe any aggregation in these samples, even after several weeks.

Although AFM measurements by Courvoisier *et al.* [4] indicate that telechelic polymers induce a significant bridging attraction between polystyrene surfaces in dilute solutions, we find that this effect is absent, or at least dominated by the hydrodynamic repulsion discussed above, in concentrated solutions of the same telechelic polymers.

A similar conclusion follows from microscopy experiments (Fig.S4). Fluorescently labelled polystyrene particles suspended in a dilute (i.e. 0.5 g/L, well below the network threshold) solution of an associative thickener, tend to cluster and sediment rapidly to the bottom of the sample (Fig.S4a and c). The same particles suspended in a concentrated solution of the same polymer (Fig.S4b and d) remain homogeneously dispersed and do not show any signs of clustering, even after several days. Both simple experiments illustrate the limited applicability of the study of colloidal interactions in dilute solutions of telechelic polymers to those in more concentrated polymer solutions.

Nevertheless, phase separation is observed in many practical cases. One manifestation is the separation of a layer of clear liquid on top of a latex paint (clear liquid separation or paint syneresis). To find out what is driving this demixing one should analyze both phases to distinguish between the two main types of phase separation mechanisms. The first is segregative demixing, in which the two in-

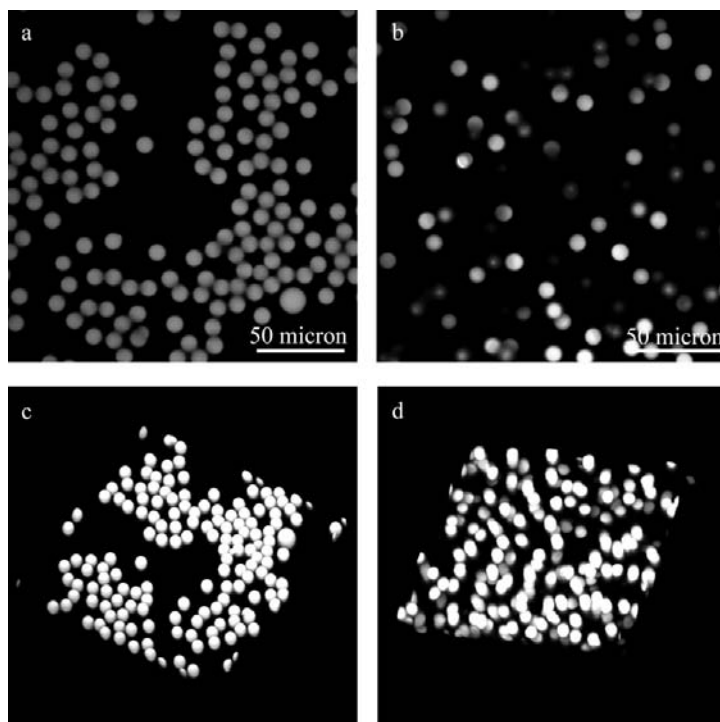


Figure S4: Confocal microscopy images of 10 μm fluorescent polystyrene particles suspended in aqueous solutions of an octadecyl-modified PEO of 35 kg/mol at 0.5 g/L (a and c) or 50 g/L (b and d). Images a and b are 2D slices, images c and d are 3D images from z-stacks.

interacting species (in this case the thickeners and the latex/pigment particles) are incompatible and will segregate into the two coexisting phases. A well-known example of such a mechanism is depletion, which occurs when polymers do not adsorb onto the surfaces of particles that are suspended in the polymer solution. In real paints such a scenario might be induced when surfactants, often present in large quantities, preferentially adsorb onto the particles, causing the polymer to desorb.

The second general phase separation mechanism is that of associative demixing, in which the two interacting species have a strong attraction to each-other, and expel excess water to reach an optimum density. In this case both thickener and particles will be in the same phase, while the coexisting phase contains mainly water and possibly some other components (e.g., surfactants). Such a scenario might result from a capillary effect [7] or from weak bridging interactions.

One thing both scenarios have in common is that the strength of the attrac-

tion depends on the difference in surface and bulk concentration of the polymer. In general, the larger the difference, the larger the attractive forces between the particles. In dilute solutions of thickeners it is quite clear that adsorption leads to a higher surface concentration than in bulk, while depletion gives a negative excess concentration at the surface. In a concentrated system these effects are naturally more subtle. Nevertheless, the experiment proposed above (i.e. analyzing the two phases in a demixed paint), seems vital as both scenarios require different measures to prevent the undesired demixing. While a depletion-driven demixing can be prevented by improving the adsorption of the polymers onto the particles, preventing an associative phase separation requires just the opposite.

(Micro)Rheology⁹

In the formulation of associative thickeners for commercial products, the strive is to accomplish an optimal interplay of all ingredients. One of the main efforts is to have a synergistic effect between colloidal particles and the polymer networks. When particles become part of the polymer network, e.g. by adsorption of the micellar nodes of polymeric chains onto the particle surface, they act as multifunctional junction points, thus increasing the modulus and viscosity of the formulation (active fillers). On the other hand, when adsorption of the network onto the particles is prevented (passive fillers), e.g., by the preferential adsorption of available surfactants onto the surfaces, this synergy is lost and particles might even act as 'flaws' in the network accomplishing an opposite effect [8, 9].

In Chapter 9 we have shown that we can distinguish between the active and passive fillers with Dynamic Light Scattering¹⁰, by analyzing the motion of the particles at short time scales. Connected, i.e. active, fillers follow the motion of the polymer chains at short time scales, whereas unconnected, i.e. passive, fillers show 'normal' diffusive motion. The polymer-like (Rouse-) dynamics of the colloids that we encountered in these experiments could be rationalized by constructing an analytical bead-spring model of a large particle connected to a set of polymer chains. With these results we are able to connect macroscopic observations of

⁹rheology: the study of the flow and deformation of matter. (Passive) microrheology: the mechanical properties of a material are deduced from the thermal motion of probe particles that are embedded in the matrix of interest.

¹⁰Dynamic Light Scattering: laser light is passed through the sample of interest. When the photons encounter a scattering object, e.g., a colloidal particle, they are scattered in all directions. A photodetector records the intensity of the light scattered by the sample. Fluctuations in the intensity of this scattered light are analyzed to give information on the internal dynamics of the sample.

synergistic effects for certain particles, to their behavior on a single particle level.

In the remainder of Part 3 we focussed on the rheology of associative thickeners under large deformation. In Chapter 10 we have shown that, due to strong shear thinning ¹¹, the flow can become mechanically unstable. This instability, known as shear banding, decomposes the sample into two (or sometime three) zones that differ in internal structure, viscosity and possibly density. Once the flow is stopped, the sample regains its quiescent state. With a variety of rheometry techniques we analyzed the shear banding transition in associative polymer networks and we showed that it is the direct result of an enhancement of the microscopic relaxation kinetics in these networks caused by the shear forces on the associating stickers.

The traditional picture of shear banding in soft materials predicts the formation of 2 bands separated by a flat interface, with which a single steady-state stress is associated. In telechelic polymer systems, such a steady state is often not reached. Under transient flow at a fixed imposed shear rate, the measured stress endlessly fluctuates. Other authors have studied such behavior in different systems [10, 11] and coined these fluctuations 'rheochaos', due to the apparent chaotic nature of these fluctuations. In Chapter 11 we have shown that in our case these apparently chaotic dynamics are characterized by an underlying statistical pattern. The statistical signature of these fluctuations reveals signs of self-organized criticality, i.e. a robust critical state reached spontaneously when highly non-linear systems are actively driven (in this case by means of shear flow) from equilibrium. Interestingly, the fluctuations associated with this self-driven critical state can be understood in the same way as critical fluctuations in liquid-fluid coexistence. This illustrates that concepts from equilibrium phase coexistence theories can be employed to understand this apparently more complex non-equilibrium, mechanically-induced phase transition.

The main feature of associative thickeners that makes them useful rheology modifiers for paints, is their shear thinning behavior. During application of the paint, which occurs at high shear rates (the estimated maximum shear rate accomplished during brushing is approximately 10^4 s^{-1}), it should have a low viscosity to facilitate the brushing. Immediately after application, the viscosity should increase to prevent sagging and dripping. As we have shown, shear thinning can be accompanied by a mechanical instability. It is also known that shear banding can induce partitioning of either the polymer [12] or the particles [13] in one of the bands. This might lead to undesirable inhomogeneities in the coating after application.

Many available techniques to study such mechanical instabilities under con-

¹¹shear thinning: a viscosity that decreases with increasing rate of deformation.

trolled shear rely on optics for visualization of the flow or for measuring the local fluid velocity across a sample. As most 'real' systems are highly opaque, these techniques cannot be employed. However, with the rheo-MRI technique, a combination of rheometry and Magnetic Resonance Imaging, sample turbidity is not an issue. Rheo-MRI, as pioneered by Paul Callaghan [14], was implemented in Wageningen during this PhD project (see Chapter 12) in a cooperation with the Wageningen NMR Centre. In addition to velocimetry experiments, rheo-MRI offers the possibility to measure local proton densities and spin relaxation times to study inhomogeneities in density. In a strong enough magnetic field one can even perform accurate and spatially resolved spectral NMR for studying structural transitions under shear on a molecular scale. This makes rheo-MRI a highly suitable technique to investigate flow instabilities in complex systems. The first results on this set-up, discussed in Chapter 12, look promising. Nonetheless, still significant efforts must be made in order to reach the full potential of the technique in the current set-up.

Outlook

Over the course of the past 4 years we have made some significant steps in understanding network-forming polymers in our study of model associative thickeners. With the lessons learned, new variables can be added to the equation, in a strive for novel materials with increased responsiveness to environmental parameters, that are biocompatible for use in drug delivery systems, that can replace food thickeners from potentially hazardous origin (e.g. gelatin) or that can act as cell-growth scaffolds. Several new projects within the Laboratory of Physical Chemistry and Colloid Science have set out in this direction.

An interesting example is the project that studies telechelic polymer systems that assemble by means of electrostatic interactions, rather than relying on hydrophobic interactions. The resulting materials should be highly responsive to environmental triggers such as ionic strength and pH, allowing more flexibility in achieving the desired properties without the need to design and synthesize new polymers, as is the case with traditional thickeners.

Another fascinating perspective lies in the development of self-associating designer proteins, now available through advanced bioengineering techniques [15]. These protein polymers use natural protein association motifs (e.g., β -sheets or collagen-like triple helices) to create biomimetic materials. The high selectivity of these natural association mechanisms, compared to 'crude' hydrophobic interactions, offers new tunability to these materials, e.g. the preparation of networks

with nodes of perfectly defined and monodisperse multiplicity [16].

I can only modestly hope that the ideas put forward in this thesis might form some sort of basis for these exciting developments.

References

- [1] Leermakers, F. A. M.; Eriksson, J. C.; Lyklema, J. In *Fundamentals of Interface and Colloid Science. Volume V: Soft Colloids*; Academic Press Ltd., London, 2005; chapter 4.
- [2] Noble, R. W.; Waugh, D. F. *J. Am. Chem. Soc.* **1965**, *87*, 2236.
- [3] Orr, F. M.; Scriven, L. E.; Rivas, A. P. *J. Fluid Mech.* **1975**, *67*, 723.
- [4] Courvoisier, A.; Isel, F.; Francois, J.; Maaloum, M. *Langmuir* **1998**, *14*, 3727.
- [5] Ligoure, C. *Macromolecules* **1991**, *24*, 2968.
- [6] Larson, R. G. *The Structure and Rheology of Complex Fluids*; Oxford University Press (USA), 1998.
- [7] Olsson, M.; Joabsson, F.; Picullel, L. *Langmuir* **2005**, *21*, 1560.
- [8] Mackay, M. E.; Dao, T. T.; Tuteja, A.; Ho, D. L.; van Horn, B.; Kim, H. C.; Hawker, C. J. *Nature Materials* **2003**, *2*, 762.
- [9] Sala, G.; van Aken, G. A.; Cohen Stuart, M. A.; van de Velde, F. *J. Texture Stud.* **2007**, *38*, 511.
- [10] Ganapathy, R.; Sood, A. *Phys. Rev. Letters* **2006**, *96*, 108301.
- [11] Fielding, S. M. *Soft Matter* **2007**, *3*, 1262.
- [12] van den Noort, A.; Briels, W. J. *J. Non-Newtonian Fluid Mech.* **2007**, *152*, 148.
- [13] Huang, N.; Bonn, D. *J. Fluid Mech.* **2007**, *590*, 497.
- [14] Callaghan, P. T. In *Encyclopedia of Nuclear Magnetic Resonance. Volume 9*; Grant, D. M., Harris, R., Eds.; Wiley & Sons, Chichester, 2002; chapter Rheo-NMR; A New Window on the Rheology of Complex Fluids.
- [15] Werten, M. W. T.; Teles, H.; Moers, A. P. H. A.; Wolbert, E. J. H.; Sprakel, J.; Eggink, G. *Biomacromolecules* **2009**, *accepted for publication*.
- [16] Skrzyszewska, P. J.; de Wolf, F. A.; Cohen Stuart, M. A.; Werten, M. W. T.; van der Gucht, J. *Soft Matter* **2009**, in press.

Nederlandse Samenvatting:
**‘Fysica van associërende polymeren;
tijd- en lengteschalen overbrugd’**

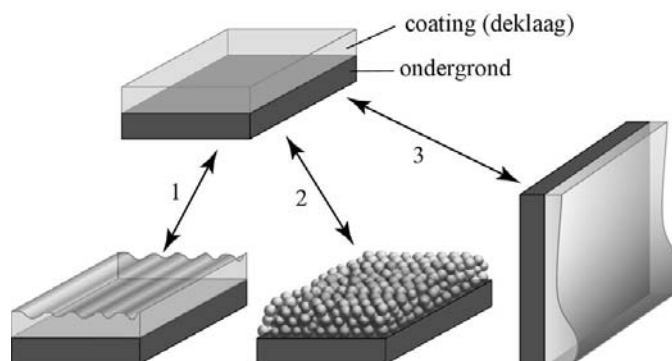


Samenvatting

Traditionele verven en lakken bevatten grote hoeveelheden vluchtige organische verbindingen (VOCs = volatile organic compounds), die als oplosmiddel dienen voor de filmvormende component (hars of 'binder') en die tijdens het droogproces in de lucht vrijkomen. In recente jaren is vast komen te staan dat langdurige blootstelling aan een VOC-rijke atmosfeer tot ernstige gezondheidsklachten kan leiden, waarvan de zogenaamde schildersziekte de meest beruchte is. Daarnaast leidt VOC uitstoot tot ozonvorming in de troposfeer, waarvan wordt gedacht dat het tot opwarming van de aarde leidt. Als op één na grootste bron van VOC emissie dragen verven, lakken en lijmen significant bij aan de huidige milieuproblematiek. Om deze redenen heeft de EU richtlijnen aangenomen voor het geleidelijk terugdringen, en uiteindelijk uitbannen, van VOC rijke coatingsproducten, en maken soortgelijke aanbevelingen deel uit van internationale verdragen zoals het Kyoto-protocol.

Bij het bereiken van VOC reductie spelen watergedragen verven, waarin (bijna) alle organische oplosmiddelen vervangen zijn door water, een belangrijke rol. Hoewel watergedragen verven het milieu en gebruikers nagenoeg niet belasten, kunnen de coatings die ze opleveren nog niet in alle opzichten concurreren met de kwaliteit van de traditionele oplosmiddelgedragen verven. Een aantal van de problemen met watergedragen verven die tot een verminderde kwaliteit van de uiteindelijke coating leiden zijn geïllustreerd in Figuur 1. Voor een verdere verdringing van VOC-rijke producten is het van belang dat deze kwaliteitsproblemen worden onderzocht en opgelost. Het onderzoek beschreven in dit proefschrift levert daar een bijdrage aan.

Watergedragen verven zijn eigenlijk dispersies van kleine polymeerdeeltjes in water; men noemt zo'n dispersie ook wel een latex. Zonder toevoeging van een verdikkingsmiddel zouden latexverven een viscositeit ('stroperigheid') hebben als die van melk. Direct na het aanbrengen zou zo'n verf uitzakken onder invloed van de zwaartekracht (zie Figuur 1 rechtsonderaan). Om dat te voorkomen en te zorgen dat de verf in een voldoende dikke laag kan worden aangebracht, worden

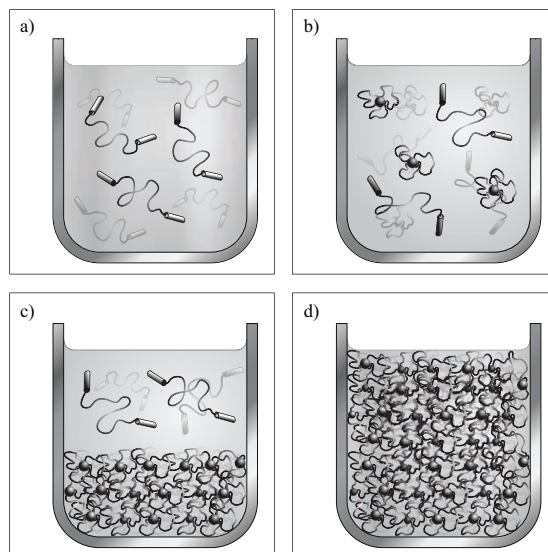


Figuur 1: Illustratie van een aantal van de problemen die tot een slechte kwaliteit van een coating kunnen leiden. Een ideale deklaag (boven) is een vlakke homogene laag van uniforme dikte. Complicaties zijn onder andere: 1) slechte uitvloeiing; borstelstreken blijven zichtbaar in de coating. 2) inhomogene film: een gebrek aan coalescentie (samenvloeien) van de latexdeeltjes geeft een onregelmatige en poreuze laag. 3) uitzakken: onder invloed van de zwaartekracht stroomt/druipt de verf naar beneden.

verdikkers toegevoegd aan moderne watergedragen verven.

Als verdikkingsmiddel worden associërende polymeren gebruikt. Dit zijn grote moleculen (macromoleculen of polymeren) die bestaan uit een lang waterminnend middenstuk en twee korte watervrezende uiteinden (Figuur 2a). Opgelost in water vormen deze moleculen uit zichzelf (spontaan) kleine objecten, bestaand uit een aantal polymeermoleculen, in een proces dat zelf-assemblage of zelf-associatie wordt genoemd. De watervrezende delen plakken aan elkaar (associëren) om het contact met water zoveel mogelijk te beperken, terwijl de waterminnende delen elkaar juist afstoten om zoveel mogelijk contact met het water te hebben. Een subtiële balans tussen deze twee tegengestelde krachten zorgt voor de vorming van nanoscopisch kleine deeltjes, die micellen worden genoemd (Figuur 2b). Vervolgens associëren deze micellen weer met elkaar totdat er uiteindelijk een netwerk van aan elkaar verbonden micellen wordt gevormd dat de gehele vloeistof overspant (Figuur 2d). Het zijn deze netwerken die de gewenste eigenschappen hebben voor toepassing als verdikkingsmiddel, niet alleen verven en cosmetica, maar ook in bijvoorbeeld boorvloeistoffen voor de extractie van aardolie.

In het eerste deel van dit proefschrift hebben we het zelf-assemblage proces van associatieve verdikkers in detail bestudeerd. We hebben een relatief simpele beschrijving gemaakt van dit proces, in de vorm van analytische formules, waarin we ons geconcentreerd hebben op de hoofdlijnen. Hierdoor hebben we een goed beeld kunnen vormen van de belangrijkste fysische aspecten. Daarnaast hebben



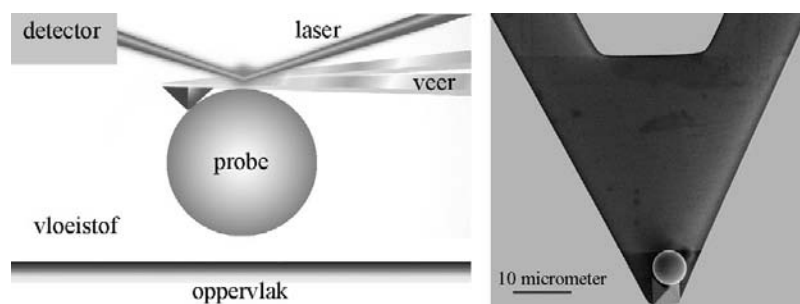
Figuur 2: Illustratie van de 4 stadia in de zelf-assemblage van associatieve verdikkers bij toenemende concentratie van a) naar d); a) bij hele lage concentraties zijn de ketens niet geassocieerd, b) boven een bepaalde drempel concentratie assembleren de polymeren in micellen, c) soms leidt de opeenvolgende associatie van micellen tot ontmenging van het systeem in een polymeer-rijke en een polymeer-arme fase, d) als de polymeerconcentratie hoog genoeg is (typisch ongeveer 1 gewichtsprocent) vormen de geassocieerde micellen een macroscopisch netwerk.

we meer gedetailleerde (en complexere) computerberekeningen uitgevoerd welke in goede overeenstemming bleken met het simpele model. Op deze manier hebben we een compleet beeld van de zelf-assemblage van associatieve polymeren verkregen. Dit heeft formules opgeleverd die als ontwerpregels kunnen worden toegepast bij het maken van nieuwe verdikkers.

In het tweede deel van dit boekje staat beschreven hoe associatieve verdikkers wisselwerken met oppervlakken. Verven bestaan voor een groot deel uit kleine deeltjes of druppeltjes, die gezamenlijk een zeer groot oppervlak vertegenwoordigen. Het totale beschikbare oppervlak in een liter latexverf, die typisch voor ongeveer 40 % bestaat uit deeltjes van 100 nanometer groot, is zo'n 12.000 vierkante meter (meer dan 2 voetbalvelden!). De vraag hoe associatieve polymeren wisselwerken met oppervlakken is daarom een centraal thema in het onderzoek naar watergedragen verven. Het vermoeden bestond dat deze verdikkers aantrekkingskrachten tussen deeltjes kunnen veroorzaken, waardoor de deeltjes de neiging hebben om samen te klonteren in plaats van homogeen over de verf verspreid te blijven. In dit

deel van mijn onderzoek hebben we 2 verschillende mechanismen blootgelegd die tot zulke aantrekkingskrachten kunnen leiden. Het eerste mechanisme, waarover al veelvuldig in de literatuur werd gesproken, is de vorming van zogenaamde bruggen tussen de oppervlakken doordat polymeerketens tegelijkertijd aan beide oppervlakken gebonden zijn. Omdat de polymeerketens als kleine veertjes werken, leidt het trekken aan deze bruggen tot een kracht in tegengestelde richting als waarin de ketens zijn uitgerekt (net als bij een gewone veer). Het tweede mechanisme, dat tot op dit punt over het hoofd was gezien, speelt zich op grotere schaal af, dat wil zeggen dat het niet door enkele moleculen wordt veroorzaakt maar door een groot aantal polymeerketens tezamen. Ingeperkt tussen twee oppervlakken kan zich uit een oplossing van deze verdikkers spontaan een onoplosbare druppel van een polymeer-rijke fase vormen; een verschijnsel dat capillaire condensatie heet. Het uitrekken van zijn druppel die aan beide oppervlakken kleeft, leidt eveneens tot een kracht in tegengestelde richting. Dit soort krachten, capillaire krachten genoemd, zijn ook de reden dat zandkorrels bij elkaar worden gehouden (in dit geval door kleine waterdruppels) in een zandkasteel. Het water werkt als een lijm die de zandkorrels bij elkaar houdt. Zonder deze kleine hoeveelheid water, dus met kurkdroog zand, kan je dan ook geen zandkasteel bouwen omdat de capillaire adhesiekracht afwezig is. Naast theoretische bestudering van deze mechanismen, hebben we beide soorten aantrekkingskrachten ook direct kunnen meten met een zogenaamde atoomkrachtmicroscop (AFM = Atomic Force Microscope), waarmee krachten tot 10 picoNewton (= 1 honderdmiljardste Newton) gemeten kunnen worden (zie Figuur 3). Omdat klontering van de deeltjes veelal ongewenst is, proberen verfproducenten dit soort aantrekkingskrachten te onderdrukken. Een gestructureerde aanpak hiervan vereist een fundamenteel begrip van de onderliggende mechanismen, waaraan we in dit deel van het proefschrift hebben bijgedragen.

In het derde, en laatste deel van dit proefschrift zijn de stromingseigenschappen van associatieve verdikkers onderzocht. Naast hun directe praktische nut fungeren deze netwerken als een geschikt modelsysteem voor een veel grotere verzameling aan visco-elastische materialen. Visco-elastische materialen, zoals silly putty, gedragen zich bij een snelle, abrupte vervorming als een vaste stof, maar als je ze de tijd geeft om zich aan een opgelegde kracht aan te passen gedragen ze zich als een vloeistof. Visco-elasticiteit is een veelvoorkomende materiaaleigenschap, denk hierbij naast verven ook aan tal van half-vloeibare levensmiddelen (sauzen, zuivelproducten, desserts), bloed, biologische weefsels, shampoo, etc. Hoewel de mechanische basiskarakteristieken van deze associatieve verdikkers zeer eenvoudig lijken te zijn, hebben wij laten zien dat het stromingsgedrag allesbehalve eenvoudig te noemen is. Kleine breukjes en zelfherstelmechanismen in het materiaal zorgen



Figuur 3: Links: Schematische tekening van de atoomkrachtmicroscop. Een laser schijnt op een reflecterende cantilever (veer) en het gereflecteerde licht valt op een detector. Doorbuiging van de cantilever, door duw- of trekkrachten tussen het oppervlak en een bolvormige deeltje, wordt waargenomen door de verplaatsing van de laser op de detector te volgen. Het oppervlak is gemonteerd op plateau waarmee het oppervlak op de nanometer nauwkeurig ten opzichte van de probe bewogen kan worden. Op deze manier kan de kracht tussen oppervlak en deeltje als functie van de onderlinge afstand worden gemeten. Rechts: Electronenmicroscopische foto van een kolloidale probe bevestigd op een standaard AFM cantilever.

voor een zeer onverwacht verschijnsel, namelijk hele grote en continue fluctuaties in de kracht benodigd om het materiaal met een constante snelheid te vervormen. Deze fluctuaties hebben nog het meest weg van hele zwakke aardbevingen (met een grootte van -6 op de schaal van Richter), dat wil zeggen de door ons gemeten fluctuaties voldoen aan dezelfde statistische wetmatigheden die ook voor aardbevingen gelden. Uit onze analyse bleek bovendien dat dit soort stromingsverschijnselen, die voorheen als zeer exotisch werden beschouwd, in feite veel algemener zijn en voor een veelvoud aan materialen verwacht mogen worden.

Veel van de resultaten die in dit boekje staan beschreven zijn van generieke aard, dat wil zeggen niet alleen toepasbaar op deze specifieke moleculen maar ook bruikbaar voor het beschrijven van andere typen zelf-assemblerende polymeren. Nieuwe projecten binnen het laboratorium voor Fysische Chemie en Kolloïdkunde hebben koers gezet naar de ontwikkeling van nieuwe, slimmere materialen, gebaseerd op gelijksoortige moleculen. Deze materialen moeten bijvoorbeeld toegang geven tot nieuwe mogelijkheden om de eigenschappen van het materiaal te sturen, bv. gevoeligheid voor de omgevingsomstandigheden, of betere biocompatibiliteit (voor gebruik in geneesmiddelen of als matrix voor weefselkweek). Hopelijk vormen de stappen die tijdens dit project zijn gezet een basis voor deze spannende ontwikkelingen.

List of Publications

THIS DISSERTATION:

- J. Sprakel, P. Skrzyszewska, J. van der Gucht, F.A.M. Leermakers and M.A. Cohen Stuart: **Physics of transient network-forming associative polymers**, in preparation. (review article)
- J. Sprakel, E. Spruijt, M.A. Cohen Stuart, M.A.J. Michels and J. van der Gucht: **Intermittent fracture and self-healing in a viscoelastic fluid**, submitted. (Chapter 11)
- J. Sprakel: **Hierarchical adsorption of network-forming associative polymers**. *Langmuir* in press (2009). (Chapter 8)
- J. Sprakel, E. Bartscherer, G. Hoffmann, M.A. Cohen Stuart and J. van der Gucht: **Dynamics of polymer bridge formation and disruption** *Physical Review E* 78, 040802 (2008). (Chapter 7)
- J. Sprakel, F.A.M. Leermakers, M.A. Cohen Stuart and N.A.M. Besseling: **Comprehensive theory for star-like polymer micelles; combining classical nucleation and polymer brush theory** *Physical Chemistry Chemical Physics* 10, 5308-5316 (2008). (Chapter 2)
- J. Sprakel, E. Spruijt, M.A. Cohen Stuart, N.A.M. Besseling, M.P. Lettinga and J. van der Gucht: **Shear banding and rheochaos in associative polymer networks** *Soft Matter* 4, 1696-1705 (2008). (Chapter 10)
- J. Sprakel, J. van der Gucht, M.A. Cohen Stuart and N.A.M. Besseling: **Brownian particles in transient polymer networks**. *Physical Review E* 77, 061502 (2008). (Chapter 9)
- J. Sprakel, N.A.M. Besseling, M.A. Cohen Stuart and F.A.M. Leermakers: **Phase behavior of flowerlike micelles in a SCF cell model**. *European Physical Journal E* 25, 163-173 (2008). (Chapter 4)
- J. Sprakel, N.A.M. Besseling, M.A. Cohen Stuart and, F.A.M. Leermakers: **Capillary adhesion in the limit of saturation: thermodynamics, self-consistent field modeling and experiment**. *Langmuir* 24, 1308-1317

(2008). (Chapter 6)

- J. Sprakel, J. van der Gucht, M. A. Cohen Stuart and N.A.M. Besseling: **Rouse dynamics of colloids bound to polymer networks.** *Physical Review Letters* 99, 208301 (2007). (Chapter 9)
- J. Sprakel, N.A.M. Besseling, F.A.M. Leermakers and M.A. Cohen Stuart: **Equilibrium capillary forces with atomic force microscopy** *Physical Review Letters* 99, 104504 (2007). (Chapter 5)
- J. Sprakel, N.A.M. Besseling, F.A.M. Leermakers and M.A. Cohen Stuart: **Micellization of telechelic associative polymers: self-consistent field modelling and comparison with scaling concepts.** *Journal of Physical Chemistry B* 111, 2903-2909 (2007). (Chapter 3)

OTHER WORK:

- I.K. Voets, R. de Vries, R. Fokking, J. Sprakel, R. May, A. de Keizer and M.A. Cohen Stuart: **On the structure of spherical complex coacervate core micelles.** submitted.
- L.E. Riemsdijk, J. Sprakel, A.J. van der Goot and R.J. Hamer: **Protein micro-particle networks; controlling the rheology of high protein products through mesostructural ordering.** submitted.
- M.W.T. Werten, H. Teles, A.P.H.A. Moers, E.J.H. Wolbert, J. Sprakel, G. Eggink and F.A. de Wolf: **Precision gels from collagen-inspired tri-block copolymers** accepted for publication *Biomacromolecules* (2009).
- F.A.M. Leermakers, J. Sprakel, N.A.M. Besseling and P.A. Barneveld: **On the curvature dependence of the interfacial tension in a symmetric three-component interface.** *Physical Chemistry Chemical Physics* 9, 167-179 (2007).
- F.A.M. Leermakers, P.A. Barneveld, J. Sprakel and N.A.M. Besseling: **Symmetric liquid-liquid interface with a non-zero spontaneous curvature.** *Physical Review Letters* 97, 066103 (2006).
- E. Scholten, J. Sprakel, L.M.C. Sagis and E. van der Linden: **Effect of interfacial permeability on droplet relaxation in biopolymer-based water-in-water emulsions.** *Biomacromolecules* 7, 339-346 (2006).
- B. Moorthaemer and J. Sprakel: **Improving the stability of a suspension.** *Pharmaceutical Technology Europe* 18, 30-34 (2006).

Dankwoord

Het is u wellicht opgevallen dat er in de voorgaande hoofdstukken steeds wordt gesproken vanuit de 1e persoon meervoud (*wij*), terwijl er slechts 1 naam op de omslag prijkt. Dit is niet wegens grootheidswaan (*pluralis majestatis*) of een meervoudige persoonlijkheidsstoornis (*me, myself and I*), maar omdat het gepresenteerde werk een teaminspanning is. Bij deze krijgt het beestje dan ook een naam!

Martien, ik vind het heel bijzonder hoe jij, ondanks je drukke agenda, van al de (vele) projecten binnen onze groep precies weet wat er gebeurt en dat je altijd op het juiste moment de juiste suggesties doet. Ik ben je dankbaar dat ik onder jouw hoede mijn promotieonderzoek heb mogen doen en dat je me het vertrouwen hebt gegeven hierin mijn eigen weg te ontdekken.

Frans, het was jouw enthousiasme op het praktikum kolloidkunde tijdens mijn studie, dat me deed kiezen voor de fysische chemie. Dit onuitputtelijke enthousiasme en optimisme, je scherpe geest en je onorthodoxe, soms wat verwarrende maar effectieve motiveringstechnieken ("dat is allemaal ruis") maken je tot een fantastische begeleider.

Klaas, tijdens de eerste helft van dit project hebben we prettig samengewerkt, en ik heb in deze periode veel van je geleerd, met name het analytisch benaderen van lastige problemen en het belang van zorgvuldigheid en precisie, waarvoor ik je dankbaar ben.

Jasper, ik kan niet anders zeggen dan dat ik heb genoten van onze samenwerking. De schijnbare moeiteloosheid waarmee jij ingewikkelde vraagstukken tot heldere en begrijpbare concepten weet te ontleden is onnavolgbaar en zeer inspirerend. Je bent een hele relaxte, stimulerende en behulpzame begeleider, die zijn AIO's echt boven zich uit kan laten stijgen. Ik hoop dat dit project slechts het begin van onze samenwerking is, want ik denk dat we een goed team vormen.

Naast dit team van begeleiders waren er vele anderen die direct of indirect een bijdrage hebben geleverd aan dit proefschrift. Evan, ik weet dat je niet van grote complimenten houdt, maar eerlijk is eerlijk, ik had natuurlijk geen betere

afstudeervakker kunnen treffen dan jij. Je bent een ontzettend slimme kerel, en nog gezellig ook. Het was echt een plezier met je te werken. Anouk, je onderzoek viel niet direct binnen mijn promotieonderzoek, maar ik had toch het genoegen je samen met Jasper te mogen begeleiden. De samenwerking was erg leuk en je hebt het heel goed gedaan.

During these 4 years I had the opportunity to collaborate with a variety of scientists from various places and backgrounds, which has enormously enriched my PhD experience. I am very thankful to Anthonie Stuiver & Karel van Streun (Akzo Nobel Coatings Research), Soren Hvidt (Roskilde University), Thijs Michels (Eindhoven University of Technology), Pavlik Lettinga (Forschungszentrum Jülich) and the guys at nAmbition/JPK Instruments. Also many thanks to the 4 distinguished gentlemen in my jury (professors Mulder, Weitz, Dhont and Berret) for taking part in this special day. Ook mijn dank voor John van Haare, Harold Gankema en de ICPs van het Dutch Polymer Institute, die vanaf het begin zeer behulpzaam en geïnteresseerd bij mijn project betrokken zijn geweest.

Voor het werk aan 'onze' rheo-MRI ben ik Frank Vergeldt, John Philippi, Henk van As en Edo Gerkema van het Wageningen NMR Centre en de heren van de Ontwikkelwerkplaats zeer erkentelijk.

In de laatste maanden van mijn AIO-schap ben ik te gast geweest in de Computational Biophysics groep van Wim Briels aan de Universiteit van Twente. Mijn grote dank aan Wim, Johan en Wouter; ik ben heel blij dat ik de kans heb gehad om bij zo'n club van experts in de leer te mogen gaan. Marten, dank voor de vele technische adviezen!

Mara, barones van Winkels tot Vink, het feit dat je vandaag als paranimf naast me staat geeft wel aan hoe speciaal onze band is. Wij hebben echt aan één blik of woord genoeg. Ik ga onze wekelijkse (vaak dagelijke) sessies enorm missen. Anita, bedankt voor je gezelligheid op de vele leuke momenten en je steun op die paar moeilijke momenten, daar heb ik meer aan gehad dan je kan voorstellen. Josie, bedankt dat je je levenswijsheid en grenzeloze optimisme met me wilde delen. Rindert, het was fijn om regelmatig (onder het genot van een peuk) te kunnen praten (en mopperen) met iemand die zo op dezelfde golflengte zit. Remco, überknutselaar, waar zouden mensen met twee linkerhanden zijn zonder zulke goede technici als jij? Gert, bedankt voor alle mooie illustraties! Alle fijne collega's van de Leerstoelgroep mijn hartelijke dank voor jullie hulp en ondersteuning.

Saskia, ik vond het erg gezellig met je op het lab, als kantoorburen en tijdens de buitenland tripjes – we halen het ranzigste in elkaar naar boven. Ilja, het was fijn om met elkaar te kunnen sparren over het werk en onze sores te kunnen delen, hopelijk komt die samenwerking er snel van. Paulinka, roommate, it is amazing to

see how quickly you went from a biotechnologist to a rheologist, good luck with your magic puddings! Marc, het was leuk om over je schouders mee te kijken bij je zoektocht naar nieuwe en betere verdikkers en om tijdens de gesprekjes in het lab te proberen die lastige chemieproblemen op te lossen. Maak er wat moois van! Wiebe en Bas, onze zeer efficiënte samenwerking in het organiseren van de PhD trip was erg plezierig en het begin van een nieuwe Fysko-traditie.

Lieve bandgenoten en aanhang, de afgelopen 1,5 jaar in Utrecht waren geweldig. De repetities en optredens met de band, de etentjes in Oudaen, de tequilas in de Vingerhoed en de late (lees: kansloze) uurtjes in Hofman zal ik nooit vergeten. Ruud, je bent echt een goede vriend, ik kan me geen loyalere en fijnere maat voorstellen. Constant, het was fijn om alle frustraties over onze studie te kunnen delen met je en het is nog mooier om te zien dat we beiden uit die hoek 'gevlucht' zijn. Geert, Ovi en Corstiaen, de mini-revival van mijn studententijd toen ik op Wanton logeerde was precies wat ik nodig had, onwijs bedankt! Knol, bedankt voor de gezellige koffiebreaaks en alle mac-adviezen. Voor alle andere vrienden, oudbanders, clubgenoten en oudhuisgenoten: bedankt voor jullie vriendschap!

Janneke, we zijn veel betere vrienden dan dat we partners waren. Ik ben je oprecht dankbaar voor het nemen van die moeilijke beslissing; het heeft voor ons beiden erg goed uitgekapt. We hebben het fijn gehad samen.

Vera en William, ik vind het fantastisch om te zien hoe jullie een heerlijk gezinnetje hebben gesticht, en bewonder hoe jullie dit moeiteloos combineren met jullie carrière, familie en vrienden. Vera, ik vind het heel bijzonder dat jij vandaag naast me staat als paranimf, zoals ik dat 5 jaar geleden voor jou mocht doen. Ik wens jullie, en mijn twee oogappels Tobias en Hanna, alle geluk van de wereld.

Lieve pap en mam, ik vrees dat een alinea in een dankwoord nauwelijks recht doet aan de dank die ik jullie verschuldigd ben. Ik hou het daarom kort: bedankt dat jullie zulke liefdevolle, open-minded en simpelweg geweldige ouders voor me zijn. Dit proefschrift draag ik op aan jullie!

JORIS

Levensloop

Joris Sprakel is op 10 juni 1980 geboren in het Brabantse Oss. In 1998 haalde hij zijn Gymnasium diploma aan het Titus Bransma Lyceum te Oss en een International Baccalaureate English A2 aan de Lorentz International School te Arnhem. In datzelfde jaar startte Joris een studie Levensmiddelentechnologie aan de toenmalige Landbouwniversiteit Wageningen. Binnen deze studie heeft hij zich gespecialiseerd in de fysische chemie en natuurkunde van levensmiddelen, waarvan een belangrijk deel bestond uit 2 afstudeervakken (uitgevoerd bij de leerstoelgroep Food Physics aan Wageningen Universiteit en bij de Biomolecules, Interactions and Assemblies groep van het INRA te Nantes, Frankrijk) en een stage binnen de Technology Department van Organon NV Oss. Na zijn afstuderen in 2005 is Joris begonnen met een promotieonderzoek aan netwerkvormende polymeren binnen de vakgroep Fysische Chemie en Kolloïdkunde van prof. Martien Cohen Stuart aan Wageningen Universiteit, waarvan dit proefschrift het resultaat is. In de zomer van 2009 zal Joris, op een Rubicon-beurs van NWO, als postdoctoraal onderzoeker aan de slag gaan in de Experimental Soft Condensed Matter groep van prof. David Weitz aan Harvard University in Cambridge (USA).

Overview of completed training activities

Courses

Molecular Modelling, Wageningen, 2005

Structure and Dynamics of Biomolecules, Wageningen, 2006

Physical Chemistry Winterschool, Han-sur-Lesse (Belgium), 2007

RPK Polymer Physics, Utrecht, 2007

Suspension Rheology, Monterey (USA), 2008

Conferences & Colloquia

Physics@FOM, Veldhoven, 2009¹.

Annual DPI Meeting, Antwerpen (Belgium), 2008¹.

Colloquium Kamerlingh Onnes Laboratorium (Leiden), 2008¹.

ECIS, Krakow (Poland), 2008.

Colloquium Weitz group (Harvard), Cambridge (USA), 2008¹.

XVth International Congress on Rheology, Monterey (USA), 2008¹.

Soft Matter Meeting, Eindhoven, 2008¹.

Dutch Polymer Days, Lunteren, 2008¹.

Liquids and Interfaces, Lunteren, 2007¹ & 2008².

Colloquium Delft ChemTech (Delft University of Technology), Delft, 2008¹.

European Student Conference, Hven (Sweden), 2007¹.

Colloquium Institut für Physik (Joh. Gutenberg Univ.), Mainz (Germany), 2007¹.

Soft Matter Days, Bonn (Germany), 2006^{1,2}.

Annual DPI Meeting, Middelburg, 2006¹.

Macromolecules Conference, Prague (Czech Republic), 2006.

Autumn Meeting Macroscopic Physical Chemistry, Schiermonnikoog, 2005

¹oral presentation, ²poster

Other Meetings & Activities

Group meetings & colloquia 2005-2009.

DPI Coating Technology meetings 2005-2009.

PhD trip Sweden & Denmark, 2007.

